Measurements of ZZ production cross section using four-lepton events and constraints on anomalous triple gauge couplings at $\sqrt{s} = 13\,\text{TeV}$ using the CMS Detector at the CERN LHC

by

Usama Hussain

A dissertation submitted in partial fulfillment of

the requirements for the degree of

Doctor of Philosophy

(Physics)

at the

University of Wisconsin – Madison

2020

Defended on 24 September 2020

Dissertation approved by the following members of the Final Oral Committee:

Sridhara Dasu · Professor of Physics

Matthew Herndon · Professor of Physics

Kevin Black · Professor of Physics

Akikazu Hashimoto · Professor of Physics

Shimon Kolkowitz · Professor of Engineering and Physics

Abstract

Studies of four-lepton production in proton-proton collisions, pp $\rightarrow$ (Z/γ^*)(Z/γ^*) $\rightarrow 4\ell$, where ℓ = e or μ, using data collected during 2016-2018 (Run II) are presented. The dataset corresponds to an integrated luminosity of 137 fb^{-1} at a center-of-mass energy of 13 TeV, collected by the CMS detector at the LHC. All reported measurements use the $2\ell 2\ell'$ final states, where ℓ, ℓ' = e or μ. The total ZZ cross section for all events with two Z bosons in the mass range 60–120 GeV is measured and found to be $\sigma(\text{pp} \rightarrow \text{ZZ}) = 17.2 \pm 0.3\,(\text{stat}) \pm 0.5\,(\text{syst}) \pm 0.4\,(\text{theo}) \pm 0.3\,(\text{lumi})$ pb. Differential cross sections are measured as functions of a number of kinematic observables. All these results agree with standard model predictions. Searches for anomalous triple gauge couplings are performed, and the four-lepton invariant mass distributions are used to set the most stringent limits to date on a number of parameters affecting neutral gauge boson interactions.

Acknowledgements

To my parents, Kishvar and Shamim, thank you for your continuous, unwavering support, encouragement and love over my lifetime, and for the excellent educational opportunities you made available to me even when it meant enduring hardships and jumping into worlds that you knew very little about. Without those solid foundations, educational and otherwise, I surely would not have made it this far.

To my advisor(s) Prof. Sridhara Dasu, Prof. Wesley Smith and Prof. Matt Herndon, thank you for your sharp and valuable analysis of my abilities over the last six years, thank you for your support and your excellent guidance which seems to have an ever-expanding impact as time progresses. I especially want to thank Wesley while I worked as a TA for him for 3 semesters. I learned to be more precise, thorough and yet ever more understanding of other people's perspectives through this teaching experience.

To Alexander Savin, thank you for teaching and guiding me through the ecosystem of the CMS collaboration, for keeping me sharp and honest, helping me develop effective goal-oriented work habits and for instilling the confidence in me to present my work in front of large audiences. I also thank Sascha for everything else I have gained from working with him, some of which I surely will realize as time passes.

The postdocs, Varun Sharma, Camilla Galloni, Deborah Pinna, Isabel and Cécile Caillol, are uniformly brilliant and endlessly helpful. To Bhawna Gomber, thank you for your guidance and support in getting started with my research and for your continued guidance on both topics included in my thesis. Without your expert advice and resourcefulness, it would have made for a very difficult endeavor.

To Dan Bradley, Ajit Mohapatra, Carl Vuosalo, and the rest of the computing team, I owe many thanks as they always entertained my endless computing queries

and concerns. Without their prompt and helpful replies, I would have had a much more difficult time with the computing infrastructure.

To Pam Klabbers and Aleš Svetek who are fountains of knowledge about the CMS trigger, special thanks as they are fully responsible for any competence I appeared to display while on shift.

I would never have accomplished anything without the other UW CMS grad students with special thanks to Kenneth Long for his unwavering friendship and guidance in all matters of particle physics and life. Nick Smith, Nate Woods, Devin Taylor, Tyler Ruggles, James Buchanan, Tom Perry, Aaron Levine, Laura Dodd, and others with whom I overlapped more briefly, have been great friends and colleagues.

A special thanks to Senka Duric for the results and figures for the anomalous triple gauge couplings and to Evan Koenig for continuing the work and development of the Mono-Z' analysis from where I left off and for his unparalleled contributions towards the full Run 2 analysis.

To Kyle Cranmer, thank you for encouraging me to explore the world of HEP and for his valuable guidance, advice and generosity over the years.

The friends I made in Madison and Geneva are far too numerous to mention individually, but they are wonderful people and I'm lucky to have them in my life. A special shoutout goes to my flatmates at Ouches, Selina, Emilien, Niki, Jonas, Alice(s) and others who made a home I wanted to go to. Finally, a big thanks to the land of Hypatia and its wonderful inhabitants where I completed this thesis and this long and extraordinary journey.

Contents

List of Figures

List of Tables

Chapter 1

Introduction

Experimental high-energy particle physics is the study of the most fundamental building blocks of nature and the Large Hadron Collider (LHC) at the European Center for Nuclear Research (CERN) is an international endeavor focused on advancing our collective understanding and knowledge of matter and its interactions. While the Greeks started talking about the **atom** more than 2000 years ago, even during most of the first half of the twentieth century, particle physicists had only discovered three fundamental particles that make up the atom; the proton, neutron and electron. However, improvements in particle accelerators and detector technology led to an avalanche of new subatomic particles in the second half of the last century. In an effort to classify all these elementary particles and their interactions, the Standard Model (SM) of particle physics, now one of the most experimentally validated scientific theories in history, emerged.

While a more detailed theoretical discussion of the SM as a Quantum field theory (QFT) will follow in Section 2.1, it is important to understand the basic framework before introducing the subject of this doctoral thesis. Fundamental particles can be grouped together and arranged diagrammatically as in Fig. 1.1 based on their spin

and other intrinsic properties such as mass and electric charge.

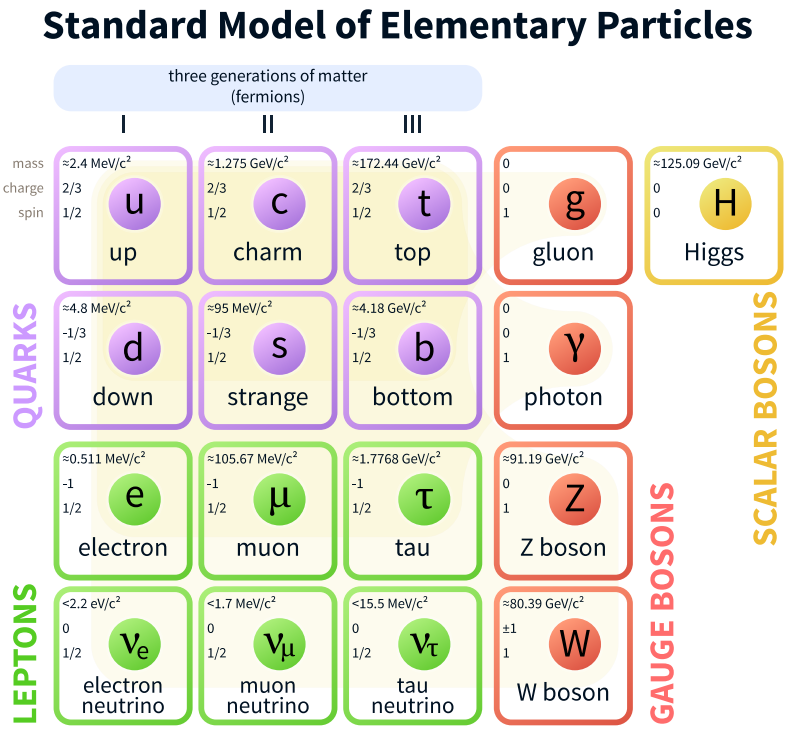

Figure 1.1: The fundamental particles of the SM and some of their properties including their: mass, electric charge, and spin. The units for mass are reported as electron volts divided by the speed of light (c) squared and use scientific notation prefixes. M for million, G for billion.

There are two classes of particles based on their spin: Fermions and bosons. While the 12 elementary fermions (6 quarks and 6 leptons) with spin $\frac{1}{2}$ constitute what we call matter, the four elementary bosons with spin 1 act as mediators between fermions and are the main carriers of three of the four fundamental forces in nature, namely: the strong nuclear force, which is the dominant force responsible for the formation of atomic nuclei; electromagnetism, the force responsible for the formation of atoms; and the weak nuclear force, which is the dominant force responsible for radioactive β decay of nuclei. The SM is a theory of strong, weak and electromagnetic interactions where the electromagnetic force and the weak nuclear force are unified into one electroweak

(EW) theory.

Chapter 2 gives an overview of the SM with specific focus on diboson processes in the electroweak sector and details some of its shortcomings that motivate continued searches for new physics. This thesis presents a precision measurement of ZZ production using events in which the two Z bosons each decay to a pair of charged leptons. Two of the three charged leptons, electrons (e) and muons (μ) can be measured with high precision using the Compact Muon Solenoid (CMS) detector which is described in extensive detail in Chapter 4, whereas the third lepton (τ) is more difficult to measure and is neglected. Details of ZZ physics are described in Chapter 3, along with a review of previous literature.

Although the SM is a powerful theory and most of its predictions are verified with ever increasing precision, it leaves some questions unanswered. Cosmological evidence indicates (See Appendix A.1) that approximately 25% of our universe is composed of some form of dark matter (i.e. matter that interacts very weakly with the SM). Several extensions of the SM that include this dark matter have been proposed and can be tested with particle colliders such as the one at CERN.

In the appendix B of this thesis, the status of an ongoing search for new physics beyond the SM looking for a unique Z' Pencil Jet signature is presented. The basic process is that dark matter is pair produced from proton-proton collisions and one of the dark matter particles can radiate a light (GeV-scale) Z' . The Z' particle from final state radiation (FSR) decays back to SM particles, focusing on the dominant decay into quarks, forming a very narrow **Pencil Jet** signature while there is still large missing transverse momentum from the dark matter particles.

Chapter 2

The Standard Model and Beyond

The Standard Model (SM) of particle physics is a renormalizable quantum field theory (QFT) with an underlying gauge symmetry group $SU(3)_C \times SU(2)_W \times U(1)_Y$ where the subscripts C, W and Y denote color, weak isospin and hypercharge respectively which are the conserved quantities for each Lie Group [1]. The $SU(2)_W \times U(1)_Y$ portion of the SM is referred to as the Glashow-Salam-Weinberg Theory [2] that unified electromagnetic interactions mediated by the massless photon described by Quantum Electrodynamics (QED) and weak interactions that are mediated by the heavy W and Z bosons. These massive electroweak mediators, W^+, W^- and Z bosons, acquire their mass through the mechanism of Electroweak Spontaneous Symmetry Breaking (EWSB) [2, 3] which is described in more detail in Section 2.2. The $SU(3)_C$ component represents the strong interactions which are mediated by massless gluons of 8 different colors described by Quantum Chromodynamics (QCD).

2.1 Matter and Interactions

The SM is a theory of interacting spin-1/2 matter and spin-1 force fields, along with a spin-0 self-interacting field as shown in Fig. 1.1. The spin 1 W and Z gauge bosons as well as the fermions acquire mass through their interactions with the spin 0 Higgs boson. We discuss EWSB and its implications on the SM in Section 2.2. Since SM is a chiral gauge theory, the fermion fields can be summarized as follows:

$$\psi_L^T = (q_{L1}, mu_{R1}^C, e_{R1}^C, d_{R1}^C, l_{L1}, (n_{R1}^C), q_{L2}, ..., ..., (n_{R3}^C)), \tag{2.1}$$

representing the quarks and leptons in the three families as shown in Fig. 1.1. All fermions as well as the charged gauge bosons have a corresponding antiparticle in the SM with same mass but opposite sign quantum numbers. All the quarks and half the leptons carry electric charge and hence interact via the electromagnetic force. The quarks come in triplets of "color" typically called red, green and blue [4] and have never been observed as free particles. Color, an analog to electric charge from QED is the charge underlying the strong force which results in colorless bound states such as mesons ($q\bar{q}$) and the more famously known baryons (qqq) such as protons and neutrons, the basic building blocks of ordinary matter. This implies that color-charged "objects" cannot exist on their own, a property known as confinement [2] and quarks are always bound together by gluons according to the $SU(3)_C$ requirement that color charge must be conserved.

While there is a lot to say about concepts like confinement, asymptotic freedom [2, 3] in the context of QCD, we want to draw particular attention to another emergent property of confinement known as hadronization. Colliders like the LHC smash protons together at high energies so that the point-like interactions are between quarks and gluons engaged in this delicate dance choreographed by the strong force inside these protons. These free partons (quarks and gluons) created at high energy scales

such as the ones seen at the LHC evolve into hadrons that are stable enough to be detected by our Compact Muon Solenoid (CMS) detector. This process of hadronization will be discussed further in Section 5.2.2 but an important feature of hadronization that will be relevant in the Appendix B of this thesis is the formation of **jets**. During hadronization, the kinematic distribution of produced hadrons is concentrated in the directions of the initial partons (quarks and gluons) and these localized "hadron showers" are know as **jets**.

While the quarks come in triplets of color,

$$q_{u,d} = \begin{pmatrix} q^r_{u,d} \\ q^g_{u,d} \\ q^b_{u,d} \end{pmatrix} \tag{2.2}$$

the left-handed quarks and leptons come in doublets of weak isospin,

$$q^\alpha_{Li} = \begin{pmatrix} u^\alpha_{Li} \\ d^\alpha_{Li} \end{pmatrix} \qquad \text{and} \qquad l_{Li} = \begin{pmatrix} \nu_{Li} \\ e_{Li} \end{pmatrix} \tag{2.3}$$

where i is the family index i=1,2,3. Pairs of these fields such as the electrically charged lepton and corresponding neutral neutrino can transform into each other through weak interactions by coupling to W and Z bosons, the mediators of the weak force. The best example of this transformation and the weak nuclear force in action is the nuclear beta decay reaction $n \to p + e^- + \nu_e$ of radioactive fame.

While all quarks and leptons interact via the weak nuclear force in addition to other interactions, neutrinos are only coupled to the SM through weak interactions which makes them impossible to detect in our particle colliders.

2.2 ElectroWeak Unification, Spontaneous Symmetry Breaking and the Higgs mechanism

As mentioned above, Glashow, Weinberg and Salam unified [5–7] the electromagnetic and weak forces into a single electroweak force, mediated by the $W^{\pm}$, Z^0 and γ bosons, represented by $SU(2)_W \times U(1)_Y$ symmetry. The U(1) weak hyper charge, Y_W is a quantum number relating the electric charge Q and T_3 which is the third (measured) component of the weak isospin T^i.

$$Q = T_3 + \frac{1}{2}Y_W \tag{2.4}$$

Electric charge, Q, is always conserved while weak hyper charge is conserved in all electromagnetic, strong and fermion-fermion weak interactions but not conserved when the Higgs is involved.

Fermions	Q	T	T_3	Y
ν_{eL}, $\nu_{\mu L}$, $\nu_{\tau L}$	0	1/2	1/2	-1
e_L, μ_L, τ_L	-1	1/2	$-1/2$	-1
ν_{eR}, $\nu_{\mu R}$, $\nu_{\tau R}$	0	0	0	0
e_R, μ_R, τ_R	-1	0	0	-2
u_L, c_L, t_L	2/3	1/2	1/2	1/3
d'_L, s'_L, b'_L	$-1/3$	1/2	$-1/2$	1/3
u_R, c_R, t_R	2/3	0	0	4/3
d'_R, s'_R, b'_R	$-1/3$	0	0	$-2/3$

Table 2.1: Quantum numbers of electric charge, weak isospin and hypercharge for quarks and lepton.

A unified but unbroken $SU(2)_W \times U(1)_Y$ symmetry implies four massless bosons but W and Z bosons are expected to be massive due to the short-range of the weak interactions. Indeed, as mentioned earlier, the W and Z bosons discovered in 1983 are the two of the most massive particles in the SM [8, 9]. Therefore, this gauge symmetry

must be spontaneously broken such that the gauge bosons acquire mass but the theory still remains renormalizable [10]. This is achieved via the Higgs mechanism [11–13]. In its minimal choice, the Higgs mechanism introduces a complex scalar field as an SU(2) doublet with four degrees of freedom,

$$\Phi = \frac{1}{\sqrt{2}} \begin{pmatrix} \phi_1^+ + i\phi_2^+ \\ \phi_3^0 + i\phi_4^0 \end{pmatrix} \tag{2.5}$$

with a Lagrangian of the form

$$\mathcal{L} = (D_\mu \phi)^\dagger (D^\mu \phi) - V(\phi) \tag{2.6}$$

where D^μ is the covariant derivative invariant under local SU(2) $\times$ U(1) transformations

$$D_\mu = \partial_\mu + ig\frac{1}{2}\overrightarrow{\sigma} \cdot \overrightarrow{\mathrm{W}_\mu} + ig' Y B_\mu, \tag{2.7}$$

and $V(\phi)$ is the potential energy of the Higgs field where μ, λ are free parameters of the SM.

$$V(\phi) = \mu^2 \phi^\dagger \phi - \lambda^2 \left(\phi^\dagger \phi\right)^2 \tag{2.8}$$

Note that the choice of $\mu^2 \leq 0$ and $\lambda \geq 0$ leads to spontaneous symmetry breaking and results in a potential $V(\phi)$ as shown in Fig. 2.1 which has a degenerate set of non-zero minimum values and the scalar doublet phi acquires a non-zero vacuum expectation value such that the potential has a minimum at

$$\phi_{min} \equiv \sqrt{\frac{1}{2}} \begin{pmatrix} 0 \\ v \end{pmatrix} \tag{2.9}$$

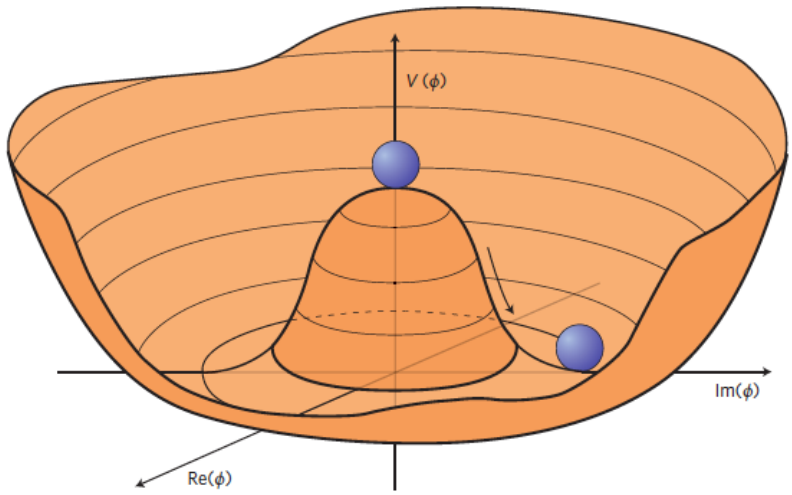

Figure 2.1: $V(\phi)$ potential in eqn. 2.8 showing a non-zero vacuum expectation value.

Hence we reduce the 4 degrees of freedom in the original Higgs doublet (see Eqn. 2.5) to a real field and the vacuum expectation value:

$$\Phi = \frac{1}{\sqrt{2}} \begin{pmatrix} 0 \\ v + h(x) \end{pmatrix} \tag{2.10}$$

using

$$\phi_1 = \phi_2 = \phi_4 = 0, \phi_3^2 = -\frac{\mu^2}{\lambda} \equiv v^2 \tag{2.11}$$

and we are left with three null components and one degree of freedom which is identified as the Higgs boson h. At the vacuum energy (h(x) $\rightarrow$ 0), substituting Eqn. 2.11

into the Lagrangian, the relevant terms are from Eqn. 15.17 in [3]

$$\begin{aligned}
&\left|\left(-ig\frac{\tau}{2}\cdot \mathrm{W}_\mu - i\frac{g'}{2}B_\mu\right)\phi\right|^2 = \frac{1}{8}\left|\begin{pmatrix} g\mathrm{W}^3_\mu + g'B_\mu & g(\mathrm{W}^1_\mu - i\mathrm{W}^2_\mu) \\ g(\mathrm{W}^1_\mu + i\mathrm{W}^2_\mu) & -g\mathrm{W}^3_\mu + g'B_\mu \end{pmatrix}\begin{pmatrix} 0 \\ v \end{pmatrix}\right|^2 \\
&= \frac{1}{8}v^2g^2\left[(\mathrm{W}^1_\mu)^2 + (\mathrm{W}^2_\mu)^2\right] + \frac{1}{8}v^2(g'B_\mu - g\mathrm{W}^3_\mu)(g'B^\mu - g\mathrm{W}^{3\mu}) \\
&= (\frac{1}{2}vg)^2\mathrm{W}^+_\mu\mathrm{W}^{-\mu} + \frac{1}{8}v^2\begin{pmatrix}\mathrm{W}^3_\mu & B_\mu\end{pmatrix}\begin{pmatrix} g^2 & -gg' \\ -gg' & g'^2 \end{pmatrix}\begin{pmatrix}\mathrm{W}^{3\mu} \\ B^\mu\end{pmatrix}
\end{aligned} \tag{2.12}$$

This altered Lagrangian has mass eigenstates where W_μ, Z_μ, A_μ are considered as the W boson, Z boson and photon respectively.

$$\begin{aligned}
\mathrm{W}^\pm_\mu &= \frac{1}{\sqrt{2}}\left(\mathrm{W}^1_\mu \mp \mathrm{W}^2_\mu\right) \\
\mathrm{Z}_\mu &= \frac{g\mathrm{W}^3_\mu - g'B_\mu}{\sqrt{g^2+g'^2}} = \mathrm{W}^3_\mu\cos\theta_W - B_\mu\sin\theta_W \\
A_\mu &= \frac{g'\mathrm{W}^3_\mu + gB_\mu}{\sqrt{g^2+g'^2}} = \mathrm{W}^3_\mu\cos\theta_W + B_\mu\sin\theta_W
\end{aligned} \tag{2.13}$$

where θ_W is the Weinberg electroweak mixing angle

$$\tan\theta_W = \frac{g'}{g}. \tag{2.14}$$

where g is the coupling from U(1) and g' is the coupling from SU(2). Including these fields in the Lagrangian above and simplifying, a mass term emerges

$$\mathcal{L}_{mass} = -M^2_\mathrm{W}\mathrm{W}^{+\mu}\mathrm{W}^-_\mu - \frac{1}{2}M^2_\mathrm{Z}\mathrm{Z}^\mu\mathrm{Z}_\mu \tag{2.15}$$

with $M_w = \frac{1}{2}vg$, $M_z = \frac{g^2+g'^2}{2}$ and $m_A = m_\gamma = 0$ identified as the masses for the W and Z bosons and the photon being massless.

The full interaction Lagrangian between the Higgs field (v+h(x)) and the W and Z bosons

$$\mathcal{L}_{Hint} = (1 + \frac{h}{v})^2(\frac{M_{\mathrm{Z}}^2}{2}\mathrm{Z}_\mu\mathrm{Z}^\mu + M_{\mathrm{W}}^2\mathrm{W}_\mu^+\mathrm{W}^{-\mu}) + \frac{3m_H^2}{v^2}(\frac{vh^3}{3!} + \frac{h^4}{4!}) \tag{2.16}$$

gives rise to all these tri-boson HZZ,HWW,HHH and tetra-boson HHZZ, HHWW and HHHH interactions. And from the Higgs potential itself, one can get the mass of the Higgs boson to be $m_H^2 = 2\lambda v^2$ which is not predicted by this theory but needs to be experimentally measured. The Higgs boson was discovered in 2012 and its most precise mass measurement comes from ATLAS and CMS collaborations to be $m_h = 125.09 \pm 0.21$ (stat.) $\pm$ 0.11 (sys.) GeV [14].

2.3 The Yukawa mechanism for fermion masses

In addition to providing a mechanism for generating W and Z boson masses through EWSB, the Higgs doublet also couples left and right-handed fermions together. This is the so-called Yukawa interaction between Dirac (e.g. fermion) fields and and scalar fields. For each fermion generation, the Yukawa Lagrangian is

$$\mathcal{L}_Y = g_f(\Psi_L \Phi f_R + h.c.), \tag{2.17}$$

where the coupling g_f is the coupling strength of the fermions to the Higgs doublet. While the details can be found in many textbooks [2, 3], it suffices here to say that the Higgs field can be substituted in the Yukawa Lagrangian to show that the mass of the fermion is $m_f = \frac{g_f v}{\sqrt{2}}$ and the interaction strength of the fermion to the Higgs boson is $\frac{m_f}{v}$.

In order of charged lepton mass, the three generations are shown in Fig. 1.1 from left to right. Electrons and muons are stable particles [15] and make up the final

	1st gen.		2nd gen.		3rd gen.	
up-type quark	g_u	2×10^{-5}	g_c	9×10^{-3}	g_t	~ 1
down-type quark	g_d	4×10^{-5}	g_s	8×10^{-4}	g_b	3×10^{-2}
charged lepton	g_e	3×10^{-6}	g_μ	6×10^{-4}	g_τ	1×10^{-2}

Table 2.2: Higgs boson Yukawa couplings for charged leptons and quarks.

states of Z boson decays but more on that in Section 2.4 on Diboson Physics. The Yukawa couplings for the nine charged fermions (3 charged leptons and six quarks) shown in Table 2.2 below are free parameters in the SM that are not predicted and must be experimentally measured through mass measurements of the fermions most of which are known experimentally to very high precision.

2.4 Diboson and MultiBoson Physics

As mentioned in the EWSB section 2.2 above, the full interaction between the Higgs field and the two massive bosons (Eqn. 2.16) gives rise to all these trilinear gauge boson couplings ($\gamma W^{\pm}W^{\pm}, ZW^{\pm}W^{\pm}, HZZ, HW^{\pm}W^{\pm}$), quartic gauge couplings ($\gamma\gamma W^{\pm}W^{\pm}, \gamma ZW^{\pm}W^{\pm}, W^{\pm}W^{\pm}W^{\pm}W^{\pm}, ZZW^{\pm}W^{\pm}, HHZZ, HHW^{\pm}W^{\pm}$) allowed at tree level in the SM as well as these Higgs boson trilinear and quartic self-coupling self-coupling vertices (HHH, HHHH).

Multiboson interactions are excellent probes of the SM electroweak and Higgs sectors and in fact, dibosons at the LHC have given us the defining results of the collider: the discovery of the Higgs boson [16, 17]. On the other hand, diboson production processes are also sensitive to the gauge-boson self interactions so their measurement provides a crucial test of the SM description of the gauge-boson dynamics. The SM makes a number of predictions in this context specifically in the production of leptonically decaying electroweak boson pairs such as two Z bosons decaying to four leptons. For example, the ZZ production cross section describes the rate at which

particle collisions result in final states with two Z bosons. The tree-level or leading order (LO) feynman diagrams for general diboson production are shown in Fig. 2.2 mainly through fermion couplings to the gauge bosons. However, gluon-gluon fusion can also contribute to diboson production at higher-order QCD calculations which proceed through a quark loop as shown in the so-called box diagram in Fig. 2.3.

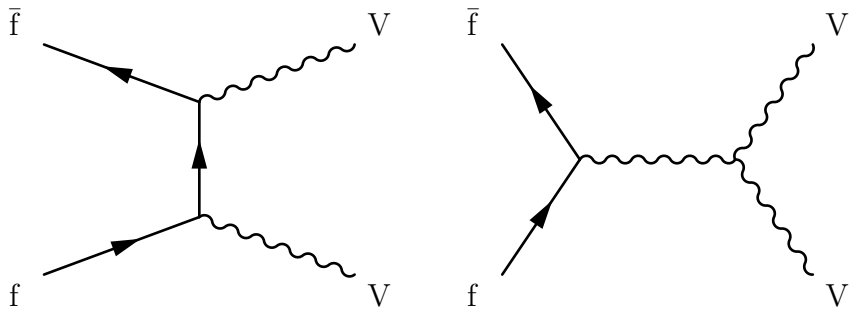

Figure 2.2: Tree-level Feynman diagrams for diboson production in fermion-anti-fermion collisions. The second diagram does not contribute for neutral gauge bosons in the SM.

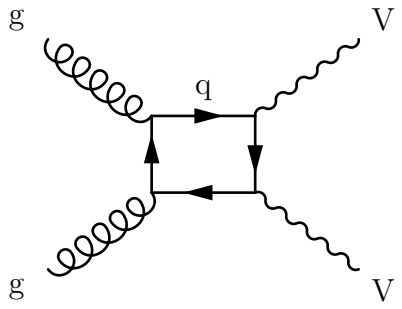

Figure 2.3: Leading order "box" diagram for diboson production through a quark loop in a gluon-gluon fusion event.

2.5 Beyond the Standard Model

The SM is the crowning achievement of particle physics and it is an elegant theory which does a wonderful job of explaining a lot of data but despite its successes, it is

widely accepted to be incomplete. Now, we try to outline some of its limitations to drive this point home.

2.5.1 Limitations

The SM does not provide a satisfactory mechanism for neutrino mass. As we know from experimental evidence [18, 19], neutrinos oscillate between their three flavors and therefore must have some mass. But, the SM fails to provide an explanation for either the mixing between the flavors or their mass. While the SM explains ordinary baryonic matter and interactions very well, if we look at the total mass-energy composition of the universe, it contains 4.9% ordinary matter, 26.8% dark matter and 68.3% dark energy [15]. Dark Matter is more than five times as abundant as baryonic matter that is composed of the elementary particles described in the SM which makes it one of the most significant unanswered questions in modern particle physics. Dark matter is only expected to interact with SM particles weakly but its gravitational pull is felt on astronomical scales [20–22] but more on this evidence in Appendix A.1. This also brings us back to the SM and its inability to incorporate gravity, one of the four (known) fundamental forces of nature.

In addition to the aforementioned limitations, there are many unexplained features of nature that also go unexplained by the SM such as the hierarchy between the observed cosmological constant and other scales from QCD, weak scale physics etc [23–25]. Then, there is the "ad-hoc"-ness to the 19 free parameters in the SM including the fermion masses which are not explained in the SM but are just free parameters. There are several others that could be mentioned such as why there are only three fermion families and why do we find integer multiples of 1/3 for the electric charge rather than some other number but it is abundantly clear that the SM is not a comprehensive theory of everything. There are several proposed theories

which modify or extend the SM such as supersymmetry [26, 27], string theory and others, some of which will be relevant for this thesis and will be discussed in more detail in the following sections.

2.5.2 Anomalous Couplings

Beyond the SM, there can be small deviations from the expected couplings of the gauge bosons which can lead to new physics. For instance, presence of neutral anomalous gauge couplings (aGCs) can explain several phenomena such as CP violation, Baryogenesis, dark matter to name a few. As shown in Fig. 2.4, these anomalous neutral couplings are forbidden in the SM.

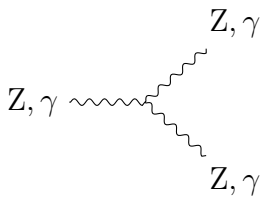

Figure 2.4: Fully-neutral anomalous triple gauge coupling vertices. These are forbidden in the SM.

The ZZ and Gamma production are the two main processes where one can study such couplings. While there are of course analogous terms for all anomalous VVV couplings (V ∈ Z,W,γ) but only the ZZZ and ZZγ are relevant to this thesis. The neutral aTGC can be obtained by adding higher dimension effective operators to the SM [28–30]. In this EFT parametrization, for on-shell outgoing Z bosons the vertex function for ZZV (where V maybe Z or γ) can be written as Eqn.2.18 [30] which corresponds to the vertex shown in Fig. 2.5.

$$g_{ZZV}\Gamma^{\alpha\beta\mu}_{ZZV} = e\frac{P^2 - M_V^2}{M_{\rm Z}^2}\left(if_4^V(P^\alpha g^{\mu\beta} + P^\beta g^{\mu\alpha}) + if_5^V\epsilon^{\mu\alpha\beta\rho}(q_1 - q_2)_\rho\right) \qquad (2.18)$$

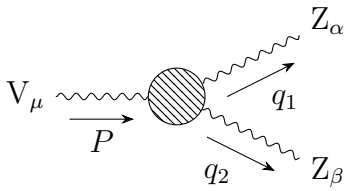

Figure 2.5: Feynman diagram of a triple gauge coupling.

where f_i^v (i=4,5) are four dimensionless complex coupling constants f_4^γ, f_4^Z, f_5^γ and f_5^Z which describe neutral aTGCs. The f_4^V coupling constants violate CP-invariance (CP-odd) and the f_5^V coupling constants violate parity conservation (CP-even) [30]. The kinematic properties of the triple gauge coupling Feynman diagrams differ from the SM gauge coupling diagrams and this is used to set a limit on the aTGCs as described in more detail in section 7.7.

The effective Lagrangians used here are low-energy approximations and the contribution from neutral TGCs grows unbounded with energy until the sum of the probabilities of all final states exceeds unity (violating unitarity). Unitarity can be preserved by introducing energy-dependent form factors [31]

$$\mathcal{F}(s) = \frac{1}{(1 + \frac{s}{\Lambda_{FF}^2})^n} \tag{2.19}$$

where Λ is the energy scale of the new physics process. The limits set in this work do not violate unitarity bound for an energy scale much larger than what is accessible at the LHC so no form factor is applied which also makes these results model independent.

Chapter 3

ZZ Phenomenology and Previous Results

The electrically neutral Z boson was experimentally discovered in 1983 at the UA1 experiment at CERN [9]. Precise electroweak measurements were performed at the Z boson resonance with e^+e^- collisions at LEP and SLC [32]. In the context of this work, the Z boson mass reported is,

$$m_Z = 91.1876 \pm 0.0021\,\text{GeV}, \tag{3.1}$$

and its full width is,

$$\Gamma_Z = 2.4952 \pm 0.0023\,\text{GeV}, \tag{3.2}$$

Z bosons can decay to a quark-antiquark pair, a neutrino-antineutrino or a pair of oppositely charged leptons and the branching fractions for each of the final states are known to be 69.9% for $q\bar{q}$, 20% for $\nu\bar{\nu}$ and 10.1% for $\ell^-\ell^+$ [32, 33]. The measurements in this thesis focus on the four-lepton final states resulting from nonresonant diboson

(ZZ) production and subsequent decay of these two on-or off-shell Z bosons

$$\mathrm{ZZ} \to \ell^+\ell^-\ell^+\ell^-$$

where $\ell = \mathrm{e}, \mu$ giving three final states $\mathrm{e^+e^-e^+e^-}$,$\mu^+\mu^-\mu^+\mu^-$ and $\mathrm{e^+e^-}\mu^+\mu^-$ with branching fractions from [33] as follows:

$$\mathcal{B}(\mathrm{ZZ} \to \mathrm{e^+e^-e^+e^-}) = 0.113 \pm 0.008\% \tag{3.3}$$

$$\mathcal{B}(\mathrm{ZZ} \to \mu^+\mu^-\mu^+\mu^-) = 0.113 \pm 0.014\% \tag{3.4}$$

$$\mathcal{B}(\mathrm{ZZ} \to \mathrm{e^+e^-}\mu^+\mu^-) = 0.226 \pm 0.016\% \tag{3.5}$$

Single-Z triboson production (WWZ) [34, 35] and $\mathrm{t\bar{t}Z}$ production also result in the same four lepton final states as above but these are considered background (section 3.3).

3.1 Nonresonant ZZ/Zγ^* Production and Decay

While four-lepton final states can originate from several physics processes such as resonant Higgs boson production, resonant single-Z production, our focus is on the nonresonant diboson ZZ production. In the SM, leading-order ZZ production proceeds via t- and u-channel quark antiquark annihilation as shown in Fig. 3.1

There is no contribution from s-channel $q\bar{q}$ annihilation as neutral triboson couplings (ZZZ,ZZγ) are forbidden in the SM.

In calculations at higher order in quantum chromodynamics (QCD), gluon-gluon fusion also contributes via box diagrams (Fig. **??**) with quark loops with gg $\to$ ZZ making about roughly 60% of the total NNLO correction [36]. Although these are

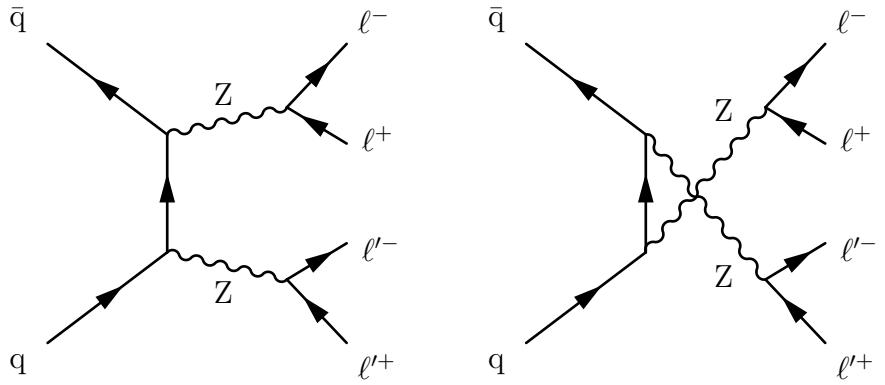

Figure 3.1: Leading order Feynman diagrams for ZZ $\rightarrow 4\ell$ production in pp collisions.

NNLO (suppressed by a factor of α_s^2), they can still contribute around 5-10% to the total ZZ production cross section [37] due to the high effective gluon luminosity at LHC energies. As can be observed from Fig. 3.3 , reproduced from Ref. [37], the contribution from the gg-initiated processes becomes significant in the region $m_{4\ell} > 2M_{\mathrm{Z}}$ where its an important background process to Higgs boson searches.

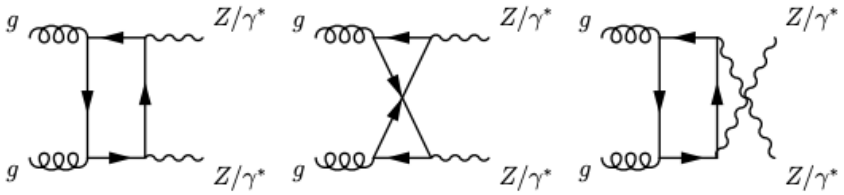

Figure 3.2: NNLO Feynamn diagrams for gg $\rightarrow$ ZZ

The so-called ZZ/Zγ production refers to the fact that final states with an off shell photon in place of a Z can be indistinguishable from the state with a Z and so the $q\bar{q} \rightarrow$ ZZ process includes a small contribution from γ^* with interference between the Z and γ^* diagrams. Nonresonant Zγ^* production is generally flat as a function of invariant mass between roughly 100 GeV and the kinematic threshold of $2m_{\mathrm{Z}} =$ 182.4 GeV where the on-shell pair production of ZZ bosons is turned on. At the

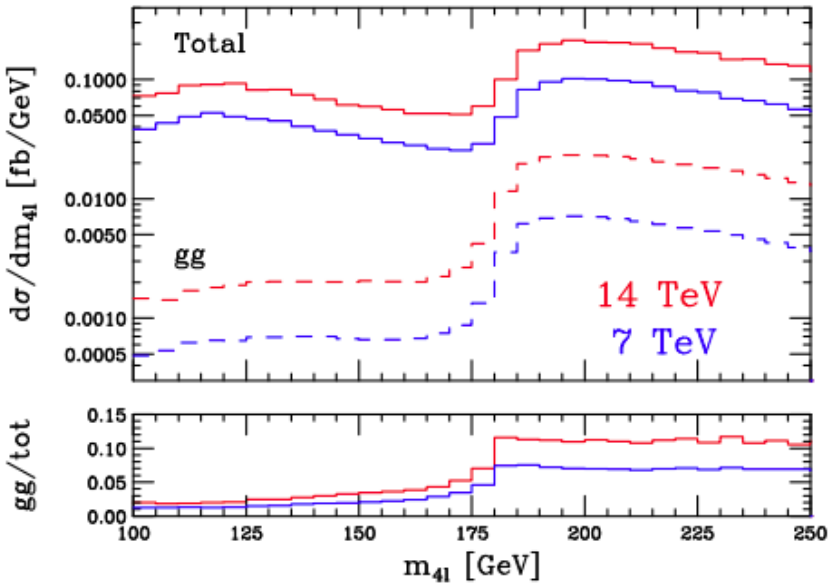

Figure 3.3: The invariant mass of the four lepton system in $Z/\gamma^*(\rightarrow e^+e^-)Z/\gamma^*(\rightarrow \mu^+\mu^-)$ production at $\sqrt{s} = 7$ and $\sqrt{s} = 14$ TeV, with the cuts of Eqn. 9.3 in Ref. [37]. In the upper panel, the total NLO prediction (upper curves) and the contribution from the gg initial state only (lower curves). In the lower panel we plot the fraction of the NLO prediction resulting from the gg initial state.

LHC energies relevant for this work, $\sqrt{s} = 13$ TeV, this on-shell ZZ production peaks around $m_{ZZ} \approx 200$ GeV before tapering off and falling steeply towards higher invariant masses.

3.1.1 Previous experimental results

Measurements of diboson ZZ production are of great interest in High Energy Particle Physics as they allow precision tests of the SM and serve as an important probe of the structure of the electroweak sector. Diboson ZZ production was first observed in e^+e^- collisions at LEP when the center of mass energy($\sqrt{s}$) of the collider first reached 183 GeV, just above the kinematic threshold for producing two on-shell Z bosons as mentioned in the previous section. The L3 experiment published the first cross section

measurement of on-shell ZZ production using 55.3 pb^{-1} of data collected at $\sqrt{s} = 183$ GeV. All visible decay-channels were used and the cross section was measured to be $\sigma_{ZZ} = 0.30^{+0.22}_{-0.16}\,^{+0.07}_{-0.03}$ pb, in very good agreement with the SM prediction.

These measurements of the ZZ production cross section in e^+e^- collisions were accomplished by all four LEP experiments eventually at center of mass energies ranging from 183 GeV to 209 GeV [38–41]. As shown in Fig. 3.4 reproduced from Figure 5.8 in Ref.[42], the measurements are in good agreement with SM predictions but were dominated by statistical uncertainties.

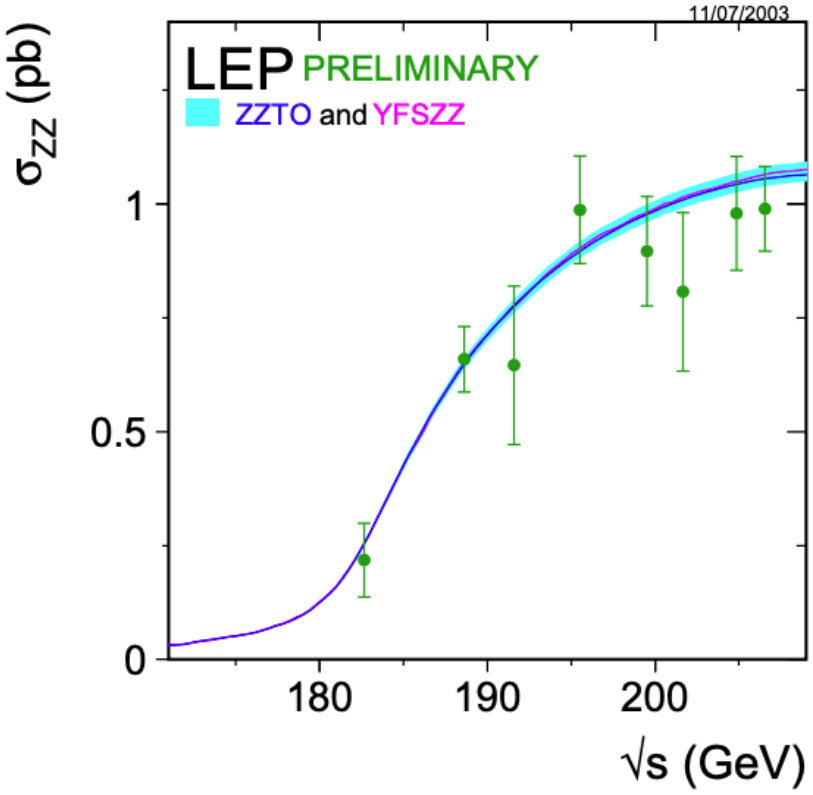

Figure 3.4: Measurements of the Z-pair production cross-section. The shaded area represent the ±2% uncertainty on the predictions. Reproduced from Ref.[42]

.

ZZ production was first observed and measured in $p\bar{p}$ collisions at a centre of mass

energy of $\sqrt{s} = 1.96$ TeV at the Tevatron by both the CDF and DO experiments [43–45]. Since there are too many background jets in $p\bar{p}$ collisions from hadronisation for the ZZ hadronic channels to be visible, these measurements were only performed in the 4ℓ and $2\ell 2\nu$ ($\ell = \mathrm{e}, \mu$) final states. Combining the two channels, DO measured the ZZ production cross section to be $\sigma(p\bar{p} \to \mathrm{ZZ}) = 1.44^{+0.31}_{-0.28}\,(\mathrm{stat})^{+0.17}_{0.19}\,(\mathrm{syst})$pb which is in good agreement with the SM prediction of $\sigma(p\bar{p} \to \mathrm{ZZ}) = 1.3 \pm 0.1$ pb [44]. Similarly CDF, combining the two channels measured the cross section to be $\sigma(p\bar{p} \to \mathrm{ZZ}) = 1.64^{+0.44}_{0.38}\,(\mathrm{stat}) + (\mathrm{syst})$pb, again in agreement with the Standard Model prediction of $\sigma(p\bar{p} \to \mathrm{ZZ}) = 1.4 \pm 0.1$ pb.

The first results for ZZ production cross section were obtained by both CMS and ATLAS $\sqrt{s} = 7$ TeV using the leptonic final states just like the Tevatron measurements quoted above. In 4ℓ final states, CMS found that the total ZZ cross section, requiring both Z bosons to be in the range $60 < m_{\mathrm{Z}} < 120$ GeV to be

$$\begin{aligned} \sigma_{\mathrm{ZZ}}(7\,\mathrm{TeV}) &= 6.24^{+0.86}_{-0.80}\,(\mathrm{stat})^{+0.41}_{-0.32}\,(\mathrm{syst}) \pm 0.14\,(\mathrm{lumi})\,\mathrm{pb} \\ \sigma_{\mathrm{ZZ}}(8\,\mathrm{TeV}) &= 7.7 \pm 0.5\,(\mathrm{stat})^{+0.5}_{-0.4}\,(\mathrm{syst}) \pm 0.4\,(\mathrm{theo}) \pm 0.2\,(\mathrm{lumi})\,\mathrm{pb}, \end{aligned} \tag{3.6}$$

at $\sqrt{s} = 7$ TeV and $\sqrt{s} = 8$ TeV respectively [46, 47] and

$$\begin{aligned} \sigma_{\mathrm{ZZ}}(7\,\mathrm{TeV}) &= 5.1^{+1.5}_{-1.4}\,(\mathrm{stat})^{+1.4}_{-1.1}\,(\mathrm{syst}) \pm 0.1\,(\mathrm{lumi})\,\mathrm{pb} \\ \sigma_{\mathrm{ZZ}}(8\,\mathrm{TeV}) &= 7.2 \pm 0.8\,(\mathrm{stat})^{+1.9}_{-1.5}\,(\mathrm{syst}) \pm 0.2\,(\mathrm{lumi})\,\mathrm{pb} \end{aligned} \tag{3.7}$$

when measured with $2\ell 2\nu$ final states [48].

Similarly, ATLAS measured

$$\begin{aligned} \sigma_{\mathrm{ZZ}}(7\,\mathrm{TeV}) &= 6.7 \pm 0.7\,(\mathrm{stat})^{+0.4}_{-0.3}\,(\mathrm{syst}) \pm 0.3\,(\mathrm{lumi})\,\mathrm{pb} \\ \sigma_{\mathrm{ZZ}}(8\,\mathrm{TeV}) &= 7.3 \pm 0.4\,(\mathrm{stat}) \pm 0.3\,(\mathrm{syst}) \pm 0.2\,(\mathrm{lumi})\,\mathrm{pb}, \end{aligned} \tag{3.8}$$

using 4ℓ final states at 7 TeV [49] and a combination of 4ℓ and $2\ell 2\nu$ ($\ell = \mathrm{e}, \mu$) final states at 8 TeV [50]. Measured cross sections from both experiments are consistent with SM predictions of 6.7 ± 0.2 pb at 7 TeV and 8.3 ± 0.2 pb at 8 TeV, both calculated at NNNLO in QCD with MATRIX, with factorization and renormalization scales $\mu_\mathrm{F} = \mu_\mathrm{R} = m_\mathrm{Z}$.

Finally, the most recent measurement was made by CMS at a center-of-mass energy of 13 TeV in 4ℓ final states where $\ell = \mathrm{e}, \mu$ requiring both Z bosons to be in the range $60 < m_\mathrm{Z} < 120$ GeV. The ZZ production cross section measured at $\sqrt{s} =$ 13 TeV with a dataset of 35.9 fb^{-1} [51] was combined with the result from 2015 also measured at $\sqrt{s} = 13$ TeV with a dataset of 2.6 fb^{-1} [52] to yield the cross section,

$$\sigma(\mathrm{pp} \to \mathrm{ZZ}) = 17.2 \pm 0.5\,(\mathrm{stat}) \pm 0.7\,(\mathrm{syst}) \pm 0.4\,(\mathrm{theo}) \pm 0.4\,(\mathrm{lumi})\,\mathrm{pb}. \tag{3.9}$$

which is consistent with the SM prediction of $16.2^{+0.6}_{-0.4}$ pb, calculated at NNLO in QCD via MATRIX v1.0.0_beta4 [36], just like all previous CMS measurements have been consistent with corresponding SM predictions.

Similarly, ATLAS made the same measurement at $\sqrt{s} = 13$ TeV with a dataset of 36.1 fb^{-1} [53]. The ATLAS measurements were performed with a Z boson mass window of 66–116 GeV, which reduces the SM expected cross section by 1.6% [54].

$$\sigma(\mathrm{pp} \to \mathrm{ZZ}) = 17.3 \pm 0.9[\pm 0.6\,(\mathrm{stat}) \pm 0.5\,(\mathrm{syst}) \pm 0.6\,(\mathrm{lumi})]\,\mathrm{pb}. \tag{3.10}$$

All these cross section measurements and the theoretical predictions are summarized in Fig. 3.5.

Unlike the Tevatron and previous measurements, the 8 TeV and 13 TeV measurements at the LHC had the statistical power to include differential cross section measurements as functions of different kinematic observables for the ZZ system. The measurements are well described by theoretical predictions but statistical uncertainties still dominate in all these differential cross section measurements and are at the

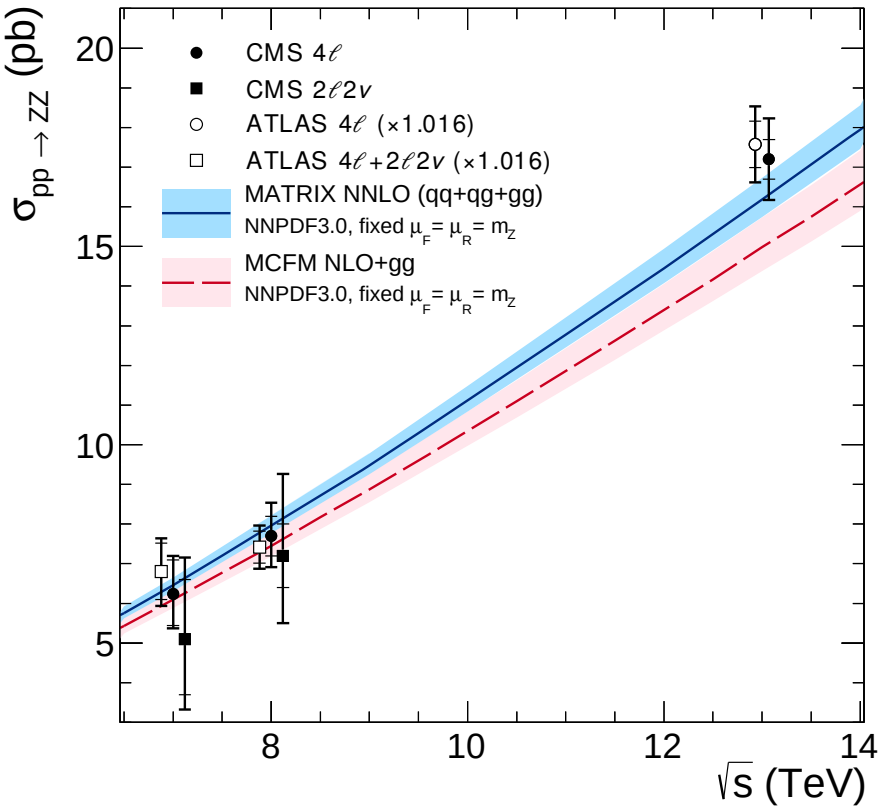

Figure 3.5: The total ZZ cross section is shown as a function of $\sqrt{s}$. Measurements from CMS and ATLAS quoted above in Eqns. 3.6– 3.10 are both shown, with the ATLAS numbers adjusted upward by 1.6% to account for differences in Z mass window choice. Points at the same center-of-mass energy are shifted slightly in the horizontal direction for clarity. Experimental measurements are compared to predictions from MCFM at NLO in QCD with additional contributions from LO gluon-gluon fusion diagrams, and MATRIX at NNLO in QCD.Both sets of predictions use the NNPDF3.0 PDF sets and fixed scales $\mu_{\mathrm{F}} = \mu_{\mathrm{R}} = m_{\mathrm{Z}}$.

.

level of 5-10% in the most recent results depending on the experiment and center-of-mass energy [47, 51–53].

3.2 Anomalous Triple Gauge Couplings

The ZZZ and ZZγ neutral triple gauge boson couplings (nTGCs) are zero at tree-level in the Standard Model, and exist only at the level of $\mathcal{O}(10^4)$ in one-loop corrections [55]. The sizes of these nTGCs are, however, enhanced in many models of new physics. Measurement of these couplings thus provides a test of the structure of the electroweak sector of the Standard Model. The effects of these anomalous couplings are enhanced at higher energies which manifest as an increase in cross section at high ZZ invariant mass ($m_{4\ell}$) and high Z transverse momentum [30]. This implies harder kinematic distributions such as the transverse momentum for the outgoing Z bosons and decay products (leptons) which can be seen in two example aTGC models in Fig. 3.6. Since the signature of non-zero nTGCs would result in higher event counts at high $m_{4\ell}$ where all other sources of prompt or non prompt four-lepton final states have negligible effects, these searches can be very effective in the quest for new physics beyond the SM.

As we can see from the invariant mass distribution in Fig. 3.8, the neutral aTGC parameters f_4^{V} and f_5^{V} are virtually indistinguishable so this distribution cannot be used to determine the relative strengths of these parameters. However, if deviations from the SM predictions are discovered, we can use their different behavior under parity transformations (section 2.5.2) in order to distinguish between these parameters. While it might have been possible to distinguish between f_4^{V} and f_5^{V} at Tevatron energies if enough events were available [30], Fig. 3.7 shows that it will be quite challenging to discriminate between f_4^{V} and f_5^{V} or to determine the sign of f_5^{V} using such

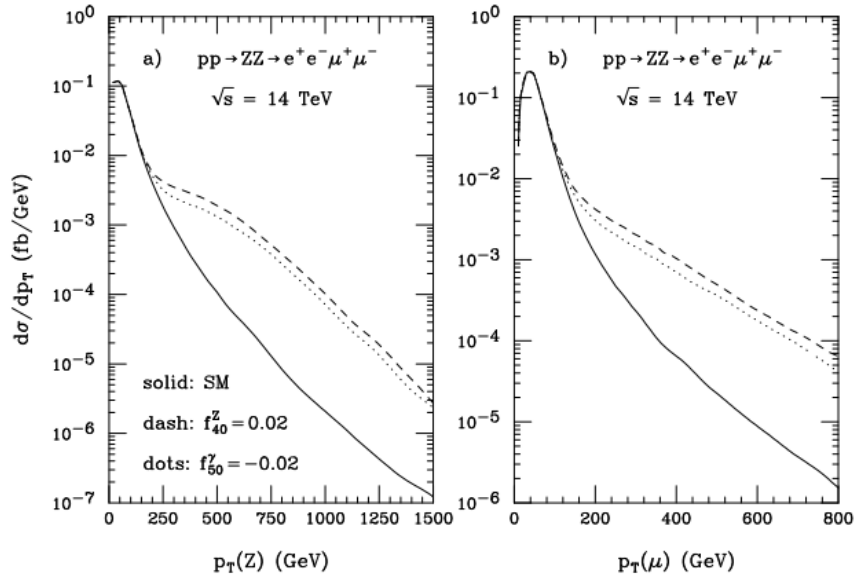

Figure 3.6: The p_T (Z) and p_T (μ) distributions in pp $\rightarrow$ ZZ $\rightarrow$ $e^+e^-\mu^+\mu^-$ at the LHC ($\sqrt{s} = 14$ TeV) in the SM (solid line), for $f_{40}^{Z} = 0.02$, and f_{50}^{γ} = -0.02. The cuts imposed are described in detail in Sec. III A [30]. The form factor scale has been set to $\Lambda_{FF} = 2$ TeV.

distributions in the ZZ $\rightarrow 4\ell$ final state at the LHC.

3.2.1 Previous Limits

The first set of limits on the ZZZ and ZZγ anomalous triple gauge couplings f_i^{V} were set by all four experiments at LEP [42] and the combined results are shown in Table 3.1. The D0 collaboration also performed these searches and set 95% confidence limits on all four couplings using unitarity-preserving cut-off of $\Lambda = 1.2\,\mathrm{TeV}$. The CDF experiment also set limits on these couplings but using 2ℓ+2jets final state [56] so those limits are not included in the table below.

Prior to this work, the most stringent limits on all four neutral aTGC parameters were set by CMS with 35.9 fb^{-1} of data collected at $\sqrt{s} = 13$ TeV. These observed 95% confidence limits on nTGCs from [51] CMS along with limits set by ATLAS

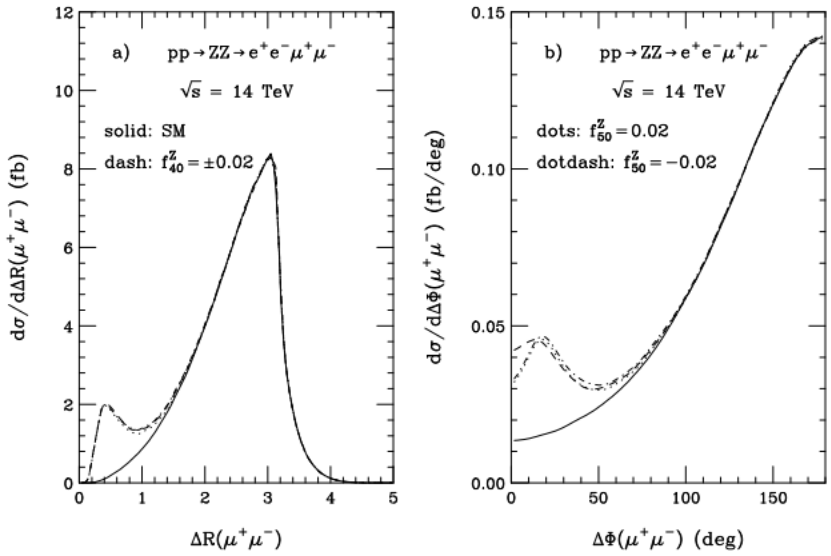

Figure 3.7: The Δ R($\mu^+\mu^-$) and $\Delta\Phi(\mu^+\mu^-)$ distributions in pp $\rightarrow$ ZZ $\rightarrow$ $e^+e^-\mu^+\mu^-$ at the LHC ($\sqrt{s}$ = 14 TeV) in the SM and in the presence of non-standard ZZZ couplings. The cuts imposed are described in detail in Sec. III A [30]. The form factor scale has been set to Λ_{FF} = 2 TeV.

	f_4^Z	f_5^Z	f_4^γ	f_5^γ
LEP	$[-0.30, 0.30]$	$[-0.34, 0.38]$	$[-0.17, 0.19]$	$[-0.32, 0.36]$
D0	$[-0.28, 0.28]$	$[-0.31, 0.29]$	$[-0.26, 0.26]$	$[-0.30, 0.28]$
ATLAS	$[-0.0015, 0.0015]$	$[-0.0015, 0.0015]$	$[-0.0018, 0.0018]$	$[-0.0018, 0.0018]$
CMS	$[-0.0012, 0.0010]$	$[-0.0010, 0.0013]$	$[-0.0012, 0.0013]$	$[-0.0012, 0.0013]$

Table 3.1: Previous limits on neutral aTGC parameters set by various experiments.

[53], LEP [42] and DO [57] in the four lepton final state are given in Table 3.1. No unitarizing form factor was used for the CMS, ATLAS and the LEP measurements while CDF used one as mentioned above.

The two-dimensional aTGC limits set by CMS with the 13TeV dataset are shown in Fig. 3.9 [51].

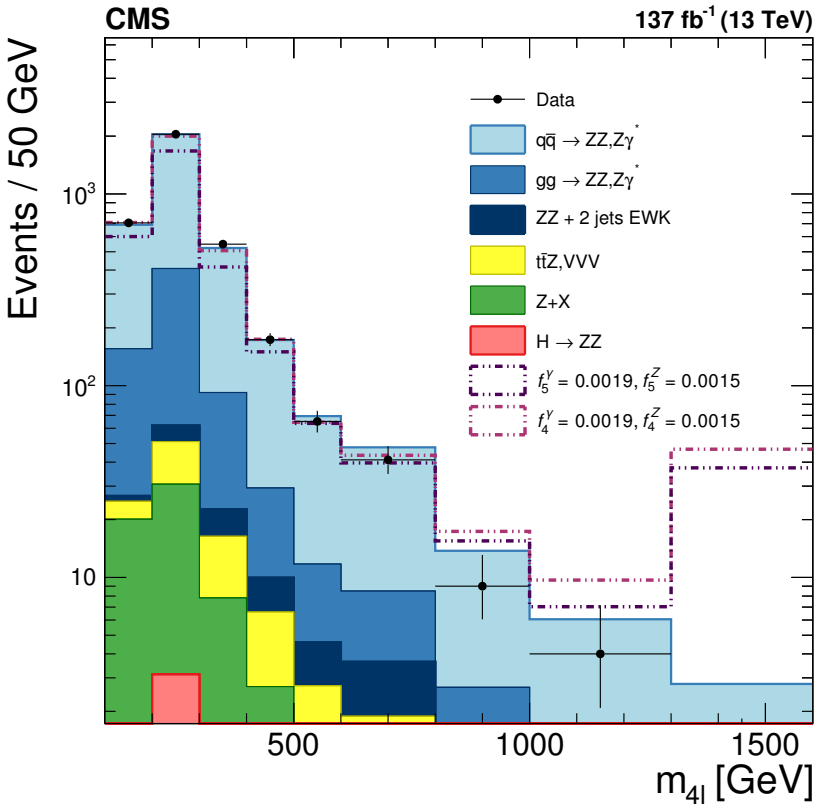

Figure 3.8: Distribution of ZZ invariant mass for all events in the on-shell selection. Points represent data, with statistical uncertainty bars. The stack of filled histograms represents the SM signal prediction and background estimate. The unfilled histograms represent two example SHERPA predictions for nonzero aTGC hypotheses (dashed) and the SHERPA SM prediction (solid), included to illustrate the shape differences between the SHERPA and POWHEG+MCFM SM predictions. The SHERPA distributions are normalized such that the SM prediction's total yield matches that of the other generators.

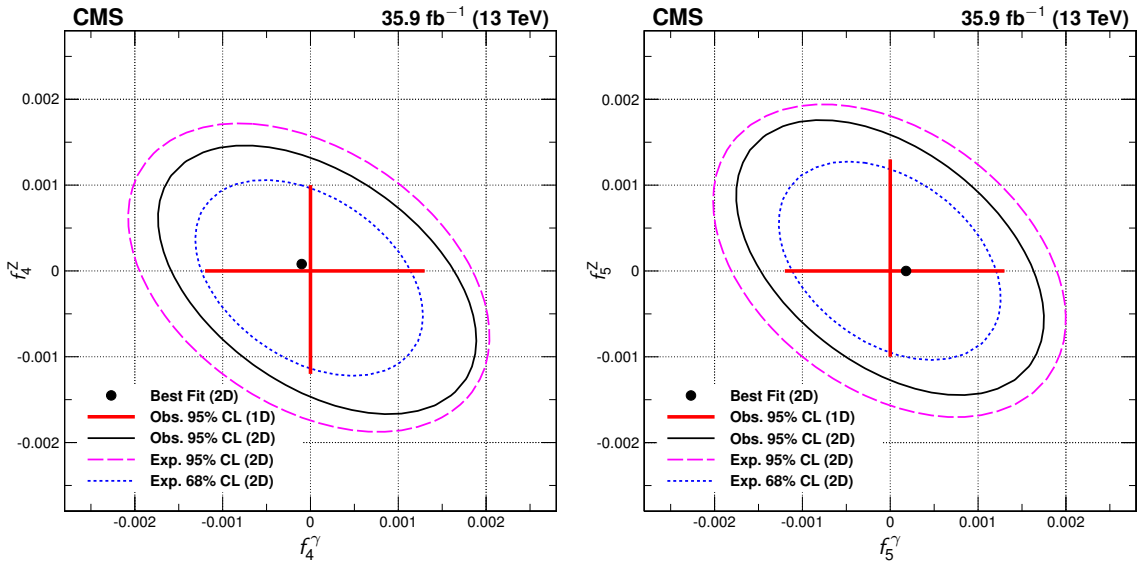

Figure 3.9: Two-dimensional observed 95% CL limits (solid contour) and expected 68 and 95% CL limits (dashed contours) in the f_4^γ-f_4^Z (left) and f_5^γ-f_5^Z (right) planes. The regions outside the contours are excluded at the corresponding confidence level. The dot is the point of maximum likelihood in the two-dimensional fits. Solid, straight lines at the center show the observed one-dimensional 95% CL limits for $f_{4,5}^\gamma$ (horizontal) and $f_{4,5}^Z$ (vertical). No form factor is used.

3.3 Background Processes

The ZZ four-lepton final state is expected to be very clean with little background, approximately 2% of the total predicted yield in each decay channel (Section 8.1). There are few other SM processes that produce four high momentum isolated leptons in the final state. A small fraction of the overall background arises from triboson ZZZ and WZZ production and from $t\bar{t}$ + V where V=$W^{+/-}$, Z where the four leptons from the boson decays tend to be isolated making these irreducible sources of background. In $t\bar{t}Z$ events, both top quarks and the Z all decay leptonically as shown in Fig. 3.10. Almost all other sources of background have a background lepton which can be defined as non-prompt leptons that arise due to jets or photons being mis-identified as a lepton or a real lepton from decays within jets or from photon conversions. These

are reducible backgrounds. The dominant contribution comes from events where a Z boson is produced in association with jets and or photons collectively termed as Z+X. Another important reducible background is WZ $\rightarrow 3\ell\nu$ where the bosons are produced in association with a jet fragment which can be misidentified as a lepton. More details about how these backgrounds are estimated in this analysis will follow in the Analysis section.

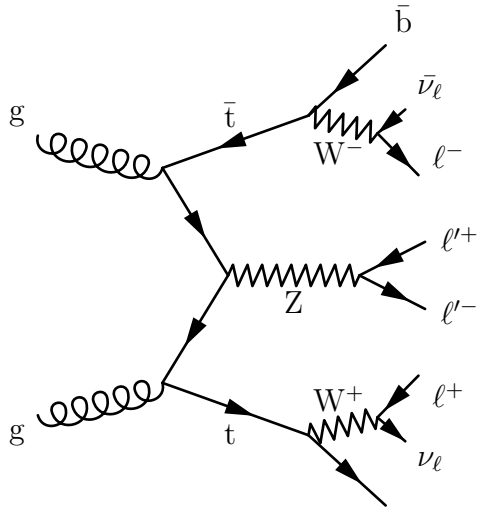

Figure 3.10: An example tree-level $t\bar{t}Z$ diagram which is an irreducible background for inclusive $ZZ/Z\gamma^*$ production.

Chapter 4

Experiment

In order to produce and perform precise measurements of properties and interactions between fundamental particles given of the SM and investigate the currently unsolved mysteries of nature such as the existence of dark matter, high energy particle accelerators are needed. A particle accelerator can accelerate a chosen particle to a suitable energy which can then be aimed at a fixed-target or collide it with another accelerated particle. The Large Hadron Collider (LHC) is the world's largest and most powerful accelerator complex located at the European Organization for Nuclear Research (CERN) on the French-Swiss border near Geneva, Switzerland [58]. At CERN, hydrogen gas is stripped off electrons and these protons are accelerated to energies up to 6.5 TeV giving rise to center of mass energy $\sqrt{s} = 13$ TeV in proton proton collisions.

Producing these high energy collisions and detecting particles created during these collisions are huge technical challenges and the experimental apparatus used to obtain results for this thesis are the result of decades of collaborative work by thousands of physicists and engineers from around the world.

There are four different experiments, CMS, ATLAS, ALICE and LHCB that are

situated at four interaction points at the LHC and many other smaller experiments that utilize these high energy collisions. CMS and ATLAS are the two main general-purpose detectors using proton-proton, proton-heavy ion and heavy ion-heavy ion collisions. Results in this thesis are based on analyses of proton-proton (pp) collisions data collected by the CMS detector over three years of operation from 2016 to 2018 (Run II). Therefore, this chapter is devoted to detailed descriptions of the design principles of the LHC and the Compact Muon Solenoid (CMS) detector along with their operating characteristics during Run II of the LHC.

4.1 The Large Hadron Collider

The LHC [58] shown in Fig. 4.1 is a circular particle accelerator and hadron collider built in the existing Large Electron Positron (LEP) collider tunnel. With a mean depth of 100 m and circumference of 26.7 km, the LHC is the largest and most expensive collider ever built. The goal of the LHC is to perform proton-proton and heavy ion collisions with high energy and high rate of collisions. The energy of the collisions determines the energy scale that can be probed and an unprecedented rate of collisions leads to statistically significant measurements. Unfortunately, accelerating charged particles loose energy proportional to m^{-4} via synchrotron radiation which means the much heavier protons are more suitable for a reasonable sized circular collider that needs to deliver energies at the TeV scale. Furthermore, much higher rate of collisions can be achieved since no antiparticles are needed. This was indeed the limiting factor at the Tevatron which was a proton antiproton collider as well as LEP. Since the electron is a fundamental particle with no substructure, the energy of an electron beam can be tuned precisely to make precise observations at a very narrow energy range. The proton, on the other hand, is composed of quarks and

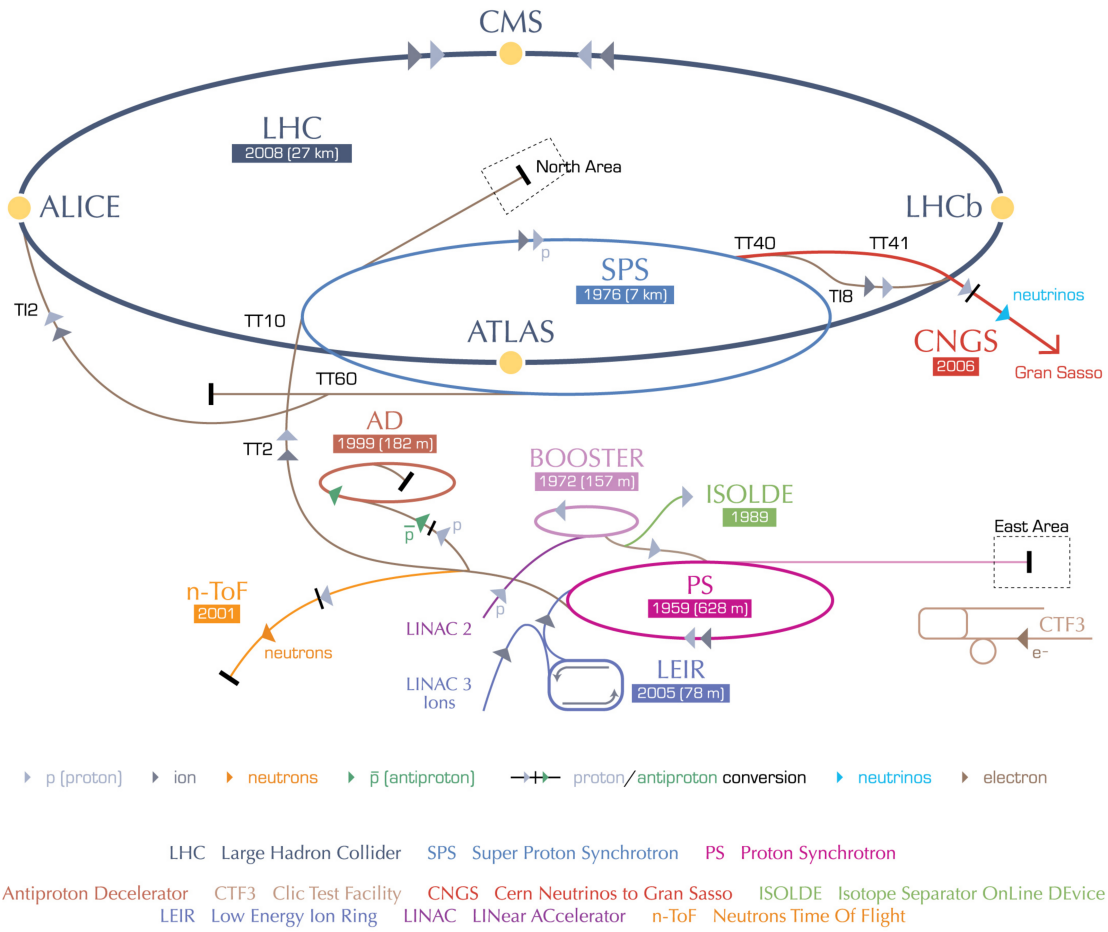

Figure 4.1: Schematic of the CERN accelerator complex, showing accelerators that feed the LHC, as well as those used for other purposes. The acceleration chain that feeds the LHC includes Linac 2, the PS Booster, the Proton Synchrotron, and the Super Proton Synchrotron. Reproduced from Ref. [59].

gluons which carry a varying fraction of the total momentum of the protons which means pp collisions are messier than collisions involving electrons. But, this is also a blessing in disguise as it enables the LHC to measure the properties of SM particles and search for physics beyond the SM through a study of interactions proceeding via quarks and gluons at a wide high energy range.

As shown in Fig. 4.1, in this two ring system, counter-rotating beams of protons are made to collide at four special interaction points. At these interaction points, four different detectors are housed to collect data for physics analyses.

- The Compact Muon Solenoid (CMS) detector, discussed in detail in Section 4.2 is located at point 5.

- A Toroidal LHC ApparatuS (ATLAS) [60] is located underground at point 1. Like CMS, it is a general purpose detector performing similar precision measurements and searches for new physics beyond the SM. With a radius close to 11 m, length of 44m and weighing around 7000 tonnes, ATLAS is a much larger detector than CMS.

- Large Hadron Collider beauty (LHCb) [61] is a 21 m long, 10m high and 13 m wide detector located at access point 8 close to the beautiful village of Ferney-Voltaire in France. The experiment specializes in investigating matter-antimatter asymmetry (one of the biggest unresolved questions in particle physics) by looking for charge-parity violations in b-quark physics.

- A Large Ion Collider experiment (ALICE) [62] of dimensions $16\times16\times26\ m^3$ and a total weight of approximately 10000 tonnes is one of the largest experiments in the world designed to study quark gluon plasmas using lead-ion collisions. This heavy-ion detector devoted to the study of strong interactions is located at point 2 in the territory of Sergy, France.

4.1.1 Design characteristics of the LHC

The protons (or lead ions) required for collisions in the LHC need to be accelerated gradually to their design energies on the TeV scale using the accelerator complex shown in Fig. 4.1. The proton accelerator chain is as follows: protons are stripped from hydrogen atoms and accelerated from rest to 50 MeV by the Linac 2 linear accelerator; these protons are then injected into a chain of circular accelerators starting with the Proton Synchotron Booster (PSB) which accelerates the protons to 1.4 GeV;

then the PSB feeds the Proton Synchotron (PS) where they are accelerated to 25 GeV; finally the Super Proton Synchotron (SPS) accelerates the protons to 450 GeV before they are injected into the main LHC tunnel. The Linac 2 and all subsequent circular accelerators in the aforementioned chain use radio frequency (RF) cavities to accelerate the protons [58].

As mentioned in Section 4.1, we can effectively neglect the affects of synchrotron radiation loss in determining the energy of the LHC pp collider. The primary limitations on energy come from the strength of the bending magnetic field B ad the radius of curvature R of the beamline

$$E_{\text{beam}} = eBRv \approx eBRc \tag{4.1}$$

where $v \approx c$ is the speed of the beam and e is the proton electron electron charge. Since the LHC tunnel size was set by the existing LEP tunnel, for given $R = 2.804$ km, the dipole bending magnets need to operate at 8.33 T to achieve the design energy of 7 TeV. This is accomplished via 1232 15- m long superconducting magnets based on NbTi Rutherford cables which must be cooled down to 1.9 K with liquid Helium to maintain superconductivity. Due to space limitations in the LEP tunnel prohibiting two independent beam systems, a **twin-bore** or **two-in-one** design was adopted for almost all LHC superconducting magnets as shown in Fig. 4.2 [58]. In addition to dipole magnets, the LHC is equipped with superconducting quadrupole, sextupole and octupole magnets which are used to focus the beam and keep it in its compact form through the whole process until interaction points. There are 8 528 m straight sections in the LHC tunnel which can serve as experimental or utility insertion points in the beamline. As mentioned in Section 4.1, four of these are **experimental insertions** which house the four main LHC experiments. Points 2 and 8 also serve as injection points for the two beams from SPS to the LHC. Points 3

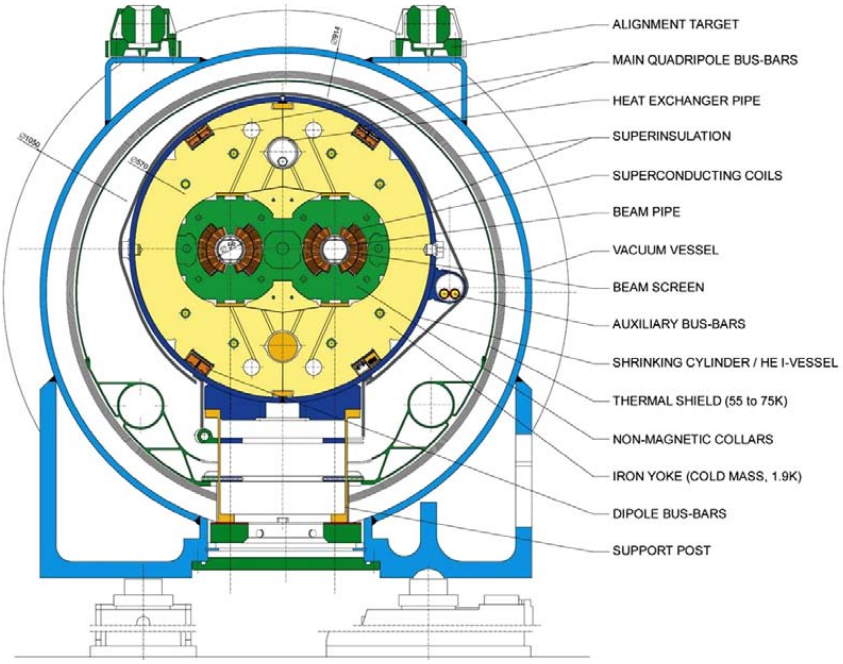

Figure 4.2: Schematic cross section of an LHC dipole and its attendent electrical and cryogenic infrastructure, reproduced from Ref. [58].

and 7 contain collimators systems to remove **beam halo** and to protect downstream detectors in case of beam control failures [58]. Point 4 contains the two RF systems; one for each beam. Finally, the beam can be safely dumped after use or in the case of a quench [63] at Point 6.

The RF system responsible for accelerating the protons from the SPS energy of 450 GeV to the collision energy is composed of RF cavities each of which oscillate at 400 MHz. Proton bunches from SPS are spaced in one of every 10 RF **buckets** as they are introduced into the main tunnel leading to the LHC collision rate of 40 MHz. This corresponds to a bunch separation of 25 ns which means a total of 3564 proton bunches can be fitted in the LHC tunnel each with a frequency of $f_{rev} = 11.245$ kHz. While more operational details are given in the next section, it is important to note that only a maximum of 2808 bunches can be placed in the LHC to allow sufficient gaps between bunches for the beam injection and beam dump (kicker) magnets to

activate [58].

4.1.2 Operation of the LHC during Run II (2016-2018)

While Run 2 technically covers 2015 as well, the operation of the LHC relevant to this work spans from 2016 to 2018 with the first beams injected on March 25,2016 and the 2018 proton run ending on Oct 24,2018. During this time, the LHC delivered pp collisions at $\sqrt{s} = 13$ TeV and the machine availability for pp collisions ranged between 76 % and 83% [64]. As shown in Table 4.1, the LHC operated with a high level of performance considering that it exceeded some of its design parameters such as instantaneous luminosity.

Beam parameter	2016 operation value	2017 operation value	2018 operation value
Protons per bunch N_b	1.25×10^{11}	1.25×10^{11}	1.2×10^{11}
Bunches per fill n_b	2076	1868	2556
Orbit frequency f_{rev}		11.245 kHz	
Gamma factor $\gamma_r = E_{\text{beam}}/m_p$	6930	6930	6930
Normalized transverse emittance ϵ_n	2.1 μm	1.8 μm	2 μm
β^* parameter	40 cm	30 cm	30 cm
Crossing angle θ_c	185 μrad	150/110 μrad	160/130 μrad
RMS longitudinal bunch length σ_z	7.87 cm	7.87 cm	7.87 cm
Instantaneous luminosity $\mathcal{L}$	$1.3 \times 10^{34}\,\text{cm}^{-2}\,\text{s}^{-1}$	$1.5 \times 10^{34}\,\text{cm}^{-2}\,\text{s}^{-1}$	

Table 4.1: Values of the various beam parameters that enter into the instantaneous luminosity formula of Eqn. 4.3. Values are given for the typical operating parameters during the 2016-2018 data-taking run [65].

As mentioned before, the rate ($\frac{\mathrm{d}N}{\mathrm{d}t}$) of collisions is an important factor in determining the success of a particle collider such as the LHC. Luminosity, measured in *barns* is:

$$\frac{\mathrm{d}N}{\mathrm{d}t} = \mathscr{L}\sigma, \tag{4.2}$$

where σ is the cross section of a process. The instantaneous luminosity $\mathscr{L}$ measures the rate of pp collisions and determines the rate of particle production through different processes in collisions. The maximum instantaneous luminosity delivered by

the LHC during Run 2 was $2.06 \times 10^{34}\,\mathrm{cm}^{-2}\,\mathrm{s}^{-1}$ but due to extreme pileup conditions for the CMS and the ALTAS detectors, it was leveled off at $1.5 \times 10^{34}\,\mathrm{cm}^{-2}\,\mathrm{s}^{-1}$ [64] which was still higher than the design luminosity of $\approx 1.1 \times 10^{34}\,\mathrm{cm}^{-2}\,\mathrm{s}^{-1}$. The instantaneous luminosity can be parametrized in terms of LHC beam parameters:

$$\mathcal{L} = \frac{N_b^2 n_b f_{\mathrm{rev}} \gamma_r}{4\pi\epsilon_n \beta^*} \left(1 + \frac{\theta_c^2 \sigma_z^2 \gamma_r}{4\epsilon_n \beta^*}\right)^{-1/2} \tag{4.3}$$

where N_b is the number of particles (protons or heavy ions) per bunch, n_b the number of bunches per beam, f_{rev} is the beam revolution frequency, γ_r is the relativistic gamma factor, ϵ_n is the normalized emittance[1], β^* is the value of the amplitude function β at the interaction point[2], θ_c the crossing angle, and σ_z the RMS longitudinal bunch length.

While instantaneous luminosity determines the rate of collisions, the more relevant term is integrated Luminosity, $\mathscr{L}_{int}$ which is obtained by integrating instantaneous luminosity over time. Integrated luminosity as seen in Fig.4.3 is reported in fb^{-1} where femto $= 10^{-15}$ and barn(b) is defined as $1b = 10^{-24} cm^2$. In total, the LHC delivered about 158.7 fb^{-1} to CMS and ATLAS in pp collisions from 2016-2018. As shown in Eqn. 4.3, luminosity or the rate of collisions can be increased by maximizing the number of particles per bunch, decreasing the collision angle or squeezing each bunch. However, due to the high density of protons per bunch, there are multiple pp interactions per bunch crossing, known as pileup. The number of inelastic collisions (pileup) per bunch crossing depends on the inelastic pp cross section, $\sigma_{\mathrm{pp}} \approx 70mb$ [66] and increases with the instantaneous luminosity

$$N_{\mathrm{pu}} = \frac{\mathcal{L}\sigma_{\mathrm{inel}}}{n_b f_{\mathrm{rev}}}.$$

[1]The emittance is a measure of the average spread in the position-and-momentum phase space of the beam. The normalized emittance is written $\beta\gamma$, where β and γ are the standard Lorentz factors.

[2]This function is related to the spread σ of the beam through $\beta^* = \frac{\sigma^2}{\epsilon}$, where σ is the spread of the bunch in the transverse plane.

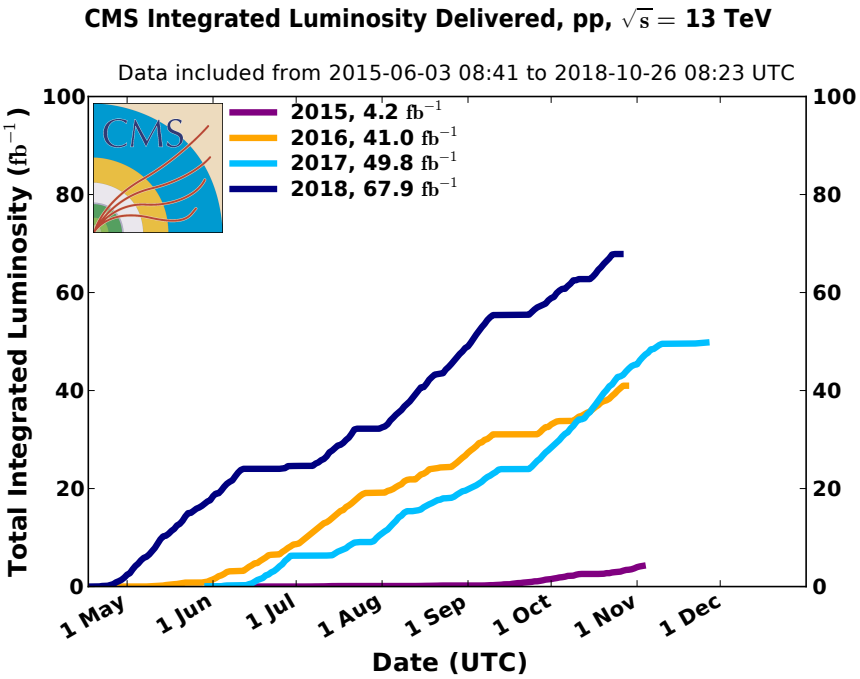

Figure 4.3: Cumulative luminosity versus day delivered to CMS during stable beams for pp collisions at $\sqrt{s} = 13$ TeV from 2015-2018 (Run II). Data taken during 2015 is not used in this thesis.

Pileup interactions increase the number of spurious particles produced in the detector and makes it harder to reconstruct events of interest. During Run 2, the average pile-up in 2016 was around 27 pp interactions per crossing and around 37 during 2017 and 2018. The pileup distributions for Run 2 for CMS are shown in Fig. 4.4 where the inelastic cross section value of 80 mb [67] is taken from the theoretical prediction from Pythia and should be used to compare to other LHC experiments.

4.2 The Compact Muon Solenoid Experiment

The SM measurements and searches for BSM physics described in this thesis were performed using the data collected with the CMS detector, a hermetic general-purpose detector located on the LHC ring. While the CMS detector design and its components

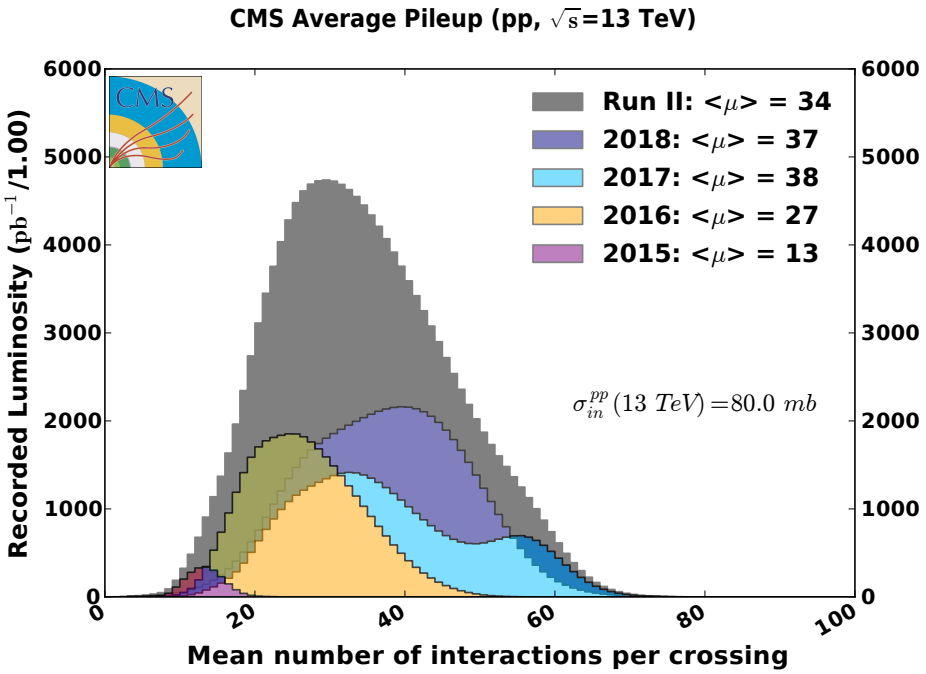

Figure 4.4: Mean number of interactions per bunch crossing for each pp running period during Run II at 13 TeV, using the online luminosity values and the "LHC standard" value of 80 mb, which is taken from the theoretical prediction from Pythia and should be used to compare to other LHC experiments.

are similar to other general purpose particle physics detectors consisting of a tracker, calorimeters and a solenoidal magnet, it was specifically designed make precision measurements in the electroweak sector and search for new physics at the TeV energy scale. In the context of EWSB and the Higgs boson predictions, the design was heavily influenced by its prospective ability to reconstruct specific final states of Higgs boson production. These design requirements as described in [68] are as follows:

- Good muon identification and high momentum resolution in order to achieve dimuon mass resolution of $\approx 1\%$ at $m_{\mu\mu} = 100\,\text{GeV}$ and accurate charge assignment of muons up to 1 TeV;

- Good charged particle momentum resolution and reconstruction efficiency for particles with momentum as low as 1 GeV and efficient identification of τ leptons

and b-jets;

- Good electromagnetic energy and momentum resolution to achieve excellent diphoton and dielectric mass resolution of $\approx 1\%$ at 100 GeV with a wide geometric coverage to maintain sufficient π^0 rejection while also ensuring efficient photon and lepton isolation;

- Good missing transverse energy and dijet mass resolution.

CMS is 28.7 m long, has an overall diameter of 15.0 m and weighs 14,000 tonnes. A schematic overview of the detector is shown Fig. 4.5 with its components. The cylindrically-shaped central part called the barrel and the two circular flat end pieces known as endcaps make up the two geometric shapes of CMS. This section will present an overview of these components and sub-detectors and how they fit into the design goals stated above. As shown in Fig. 4.5, CMS features a silicon inner tracker, a crystal electromagnetic calorimeter (ECAL) and a hermetic hadronic calorimeter (HCAL) all housed inside a 3.8 T superconducting magnet. This unique feature of CMS makes it **compact** and allows for high electromagnetic energy resolution. The outer part of the detector, the steel flux **return yoke**, confines the magnetic field and stops all remaining particles except for muons and neutrinos. The muon detectors, a set of gas ionization detectors, are interleaved with the iron yoke as shown in the sectional view of the detector in Fig. 4.5 .

The CMS coordinate system is a right-handed coordinate system centered at the nominal collision point. The x axis is perpendicular to the beam and points radially inwards towards the center of the LHC ring, the y axis points vertically upwards and the z axis is pointed anti clockwise along the beam direction when viewed from above as shown in Fig. 4.5. The azimuthal angle ϕ is measured from the x axis in the x-y plane and the radial coordinate is denoted by r. The polar angle θ is measured with

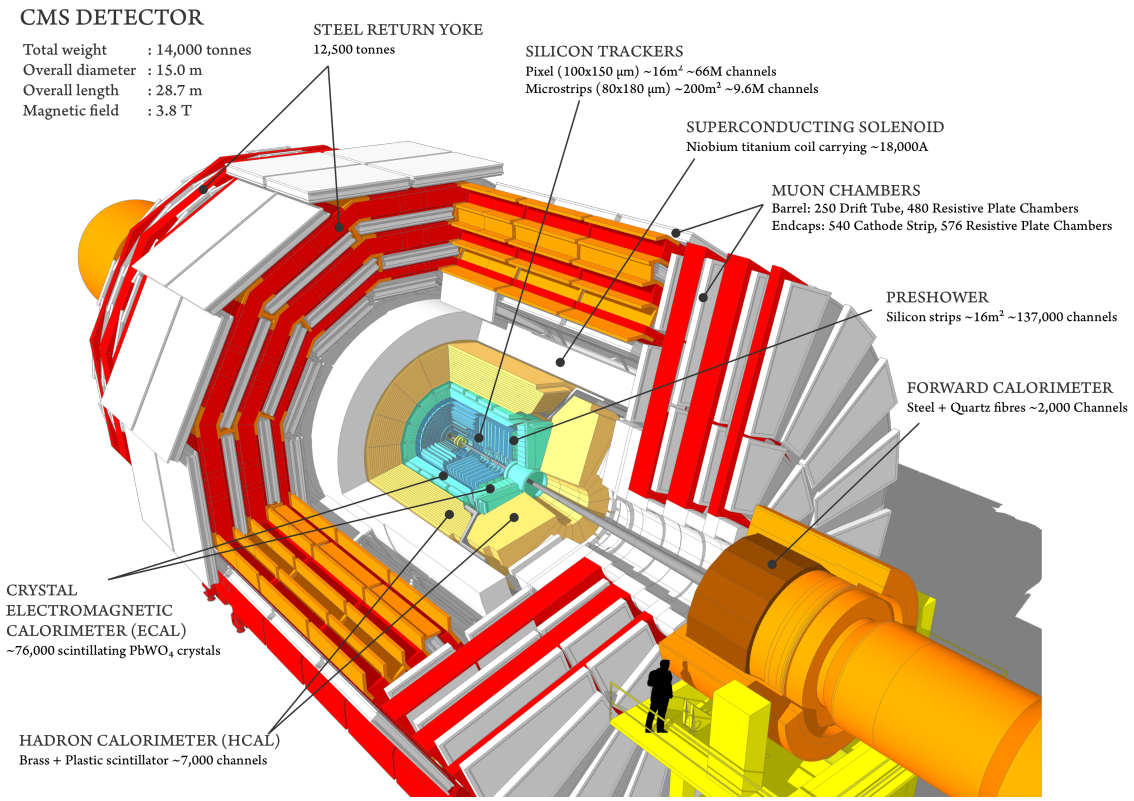

Figure 4.5: Diagram of the components of the CMS detector.

respect to the z axis. The polar angle is converted into pseudorapidity,

$$\eta = -\ln \tan\left(\frac{\theta}{2}\right),$$

since differences in pseudorapidity are invariant under Lorentz boosts along the z axis. Due to the conservation of momentum (p_{T}) in the transverse (x-y) plane, the 3-momentum of a particle can be expressed as

$$\vec{p} = (p_{\mathrm{T}}, \eta, \phi),$$

4.2.1 CMS Magnet

The CMS magnet constructed from a 4-layer winding of stabilized reinforced NbTi conductor is designed to reach a 4 T field. The solenoid magnet is a key feature of the

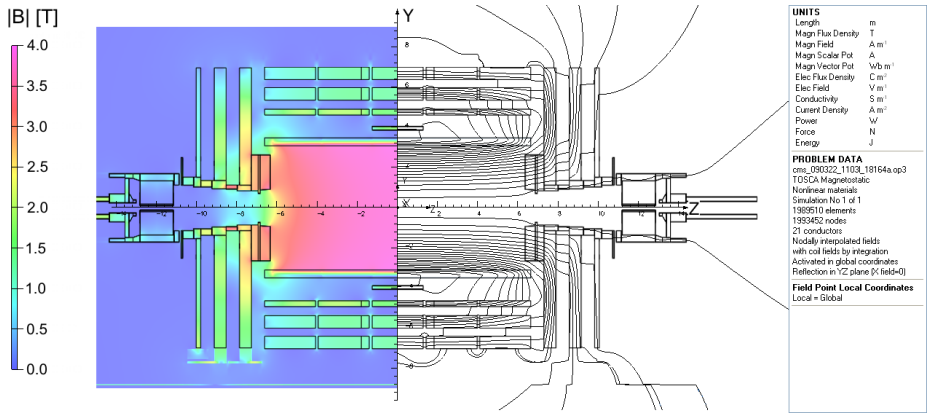

Figure 4.6: Value of B (left) and field lines (right) predicted on a longitudinal section of the CMS detector, for the underground model at a central magnetic flux density of 3.8 T. There is a magnetic flux increment of 6 Wb for each field line. Reproduced from [69], Fig. 5.

detector and the strong magnetic field allows good momentum resolution for charged particles. The Superconducting solenoid of 6 m internal diameter and 12.5 m in length has a cold mass of 220 tons which cools the magnet to 4.7 K when in operation [68]. While it is designed to reach 4 T it is operated at 3.8 T to prolong the lifetime of the magnet [69]. Outside the magnet, the field drops to 2 T in the steel flux return yoke. A map of the magnetic field in the CMS detector is shown in Fig. 4.6. It is one of the largest superconducting magnets ever built and it is the most powerful magnet in the world by stored energy (2.6 gigajoules).

Both calorimeters and the tracker are situated inside the solenoid while the muon detectors (Section 4.2.5) are embedded in the steel yoke outside. The large magnetic field inside the magnet leads to a powerful bending radius for charged particles passing through the tracker and the calorimeters while the 2 T return field outside allows to measure muon momentum independent of the inner tracker.

4.2.2 The inner tracker

A charged particle's trajectory from the collision point is affected by the Lorentz force,

$$F = \frac{q}{\gamma m}\vec{p} \times \vec{B},$$

where q is the charge of the particle, m its mass and γ is the relativistic factor. With a uniform B field along the z axis (beam line), track path is a helix of radius R given by

$$R = \frac{p_{\mathrm{T}}}{|q|B}, \tag{4.4}$$

Therefore, one can measure the transverse momentum of a particle using

$$p_{\mathrm{T}} \approx \frac{0.3L^2B}{8s},$$

where the sagitta (s) and distance from interaction point (L) are related to the radius of the track ($R \approx \frac{L^2}{2s}$) and calculated during event reconstruction which is discussed in Chapter 6. The transverse momentum resolution is given by

$$\frac{\delta p_{\mathrm{T}}}{p_{\mathrm{T}}} \propto \frac{p_{\mathrm{T}}}{BL^2}, \tag{4.5}$$

which means a strong magnetic field and a large tracking volume are essential for precise momentum measurements at high energies.

The inner tracker surrounds the interaction region and serves to reconstruct charged tracks, measure their momenta and reconstruct the vertices from which the particles originate. Over 200 m^2 silicon is cooled to 253 K ($\approx$ 10 °C) to prevent lasting radiation damage to the tracker. It is made up of the 66 million channel Pixel detector on the inside and 9.3 million channel Silicon strip detector on the outside. As mentioned in Section 4.1.2, during most of Run 2, with a typical maximum of 50 collisions per bunch crossing and roughly 30 charged particles per collision, there is

a high flux of charged particles through the tracker. Therefore, the high granularity provided by millions of individual pixels and strips in the tracker is essential for achieving high performance in track reconstruction and momentum resolution.

The pixel detector consists of 3 barrel layers and 2 endcap disks, and the strip tracker consists of 10 barrel layers and 12 endcap disks. During the 2016-2017 extended year end technical stop, the pixel tracker was upgraded to have a fourth detection layer. More details about the upgrade can be found in the CMS Technical Design Report for the Pixel Detector Upgrade [70]. The tracker geometry, including the layout of the silicon sensors, is shown in Fig. 4.7. As particles travel through the tracker the pixels and microstrips produce tiny electric signals that are amplified and detected. The tracker employs sensors covering an area the size of a tennis court, with 75 million separate electronic read-out channels. The track p_{T} resolution is roughly 0.5–2% for most of the relevant kinematic range and a little worse track p_{T} resolution (up to 5%) for low p_{T} tracks (less than 1 GeV) at high pseudorapidities [71].

4.2.3 Electromagnetic calorimeter and the preshower

The electromagnetic calorimeter (ECAL) surrounds the inner tracker but its also contained inside the solenoid. The ECAL is designed to make high resolution position and energy measurements for electrons and photons. For example, the energy resolution for photons from SM Higgs decays is between 1.1% to 2.6% in the barrel and between 2.2% to 5% in the forward endcaps [72]. Electrons from Z boson decays have even better resolution of 0.4% (0.8%) in the barrel (endcaps) [72].

It is composed of over 75k Lead Tungstate crystals read out by photodetectors. The high density ($8.3\,\mathrm{g/cm^3}$) lead tungstate was chosen due to its short radiation length (the mean distance an electron travels in the material before losing $1-\frac{1}{\mathrm{e}}$ of its initial energy) of 0.89 cm and its small Molière radius (the radius at which 90% of the

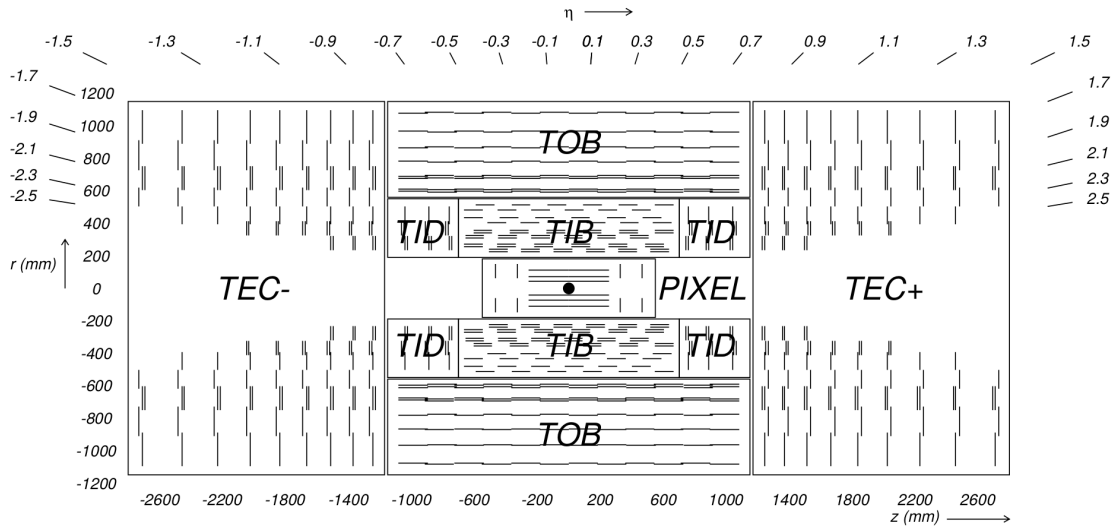

Figure 4.7: Diagram of the inner tracker layout, reproduced from Ref. [68], comprised of the pixels, tracker inner barrel (TIB), tracker outer barrel (TOB), tracker inner disk (TID), and tracker endcap (TEC) components. Each line represents a detector module. Double lines represent stereo modules, where two two modules are mounted back-to-back to provide two closely-spaced hit layers.

electromagnetic shower is contained on average) of 2.2 cm. These features allow for a fine granularity for high resolution measurements, containing the electromagnetic shower laterally and result in a compact calorimeter which helps reduce the volume and cost of the solenoid. Furthermore, the material has a fast response as about 80% of the light is emitted within one bunch crossing (25 ns).

There are about 61k crystals in the cylindrical barrel (EB) covering $|\eta| < 1.479$ and 14600 in the 2 endcaps (EE) covering the η range $1.479 < |\eta| < 3.0$. The crystal length in EB is 230 mm (220 mm in EE) corresponding to ~ 26 (25) radiation lengths which is sufficient to contain 98% of the energy of electrons and photons up to 1 TeV. The transverse size of the crystals at the front face is $2.2 \times 2.2\,\mathrm{cm}^2$ in EB ($2.86 \times 2.86\,\mathrm{cm}^2$ in EE). A silicon-lead sampling calorimeter, known as the ECAL preshower, is installed in front of EE, in the $1.653 < |\eta| < 2.6$ region to better discriminate photons against π^0 decaying into photon pairs. The total thickness of

the preshower detector(ES) is ∼3 radiation lengths [68]. A schematic layout of the ECAL is shown in Fig. 4.8.

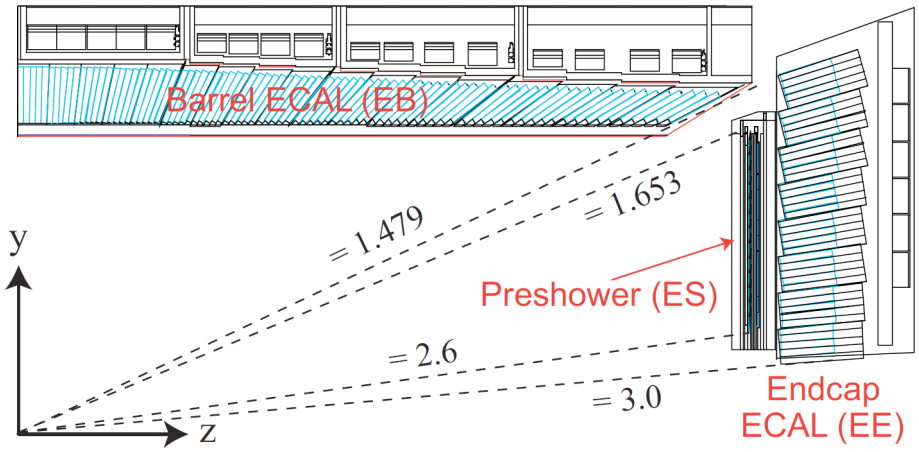

Figure 4.8: Diagram of CMS ECAL geometry, reproduced from Ref. [73],including the barrel, endcap, and preshower components. Dashed lines show reference pseudo-rapidity values with respect to the center of the detector.

($PbWO_4$) crystals emit blue-green light (420-430 nm) which is converted to electrical pulses with about 4.5 photoelectrons per MeV at 18 °C by silicon avalanche photodiodes (APDs) in EB and via vacuum phototriodes (VPTs) in EE. APDs are chosen for the barrel ECAL because they provide the required gain in the 3.8T magnetic field. VPTs in the endcaps can sustain higher radiation losses than APDs [68]. The crystals in the barrel are grouped into 5×5 towers and the endcap crystals are grouped to approximate projective towers, which provide trigger information (section 4.2.6) through off-detector electronics. This formation into towers also allows full crystal readout for select regions of interest.

The ECAL barrel energy resolution was measured [74] in beam tests and the resolution is parametrized as follows:

$$\left(\frac{\sigma}{E}\right)^2 = \left(\frac{2.8\%}{\sqrt{E}}\right)^2 + \left(\frac{0.12}{E}\right)^2 + (0.30\%)^2 \,. \tag{4.6}$$

where the mean stochastic term, representing Poisson fluctuations in the showers, was measured to be 2.8%. The second term comes from electronic noise and noise from pileup (both in-time and out-of-time), and the constant term represents any intrinsic differences between crystals and light yield as well as the uncertainty in energy calibration.

4.2.4 Hadronic calorimeter

Surrounding the ECAL , the hadronic calorimeter (HCAL) is a compact (inside solenoid), hermetic ($|\eta| < 5$) sampling calorimeter responsible for measuring the energy of charged and neutral hadrons for identification and measurement of hadronic jets. Combined with the measured energies in the ECAL, these measurements also lead to the measurement of the missing transverse energy in an event of interest. The expected jet transverse energy resolution reconstructed from calorimeter information is shown in Fig. 4.9 for various pseudorapidity regions. Further details about the reconstruction of jets using calorimeter and tracking information are discussed in section 6.6.5.

The CMS HCAL can be split into barrel ($|\eta| < 1.3$) , endcap ($1.3 < |\eta| < 3.0$), Outer (HO) and Forward regions. The barrel and endcap regions consist of flat steel and brass absorber plates interleaved with plastic scintillator tiles which have fiber optic cables embedded into them. These fibers are divided into readout **towers** corresponding to rectangular η-ϕ regions of the detector where the fibers in each tower read out to hybrid photodiodes (HPDs) that can operate in high magnetic fields [75]. HB and HE are compact calorimeters with a thickness of around 5.4 nuclear interaction lengths (mean distance travelled by a hadronic particle before undergoing an inelastic nuclear interaction) in the central barrel to more than 10 in the endcaps. Therefore, this central calorimetry is complemented by a **tail-catcher** outer component (HO) in

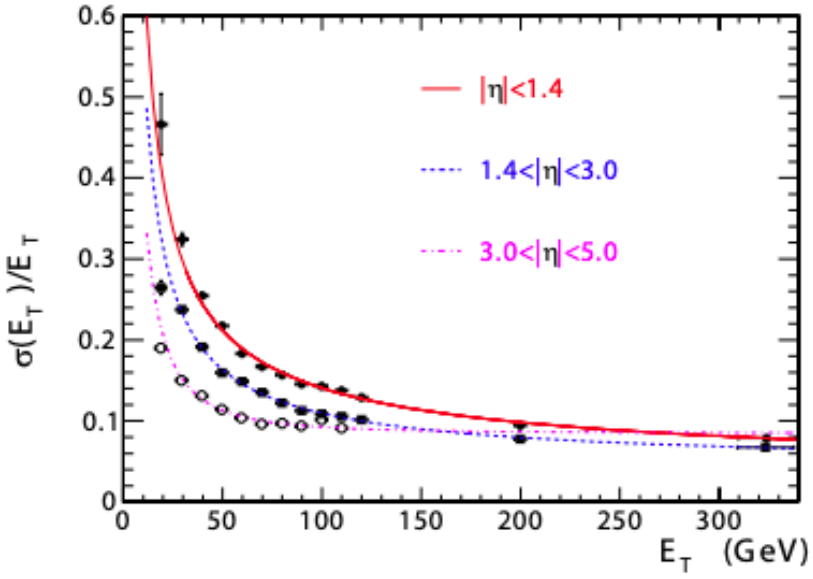

Figure 4.9: The jet transverse-energy resolution as a function of the jet transverse energy for barrel jets ($|\eta| < 1.4$), endcap jets ($1.4 < |\eta| < 3.0$), and very forward jets ($3.0 < |\eta| < 5.0$). The jets are reconstructed with an iterative cone algorithm (cone radius = 0.5). Reproduced from [68].

the barrel region ensuring that hadronic showers are sampled with nearly eleven interaction lengths and minimizing any hadronic flux interacting with the muon system. The HO uses the steel return yoke as the absorber instead of the brass material in the barrel and endcaps. HCAL Forward (HF) is a cherenkov-based, iron/quartz-fiber, radiation-hard detector which measures EM rich jets outside of ECAL acceptance. The Cherenkov light is detected by photomultiplier tubes (PMTs). Its coverage runs from $3 < |\eta| < 5$ and its resolution is lower than the HCAL barrel/endcap resolution but its essential for ensuring maximum geometric coverage for the measurement of the transverse energy in the event [68]. A schematic of the HCAL is shown in Fig. 4.10. The HF PMTs were upgraded to use multi-anode output and the HPDs in HB and HE were replaced by silicon photomultipliers (SiPMs) during Phase-I upgrade operations in 2017 [70]. During the 2016-2017 extended year-technical stop, four of the HPDs

in the HE sector HEP17 were replaced with SiPMs. Radiation damage suffered by the HCAL detector had been worse than anticipated and the upgraded SiPM-based system has been reported to bring more than 50% improvement in radiation-induced response degradation [76]. After the HE segment change in 2017, the analysis of 2017 data showed that up to 60% of the signal loss in HE was caused by HPD deterioration rather than being exclusively due to radiation damage of the scintillator. Overall, the SiPM give factor of three improvement in photon-detection efficiency, increased longitudnal segmenation, mitigate scintillator radiation damage and simplify calibration [76]. Considering all these substantial performance imporovements over HPDs, at the beginning of 2018, the full HE detector has been equipped with SiPMs.

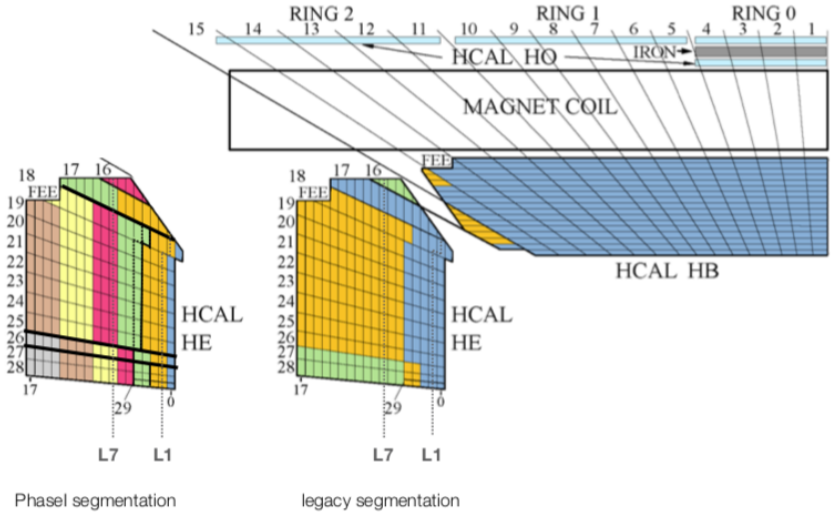

Figure 4.10: Longitudnal section of the HB, HE and HO detectors. The segmentation of the upgraded HE (left) is compared with the one for the legacy detector (right). Shading of the layers of HB and HE show the longitudinal (depth) segmentation of the readout channels. Figure 1. from Ref. [76].

The characteristic resolution of the HCAL can be parametrized in the same way as for ECAL with charged hadrons having a resolution of

$$\left(\frac{\sigma}{E}\right)^2 = \left(\frac{115\%}{\sqrt{E}}\right)^2 + (5.5\%)^2 \,. \tag{4.7}$$

measured in the barrel using test beams [77] and

$$\left(\frac{\sigma}{E}\right)^2 = \left(\frac{280\%}{\sqrt{E}}\right)^2 + (11\%)^2 . \tag{4.8}$$

in the HF [78, 79]. Compared to the ECAL, the HCAL has significantly poorer resolution because its a sampling calorimeter with most of the energy deposits taking place in the absorber layers rather than the scintillating material. Regardless, the HCAL is essential for an accurate account of the missing transverse energy and provides essential trigger information (Section 4.2.6).

4.2.5 Muon System

The Muon system is responsible for triggering, identification and assisting the inner tracker in measuring high-p_{T} muons. High energy muons are produced in many SM final states including the diboson (ZZ) decays to four leptons relevant to this thesis. As we can see from these Fig. 4.11, momentum measurement below 200 GeV is tracker dominated but above that the full system has better resolution. However, the tracker alone is not able to distinguish between charged muon tracks and the more commonly produced charged hadrons. High energy muons are minimum-ionizing particles (MIPs) and hence interact minimally with the calorimeter system. The vast majority of charged hadrons do not make it out of more than 16 radiation lengths of inner material on average so placing the muon detector system outside all other detector systems is ideal.

The muon system is composed of three gas ionization detectors embedded in the iron return yoke which is fully saturated with the 2 T magnetic field form the solenoid. Ionizing gas chambers provide hits which form a track in all three sub detectors; drift tubes (DTs), cathode strip chambers (CSCs), and resistive plate chambers (RPCs). A schematic overview of the muon system is shown in Fig. 4.12

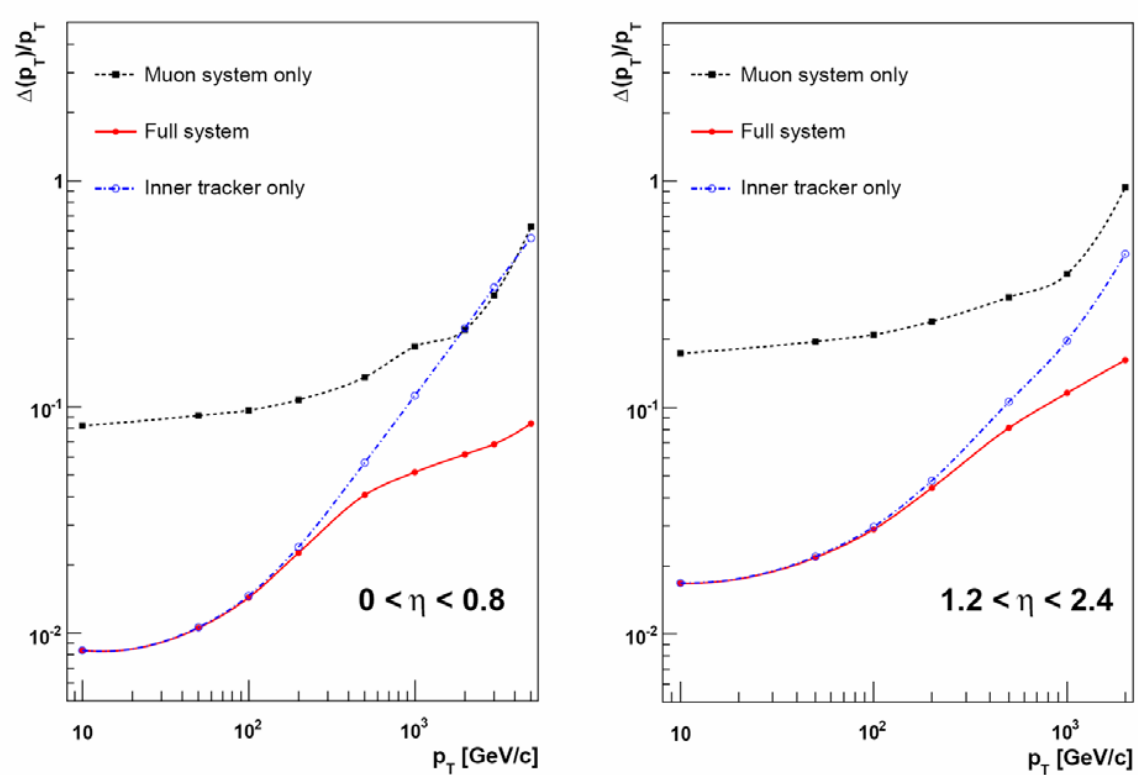

Figure 4.11: Muon p_{T} resolution as a function of muon p_{T} separated by muon system only, inner tracker only and the full system combined together.

4.2.5.1 Drift tubes

In the barrel, Drift tubes (DTs) cover the region up to $|\eta| < 1.2$. The DTs are designed for the low muon rates in the barrel and the relatively low strength of the magnetic field. They are arranged into four **stations** around the beam line such that the three inner cylindrical stations have 60 drift chambers each while the outer one has 70. Each DT chamber is composed of two or three **super layers** (SL), each made of 4 layers of rectangular drift tubes with each layer staggered by half a tube in ϕ , to eliminate dead spots in the efficiency. The drift tubes have a cross section of $13 \times 42\,\mathrm{mm}^2$ and are 2.4 m in length. As shown in Fig. 4.13, each tube contains an anode wire, two cathode strips, and two field-forming strips, held at specific electric potentials. When a charged particle traverses the Ar-CO_2 gas mixture inside the

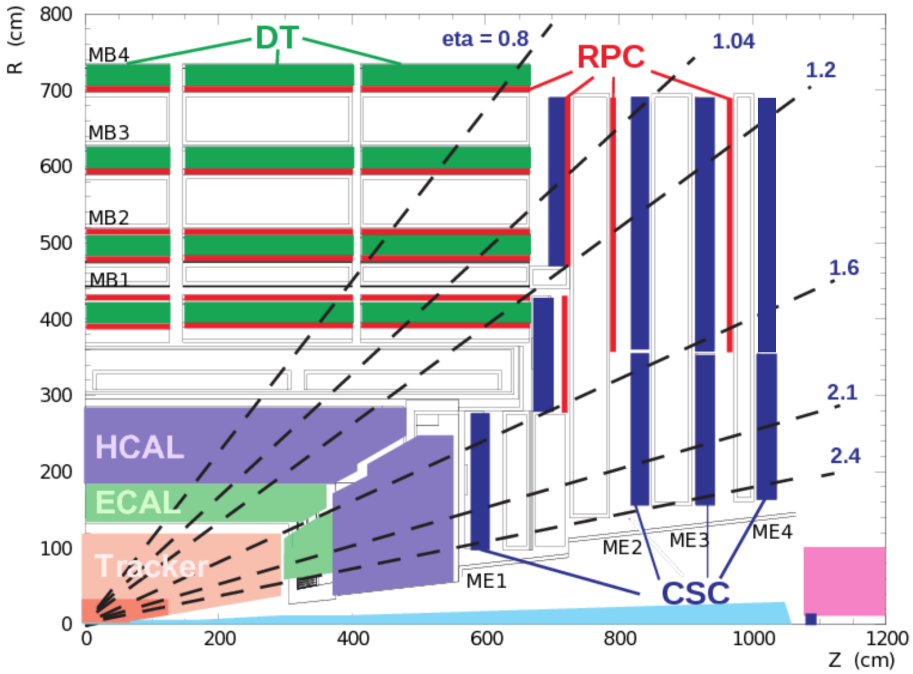

Figure 4.12: Diagram of the CMS muon systems, including the drift tubes (DTs), resistive plate chambers (RPCs), and the cathode strip chambers (CSCs). Dashed lines show reference pseudorapidity values with respect to the center of the detector.

42 mm wide tube, free electrons created by the ionizing radiation drift in the electric field towards the anode wire where they trigger a signal. The resulting electric pulse is then amplified, digitized with a time-to-digital converter (TDC) and read out. The r-ϕ position resolution in the DTs is around 100 µm at each **station** while the timing resolution in each SL is a few nanoseconds [68].

4.2.5.2 Cathode strip chambers

Cathode strip chambers (CSC) cover the endcap regions providing muon detection in the region $0.9 < |\eta| < 2.4$ where magnetic field is large and non-uniform and muon rates are high. Therefore, CSCs have a fast response time which is useful for triggering [80, 81], fine segmentation which allows for a good spatial resolution ($40 - 150$ µm) even with the high muon and background and are more radiation resistant than the

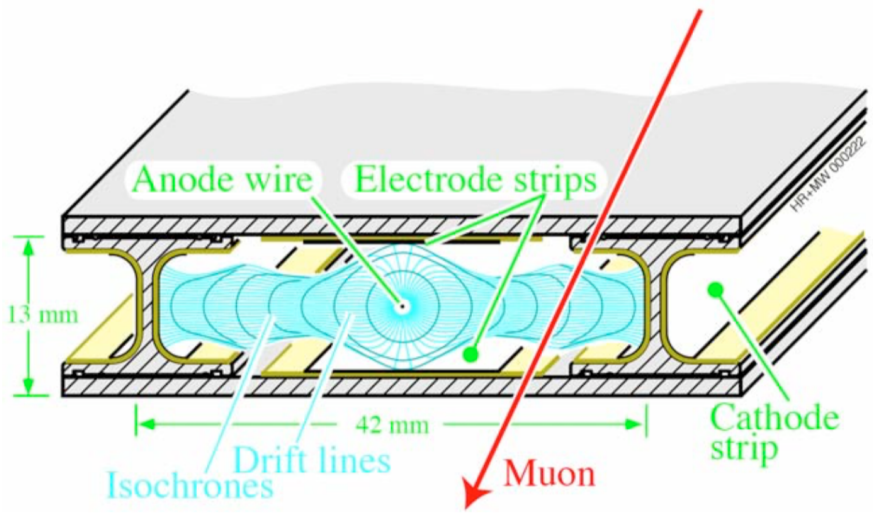

Figure 4.13: Schematic of a drift tube cell showing drift lines leading to/from the anode wire and isochrones three of which are seen as the concentric lines surrounding the anode wire. The voltages applied to the electrodes are +3,600 V for wires, +1,800 V for strips, and -1,200 V for cathodes.

DTs.

As shown in Fig. 4.14, the CSC chambers are trapezoidal arrays of aluminum cathode strips crossed with anode wires within a Ar-$CO_2 - CF_4$ gas mixture. When muons pass through, they create an avalanche of electrons at the anode wires positive ions moving towards the cathode strips create a charge pulse in the strips. Each cathode strip is read out, whereas anode strips are read out in groups of 16 giving two position coordinates both in the r-ϕ and η planes. The position resolution of a CSC chamber is around 100 m, and the timing resolution is 7 ns, more details can be found in Ref.[68].

4.2.5.3 Resistive plate chambers

While the DTs and CSCs provide fast readout and are able to trigger on the p_{T} of muons with good efficiency and high background rejection, due to the uncertainty in

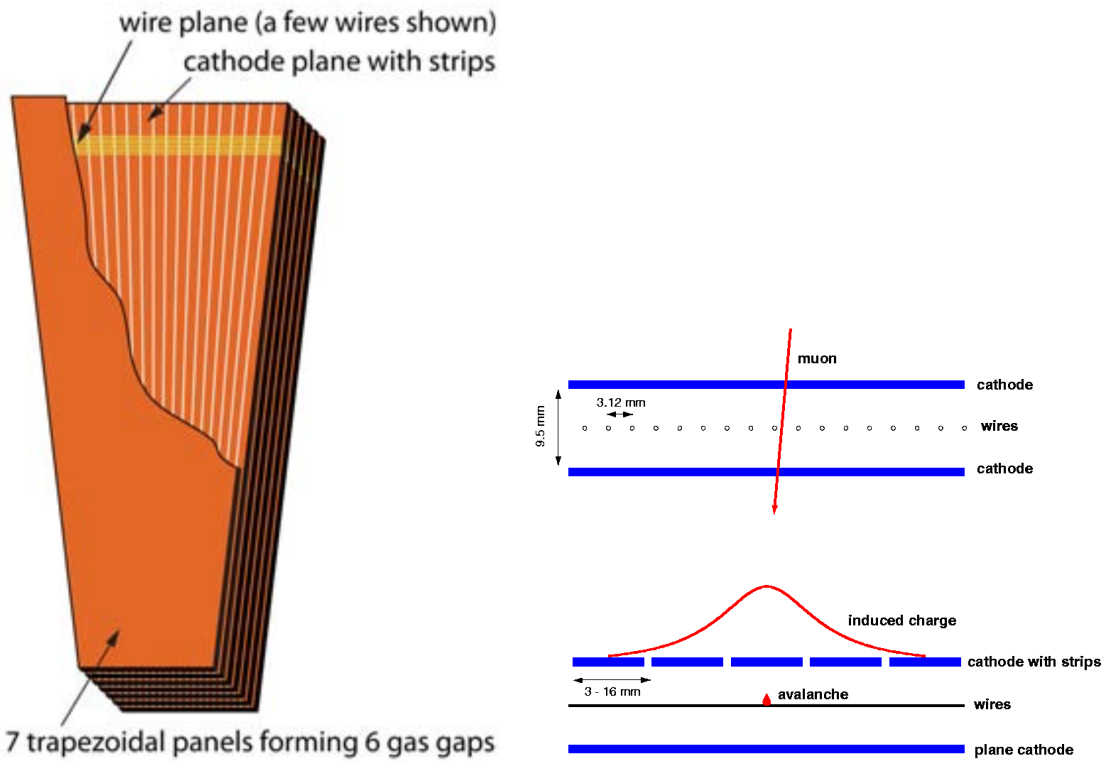

Figure 4.14: (left) Schematic of a CSC module composed of 7 trapezoidal panels with 6 gas gaps between the panels. The cut away of the top panel reveals the anode wires used to detect ionized molecules from a passing muon. The anode wires run horizontally and the cathode strips run vertically in this orientation. (right) Principle of operation for a CSC layer, showing the avalanche around the anode wires and the pulse shape on the cathode strips, which are combined for accurate position measurement. Both figures are reproduced from Ref.[68]

the eventual background rates at full luminosity, a complimentary detector system was needed. Thus, resistive plate chambers (RPCs) cover both the barrel and endcap regions up to $|\eta| < 1.6$ and provide a relatively lower position resolution but excellent time resolution of $\approx 1\,\text{ns}$ (well within the 25 ns bunch spacing).

As shown in Fig. 4.15, the RPCs are parallel-plate (a positively-charged anode and a negatively-charged cathode) ionizing gas detectors with two gas chambers per module filled predominately with $C_2H_2F_4$ gas. Both chambers are operated in avalanche mode where the total induced signal is the sum total of the signal created by an

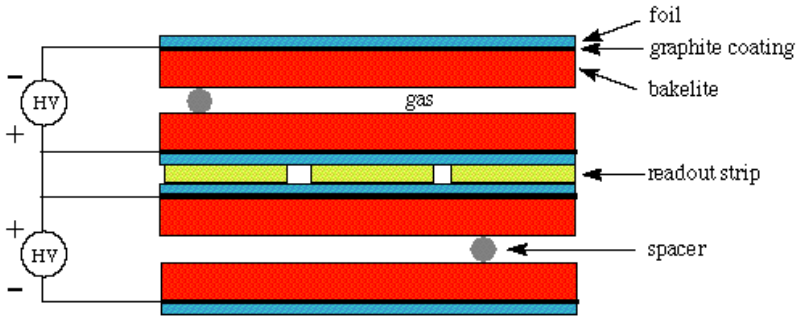

Figure 4.15: Diagram of a double-chamber RPC. The gas chamber is 2 mm wide and is surrounded by two bakelite layers 2 mm thick each.

interacting muon in each of the chambers is read out on strips at the center plate. There are six layers of RPCs embedded alongside the DTs in the barrel and three layers in the endcaps alongside the CSCs. Overall, RPCs provide a fast response at high rates, with great time resolution and they also help to resolve ambiguities in attempting to make tracks from multiple hits in a chamber [68].

4.2.6 Trigger and Data Acquisition

The LHC collides bunches of protons at the rate of 40 MHz which is about 25 ns between bunch crossings. With nearly 1 billion events/second and 1 MB per event, it is impossible to store and process data at about 40 TB/ s. Since the majority of LHC collisions are inelastic collisions and the event rate of rare SM processes and possible BSM interactions is many orders of magnitude lower than this rate, only a small fraction of these collisions are of interest for the CMS physics program. Therefore, this rate reduction is performed by the trigger system which decides whether to store or reject an event.

The CMS trigger system performs rate reduction and selects events of interest

in two steps: the Level-1 trigger (L1) uses custom hardware and constructs simple physics objects based on prompt macro-granular information from the calorimeters and muon detectors. It makes a rapid (within 4 μs) filtering decision reducing the rate to 100 kHz. The second step is the High-Level Trigger (HLT) where data at 100 kHz is fed into several thousand CPU core farms where events are reconstructed using full detector information. It reduces the rate to about 1 kHz. Only the data collected via this two-tiered trigger system is moved to offline storage for further analysis.

4.2.6.1 Level-1 Trigger

The L1 trigger system [82–84] is implemented using custom hardware such as field-programmable gate arrays (FPGAs) for processing and application-specific integrated circuits (ASICs) where needed. It selects events of interest based on information from ECAL, HCAL and the muon systems. The maximum allowed rate of 100 kHz imposes the constraint that the L1 decision needs to be made and distributed to the detector front-end electronics within 3.8 μs [82]. The latency requirement means that L1 does not use the full detector information such as inner tracker information, due to its 7 s readout time, and full ECAL crystal-level granularity.

The L1 trigger system has a bottom-up approach starting from detector signals and following the structure illustrated in Fig. 4.16 Information from the calorimeters and the muon detectors are processed in parallel.

At the lowest level, the calorimeter pipeline starts with the generation of transverse energy sums from the towers of ECAL and HCAL along with quality information. Each **tower** consists of a 5×5 clusters of barrel or endcap crystals and the ECAL and HCAL detector channels are mapped to towers (e.g. 25 EB crystals per HB tower) such that each tower covers the same projective η-ϕ region (0.087×0.087) of both calorimeters. This so-called Layer-1 Calorimeter trigger aggregates the infor-

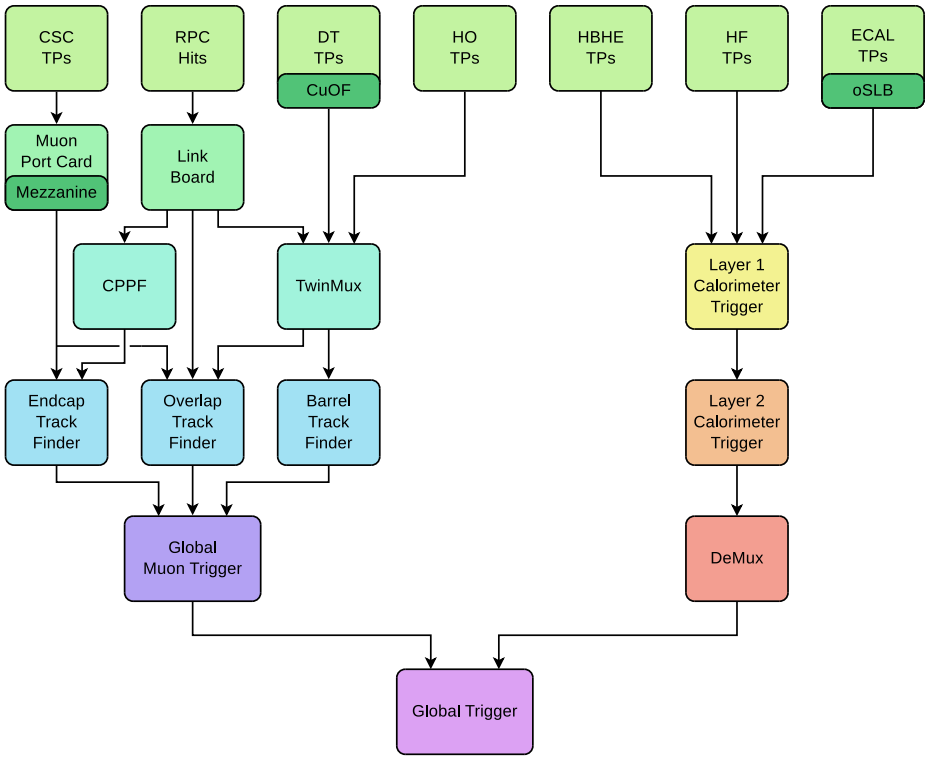

Figure 4.16: Schematic of the CMS Level-1 trigger system, showing the complete trigger system, and input detector subsystems.

mation from these ECAL and HCAL towers, applying trigger algorithms for e, γ, τ, jets and energy sums and calibrating these energies. The Calorimeter Layer-1 trigger systems were designed and built by the University of Wisconsin-Madison CMS group and is currently operated by a team of scientists, engineers and graduate students like me. Layer-1 is composed of 18 FPGA-based Calorimeter Trigger Processors 7 (CTP7) cards [85] with optical links to pass this data on to one of the nine layer 2 time-multiplexed calorimeter trigger processors (MP7s), each of which can process a full view of the detector to compute global quantities for whole events in parallel. These global quantities or L1 objects (L1 EGamma, L1 Jets, L1 Taus) are forwarded to the global trigger after passing through the demultiplexer which sorts the objects in p_T. This event information is then forwarded to the global trigger for an event-wide decision in conjunction with information from the Global Muon Trigger.

The muon trigger system begins with track segments from DTs and CSCs and hits from the RPC muon detectors. The muon track finder that is partitioned into barrel ($|\eta| < 0.85$), endcap ($1.25 < |\eta| < 2.4$) and overlap ($0.85 < |\eta| < 1.25$) regions uses the full set of parallel inputs from the CSC and RPC systems and the DT system to reconstruct muon tracks creating creating L1 muon candidates with charge, p_T and quality information defined. The global muon trigger receives information from the three track finders, removes duplicate muons, sorts them in p_T and delivers them to the global trigger. The global trigger receives these candidate objects from the two pipelines and makes event-wide decisions based on predetermined quality or minimum energy thresholds (each of which is referred to as a trigger path). It then accepts or rejects the event and these L1 Trigger Accept (L1A) signals are sent to the data acquisition system. A collection of trigger paths make up the trigger menu which is prepared ahead of collisions considering the luminosity and the physics events of interest. Some paths are prescaled, such that for some prescale n, only 1 in n events is recorded. During my time at CERN, I was not only involved with maintaining the Calorimeter Layer-1 system but also performed several data cross-validation and trigger efficiency studies which typically use such prescaled events.

4.2.6.2 High-Level Trigger

The high-level trigger (HLT) is a software based system implemented on a dedicated computer farm that has access to the full event information from all detector subsystems and about 220 ms average processing time to take a decision. It performs the second level of event selection on events accepted by the L1 trigger. The reconstruction modules and selection filters of the HLT use the software framework that is also used for offline reconstruction (Chapter 6) and analyses, but more rigorous timing constraints are imposed due to the limited number of CPUs available for the HLT

and the high incoming event rate of 100 kHz from Level-1.

Similar to L1, there is an HLT trigger menu which consists of ORs of various trigger paths. Each trigger path is a succession of filters and selection steps of increasing complexity. Faster reconstruction steps take place early in the sequence so if an event fails one of the filter criteria, filters can stop the execution of the path and save time on downstream complex reconstruction steps. Trigger paths are run independently of each other and selected events are output to different data streams with different rates, content and size. The HLT output rate is about 1000 Hz which is determined by offline computing and storage constraints [86].

4.2.7 Luminosity measurement

As described in Section 4.1.2, instantaneous luminosity delivered by the LHC to the CMS interaction point is an important design parameter of the LHC so an online precise measurement of the luminosity delivered provides real time feedback on the LHC performance as well as to CMS operations for important tasks such as measurements of trigger rates [87]. An accurate measurement of the integrated luminosity is also a critical component of any physics analysis, whether its for measuring the cross section of SM processes such as ZZ production cross section or for setting upper limits in searches for BSM physics such as in the Mono-Z' dark matter analysis.

In principle, instantaneous luminosity is defined in terms of the LHC parameters as given by Eqn. 4.3. However, the uncertainties associated with some of these parameters such as beam width means a dedicated setup is needed to measure luminosity accurately and precisely. Therefore, CMS uses rate measurements from a variety of observables from five systems; the pixel detector, the barrel DT, the HF and two specialized detectors for luminosity measurements namely the Fast Beam Conditions Monitor (BCM1fF) and the Pixel Luminosity Telescope (PLT) [88]. The

observables from each luminometer are chosen such that the rate, R, of these specific quantities is directly proportional to the instantaneous luminosity fixed by the constant of proportionality given by the visible cross section,σ_{vis}, seen by each detector system involved in the measurement.

$$\mathcal{L} = R\sigma_{\text{vis}},$$

In order to establish this absolute scale, σ_{vis} is measured van der Meer (VdM) scans [89] which are usually performed at the beginning of yearly runs with a dedicated LHC machine setup. VdM scans are basically separate the two beams and then passed across each other to measure the beam overlap width which can subsequently be used in conjunction with other beam parameters to give an absolute scale for the instantaneous luminosity. More details on VdM scans can be found in Ref. [21]. Under specific LHC running conditions, these values of instantaneous luminosity are calibrated and made available for each lumisection, which represents a fixed period of event-taking equal to 218 orbits of the beams, or 23.3 s. For the 2016 and 2018 dataset used in both analyses, the integrated luminosity is measured with a systematic uncertainty of 2.5% [88, 90] whereas the total systematic uncertainty in the integrated luminosity measurement of the 2017 dataset is 2.3% [87].

4.2.8 CMS Performance and data quality during Run 2 (2016-2018)

The operation of the LHC relevant to this thesis spans from 2016 to 2018 with the first beams injected on March 25,2016 and the 2018 proton run ending on Oct 24,2018. During this time, 158 fb^{-1} of integrated luminosity was delivered to the CMS interaction point. Of this, 146 fb^{-1} was recorded by CMS with data losses occurring due to various issues including but not limited to temporary failures of detector compo-

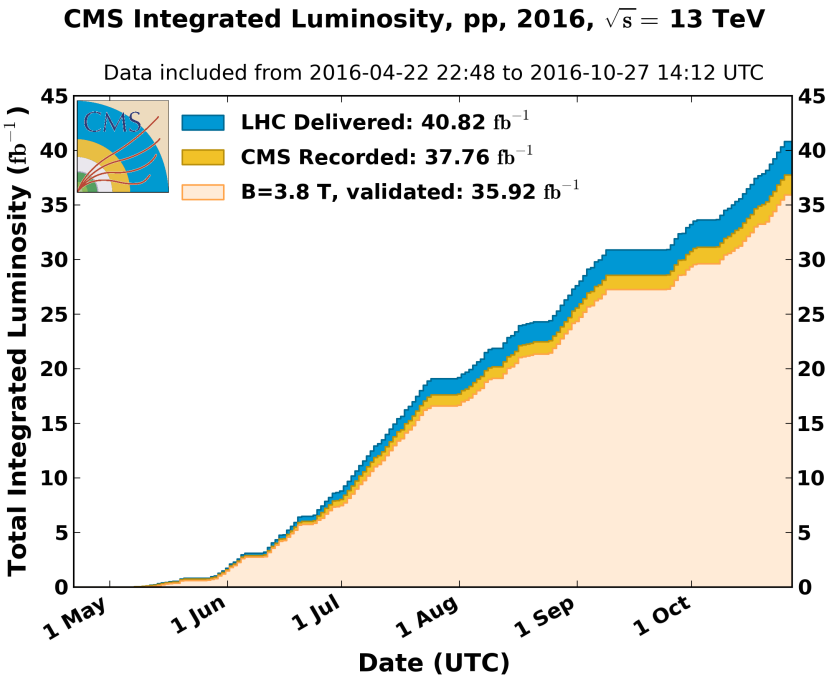

Figure 4.17: Cumulative integrated luminosity produced, recorded, and certified by the CMS experiment in 2016.

nents or services to them (e.g. power supplies) that prevented data collection, trigger deadtime, or human error. The data collected by CMS is evaluated by experts from each detector subsystem to ensure the quality of data required for subsequent physics analyses. There can be severe localized inefficiencies, dead zones or spurious noise that could impact accurate and efficient object reconstruction in a certain region and these problematic regions are excluded from the final dataset that is certified by the CMS experiment for physics analysis. Data is certified or rejected in units no smaller than a lumisection. The total integrated luminosity of data certified and used for the two analyses in this thesis is 137 fb^{-1}. The cumulative integrated luminosities delivered, recorded and validated by the CMS experiment over three years of operation are shown in Fig. 4.17, Fig. 4.18 and Fig. 4.19.

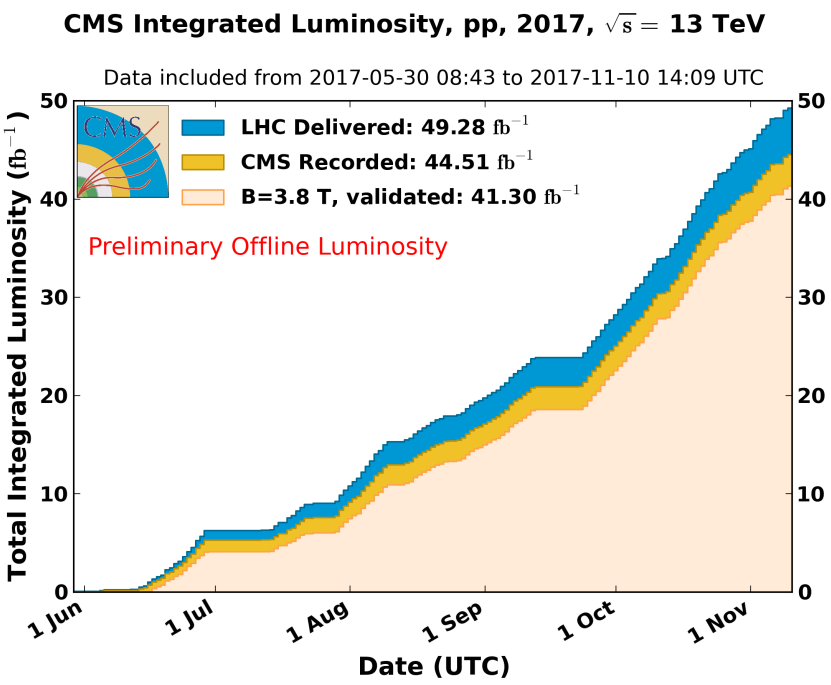

Figure 4.18: Cumulative integrated luminosity produced, recorded, and certified by the CMS experiment in 2017.

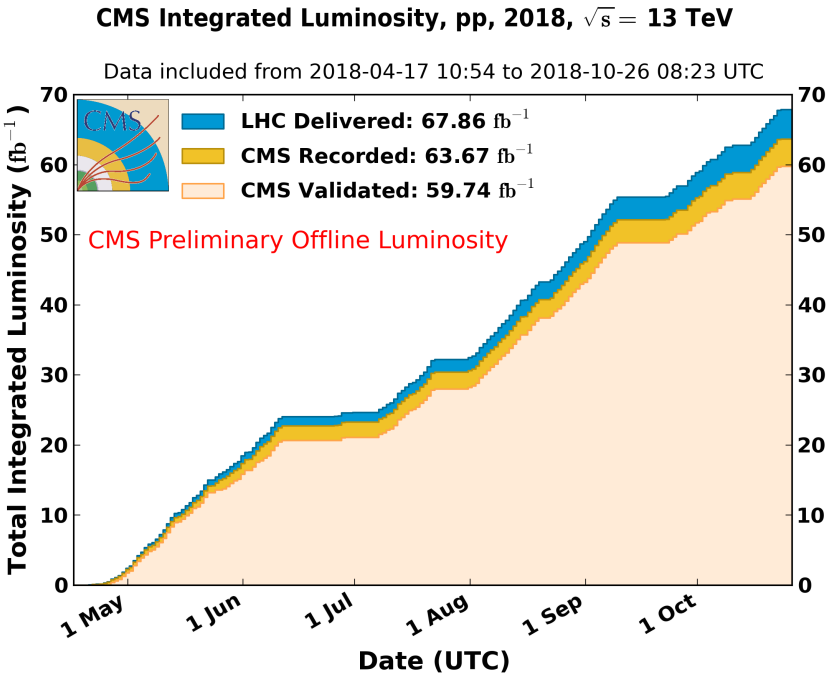

Figure 4.19: Cumulative integrated luminosity produced, recorded, and certified by the CMS experiment in 2018.

Chapter 5

Event simulation

5.1 Introduction

Comparing the experimental event data collected by a detector with theoretical predictions based on the principles of QFT and the SM is the main goal of experimental particle physics. Whether its the measurement of SM processes such as the production cross section of ZZ from pp collisions or searches for BSM physics, analysts need to provide accurate estimates of contributions from background processes, the signal selection efficiency and the resolution of relevant kinematic quantities considering the acceptance and efficiencies of the particle detector. Since event generation in particle physics involves multi-dimensional integrations, the Monte Carlo (MC) method [15, 91] is used for event generation. A big advantage of a MC simulation is the possibility to start with a simple model and follow a factorized approach (leveraging approximations and tuning to experimental data) until the desired simulation accuracy is reached. Starting from the initial state of parton collisions (Section 5.2.1), simulation of primary particle production, formation of bound states and particle decay and ending with simulating the resulting signals in the CMS detector. Finally, simulated

samples are stored in the same format as the data collected from the experiment so they can be reconstructed similarly (discussed in Chapter 6). Event simulation is a multi-step endeavor that is critical to the success of the high energy, high-luminosity collider physics program at the LHC so a brief overview is presented in the following sections.

5.2 Monte Carlo Event Generation

Monte Carlo event generation is used "to simulate the final states of high-energy collisions in full detail down to the level of individual stable particles. The aim is to generate a large number of simulated collision events, each consisting of a list of final-state particles and their momenta, such that the probability to produce an event with a given list is proportional (approximately) to the probability that the corresponding actual event is produced in the real world" [92]. The Monte Carlo simulation of each event starts with the matrix element computation of a hard subprocess at a chosen perturbative order [93]. Generally, MadGraph5_aMC@NLO or POWHEG are the MC event generators used for this hard-scattering process. After this, a Shower Monte Carlo (SMC) event generator like Pythia8, Herwig or SHERPA is used to simulate the parton interactions, the subsequent parton shower that follows, hadronisation, the underlying event activity including multiple parton interactions (MPI) and any additional activity expected from pileup. This complicated event structure is shown in the Fig. 5.1 which highlights the four main elements of a General Purpose Monte Carlo (GPMC) event simulation at the LHC.

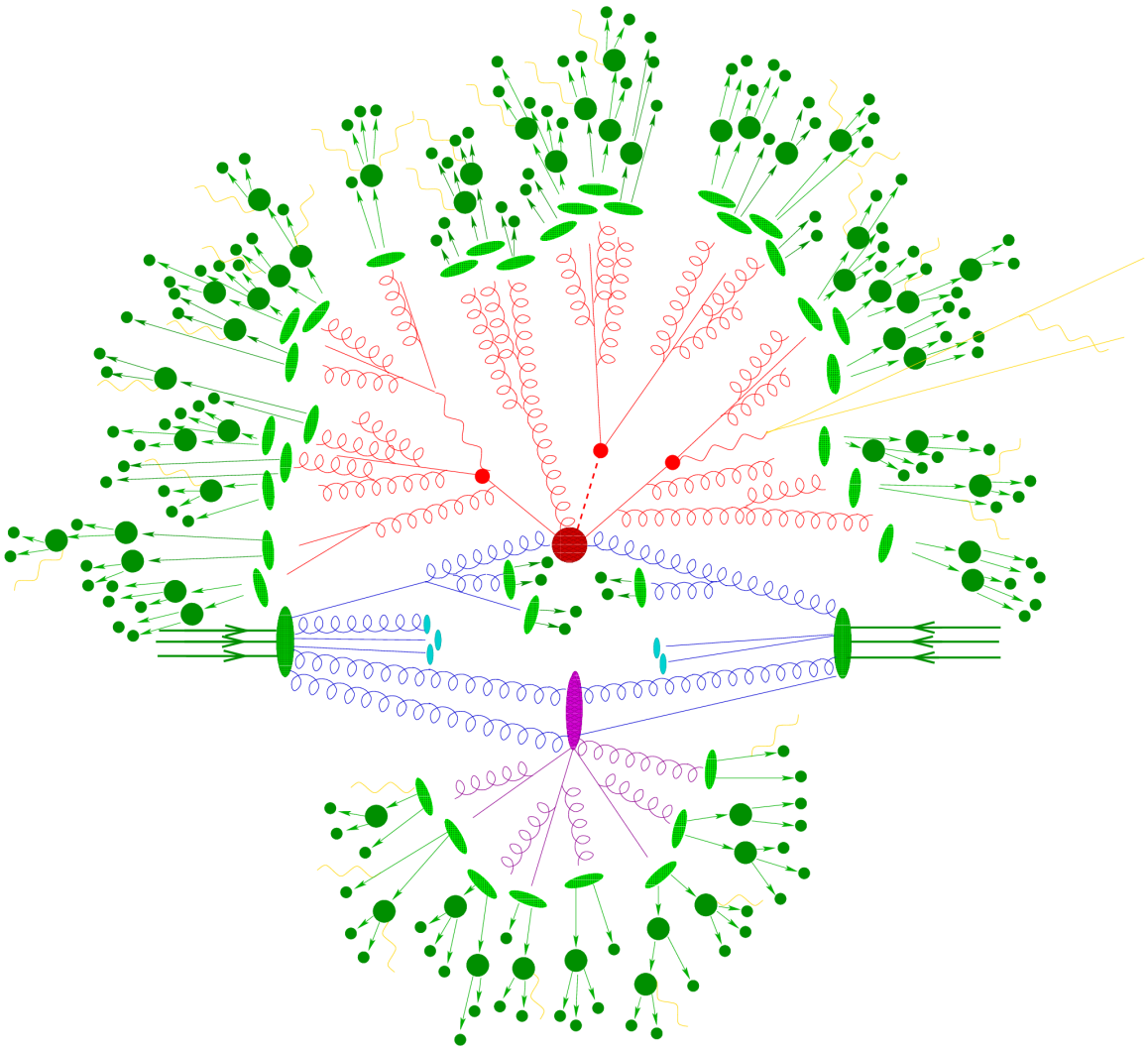

Figure 5.1: Illustration of an event showing the hard scattering and the ensuing parton shower (red), the hadronisation (green) with hadron decays (dark green) and radiated photons (yellow), and the underlying event coming from beam remnants (blue) and multiple parton interactions (purple). Figure reproduced from Ref. [94].

5.2.1 Hard Process Generation

As mentioned above, event simulation begins with the hard scatter calculation which describes the interaction and annihilation of the two partons from the colliding protons. The quarks or gluon constituents of the protons, called partons, interact with a certain probability at a given momentum transfer characterized by the parton distribution functions (PDFs), $f_i(x, Q^2)$, where x is the fraction of the proton momentum carried by the parton of type i and Q^2 is the momentum transfer scale [95]. PDFs are nonperturbative and experimentally determined using fits to data from deep inelastic scattering (DIS) of lepton and proton beams and from hadron collider data [96, 97]. These PDFs are available from several groups including e.g. CTEQ [98], MRST/MSTW [99], and NNPDF [96]. The NNPDF3.1 [97] has been released and are reproduced in Fig. 5.2 and CMS simulated samples for 2017 and 2018 use these updated PDFs. The proton PDF NNPDF3.0 [96] was used for production of simulated samples in 2016 which are also part of both analyses described in this thesis.

The cross section, σ, of a hard scattering process is given by,

$$\sigma\left(\mathrm{pp} \to X\right) = \sum_{p_1, p_2 \in \mathrm{q}, \bar{\mathrm{q}}, \mathrm{g}} C_{p_1, p_2} \int \mathrm{d}x_1 \mathrm{d}x_2 f_{p_1}(x_1, Q^2) f_{p_2}(x_2, Q^2) \sigma_{\mathrm{ME}}(p_1 + p_2 \to X), \tag{5.1}$$

It is a convolution of these PDFs with the matrix element-level (σ_{ME}) cross section of a parton-parton interaction at a chosen perturbative scale. $C_{p1,p2}$ is a combinatoric factor based on the number of possible color combinations of the initial state particles p_1 and p_2. The matrix element of the hard scattering process is calculated using event

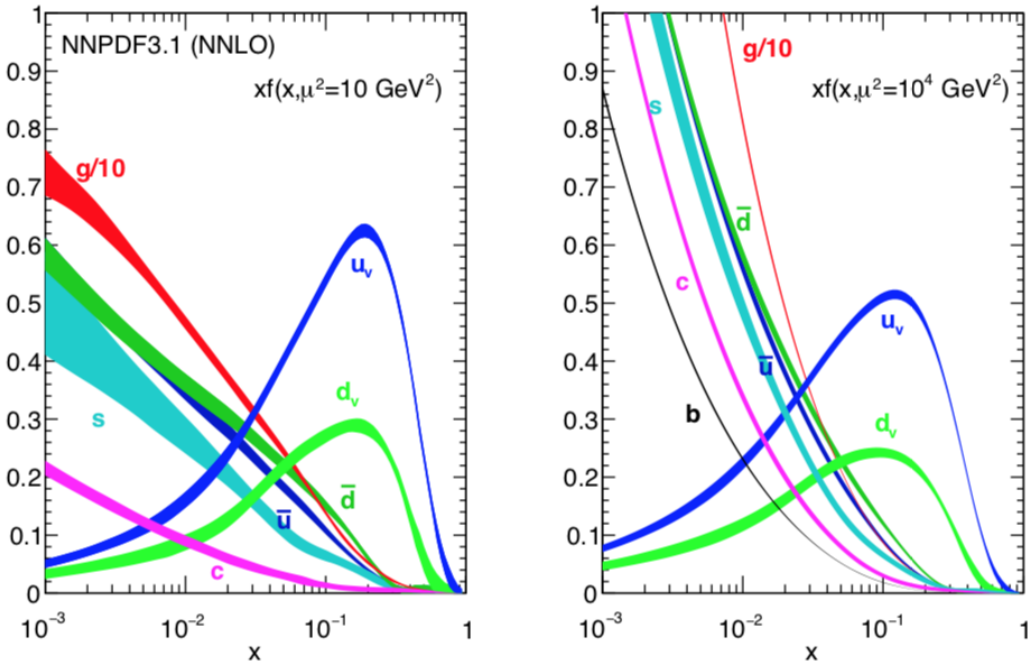

Figure 5.2: The NNPDF3.1 parton distribution functions for demonstration of general PDF structure reproduced from Ref. [97], which used μ for the momentum transfer denoted Q in the text.. This figure shows that the valence quarks in the proton, namely the up and down quarks it is made of, have a larger momentum fraction than the remaining sea quarks, which appear as virtual quark antiquark pairs forming from gluons and annihilating again.

generators such as MadGraph5_aMC@NLO [1] [103] and POWHEG [2] [104]. While both generators can calculate the matrix element at Leading Order (LO) and Next-to-Leading-Order (NLO), NLO computations are computationally expensive so its an accepted practice to use the so-called kfactor (ratio of the NLO and LO cross sections) to scale a LO cross section to the NLO level for a particular sample. More

[1] MadGraph5_aMC@NLO is the new version of MADGRAPH5 and aMC@NLO, unifying the leading order (LO) and next-to-leading order (NLO) developments of this automated tool. It is a Monte Carlo generator which can compute cross sections and generate hard scattering events for many Standard Model and new physics processes. At LO, FeynRules [100–102] supply the Feynman diagrams and it is fully automated. At NLO, the NLO QCD,the process is fully automated via FeynRules; other NLO contributions must be added with dedicated computations

[2] POWHEG is a framework for implementing NLO calculations for specific processes. It is not automated like MG and each physics process must be coded separately.

details on specific samples and associated kfactors is given in section 5.2.4.

5.2.2 Parton Shower, Hadronization and Underlying Event

Since we are interested in colliding partons that carry a color charge, the hard interaction is accompanied by partons radiating soft gluons or splitting into two collinear partons. This results in a cascade of radiation which is the process known as the parton shower. This radiation can originate from the initial state partons, which is referred to as initial state radiation (ISR), final state partons, known as the so-called final state radiation (FSR), or from partons from the underlying event (UE) which includes all the activity and interactions that do not originate from the hard interaction such as MPI [105, 106]. Thus, parton shower is a probabilistic process where each parton has a probability of radiating another parton at an energy scale. This perturbative evolution of the shower from a high energy scale down to the hadronization energy scale ($\Lambda_{QCD} \approx 10\,\text{GeV}$) is accomplished via splitting functions [94] and Sudakov form factors [107] using the DGLAP formalism.

After the parton shower, as partons reach the hadronization scale, these colored partons transform into color-neutral hadrons. In this non-perturbative domain of QCD, phenomenological models need to be used for hadronization and the UE. There are three well known parton shower monte carlo (PSMC) event generators, each with its own phenomenological model for hadronization: Pythia8 [108], Herwig [109], and sherpa [110]. Each model uses a standard set of parameters, some of which can be tuned or adjusted based on experimental data. In this thesis, mainly Pythia8 and sherpa based samples are used but more details about each and the different Pythia8 tunes in 2016 and 2017/2018 samples are discussed in section 5.2.4 and appendix C. As an example, Pythia8 uses the Lund String Model of jet hadronization based on string fragmentation [111].

5.2.3 Pileup Simulation

As mentioned in Section 4.1.2, the average pile-up in 2016 was around 27 pp interactions per bunch crossing and around 37 during 2017 and 2018. In any bunch crossing with a hard-scattering process, there are several additional collisions between protons from the same bunch crossing (referred as in-time pileup) or from a previous or future bunch crossing (out-of-time pileup). This extra activity in the event is simulated by including extra minimum-bias collision events overlaid on top of the primary collision [112, 113]. Usually, the simulated samples are produced before the pileup profile is extracted from real data so the simulation does not completely agree with the data. Therefore, simulated events need to be reweighted based on the number of pileup interactions such that the MC events match the data. The distribution of the number of reconstructed vertices is used for this reweighting process which is highlighted in relevant analysis chapters in this thesis.

5.2.4 Samples Used in ZZ Analysis

The $q\bar{q} \to ZZ$, $gg \to H \to ZZ^*$ samples are produced at NLO with POWHEG 2.0 [104, 114–117] and scaled to the NNLO total cross section with k factors of 1.7 for the Higgs sample and 1.1 for the $q\bar{q} \to ZZ$ sample [36]. The $q\bar{q} \to ZZ$ POWHEG samples include ZZ, Z/γ^*, and $\gamma^*\gamma^*$ production where generator-level constraints on the invariant mass of oppositely charged lepton pairs ($m_{\ell\ell'} > 4\,\text{GeV}$) limit the generated phase space to regions of interest in this analysis and far from infrared divergences. The POWHEG sample is considered as the primary theoretical prediction for both inclusive cross sections as well as differential cross sections. However, an additional $q\bar{q} \to ZZ$ sample is generated with MadGraph5_aMC@NLO [103] which is used as an alternative theoretical prediction for the differential cross sections. The

box diagram ZZ production through gluon gluon fusion ($gg \rightarrow ZZ$) is simulated at Leading Order (LO) with MCFM [118] and its cross section is scaled to NLO with a k factor of 1.7 [119].

The background WZ, $t\bar{t}$ and VVV samples are all produced with MadGraph-5_aMC@NLO. The electroweak ZZjj samples are also produced with madgraph interfaced with Pythia8. Samples with nonzero aTGCs are generated at LO with sherpa 2.1.1 [153] and scaled such that the total yield from the SM sherpa sample is the same as the yield from the powheg ZZ sample.

The 2016 samples use the NNPDF3.0 PDF sets [96] whereas the 2017 and 2018 MC samples use the NNPDF3.1 [97] PDF sets. The simulation steps including parton showering, hadronization and UE simulation are done with Pythia8 using the CUETP8M1 tune [120] for the 2016 samples, CP5 tune [121] for the 2017,2018 samples except the 2016 aTGC samples which are produced with sherpa.

5.3 Detector Simulation

The output from the sequence of event generation steps described above is finally passed through the CMS detector simulation step. This is accomplished through the GEometry ANd Tracking (Geant4) [122, 123] toolkit which simulates the decay of long-lived ($0.01\,\mathrm{m}/c \lesssim$ lifetime $\lesssim 10\,\mathrm{m}/c$) particles within the detector volume, their interactions with the detector material, including effects such as bremsstrahlung of charged particles, photon conversions, energy loss of charged particles by ionization, electromagnetic showers, hadron showers and the energy deposits in sub detector systems. All detector materials are included in the simulation software; a precise map of the magnetic field of the CMS detector as well as dead material regions such as cooling pipes and electronic cables. As the particles are propagated through different materi-

als of the detector, these particle-matter interactions are weighted by their respective probabilities using the Monte Carlo method. Finally, the energy deposits in the active detector material are digitized and the electronic readouts of the real CMS detector are simulated using models developed and validated with both test beam [124] and collision data [125, 126]. During this process, effects of data transmission and any reconstruction performed in the electronics such as generation of trigger primitives and selective readout (zero-suppression) are simulated as well. After passing this final step, these simulated events can be passed through the same reconstruction software and algorithms (see Chapter 6) which are used for data collected from the real CMS detector.

Chapter 6

Event reconstruction

6.1 Introduction

Building on our understanding of the CMS detector and data collection from chapter 4 and event simulation from chapter 5, the next step in the pipeline is event reconstruction. The development and optimization of reconstruction algorithms used by CMS has happened over many decades as these algorithms have evolved together with successive particle detector experiments. The same reconstruction algorithms are applied for simulated events and for data collected in the CMS detector. As described in Chapter 4, CMS has an excellent tracker, highly granular and hermetic calorimeters, a strong solenoidal magnetic field and a dedicated muon spectrometer. Therefore, CMS uses the particle flow (PF) technique [127] which successfully employs all these features and detector information to reconstruct all particles produced in an event selected by the trigger system and stored for analysis. The PF algorithm reconstructs muons, electrons, charged hadrons, neutral hadrons and photons directly from their respective interactions with different parts of the detector as shown in Fig. 6.1. As described in subsequent sections, the PF algorithm starts

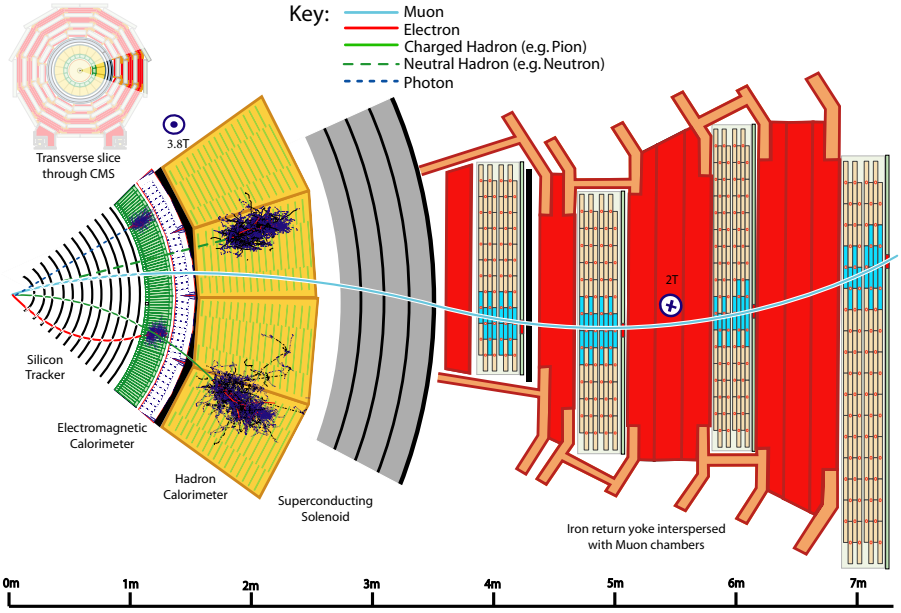

Figure 6.1: A sketch of the specific particle interactions in a transverse slice of the CMS detector, from the beam interaction region to the muon detector. The muon and the charged pion are positively charged, and the electron is negatively charged. Reproduced from [127], Fig. 1.

the reconstruction process with algorithms that form tracks and calorimeter clusters. From these components, the main physics objects used in the two analyses for this thesis are formed and identified: isolated muons, isolated electrons, isolated photons, jets, isolated tau leptons and the missing energy of the event, $\vec{p}_{\mathrm{T}}^{\,\mathrm{miss}}$.

6.2 Tracks

6.2.1 General tracks

The precise measurement of the trajectories of charged particles in the CMS detector is essential for the success of the PF algorithm and global event reconstruction. As mentioned in Section 4.2.2, the pixel tracker was upgraded in 2017 with an additional layer which improves track impact parameter resolution and vertexing perfor-

mance [127]. The process of track reconstruction begins with energy deposits, "hits", recorded by the pixel and strip tracker and the muon detectors. The tracker employs sensors covering an area the size of a tennis court, with over 70 million separate electronic read-out channels which means trying to reconstruct tracks from every possible hit combination in one pass would be a combinatorial and computational nightmare. Therefore, track reconstruction is performed in ten iterations, beginning with tracks that have less possible combinations and are high-quality, high-p_{T} tracks associated with the beam crossing region, or *beam spot* (see section 6.3 of [71] for details on the reconstruction of the LHC beam spot). After each iteration, quality criteria is progressively relaxed and hits used in a previous iteration and associated with a found track are removed from the collection available to the next available iteration to reduce complexity. Each iteration follows four steps

1. **Seed generation**: In the first step, hits from two or three detector layers are combined into seeds which provide the initial estimates of the track trajectory parameters and their uncertainties and lead towards subsequent track finding.

2. **Track finding**: Then the seeds are used as a starting point and other compatible hits are added in succession to the seed track by extrapolating the seed trajectory (outward or inward) into the next layers using the Combinatorial Track Finder (CTF) method, which is a type of Kalman filter [71, 128, 129].

3. **Track fitting**: After the building of CTF tracks, the track-fitting module is used to find the best fit parameters of each trajectory using a Kalman filter and smoother.

4. **Track selection**: Finally, track selection criteria such as the number of layers that have hits, the $\frac{\chi^2}{dof}$ and distance to a primary vertex are used to select quality tracks and discard tracks that fail these selections.

In the first three iterations of the track finding process, seeds are generated from triplets of pixel hits which capture most prompt high-p_{T} tracks and some tracks from b decays. The fourth iteration uses only pairs of pixel hits from the beam crossing region to recover any remaining high-p_{T} tracks. While iterations five through seven focus on displaced tracks, the eight iteration aims to resolve merged tracks in the cone of high-p_{T} jets by splitting hit clusters as needed. The last two iterations are seeded by hits in the muon detectors using an outward-inward propagating track finding approach. The efficiency of track finding and the track misreconstruction rate for this method is shown in Fig. 6.2. Furthermore, its important to mention the improvements in the iterative tracking algorithm due to the new Pixel detector upgrade and comparing tracking efficiencies and the fake rates between 2016 and 2017. The CA seeding technique [130] as described in more detail in [127] is the most relevant improvement and the comparison between the two scenarios can be seen in Fig. 6.3.

6.2.2 Electron tracks

Unlike muons, charged pions or other charged particles going through the tracker, electrons have a high probability of radiating photons (bremsstrahlung radiation) as they pass through the tracking material ($\sim$1.8 radiation lengths) before reaching the electromagnetic calorimeter. Therefore electron tracks can exhibit sharp kinks due to this radiation loss in the tracker which means the CTF tracking procedure described in section 6.2.1 fails to find the next hit because the CTF algorithm, through the Kalman filter (KF), relies on Gaussian smearing around the hit location for material locations. Since the bremsstrahlung radiation causes non-Gaussian contributions to these interactions for electrons, the electron track reconstruction employs a dedicated "Gaussian Sum Filter" (GSF) [132] which can account for such electron energy loss.

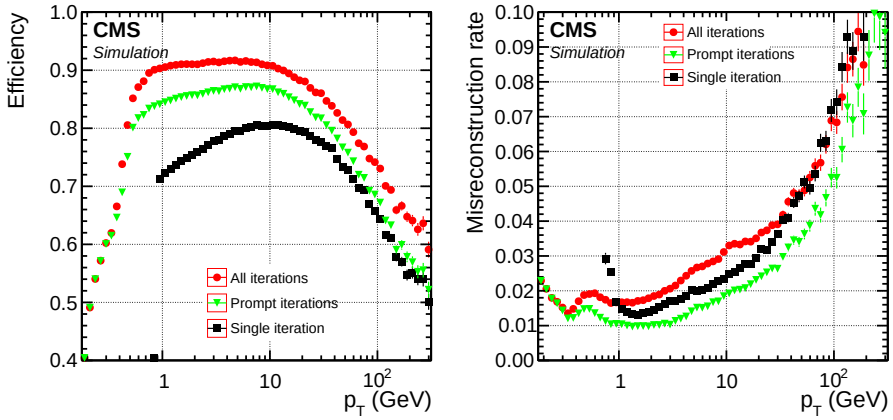

Figure 6.2: Efficiency (left) and misreconstruction rate (right) of the global combinatorial track finder (black squares); and of the iterative tracking method (green triangles: prompt iterations based on seeds with at least one hit in the pixel detector; red circles: all iterations, including those with displaced seeds), as a function of the track p_{T}, for charged hadrons in multijet events without pileup interactions. Only tracks with $|\eta| < 2.5$ are considered in the efficiency and misreconstruction rate determination. The efficiency is displayed for tracks originating from within 3.5 cm of the beam axis and ± 30 cm of the nominal center of CMS along the beam axis. Reproduced from [127], Fig. 4.

The GSF models the energy loss as a mixture of multiple gaussian PDFs instead of a single gaussian PDF like the KF algorithm. Generating seeds for electron tracks happens via the combination of two complementary set of inputs: calorimeter superclusters and general tracks. The tracker based seeding works best for electrons with minimal bremsstrahlung that are extrapolated towards the ECAL and matched with a SuperCluster(SC) to discriminate against charged hadrons. In the ECAL-based seeding, isolated clusters with $E_T > 4$ GeV and a hadronic to electromagnetic ration below 0.15 is considered and the initial momentum is assigned by back-propagating the SC energy and position. For simulated electrons from Z boson decays, the overall efficiency of this seeding method is $\approx$92% [133]. Finally, electron candidates from both algorithms are merged to seed a final GSF tracking iteration to determine the final electron tracks and the overall electron track reconstruction efficiency is above

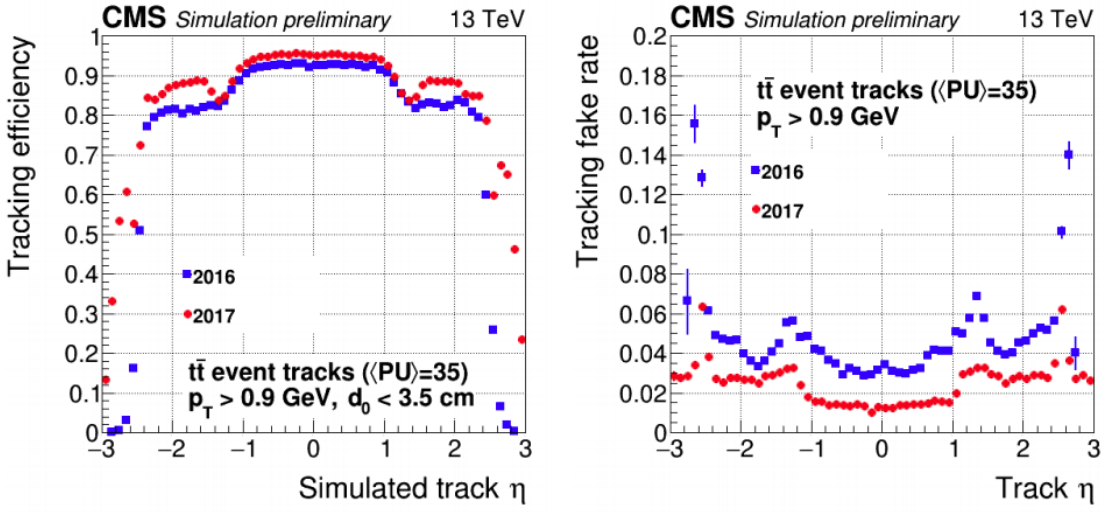

Figure 6.3: The efficiency of track finding and the track misreconstruction rate for this iterative method is shown in Fig. 6.2. The efficiency and misreconstruction rate in this figure shows the cumulative results after the initial pass through the tracking algorithm, after all passes which require the track seed to contain hits in the pixel detector,and after considering displaced tracks. Displaced tracks are tracks which do not originate from the collision region. They can be created from a number of processes included Bremsstrahlung and the inelastic nuclear interaction of particles with the tracker material. After all iterations the efficiency is about 90% for a charged pion with $p_{\mathrm{T}} = 10\,\mathrm{GeV}$ for a misreconstruction rate of 3%. Reproduced from [131].

95% for electron superclusters with $E_T > 20\,\mathrm{GeV}$ and $|\eta| < 2$ [133].

6.2.3 Muon tracks

Muon tracks are reconstructed from a combination of inner tracker information and the hits in the gaseous muon detector systems. Between the tracker and the muon spectrometers, the calorimeters and the solenoid absorb the vast majority of non-muon particles (except neutrinos) and ensure that the hits in the muon detectors are genuine muons. There are there categories of muon tracks that are reconstructed using the KF algorithm:

- Stand-alone muon tracks are reconstructed purely from hits in the muon de-

tector systems. Hits within DT and CSC subsystems are reconstructed locally, combined into track segments which seed a KF track finding algorithm that combines hits from all three muon detectors (DTs, CSCs and RPCs) along the track trajectory.

- Global muon tracks are reconstructed with an "outside-in" approach by matching a standalone-muon track to inner tracker tracks. The trajectories of both tracks are extrapolated onto a common surface (namely, the tracker outer surface) and matched to check if they are compatible. The hits from these compatible tracks are used to perform a combined fit with the KF algorithm to form a global-muon track.

- Tracker muons are reconstructed **inside-out** by extrapolating a track (from the inner tracker) with $p_{\mathrm{T}} < 0.5\,\mathrm{GeV}$ and total momentum $p > 2.5\,\mathrm{GeV}$ to the muon system. If at least one muon segment matches the extrapolated track, the tracker track qualifies as a tracker muon.

Overall, about 99% of the muons produced within the geometrical acceptance of the muon system are reconstructed either as a global muon or a tracker muon and very often as both [134]. Furthermore as shown in Fig. 4.11, for muons with $p_{\mathrm{T}} > 200\,\mathrm{GeV}$, the momentum resolution improves significantly by combining the tracker information with the muon system whereas for muons with $p_{\mathrm{T}} < 200\,\mathrm{GeV}$, the inner tracker already provides a precise measurement of their momentum.

6.3 Primary vertices

In a pp collision event, there are several interaction vertices which means tracks can originate from a variety of vertices. Primary vertices are defined as vertices from

which tracks associated with initial pp collisions emanate whereas secondary vertices are associated with tracks originating from particle decays or interactions with the detector material. In order to reconstruct secondary vertices, it is crucial to be able to identify and reconstruct the primary vertex. Primary vertices are reconstructed by clustering a subset of the reconstructed tracks that are consistent with the beam spot. The deterministic annealing algorithm [135] is used to cluster tracks based on their z-coordinates at their point of closest approach to the centre of the beam spot [71] and the vertex coordinates are then found by a maximum likelihood fit to the tracks belonging to a given cluster. Among these primary vertices, the hard-scatter vertex is the one with the largest quadratic sum of the p_{T} of the associated physics-objects and is identified as the primary vertex (PV). The sum considers trackjets, clustered using the anti-k_t algorithm (see Section 6.6.5), and the associated missing transverse momentum, taken as the negative vector sum of the pT of the track-jets associated with the vertex.

Since the mono-Z' model requires events with large $E_{\mathrm{T}}^{\mathrm{miss}}$, choosing a quality primary vertex is especially important. Furthermore, many analysis observables used in both analyses in this thesis rely on the number of secondary pp interaction vertices in the event, known as pileup. As mentioned in Section 5.2.3, pileup distributions used in MC samples are not the same as the distribution in data and hence MC events need to be reweighted based on the number of simulated pileup vertices such that the overall N_{vtx} (number of proton-proton interaction vertices) distributions match.

6.4 Calorimeter clusters

Calorimeter clustering plays a significant part in event reconstruction in CMS. Since photons and neutral hadrons (both important for the mono-Z' signal) are only de-

tectable in the calorimeters, the clustering algorithm is responsible for measuring the position and energy of these particles. Clustering also helps to improve the energy measurement of charged hadrons whose tracks are not measured accurately in the tracker which is usually the case for low-quality and high-p_{T} tracks. In the same context, clustering separates the neutral particles from charged hadron energy deposits. Finally, as mentioned in Section 6.2.2, one part of electron track reconstruction is seeded through ECAL superclusters which are contiguous ECAL clusters containing electron and bremsstrahlung photon energy deposits. These clusters of energy are formed separately in each subdetector: ECAL barrel and endcap, HCAL barrel and endcaps and the ECAL preshower. In the HF, no clustering is performed and the electromagnetic or hadronic components of each cell becomes a cluster.

The first step in the clustering algorithm is quite intuitive. A detector element with energy larger than its neighbors and larger than a set threshold, E_{seed}, is identified as the seed element. Then, this "topological" cluster is grown by adding neighboring cells (either the four sharing a side or the eight sharing a corner) given that each aggregated cell has energy greater than the cell threshold which is set to twice the noise level. The noise level varies in each sub detector and these E_{seed} values are giving in Table 2 of Ref. [127]. After the topological clustering, an expectation-maximization algorithm based on a Gaussian-mixture model is used to further refine the position and energy of these clusters. A more detailed explanation of this iterative algorithm can be found in section 3.4 of Ref. [127].

6.5 Particle-flow linking

The algorithm that links the inner tracks, muon system tracks, and calorimeter clusters to form Particle Flow (PF) candidates is the so-called particle-flow (PF) algo-

rithm. The PF candidates are categorized as electrons, muons, photons, neutral and charged hadrons and these categories are used to correct the energy response of the detector and build identified physics objects that are selected for analyses. While neutrinos have a long enough lifetime to exit the beam pipe and traverse the detector, they do not interact with any of the subdetectors and hence their reconstruction is not attempted by this algorithm. While a detailed explanation of the PF algorithm can be found in [127], a general overview is presented here.

As described above, the PF elements from different subdetectors are connected by a link algorithm which quantifies the quality of the link by defining a geometrical distance between the elements. If an element is linked to multiple other elements, only the link with the shortest distance is kept. More specifically, a link between a track and a calorimeter cluster is made by extrapolating from the last hit of each inner track to the calorimeters. Tracks and clusters are linked if a cluster is found within one ECAL or HCAL crystal. Furthermore, clusters in the Preshower, ECAL and HCAL are linked if the clusters in the detector with finer granularity (PS, ECAL, HCAL in order of worsening granularity) overlaps with the other cluster. In order to account for the energy of the bremsstrahlung photons from electron interactions with the tracker material, tangents to the electron GSF tracks are extrapolated to the ECAL and links are formed. Charged particle tracks can also be linked by a common secondary vertex. Finally, tracks from the inner tracker and the ones in the muon systems are linked.

This results in several PF blocks of physics objects obtained by linking the multiple PF elements and these blocks are classified as muons, electrons or isolated photons. In each step of this identification, the corresponding identified elements are then excluded from further consideration. After electrons, muons and isolated photons have been identified, the remaining blocks are categorized as charged hadrons,

neutral hadrons or non-isolated photons from jet hadronization. Within the tracker acceptance, the ECAL clusters not linked to any track are identified as photons and the HCAL clusters without a matching track are labelled as neutral hadrons. As the most common neutral hadron, π^0 decays to two photons (an important part of the mono-Z' Pencil Jet signal), neutral candidates are dominated by photons which are measured with significantly better energy resolution than neutral hadrons. Outside of the tracker acceptance ($|\eta| > 2.5$), it is not possible to distinguish between charged and neutral hadrons so linked ECAL and HCAL clusters from neutral hadron candidates and unlinked ECAL clusters are identified as photons. The remaining HCAL clusters are linked to one or several inner tracks to form charged hadron candidates (π^+,π^- for example which make most of our mono-Z' signal). Finally in the HF, the ratio of energy deposits in the long to short fibers is used to categorize HF clusters as HF photon or HF hadron candidates. Energy calibrations are applied to calorimeter clusters as a function of E, ηbased on the identified PF candidates.

Finally when all PF blocks have been process and all PF candidates identified, the reconstructed event is revisited by a post-processing event described in detail in section 4.6 of Ref. [127] which checks for spurious $p_{\mathrm{T}}^{\mathrm{miss}}$. As an example, which will also be mentioned later in one of the mono-Z' analysis chapters (Appendix B), an artificially large $p_{\mathrm{T}}^{\mathrm{miss}}$ might be created by reconstruction of a coincident cosmic ray muon in the event, mis-reconstruction of a charged hadron as a muon and neutral hadron in the case that the charged hadron is energetic enough for its shower to produce segments in the muon systems (punch-through), which causes a double-counting of the energy of the charged hadron. There are several methods to deal with this issue, one will be outlined in the event selection of the mono-Z' analysis, such as comparing the PF $p_{\mathrm{T}}^{\mathrm{miss}}$ with the calorimetric $p_{\mathrm{T}}^{\mathrm{miss}}$ and others are highlighted in section 4.6 of Ref. [127].

6.6 Physics objects

The reconstruction algorithms mentioned so far in this chapter are general purpose reconstruction algorithms that serve as a starting point in nearly all CMS analyses but further selections are required for a particular analysis to optimize object efficiency and purity for studying a specific physics process. For instance, the leptons used in the ZZ analysis in this thesis are required to pass identification requirements on top of those basic requirements imposed during PF reconstruction and are required to be isolated from other particles in the event in order to reject fake objects from jet fragmentation. The ZZ to four lepton process has low reducible backgrounds so the selections are generally loose, optimized for high efficiency whereas the mono-Z' analysis uses a range of selections from loose to tight requirements used for the lepton control regions.

6.6.1 Muons

In order to ensure the quality of muons used for any analysis, there are standard muon identification requirements known as **tight**, **medium**, **loose**,**very loose** which provide a trade-off between muon identification efficiency and misidentification (fakes). In the ZZ and mono-Z' analysis (except the control regions), the loose identification requirements are used which require the muon candidates to be tracker or global muons with $p_{\mathrm{T}} > 5\,\mathrm{GeV}$ within the muon system acceptance ($|\eta| < 2.4$) in addition to being identified as a PF muon. They are also required to follow the Primary Vertex (PV) compatibility criteria, with minimum track-PV distance $d_z < 1\,\mathrm{cm}$ in the z direction and $d_{xy} < 5\,\mathrm{mm}$ in the plane transverse to the beam. For the ZZ analysis, each muon's 3-dimensional impact parameter (IP) d_{3D} must satisfy a requirement on

its significance,

$$\mathrm{SIP}_{\mathrm{3D}} \equiv \frac{d_{\mathrm{3D}}}{\sigma_{d_{\mathrm{3D}}}}, \tag{6.1}$$

where IP is the distance of closest approach of each muon track to the even vertex and $\sigma_{d_{\mathrm{3D}}}$ is the uncertainty on the IP. The $\mathrm{SIP}_{\mathrm{3D}}$ requirement is $\mathrm{SIP}_{\mathrm{3D}} < 4$ everywhere in the ZZ analysis wherever muon identification requirements are applied. Muon candidates are also required to be isolated from other particles in the event. The relative isolation is defined as

$$R_{\mathrm{Iso}} = \left(\sum_{\mathrm{charged}} p_{\mathrm{T}} + \max \left[0, \sum_{\mathrm{neutral}} p_{\mathrm{T}} + \sum_{\mathrm{photons}} p_{\mathrm{T}} - p_{\mathrm{T}}^{\mathrm{PU}} \left(\ell \right) \right] \right) \Big/ p_{\mathrm{T}}^{\ell} \tag{6.2}$$

where the neutral pileup contribution for muons is half the p_{T} sum of all charged particles in the cone originating from pileup vertices. The radius of the isolation cone is 0.3 in the η-ϕ plane and the selection criterion is $R_{\mathrm{iso}} < 0.35$.

$$p_{\mathrm{T}}^{\mathrm{PU}} \left(\mu \right) \equiv 0.5 \sum_{\mathrm{charged}} p_{\mathrm{T}}^{\mathrm{PU}}, \tag{6.3}$$

The factor of one-half accounts for the expected ratio of charged to neutral particle production in hadronic interactions. The muon reconstruction, identification and isolation efficiencies are measured with a **tag-and-probe** technique [136] applied to a sample of $\mathrm{Z} \to \ell^{+}\ell^{-}$ data events. The measurements are performed as a function of p_{T}^{ℓ} and $|\eta|^{\ell}$. The muon efficiencies are found to be above 98% within $|\eta|^{\mu} < 2.4$.

In the case of the mono-Z' analysis described in Appendix B, the loose muon identification is used to select muons for the muon veto with $p_{\mathrm{T}} > 10\,\mathrm{GeV}$. An additional isolation cut of 0.2 is applied in order to reject muons inside jets. The isolation value is computed as the sum of the transverse momenta of all charged hadrons associated to the primary vertex, neutral hadrons and photons in a cone of

$\Delta R < 0.4$ around the muon relative to p_{T} of the muon. The tight muon identification is used as well, to select events in the dimuon and single muon control regions with muon $p_{\mathrm{T}} > 20\,\mathrm{GeV}$. The tight identification requires the muon to be a global muon in addition to being a PF muon. The normalized χ^2 of the global muon track fit should be less than 10, the track fit must use at least one muon chamber hit and there must be compatible muon segments in at least two muon stations. Furthermore, the tracker track is required to have $|d_{xy}| < 2\,\mathrm{mm}$ and $|d_z| < 5\,\mathrm{mm}$ where d_{xy} is the transverse impact parameter and d_z is the longitudinal distance of the track with respect to its associated PV. The track must also require at least one pixel hit as well as hits in at least 5 tracker layers for a good p_{T} measurement. All these requirements primarily suppress cosmic muons, tracks from pileup, charged hadron punch-through and non-prompt muons from B meson decays.

6.6.2 Electrons

In the case of electrons, two methods of identification are available; a cut-based identification derived and approved by the EGamma POG and a multivariate (mva) discriminant derived and trained by the Higgs to four lepton working group and approved by the EGamma POG. For the mono-Z' analysis, the cut-based identification is used and naturally for the ZZ analysis, the mva discriminant is used. Both set of identification requirements are summarized in this section.

Similar to the muon identification requirements for the mono-Z' analysis, the loose electron for the "electron veto" requires electrons with $p_{\mathrm{T}} > 10\,\mathrm{GeV}$ whereas the tight electrons for the electron control regions require electrons with $p_{\mathrm{T}} > 40\,\mathrm{GeV}$ with the full selection criteria given in Table 6.1. The isolation value is calculated based on the sum of the energies of the PF candidates within a cone of $\Delta R < 0.3$ around the electron. The mean energy deposit in the isolation cone of the electron coming from

pileup is estimated following the method described in Ref. [133] and subtracted from the isolation sum.

Variable	**Selection Tight** **Barrel (Endcap)**	**Selection Veto** **Barrel (Encap)**
Full 5×5 $\sigma_{i\eta i\eta}$	< 0.0104 (< 0.0353)	< 0.0126 (< 0.0457)
$\lvert\Delta\eta_{i\eta}\rvert$	< 0.00255 (< 0.00501)	< 0.00463 (< 0.00814)
$\lvert\Delta\phi_{i\eta}\rvert$	< 0.022 (< 0.0236)	< 0.148 (< 0.19)
H/E	$< 0.026 + 1.15/E_{SC} + 0.0324\rho/E_{SC}$ $< 0.0188 + 2.06/E_{SC} + 0.183 * \rho/E_{SC}$	$< 0.05 + 1.16/E_{SC} + 0.0324\rho/E_{SC}$ $< 0.05 + 2.54/E_{SC} + 0.183\rho/E_{SC}$
Relative isolation (ρ correction)	$< 0.0287 + 0.506/p_{\mathrm{T}}$ $< 0.0445 + 0.963/p_{\mathrm{T}}$	$< 0.198 + 0.506/p_{\mathrm{T}}$ $< 0.203 + 0.963/p_{\mathrm{T}}$
$1/E - 1/p$	< 0.159 (< 0.0197)	< 0.209 (< 0.132)
$\lvert d_{xy}(vtx)\rvert$	< 0.050 (< 0.100)	< 0.050 (< 0.100)
$\lvert d_z(vtx)\rvert$	< 0.100 (< 0.200)	< 0.100 (< 0.200)
Expected Inner Missing Hits	≤ 1 (≤ 1)	≤ 2 (≤ 3)
Pass conversion veto	Yes (Yes)	Yes (Yes)

Table 6.1: Loose (selection veto) and tight electron identification criteria. The isolation is computed in a cone of $\Delta\mathrm{R} < 0.3$ around the electron.

In the ZZ analysis, electrons are required to have $p_{\mathrm{T}} > 7\,\mathrm{GeV}$ and to be in the tracker acceptance $|\eta| < 2.5$ with $d_z < 1\,\mathrm{cm}$, $d_{xy} < 5\,\mathrm{mm}$ and the $\mathrm{SIP}_{3\mathrm{D}} < 4$ just like for muons described above. In addition to these loose requirements, electrons are identified using a multivariate discriminant derived and trained by the Higgs to four lepton working group which includes observables as features outlined in Table 6.2. The inclusion of isolation sums helps suppressing electrons originating from electroweak decays of hadrons within jets [137]. The package eXtreme Gradient Boosting (XGBoost) [138] is used for the training and optimization of the multivariate discriminant employed for electron identification and isolation. They are performed using simulation and are divided into six regions formed from two transverse momentum ranges (7–10 GeV and $>$ 10 GeV) and three pseudorapidity regions: central barrel

($|\eta| < 0.8$), outer barrel ($0.8 < |\eta| < 1.479$), and endcaps ($1.479 < |\eta| < 2.5$). The model is trained separately for 2016, 2017 and 2018 which guarantees optimal performance during the whole Run 2 data taking period with average reconstruction and identification efficiencies of about 95% across Run 2 [139].

Observable type	**Observable name**
Cluster Shape	RMS of the energy-crystal number spectrum along η and ϕ;$\sigma_{i\eta i\eta}$, $\sigma_{i\phi i\phi}$
	Super cluster with along η and ϕ
	Ratio of the hadronic energy behind the electron supercluster to the supercluster energy, H/E
	Circularity $(E_{5\times5} - E_{5\times1})/E_{5\times5}$
	Sum of the seed and adjacent crystal over the super cluster energy R_9
	For endcap training bins: energy fraction in pre-shower E_{PS}/E_{raw}
Track-cluster matching	Energy-momentum agreement E_{tot}/p_{in}, E_{ele}/p_{out}, $1/E_{tot} - 1/p_{in}$
	Position matching $\Delta\eta_{in}$, $\Delta\phi_{in}$, $\Delta\eta_{seed}$
tracking	Fractional momentum loss $f_{brem} = 1 - p_{out}/p_{in}$
	Number of hits of the KF and GSF track N_{KF}, N_{GSF}
	Reduced χ^2 of the KF and GSF track χ^2_{KF}, χ^2_{GSF}
	Number of expected but missing inner hits
	Probability transform of conversion vertex fit χ^2
isolation	Particle Flow photon isolation sum
	Particle Flow charged hadrons isolation sum
	Particle Flow neutral hadrons isolation sum
For PU-resilience	Mean energy density in the event ρ

Table 6.2: Overview of input features to the electron identification classifier.

6.6.3 Photons

Similar to the leptons, in the mono-Z' analysis, **loose** photons with an average efficiency of about 70% are used to reject events with unwanted photons (the so-called photon "veto"). These photons must pass the "loose" identification criteria specified by the EGamma POG [140] with $p_{\mathrm{T}} > 15\,\mathrm{GeV}$ and $|\eta| < 2.5$. The detailed identification requirements for this "loose" ID are given in Table 6.3. "Tight" photon identification requirements are used for the photon control region where endcap photons are not taken into account thus requiring $|\eta| < 1.479$ (barrel region) with $p_{\mathrm{T}} > 230\,\mathrm{GeV}$. The POG medium ID is used which is summarized in Table 6.4.

In the ZZ analysis, only the final-state radiation (FSR) photons are relevant and starting from the PF photons, the selection of FSR photons and their association to

Variable	**Selection** **Barrel (Endcap)**
Full 5×5 $\sigma_{i\eta i\eta}$	$< 0.0106 (< 0.0272)$
H/E	$< 0.04596 (< 0.0590)$
charged hadron isolation	$< 1.694 (< 2.089)$
neutral hadron isolation	$< 24.032 (19.722) + 0.01512 (0.0117) \times p_{\mathrm{T}} + 2.259 (2.3) \times 10^{-5} \times p_{\mathrm{T}}^2$
photon isolation	$< 2.876 (4.162) + 0.004017 (0.0037) \times p_{\mathrm{T}}$
Conversion safe electron veto	Yes (Yes)

Table 6.3: Loose photon identification criteria.

Variable	**Selection** **Barrel**
Full 5×5 $\sigma_{i\eta i\eta}$	< 0.01015
H/E	< 0.02197
charged hadron isolation	< 1.141
neutral hadron isolation	$< 1.189 + 0.01512 \times p_{\mathrm{T}} + 2.259 \times 10^{-5} \times p_{\mathrm{T}}^2$
photon isolation	$< 2.08 + 0.004017 \times p_{\mathrm{T}}$
Conversion safe electron veto	Yes

Table 6.4: Tight photon identification criteria. The criteria are only given for the barrel region since endcap photons are not taken into account.

a lepton proceeds as follows [141];

- Photons are considered FSR candidates if they have $p_{T,\gamma} > 2\,\mathrm{GeV}$, $|\eta|^{\gamma} < 2.4$ and a relative PF isolation less than 1.8 as defined in eqn. 6.2 above (with no neutral pileup correction). The PF isolation is computed using a cone of 0.3, a threshold of 0.2 GeV on charged hadrons with a veto cone of 0.0001, and 0.5 GeV on neutral hadrons and photons with a veto cone of 0.01, including also the contribution from PU vertices (same radius and threshold as per charged isolation).

- All PF photons that match with any electron passing both the loose ID and SIP cuts are removed. The matching is peformed by directly associating the two PF candidates.

- Photons are associated to the closest lepton in the event among all those passing

loose ID and SIP cut.

- Photons that do not satisfy the cuts $\Delta R\left(\ell,\gamma\right)/E_{\mathrm{T}_\gamma}^2 < 0.012$, and $\Delta R\left(\ell,\gamma\right) < 0.5$ are discarded.

- If more than one photon is associated to the same lepton, the lowest $\Delta R\left(\ell,\gamma\right)/E_{\mathrm{T}_\gamma}^2$ is selected.

- For each FSR photon selected, the photon from the isolation sum of all leptons in the event passing loose ID and SIP cuts is excluded. This is relevant for photons that are found in the isolation cone and outside the isolation veto of these leptons ($\Delta R < 0.4$ and $\Delta R > 0.01$ for muons and $\Delta R < 0.4$ and ($|\eta|^{SC} < 1.479$ or $DeltaR > 0.08$) for electrons).

6.6.4 Taus

Tau leptons decay primarily hadronically (65% of τ decays [15]) but they can also decay to charged leptons with two neutrinos. Hadronic tau decays, τ_h, can be differentiated from quark or gluon jets by analyzing the multiplicity, collimation and isolation of the decay products. The PF algorithm is able to resolve the particles originating from the tau decay and to determine its isolation hence providing useful information for τ_h identification. These particles are used by the hadrons-plus-strips (HPS) algorithm [142] to identify and reconstruct PF τ_h candidates. Reconstruction is seeded by jets of $p_{\mathrm{T}} > 14\,\mathrm{GeV}$ and $|\eta| < 2.5$ reconstructed with the anti-k_t algorithm (section 6.6.5) where the PF candidate constituents of each jet are combined into τ_h candidates compatible with one of the main τ_h decay modes: one charged hadron $h^{\pm}$; one charged hadron plus a reconstructed π^0 decay (a **strip** of PF e/γ objects, as the photons of $\pi^0 \to \gamma\gamma$ have a high probability to convert in the tracker material), $h^{\pm}\pi^0$; one charged hadron plus two strips $h^{\pm}\pi^0\pi^0$;and three charged hadrons $h^{\pm}h^{\pm}h^{\mp}$. This

PF reconstruction of taus has significantly improved the reconstruction and identification of the tau leptons compared to the previous method of using calorimetric energy deposits to reconstruct τ_h candidates as collimated and isolated calorimetric jets, known as Calo τ_h [143].

6.6.5 Jets

Jets are among the most common physics objects at the LHC and central to many physics searches at the LHC including the mono-Z' dark matter search described in Appendix B. As discussed in chapter 2 and chapter 4, partons (quarks and gluons) produced in the hard interaction are observed in the CMS detectors as clusters of hadronized particles. There are several clustering algorithms (a detailed review can be found in Ref. [144]) but this thesis and most CMS and ATLAS analyses use the infrared and collinear (IRC) safe anti-k_t algorithm [145]. With distance parameter $R = 0.4$ (hereafter, AK4) and in addition to being IRC safe, its a soft-resilient jet algorithm which leads to jets whose shape is not influenced by soft radiation. This not only simplifies experimental calibration procedures, simplifies certain theoretical calculations and eliminates some momentum-resolution loss that may be caused by underlying-event (UE) and pileup contamination [145]. The AK4 algorithm can cluster generated particles from the event simulation, energy deposits in calorimeters (Calo jets) or PF candidates in the even resulting in PF jets. The procedure is as follows: starting with the transverse momentum p_{T} (also called k_T) of each PF particle in the event, a collection of pseudojets is generated and then the distance parameters d_{ij} (between each pair of particles) and d_{iB} (between each particle and the beam) are

computed,

$$d_{ij} = \min(k_{t,i}^{-2}, k_{t,j}^{-2})\frac{\Delta_{ij}^2}{R^2}, \qquad d_{iB} = k_{t,i}^{-2}, \tag{6.4}$$

where $\Delta_{ij}^2 = (y_j - y_i)^2 + (\phi_j - \phi_i)^2$, and $k_{t,i}$, y_i, and ϕ_i are respectively the rapidity and azimuthal angle of the pseudojet i. The minimum of d_{ij} and d_{iB} is determined and if it is d_{ij}, the pseudojets i and j are merged into a new pseudojet by adding the four-momenta of i and j. If the minimum is d_{iB}, pseudojet i is declared to be a jet and removed from further consideration. The procedure is repeated until no pseudojet remain and the resulting particles that did not get merged are referred to as unclustered particles and the summed pseudojets result in the final jet collection. In the analyses discussed in this thesis, this jet collection is further modified to mitigate the effects of pileup such that any charged hadron not associated with the chosen PV of the event is discarded prior to clustering in a procedure known as charged-hadron subtraction (CHS) [146]. As far as the determination of jet energy is concerned, several effects such as the calorimeter response, inefficiencies in particle reconstruction, the underlying event (UE), pileup can distort the result. Therefore jet energy corrections are applied using a factorized approach as shown in Fig. 6.4 below and described in the following steps:

- **Pileup Correction (L1)** The neutral pileup contribution is determined from simulation as a function of p_{T} and η of the jet, the average p_{T} density in the event and the effective jet area (area-median approach) [147] and subtracted from the jet energy.

- **Relative η and absolute p_{T} corrections (L2L3)** These corrections are also determined from simulations by comparing the reconstructed jets with generator level jets and account for detector response and inefficiencies.

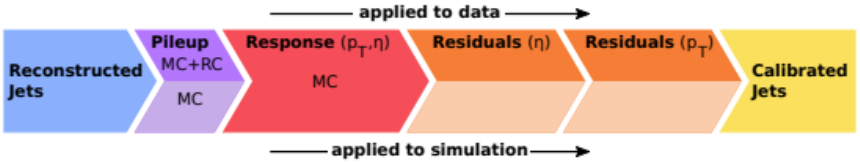

Figure 6.4: Graphical overview of the factorized approach used at CMS to apply jet energy corrections to data and simulated events.

- **Residual $\eta$and $p_T$corrections (L2L3Residual)** After the L2L3 corrections derived from simulation are applied, addition residual differences between the jet response in data and simulation is corrected for by measuring the jet energies in data and MC for samples of Z+jet, γ+jet and dijet events.

Jets used in this analysis are further required to have $p_T > 30\,\text{GeV}$ and $|\eta| < 2.5$ except for b-tagged jets (see more below). There are several quality requirements to remove detector noise through selections on multiplicity and energy fractions of the PF constituents of the jet. Jets are also required to pass tight jet identification requirements [148–150] in addition to removing jets that are within a cone of $R < 0.4$ around a lepton or a photon in the $\eta - \phi$ plane. The **tight** jet identification used in this analysis has better than 99% efficiency in all η regions [149]. There are other requirements to suppress non-collision backgrounds which will be detailed in the analysis chapters of the mono-Z' analysis in Appendix B.

6.6.5.1 b-Jets

In the reconstruction and identification of jets originating from bottom quarks (b-jets), the relatively long lifetimes of many B mesons (e.g. $c\tau$ for $B^{\pm}$ is $491\,\mu\text{m}$ [15]) is utilized as the charged hadrons from the decay of such B mesons in a b-jet will originate from a displaced vertex. A b-tagging algorithm such as the one described below analyzes the PF charged hadron candidates in a given jet and combines in-

formation of displaced tracks with information on secondary vertices associated with the jet using multivariate analysis techniques to identify or **tag** b-jets.

The b-jets in the mono-Z' analysis are identified using the combined secondary vertex b-tagging algorithm with a **medium** working point defined in [151]. This **DeepCSV** tagger is developed using a deep neural network with simultaneous training in all vertex categories and for all jet flavors. For more details on this tagger see section 5.1.2.2 in Ref. [151]. B jets with $p_{\mathrm{T}} > 20\,\mathrm{GeV}$ and $|\eta| < 2.4$ are correctly identified with an efficiency of 68% with a misidentification probability of 1% for the working point used in this analysis.

6.6.6 Missing transverse momentum

The negative vector sum of the transverse momenta of all PF candidates reconstructed in an event is called the missing transverse momentum,

$$\vec{p}_{\mathrm{T}}^{\,\mathrm{miss}} = -\sum_{i\in\{h^{\pm},h^{0},e,\mu,\gamma,h^{\pm,PU}\}} \vec{p}_{\mathrm{T},i}. \tag{6.5}$$

Since the vector sum of the transverse momenta of all true particles in an event must be zero due to momentum conservation in the plan transverse to the beam axis, $p_{\mathrm{T}}^{\mathrm{miss}}$ corresponds to the transverse momentum sum of all such particles that pass undetected through the CMS detector such as neutrinos (or weakly interacting DM particles in BSM theories). So, the PF $p_{\mathrm{T}}^{\mathrm{miss}}$ gives an estimate of the sum of the transverse momenta of all such "invisible" or undetected particles in an event. Therefore, the vector $\vec{p}_{\mathrm{T}}^{\,\mathrm{miss}}$ (and its associated magnitude $p_{\mathrm{T}}^{\mathrm{miss}}$) is one of the most important quantities in BSM dark matter searches such as the mono-Z' analysis.

As given in eq. 6.5 above, all PF candidates are included in this sum including any charged hadrons associated with pileup primary vertices because pileup collisions (soft hadronic interactions) do not produce significant $p_{\mathrm{T}}^{\mathrm{miss}}$. Since PF candidates in

the vector sum include PF jets and jet energy corrections mentioned in section 6.6.5 would alter the equality in eq. 6.5, the effect of jet energy corrections is propagated to $\vec{p}_{\mathrm{T}}^{\mathrm{miss}}$ for all jets with $p_{\mathrm{T}} > 15\,\mathrm{GeV}$ and passing loose identification criteria. This is done by subtracting the change in $\vec{p}_{\mathrm{T}}$,j due to these corrections,

$$\text{Corrected } \vec{p}_{\mathrm{T}}^{\mathrm{miss}} = \vec{p}_{\mathrm{T}}^{\mathrm{miss}} + \sum_{j \in \mathrm{jets}} \vec{p}_{\mathrm{T},j} - \vec{p}_{\mathrm{T},j}^{corr}. \tag{6.6}$$

It should be noted that propagating these jet energy corrections improves the $p_{\mathrm{T}}^{\mathrm{miss}}$ resolution and more details on such studies can be found in Ref. [152, 153].

There are several possible sources (deficiencies in the detector and reconstruction algorithms) of anomalous high-p_{T} events that have been identified in data. Such events are vetoed using dedicated $p_{\mathrm{T}}^{\mathrm{miss}}$ filters which are listed in Table below and applied in the mono-Z' analysis.The filters exclude events where any of the following phenomenon results in anomalous high-$p_{\mathrm{T}}^{\mathrm{miss}}$ events. Dead cells in the ECAL can lead to real energy deposits going unaccounted leading to a spurious imbalance. Significant anomalous energy deposits can arise due to spurious spikes in a single ECAL crystal due to a faulty readout or from HCAL readout due to noise from high-voltage discharges in the hybrid photodiodes. Spurious energy deposits in the calorimeters and the CSCs can result due to muon interactions that are symmetric in ϕ which are indicative of beam halo muons that are produced in non-collision sources such as proton beam interactions with beam pipe material. Furthermore, there can be errors in reconstruction algorithms where a poor quality and high p_{T}false muon track (usually from an already accounted charged hadron) is reconstructed as a PF muon. These filters have been developed and recommended by the JME POG [154] and applied both in data and simulation. As none of these anomalies are simulated, the filtering efficiency in simulation samples is more than 99.9% [153]. Finally, in the 2017 dataset, significant noise contributions in the endcap ECAL lead to spurious

jets with misreconstucted energies. These jets lead to anomalous contributions to $p_{\mathrm{T}}^{\mathrm{miss}}$ which are overcome through mitigation technique aptly named as the **EE noise mitigation** [155] where jets and unclustered PF candidates with $2.65 < |\eta| < 3.139$ and uncorrected $p_{\mathrm{T}} < 50\,\mathrm{GeV}$ are excluded from the $p_{\mathrm{T}}^{\mathrm{miss}}$ calculation.

Chapter 7

Analysis Strategy

The four-lepton final state is formed by selecting events which contain two opposite-charged same-flavor lepton objects (*i.e.* e^+e^-,$\mu^+\mu^-$) which are reconstructed and identified according to the selections described in chapter 6. Four-lepton signal processes are generally well modeled with negligible backgrounds so a simple "cut and count" comparison between data and Monte Carlo samples' yields after applying relevant selections is an adequate strategy for this analysis as well. The comparisons include the contribution from reducible backgrounds, which is estimated with using control regions (CRs) in data. Inclusive and differential cross sections for nonresonant production of pairs of Z bosons, pp $\rightarrow$ ZZ, with two on-shell Z bosons, produced in the dilepton mass range 60-120 GeV, are extracted from the observed yields with maximum likelihood estimation techniques. Finally, searches for triple anomalous gauge couplings use a profile likelihood method to extract limits from the bin-by-bin yields in the $m_{4\ell}$ distribution. These techniques are all described in this chapter, as are the relevant systematic uncertainties, which are taken into account by varying the input parameters to the yields and observing the resulting changes in yield and spectrum shape.

7.1 Event triggering

Collision events are selected by the trigger system that requires the presence of a pair of loosely isolated leptons or a triplet of leptons, with lepton p_{T} thresholds varying by lepton combination. Further triggers include a set of single-electron and single-muon triggers, and a set of triple lepton triggers and triggers for leptons of different flavors. The trigger efficiency within the acceptance of this analysis is greater than 98%. Exact HLT parameters changed over the course of three years of datataking as instantaneous luminosities changed and trigger rates rose so a full list of trigger paths used for this analysis is provided in Tables 7.1,7.2,7.3 below. Events passing any listed triggers are considered.

The trigger efficiency in Data and MC is presented in Fig. 7.1. The plot is taken from the HZZ analysis, AN2017-342-v10, the efficiency is measured in ZZ events where the leading lepton triggers the single lepton trigger, while other leptons are used as a probe. For details see AN. The plot shows efficiency of the full set of used triggers as a function of p_{T} of the 3rd probe lepton. Most of the events in this analysis, since both Z bosons are on-shell and have lepton $p_{\mathrm{T}} > 20\,\mathrm{GeV}$.

7.2 Event Selection and ZZ Candidate Selection

Since this measurement involves a four-lepton final state, an event is required to have four leptons. Each event should contain at least one lepton with $p_{\mathrm{T}} > 20\,\mathrm{GeV}$, two electrons (muons) with $p_{\mathrm{T}} > 12(10)\,\mathrm{GeV}$, and four leptons with $p_{\mathrm{T}} > 7(5)\,\mathrm{GeV}$ for electrons (muons). All leptons should pass the "tight" lepton identification requirements and isolation requirements as described in section 6.6.1 and section 6.6.2.

All leptons are required to be separated by $\Delta R\,(\ell_1, \ell_2) > 0.02$, and electrons are required to be separated from muons by $\Delta R\,(\mathrm{e}, \mu) > 0.05$, to remove spurious "ghost"

Trigger Paths (pp collisions 2016)
Muon triggers
HLT_IsoMu20_v*
HLT_IsoTkMu20_v*
HLT_IsoMu22_v*
HLT_IsoTkMu22_v*
HLT_IsoMu24_v*
HLT_IsoTkMu24_v*
HLT_Mu17_TrkIsoVVL_Mu8_TrkIsoVVL_DZ_v*
HLT_Mu17_TrkIsoVVL_TkMu8_TrkIsoVVL_DZ_v*
HLT_Mu17_TrkIsoVVL_Mu8_TrkIsoVVL_v*
HLT_Mu17_TrkIsoVVL_TkMu8_TrkIsoVVL_v*
HLT_TripleMu_12_10_5_v*
Electron triggers
HLT_Ele25_eta2p1_WPTight_Gsf_v*
HLT_Ele27_WPTight_Gsf_v*
HLT_Ele27_eta2p1_WPLoose_Gsf_v*
HLT_Ele32_eta2p1_WPTight_Gsf_v*
HLT_Ele17_Ele12_CaloIdL_TrackIdL_IsoVL_DZ_v*
HLT_Ele23_Ele12_CaloIdL_TrackIdL_IsoVL_DZ_v*
HLT_DoubleEle33_CaloIdL_GsfTrkIdVLP_v*
HLT_Ele16_Ele12_Ele8_CaloIdL_TrackIdL_v*
Cross triggers
HLT_Mu23_TrkIsoVVL_Ele12_CaloIdL_TrackIdL_IsoVL_v*
HLT_Mu8_TrkIsoVVL_Ele23_CaloIdL_TrackIdL_IsoVL_v*
HLT_Mu8_TrkIsoVVL_Ele23_CaloIdL_TrackIdL_IsoVL_DZ_v*
HLT_Mu12_TrkIsoVVL_Ele23_CaloIdL_TrackIdL_IsoVL_DZ_v*
HLT_Mu23_TrkIsoVVL_Ele12_CaloIdL_TrackIdL_IsoVL_v*
HLT_Mu23_TrkIsoVVL_Ele12_CaloIdL_TrackIdL_IsoVL_DZ_v*
HLT_Mu23_TrkIsoVVL_Ele8_CaloIdL_TrackIdL_IsoVL_v*
HLT_DiMu9_Ele9_CaloIdL_TrackIdL_v*
HLT_Mu8_DiEle12_CaloIdL_TrackIdL_v*

Table 7.1: Triggers used in the 2016 analysis.

leptons formed from ambiguities in track reconstruction. Lepton pairs originating from hadronic decays are removed by requiring that all opposite-sign lepton pairs in the candidate have $m_{\ell_1\ell_2} > 4$ GeV regardless of flavor, omitting any contribution from FSR photons which are described in section 6.6.3.

Z candidates are build using two oppositely charged leptons of the same flavor. Each pair is retained if it satisfies $4 < m_{\mathrm{Z}} < 120\,\mathrm{GeV}$. All possible four-lepton candidates in an event are then considered. Within each candidate, the dilepton pair with invariant mass closest to nominal m_{Z} is designated Z_1, the other Z_2. The event

Trigger Paths (pp collisions 2017)
Muon triggers
HLT_IsoMu27_v*
HLT_Mu17_TrkIsoVVL_Mu8_TrkIsoVVL_DZ_Mass3p8_v*
HLT_Mu17_TrkIsoVVL_Mu8_TrkIsoVVL_DZ_Mass8_v*
HLT_TripleMu_10_5_5_DZ_v*
HLT_TripleMu_12_10_5_v*
Electron triggers
HLT_Ele35_WPTight_Gsf_v*
HLT_Ele38_WPTight_Gsf_v*
HLT_Ele40_WPTight_Gsf_v*
HLT_Ele23_Ele12_CaloIdL_TrackIdL_IsoVL_v*
HLT_DoubleEle33_CaloIdL_MW_v*
HLT_Ele16_Ele12_Ele8_CaloIdL_TrackIdL_v*
Cross triggers
HLT_Mu8_TrkIsoVVL_Ele17_CaloIdL_TrackIdL_IsoVL_v*
HLT_Mu8_TrkIsoVVL_Ele23_CaloIdL_TrackIdL_IsoVL_DZ_v*
HLT_Mu12_TrkIsoVVL_Ele23_CaloIdL_TrackIdL_IsoVL_DZ_v*
HLT_Mu23_TrkIsoVVL_Ele12_CaloIdL_TrackIdL_IsoVL_DZ_v*
HLT_DiMu9_Ele9_CaloIdL_TrackIdL_v*
HLT_Mu8_DiEle12_CaloIdL_TrackIdL_v*

Table 7.2: Triggers used in the 2017 analysis.

Trigger Paths (pp collisions 2018)
Muon triggers
HLT_IsoMu24_v*
HLT_Mu17_TrkIsoVVL_Mu8_TrkIsoVVL_DZ_Mass3p8_v*
HLT_TripleMu_10_5_5_DZ_v*
HLT_TripleMu_12_10_5_v*
Electron triggers
HLT_Ele32_WPTight_Gsf_v*
HLT_Ele23_Ele12_CaloIdL_TrackIdL_IsoVL_v*
HLT_DoubleEle25_CaloIdL_MW_v*
Cross triggers
HLT_Mu23_TrkIsoVVL_Ele12_CaloIdL_TrackIdL_IsoVL_v*
HLT_Mu8_TrkIsoVVL_Ele23_CaloIdL_TrackIdL_IsoVL_DZ_v*
HLT_Mu12_TrkIsoVVL_Ele23_CaloIdL_TrackIdL_IsoVL_DZ_v*
HLT_Mu23_TrkIsoVVL_Ele12_CaloIdL_TrackIdL_IsoVL_v*
HLT_DiMu9_Ele9_CaloIdL_TrackIdL_DZ_v*
HLT_Mu8_DiEle12_CaloIdL_TrackIdL_DZ_v*

Table 7.3: Triggers used in the 2018 analysis.

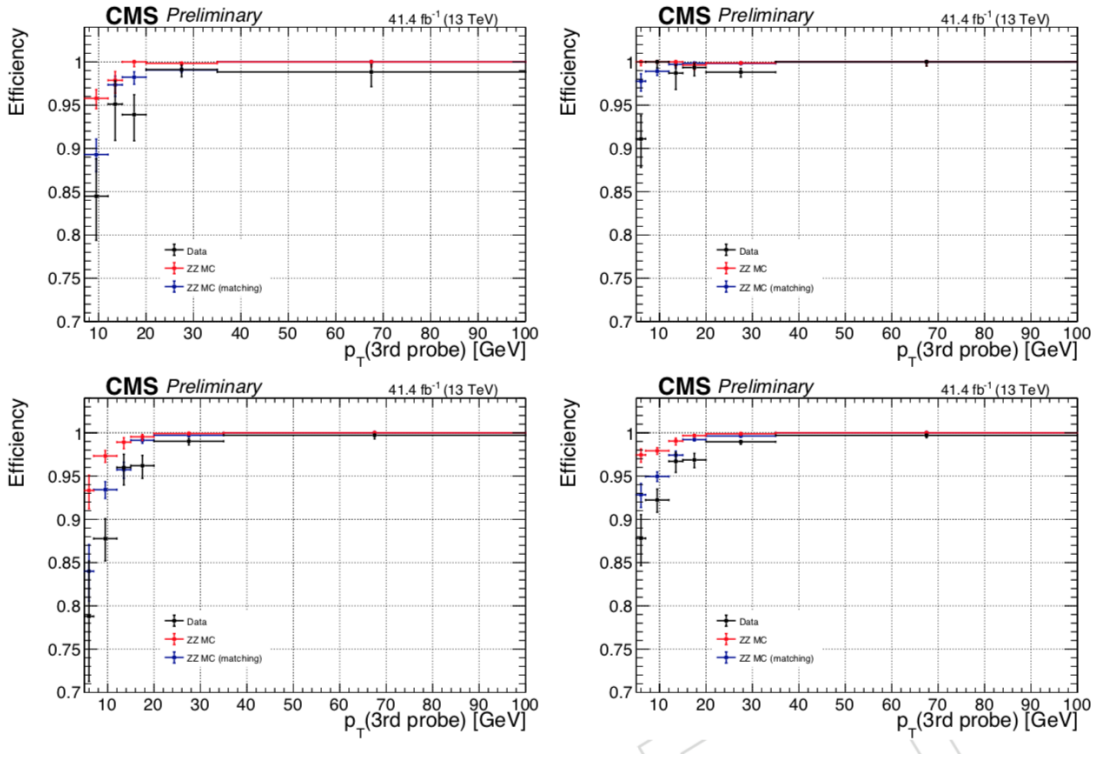

Figure 7.1: Trigger efficiency measured in data using 4ℓ events collected by single lepton triggers for the 4e (top left), 4μ (top right), $2e2\mu$ (bottom left), and 4ℓ (bottom right). Plot is taken from AN2017-342-v10.

is kept if $40 < m_{Z_1} < 120\,\text{GeV}$, $4 < m_{Z_2} < 120\,\text{GeV}$.

In the case of multiple candidates within an event passing all cuts, the ambiguity is resolved by selecting the candidate where m_{Z_1} is closest to the nominal Z. In the rare case of further ambiguity, which may arise in events with five or more leptons, the Z_2 candidate is chosen to maximize the scalar p_T sum of the four leptons. This best candidate selection is done after the full selection is applied.

The $pp \to ZZ$ cross section is measured in events where both m_{Z_1} and m_{Z_2} are required to be greater than 60 GeV and less than 120 GeV.

7.3 Background Estimation

The contribution from background processes with nonprompt leptons is evaulated with control regions of events in data. These so-called reducible backgrounds for four-lepton events typically have two or three prompt leptons and one or two other objects—typically jet fragments, sometimes photons—which are misidentified as prompt leptons. The requirement of four well-reconstructed and isolated lepton candidates strongly suppresses any background; therefore this analysis has very low background contributions, dominated by Z boson and W Z diboson production in association with jets, and by $\mathrm{t\bar{t}}$ events in which both top quarks decay to a lepton, a neutrino, and a b quark jet. In all these cases, particles from jet fragmentation satisfy both lepton identification and isolation criteria, and are thus misidentified as signal leptons. For simplicity, the two sets of processes are not treated separately in what follows, and are collectively labeled "Z + X" events[1].

The contributions of the reducible backgrounds to the selected four-lepton signal samples are evaluated using the tight-to-loose "fake rates" method, described in Ref. [156]. In this procedure, the likelihood of a nonprompt ("fake") object to be misidentified as a prompt lepton is estimated and applied to control regions enriched with Z + X events to estimate their contribution to the signal region. The lepton misidentification rate $f_\ell\left(p_{\mathrm{T}}^{\ell}, \eta^{\ell}\right)$ is measured from a sample of $\mathrm{Z} + \ell_{\mathrm{fake}}$ events, where the Z boson candidate is selected as in the signal region but with $|m_{\ell\ell} - m_{\mathrm{Z}}| < 7\,\mathrm{GeV}$, and the ℓ_{fake} object is a lepton candidate that passes relaxed ID requirements as defined in sections 6.6.1– 6.6.2, with no isolation or tight ID requirements applied.

The misidentification rate is defined as the fraction of ℓ_{fake} candidates which pass full lepton identification and isolation critera, in bins of p_{T} and η. One should

[1]This is a bit of a misnomer, as "Z + X" does not accurately describe $\mathrm{t\bar{t}}$ events, but the terminology is retained here for consistency with the CMS papers on these analyses.

note that the misidentification rate cannot be interpreted as a probability in the usual sense, and if fact there is no simple physical interpretation of it. The contamination from W Z is suppressed by requiring that the missing transverse energy $E_{\mathrm{T}}^{\mathrm{miss}}$ in the event is below 25 GeV. Furthermore that the transverse mass $m_{\mathrm{T}} \equiv \sqrt{(p_{\mathrm{T}}^{\ell} + p_{\mathrm{T}}^{\mathrm{miss}})^2 - (\vec{p}_{\mathrm{T}}^{\,\ell} + \vec{p}_{\mathrm{T}}^{\,\mathrm{miss}})^2}$ of the $\ell_{\mathrm{candidate}}$ and the missing transverse momentum vector be less than 30 GeV. The remnant contribution of WZ and ZZ events is estimated from MC and subtracted. Figures 7.2– 7.4 show the misidentification rates for electrons and muons separately as a function of $p_{\mathrm{T}}$and η for 2016,2017 and 2018 respectively.

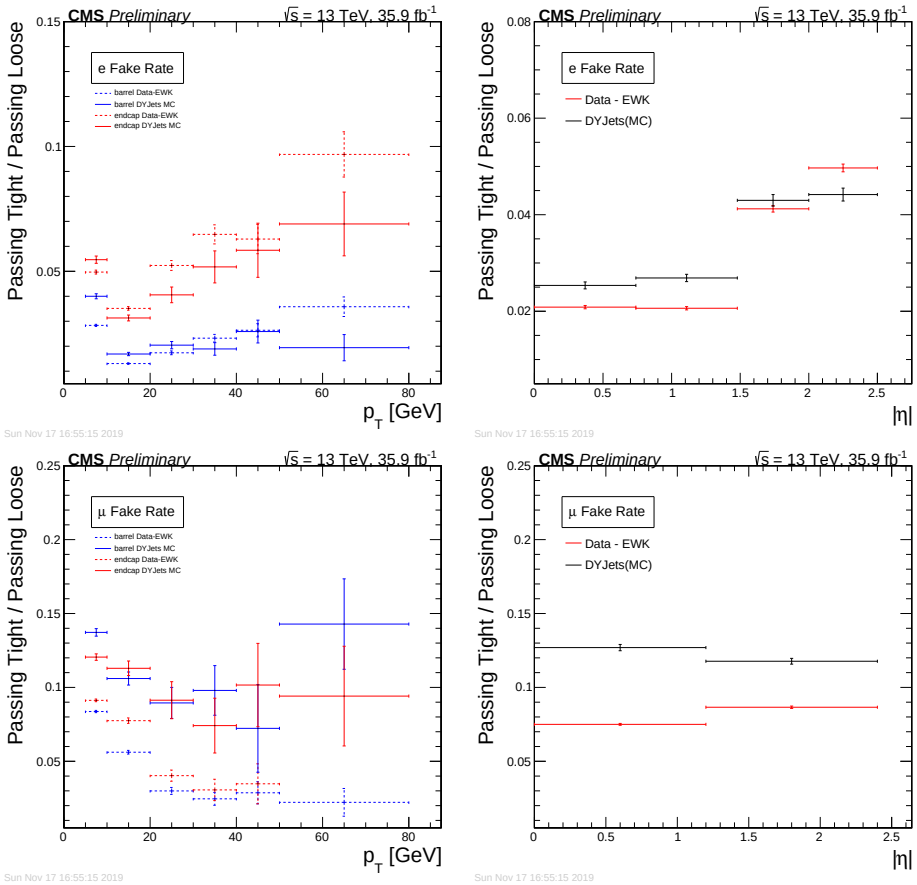

Figure 7.2: Fake rate for electrons (top) and muons (bottom) as a function of p_{T} (left) and η (right) in 2016.

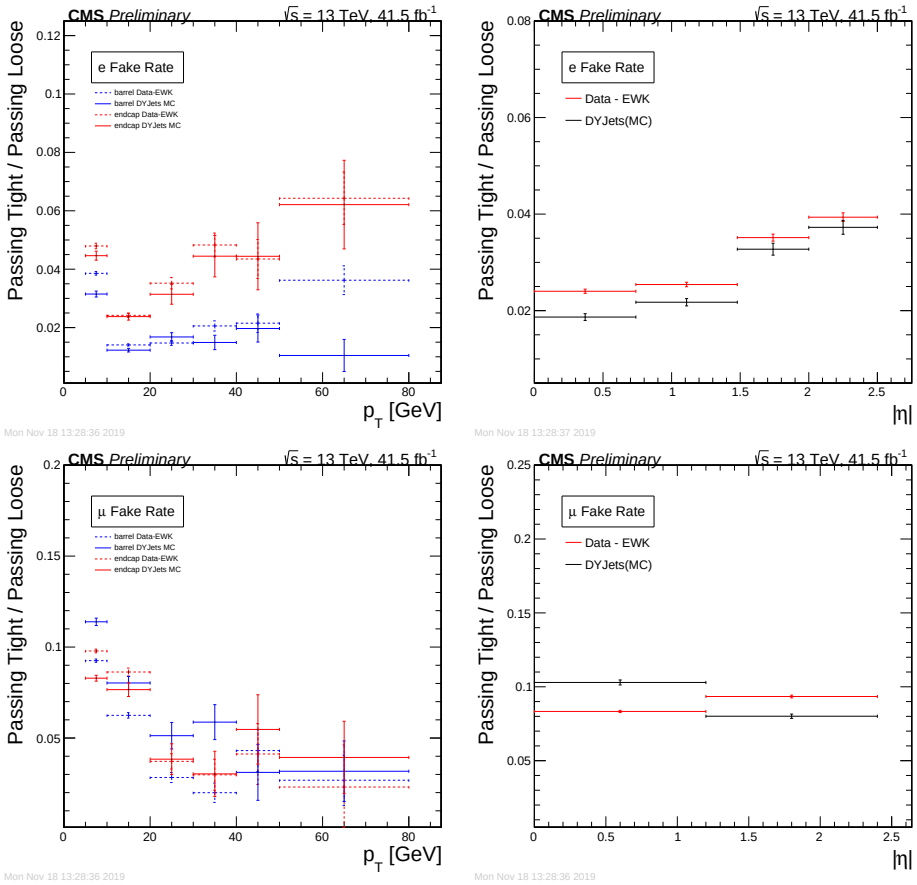

Figure 7.3: Fake rate for electrons (top) and muons (bottom) as a function of p_{T} (left) and η (right) in 2017.

As mentioned above, the major background contributions in this analysis arise from the production of Z and WZ in association with jets, as well as $t\bar{t}$. In all these cases, a jet or non-isolated lepton is misidentified as a e or μ. Additional contribution can arise from the production of a Z with a photon (and jets), where photon converts in the detector, giving a raise in additional non prompt leptons. A lepton is defined as "passed" (P) if it passes the full isolation and identification criteria, and "failed" (F) if it passed the criteria for ℓ_{loose} above but failed the isolation or the tight identification criteria.

In order to estimate the expected number of background events in the signal

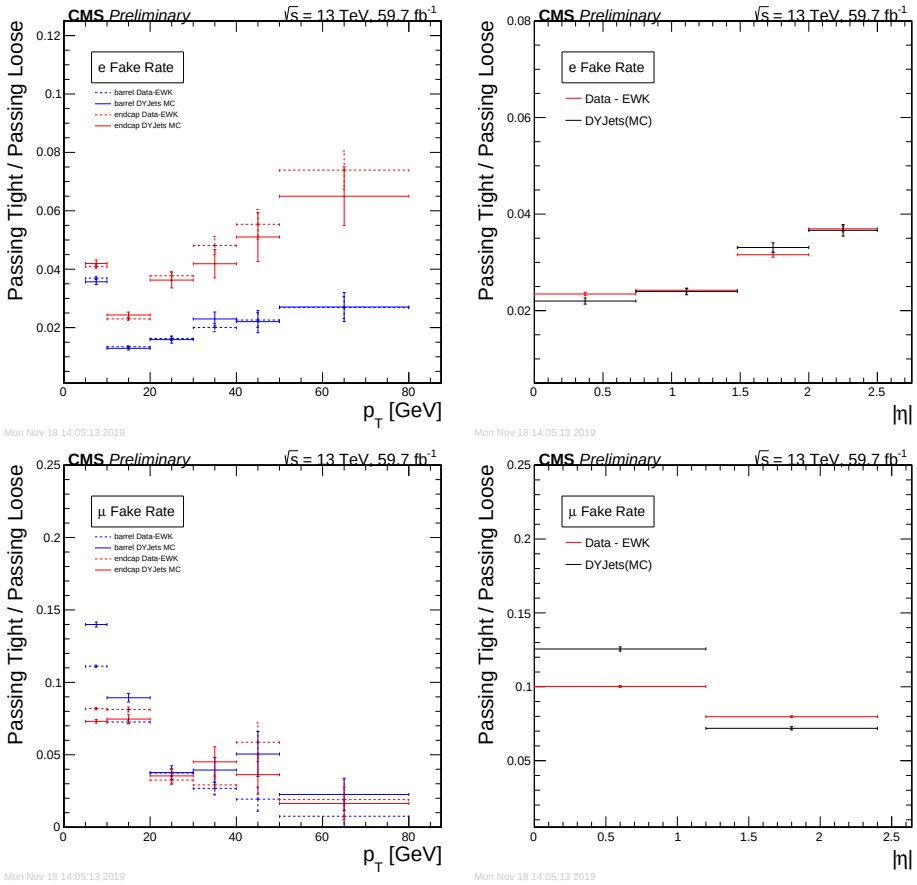

Figure 7.4: Fake rate for electrons (top) and muons (bottom) as a function of p_{T} (left) and η (right) in 2018.

region, two control data samples are obtained by selecting events containing a lepton pair Z_1 which passes all selection requirements, and two additional lepton candidates $\ell'\ell'$, of which one (the "3P1F" control region) or both ("2P2F") are identified as failed. The additional lepton pair must have opposite charge and matching flavor ($\mathrm{e}^{\pm}\mathrm{e}^{\mp}, \mu^{\pm}\mu^{\mp}$). The sample with one failing lepton, called the "3P1F" sample for "3 prompt 1 fake," covers the contribution from WZ events, while the sample with both leptons in the second Z boson failing ("2P2F") covers Z+jets, Zγ+jets, and $\mathrm{t\bar{t}}$ events. The fake object transfer factor

$$F_\ell\left(p_{\mathrm{T}}^\ell, \eta^\ell\right) = \frac{f_\ell\left(p_{\mathrm{T}}^\ell, \eta^\ell\right)}{1 - f_\ell\left(p_{\mathrm{T}}^\ell, \eta^\ell\right)} \tag{7.1}$$

is the ratio of nonprompt objects passing the relaxed and full selection criteria, and thus serves as a per-lepton extrapolation factor between control sample yields and signal sample yields.

The procedure excludes a possible double counting due to events that can be found in two control regions. A correction for the small contribution of ZZ events in the control region is applied based on MC simulation. To estimate the number of background events in the signal region, N_B, the measured fake rate $f_\ell\left(p_{\mathrm{T}}, \eta\right)$ is applied to the correspondent control regions. To get the final estimate one needs to sum up all contribution and correct for double counting, since the 2P2F region will contribute to the 3P1F region.

The final formula for the background estimation is :

$$N_B^{est} = \sum_{\ell \in \mathrm{3P1F}} \frac{f_\ell}{1 - f_\ell} - \sum_{\ell_1, \ell_2 \in \mathrm{2P2F}} \frac{f_{\ell_1} f_{\ell_2}}{\left(1 - f_{\ell_1}\right)\left(1 - f_{\ell_2}\right)} \tag{7.2}$$

Subtraction of contamination from signal events, estimated from Monte Carlo simulation, is implicit in Eq. 7.2.

There are also irreducible background contributions from $\mathrm{t\bar{t}Z}$ and WWZ events, which can have four prompt leptons. Expected yields for these processes are taken from simulation.

7.4 Systematic Uncertainties

Systematic uncertainties for trigger efficiency are taken to be the difference between trigger efficiencies in data and in simulated signal events, found to be around 1-2% of the final event yield. In both data and simulated events, trigger efficiencies are found with a tag-and-probe technique [136], performed on four-lepton events.

The lepton identification and isolation efficiencies in simulation are corrected with scaling factors derived with the tag-and-probe method, performed on $Z \to \ell^+\ell^-$ events in data and a single-Z Monte Carlo sample. In order to calculate the uncertainties associated with these corrections, the total yield is recomputed with the scaling factors varied up and down by one standard deviation of the uncertainties from the tag-and-probe method, treating all bins as correlated. The uncertainties associated with the lepton efficiency in the $ZZ \to 2\ell'\ell$ signal regions are found to be 5% in the 4e final state, 3% in the 2e2μ final state, and 2% in the 4μ final state.

The uncertainty on the integrated luminosity of the data sample is 2.5% (2016) [90], 2.3% (2017) [87], and 2.5% (2018) [88]. Since the luminosity uncertainty contains a significant uncorrelated portion, the relative luminosity uncertainty of the whole sample is smaller than for each individual year.

The uncertainty on lepton fake rates is 40%, which includes both statistical uncertainty and systematic uncertainties associated with the loosened lepton selections defined in sections 6.6.1– 6.6.2 and the differences in the underlying physics processes between events in the $Z + \ell_{\text{fake}}$, 3P1F, and 2P2F control samples [47]. Statistical uncertainties arising from the limited size of the Z + X control samples are also included as a systematic uncertainty on the background yield. The total uncertainty on the background yield varies by channel but is below 1% of the expected total yield.

The modeling of pileup relies on the total inelastic pp cross section [66]. The pileup uncertainty is evaluated by varying this cross section up and down by 5%.

Uncertainties because of factorization (μ_{F}) and renormalization (μ_{R}) scale choices on the $ZZ \to 4\ell$ acceptance are evaluated with POWHEG and MCFM, by varying the QCD scales up and down by a factor of two with respect to the default $\mu_R = \mu_F = m_{\text{ZZ}}$. All combinations are considered except those in which (μ_{F}) and (μ_{R}) differ by a factor of four. Parametric uncertainties (PDF+α_s) are evaluated according to

the PDF4LHC prescription in the acceptance calculation [157], and with NNPDF3.0 in the cross section calculations. An additional theoretical uncertainty arises from scaling the $q\bar{q} \to ZZ$ and $gg \to ZZ$ simulated samples to their NNLO and NLO predicted cross sections, respectively, with the K factors described in Section 5.2.4. The corresponding change in the acceptance, about 1%, is added to the previous theoretical errors in quadrature.

Systematic uncertainties on expected signal yield are summarized in Table 7.4. To obtain uncertainties in the inclusive fiducial and total cross sections, each uncertainty source is treated as a nuisance parameter in the fits described in Section 7.5.1. For differential cross section and other shape uncertainties, the calculation is fully redone for each uncertainty source, with the inputs shifted by one standard deviation in each direction. Variations across bins are taken to be fully correlated for each uncertainty source. Lepton and jet momentum scale and resolution uncertainties are taken to be trivial for the overall yield, but they are considered among the shape uncertainties.

Table 7.4: The contributions of each source of signal systematic uncertainty in the total yields. The integrated luminosity uncertainty and the PDF and scale uncertainties are considered separately. All other uncertainties are added in quadrature into a single systematic uncertainty. Uncertainties that vary by decay channel are listed as a range.

Uncertainty	$ZZ \to 4\ell$
Lepton efficiency	2–5%
Trigger efficiency	1-2%
Background	0.6–1.3%
Pileup	1%
PDF	1%
QCD Scales	1%
NNLO/NLO corrections	1%
Integrated luminosity	2.5% (2016), 2.3% (2017), 2.5%(2018)

7.5 Fiducial and Total Cross Section Calculation

As discussed in the beginning of this chapter, the inclusive cross section measurement of ZZ production can be treated as a simple binned counting experiment where the bins are the three decay channels (4e, 2e2μ, and 4μ). The distribution of data events in any quantum process is fundamentally stochastic in nature. So, if ν events are expected in a given bin, the probability of observing n events is given by the Poisson distribution,

$$f\left(n;\nu\right) = e^{-\nu}\frac{\nu^{n}}{n!}. \tag{7.3}$$

Since, expected events arise from both signal and background processes,

$$\nu = \nu_{s} + \nu_{b} \tag{7.4}$$

where ν_{b} and ν_{s} represent the expected event yields from background and signal processes respectively. Furthermore, in order to extract information from the data about the signal processes (which may differ from the expectation in general but not so much in this analysis with negligible backgrounds), the variability of the signal expectation is quantified by a rate modifier μ which is referred to as the "signal strength" which compares our expectation to what we actually measure:

$$\mu = \frac{\sigma_{meas}}{\sigma_{SM}}. \tag{7.5}$$

Overall, the expected events, ν, in a given bin can be written as,

$$\nu = \nu_{s}\left(\vec{\theta_{s}}\right) + \nu_{b}\left(\vec{\theta_{b}}\right) = \mu\left(\vec{\theta_{s}}\right)\mathscr{L}_{int}\sigma_{SM}\epsilon + \nu_{b}\left(\vec{\theta_{b}}\right) \tag{7.6}$$

where σ_{SM} is the standard model expectation for the cross section of the signal process and ϵ is our efficiency for detecting and identifying its events. The signal and background nuisance parameter vectors $\vec{\theta_{s}}$ and $\vec{\theta_{b}}$ represent hidden quantities that are not measured directly but which affect our yields, i.e. systematic effects.

Of the variables in Eqs. (7.3) and (7.6), σ_{SM} is known from theoretical calculations, and ϵ is determined from simulation. The CMS detector is designed to measure n and $\mathscr{L}_{int}$, ν_b is estimated from data or simulation, and inferring σ_{meas} is a matter of finding the most likely value of the signal strength μ given the observed data. Then the measured cross section is simply

$$\sigma_{meas} = \mu\sigma_{SM}. \tag{7.7}$$

It is important to note that σ_{SM} is used in the calculation of μ (Eq. 7.6) and in the final cross section (Eq. 7.7) in such a way that it cancels out, and in fact anything proportional to the true cross section may be used. Therefore, the order at which σ_{SM} is calculated does not matter provided that the efficiency, ϵ, for reconstructing and identifying signal events is not affected by higher order corrections to the kinematics of the events. In terms of efficiency for reconstruction, ϵ is given by the ratio of expected events in the fiducial volume to the number of reconstructed events, $\epsilon = n_{th}/n_{reco}$.

In the expression above, n_{th} excludes events outside the fiducial volume of the detector, or outside the kinematic region where events can be reliably reconstructed, e.g. leptons at very low p_{T}. Hence, σ_{meas} in Eq. (7.7) is referred to as the fiducial cross section, the cross section for the process in a phase space similar to (typically, slightly larger than) the phase space in which the experimental analysis can in principle detect events. In the four-lepton case, the fiducial phase space is a space of $2\ell 2\ell'$ ($\ell, \ell' \in \mathrm{e}, \mu$) events defined by criteria on lepton kinematics, dilepton invariant masses, and four-lepton mass. Table 7.5 shows the fiducial definitions for the $\mathrm{ZZ} \to 4\ell$ cross section measurement.

The total ZZ cross section is defined subject to no constraints except the requirement that m_{Z_1} and m_{Z_2} be between 60 and 120 GeV, which serves as the definition of a Z boson. The fiducial cross section is related to the total cross section by the

branching fraction $\mathcal{B}$ to the final state in question—here, two factors of the Z/γ^* branching ratio to electron and muon pairs—and an acceptance factor $\mathcal{A}$ which is the fraction of events falling in the fiducial phase space,

$$\sigma_{fid} = \mathcal{A}\sigma_{tot} \left(\mathcal{B}\left(Z \to 2\ell\right)\right)^2 . \tag{7.8}$$

The acceptance factor $\mathcal{A}$ is defined as $\mathcal{A} = \sigma_{report,th}/\sigma_{meas,th}$ where $\sigma_{meas,th}$ and $\sigma_{report,th}$ are the predicted cross sections in the region of measurement and reported region respectively. It is determined entirely from theory, and is well known [15], so it is straightforward to calculate the total cross section once the fiducial cross section is known.

Calculating both fiducial and total cross sections also gives the extra benefit of factorizing the experimental and theoretical uncertainties. The experimental uncertainties in this calculation have their source in the uncertainties on ϵ, $\mathscr{L}_{int}$, and ν_b in Eq. (7.6), which have little or no dependence on theory, while the fully theoretical quantity, known as acceptance, introduces a theoretical uncertainty to the measurement. Thus the uncertainty on σ_{fid} is entirely experimental, and the theoretical uncertainties enter only in the uncertainty on σ_{tot}.

Table 7.5: Fiducial phase space definitions for the $ZZ \to 4\ell$ cross section measurement.

Measurement	Fiducial requirements
Basic	$p_T^{\ell_1} > 20\,\text{GeV}$, $p_T^{\ell_2} > 10\,\text{GeV}$, $p_T^{\ell_{3,4}} > 5\,\text{GeV}$, $\left\lvert\eta^\ell\right\rvert < 2.5$, $m_{\ell^+\ell^-} > 4\,\text{GeV}$
$ZZ \to 4\ell$	$60 < m_{Z_1}, m_{Z_2} < 120\,\text{GeV}$

7.5.1 Statistical Procedure for Signal Strength Extraction

The signal strength is found by the method of maximum likelihood estimation, or maximum likelihood fit [15, 158]. The technique sets out to estimate the underlying parameters of the model from which the data set is drawn, using knowledge of the expected distribution of the model parameters. The technique is built around the likelihood function which is built from the expected probability distributions for the outcome of an experiment. The likelihood function which is the product of the probability distributions across all bins,

$$L\left(\vec{\theta_s}, \vec{\theta_b}\right) = \prod_{bins} f\left(n; \nu\left(\vec{\theta_s}, \vec{\theta_b}\right)\right). \tag{7.9}$$

The most likely value of ν is the one that maximizes L. In practice, $\log L$ is typically maximized instead because it is easier to work with,

$$\frac{\partial^2 \log L}{\partial \vec{\theta_s} \partial \vec{\theta_b}} = 0. \tag{7.10}$$

This maximization is performed simultaneously for all bins, yielding a single signal strength across all channels. Systematic uncertainties enter as log-normal constraints imposed on the fit, encoded in $\vec{\theta_s}$ and $\vec{\theta_b}$. The fit is performed numerically using the MINUIT software package in the ROOFIT framework.

7.6 Differential Cross Sections

In any experiment, the distributions of measured observables differ from the corresponding "true" physics quantities due to limitations of physical detectors and CMS is no different in this regard. Hence, the measurement of a differential fiducial cross section entails finding the most likely true distribution given observed yields in multiple bins, subtracting the simulated background yields, and correcting these background

subtracted data distributions back to the particle level using a procedure called unfolding which takes into account detector effects such as efficiency and resolution understood through simulation. Unlike the inclusive cross section, finite detector resolution leads to "smearing" effects that cause events to migrate across bins, in addition to the same inefficiencies. The mean detector-level distribution $\vec{\delta}$ is related to the true distribution $\vec{\theta}$ by a response matrix $\mathbf{R}$:

$$\vec{\delta} = \mathbf{R}\vec{\theta}. \tag{7.11}$$

The observed distribution in data $\vec{d}$ is sampled from the Poisson distribution with mean $\vec{\delta}$ independently in each bin. CMS simulation software is sufficiently sophisticated to give a good estimate of R, reproducing the real detector's resolution and smearing effects at the level of a few per cent or better for all distributions of interest. However, a proper phase space at generator level is determined before building this response matrix and the fiducial requirements outlined in Table 7.5 for $\mathrm{ZZ} \to 4\ell$ are used to apply selection cuts to generator level samples.

If $\mathbf{R}$ is square and invertible, the maximum likelihood estimate (MLE) of the true distribution, $\hat{\vec{\theta}}$, is given by

$$\hat{\vec{\theta}} = \mathbf{R}^{-1}\vec{d}. \tag{7.12}$$

The variables used for differential cross sections in this analysis are in general well-measured and well-conditioned so bin-to-bin fluctuations are small and the response matrices are diagonal and invertible using the technique described below.

7.6.1 Unfolding

In order to obtain differential cross sections and allow CMS data to be compared to arbitrary theoretical models, the data are "unfolded" to remove detector resolution, efficiency, and acceptance effects. For each distribution to be unfolded, a response

matrix is obtained using simulated signal samples. The matrix maps distributions found after full detector simulation, reconstruction, and selection, to the generated distributions they originate from. The response matrix is then inverted, and the inverse is used to extrapolate true physical distributions from observed data.

The data are corrected for background contributions and unfolded for detector effects using a matrix inversion method without regularization as described in Ref. [159] and compared with the theoretical predictions from POWHEG +MCFM, and MADGRAPH5_aMC@NLO+MCFM.

The true-level distributions used for unfolding use generator-level leptons "dressed" by adding the momenta of generator-level photons within $\Delta R\,(\ell, \gamma) < 0.1$.

The response matrices for various quantities are shown in Appendix A.

7.6.2 Uncertainties

The largest uncertainties in the unfolded distributions arise from the unfolding procedure itself, which can inflate statistical uncertainties present in the detector-level distributions. Some example correlation matrices which give the full uncertainty—considered the statistical uncertainty of the unfolded distribution—are shown in Appendix A.

Most systematic uncertainties are propagated through unfolding by recomputing the response matrix with the training sample shifted or reweighted to reflect a 1σ shift in the quantity in question. The uncertainty related to that quantity is taken to be the resulting shape difference in the final unfolded distribution. Systematic uncertainties are generally negligible compared to the statistical uncertainty propagated through the unfolding procedure.

Several closure tests were performed to ensure the reliability of the unfolding procedure and a summmary is provided here. In order to demonstrate how much

unfolding smoothens the original distribution, the results of unfolding without (results in the thesis) and with (expected to smoothen) regularization were compared. The technique used for regularization is an iterative frequentist method developed in high energy physics by D'Agostini [160] and independently in other fields [161–164], as implemented in RooUnfold [159]. Since distributions of interest have response matrices that are well-conditioned and diagonal, the method is iterated to convergence within eight iterations. The unfolded distributions from the two methods showed no significant difference and hence the effect of smoothing can be neglected.

Furthermore, toy samples and existing MC samples were used to perform even more closure tests. In the toy method, the response matrix is used to generate random pseudoevents with statistics corresponding to those in data. Then, we have data" and true" distributions which were used to unfold data to get **Nunfolded** and compare it with **Ntrue**. For each measurement, $\frac{Nunfolded-Ntrue}{\sigma}$ is calculated per bin for each differential distribution. Following this procedure, 100 such measurements are geneated, the results are fit with the Gaussian distribution and the mean and standard deviation of the pulls in each bin is shown in Figs. 7.5– 7.7. Similarly for the MC method, there are 3 lepton channels for each of 3 years of samples so those were used to produce pseudodata, once using POWHEG as data" and unfolding it with MadGraph5_aMC@NLO and then using MadGraph5_aMC@NLO as data and unfolding it with POWHEG. This results in 18 measurements (3 years $\times$3 channels $\times$2 sets) which are fit with the Gaussian as mentioned above and results presented below alongside the toy results in Figs. 7.5– 7.7. Overall, these studies demonstrate that unfolding works as expected and the mean of each pull is centered at 0 with only small deviations and hence establishes confidence in the unfolding procedure.

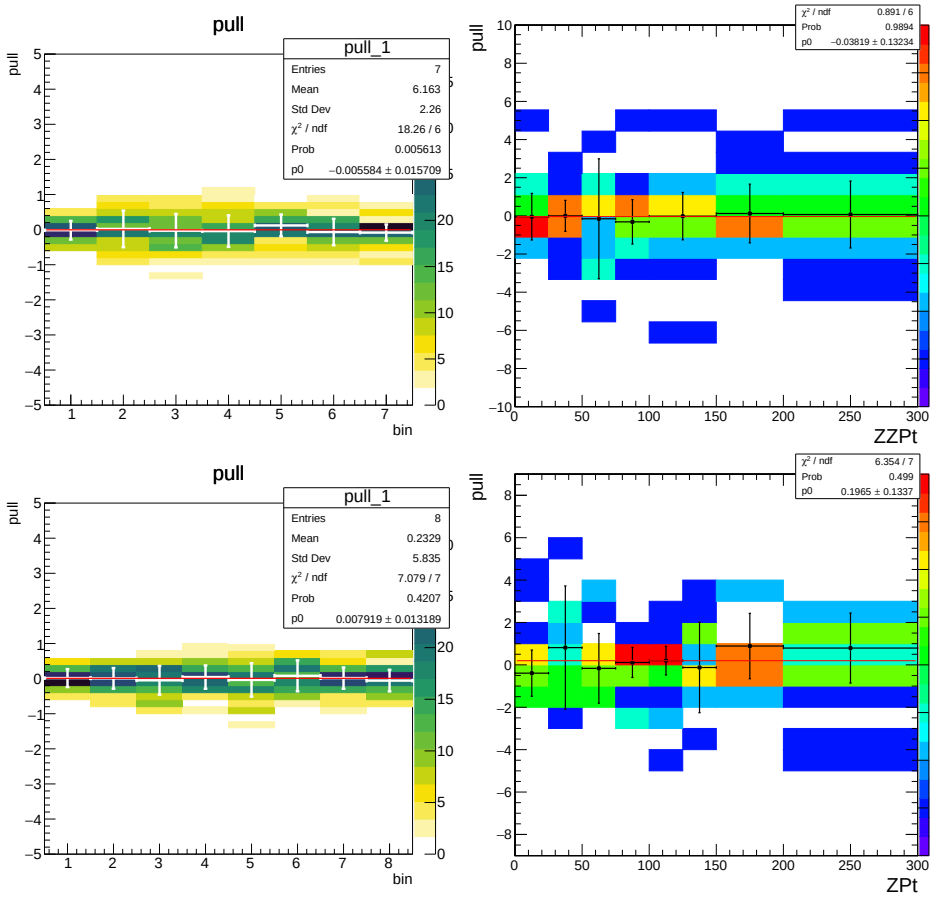

Figure 7.5: From the toy (left) plots, it can be concluded that unfolding works as expected. All values are centered at 0. The uncertainties are slightly overestimated which means that the uncertainty in data unfolding is quite conservative, but since the uncertainties are small it is acceptable. From the plots (right), it is observed that using MadGraph or Powheg does not introduce any bias as measurements are centered. The uncertainties look as expected.

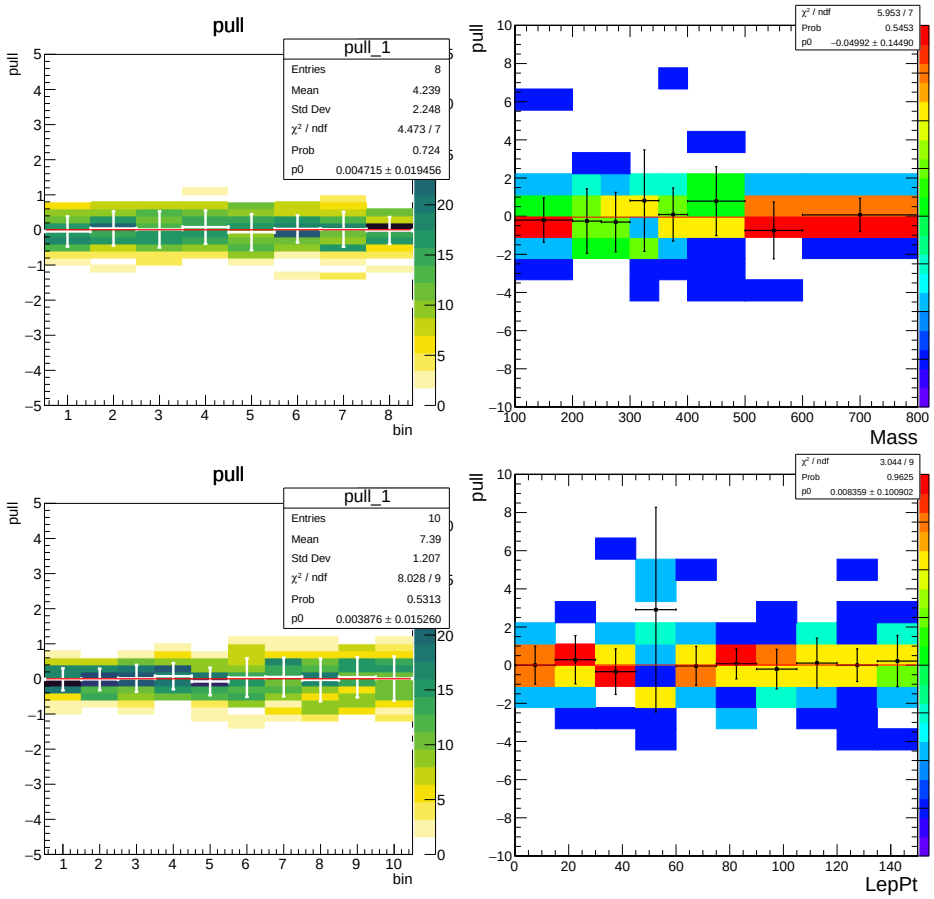

Figure 7.6: Same conclusions as in Fig. 7.5. The fit sometimes does not work well (bin 4 of bottom-right plot) but the mean calculated by hand is close to 0 and errors are similar to other bins.

7.7 Anomalous Triple Gauge Coupling Searches

As discussed previously in section 2.5.2, the new physics represented by aTGCs would generally manifest as an increase in events with high invariant mass in the four-lepton final state so it is natural to use the shape of the $m_{4\ell}$ distribution for the search. In the aTGC search reported in this thesis,doubly on-shell ZZ selection is used.

Monte Carlo samples with nonzero aTGCs are generated at grids of points in the f_4^Z-f_4^γ and f_5^Z-f_5^γ for all three years as described in section 5.2.4. Figure 7.8 presents the distribution of the four-lepton reconstructed mass for the combined 4e, 2e2μ, and

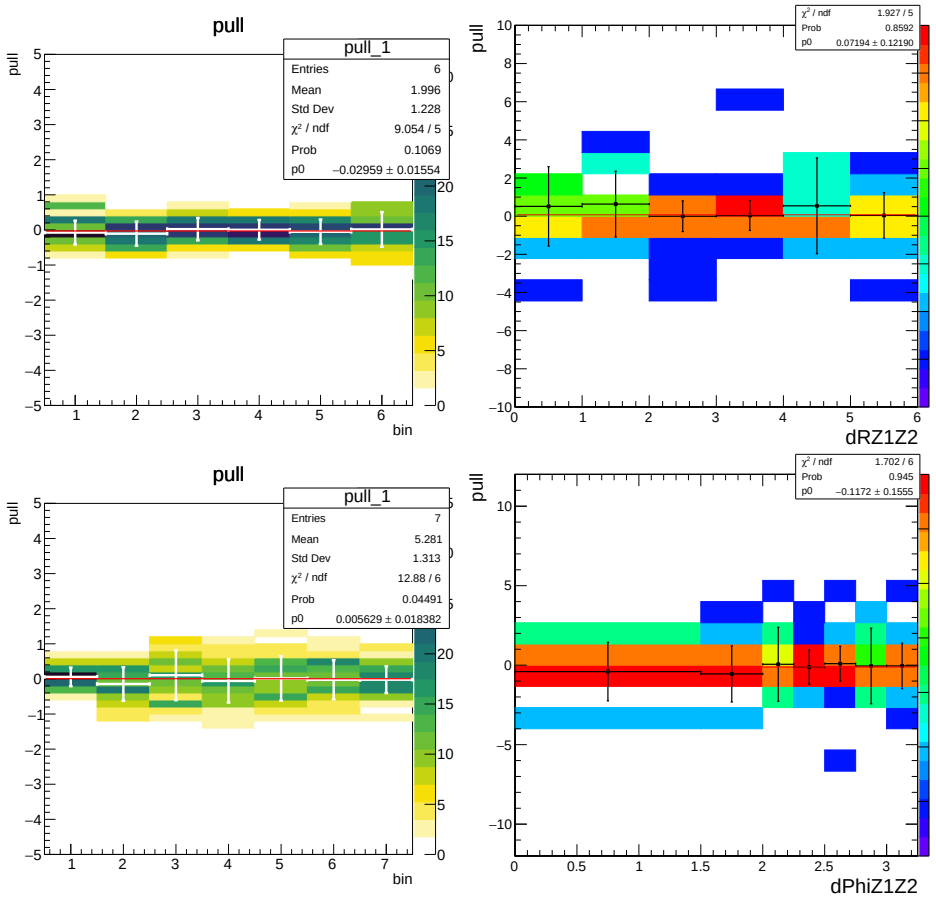

Figure 7.7: Similar conclusions can be drawn as discussed in the caption of Fig. 7.5 .

4μ channels, for the SM and an example of nonzero aTGC value with f_4^γ=0, and f_4^Z=0.0015. Limits on aTGCs are derived from fits to this distribution. The shaded histograms represent the SM predictions and the dashed curve shows the SHERPA prediction. The SHERPA SM predictions are normalized to the POWHEG predictions; after normalization both predictions agree well for masses below 1000 GeV. The presence of aTGC contribution increases the expected event yields at masses above 1300 GeV.

The invariant mass distributions are interpolated from those obtained from the SHERPA simulation for different values of the anomalous couplings in the range be-

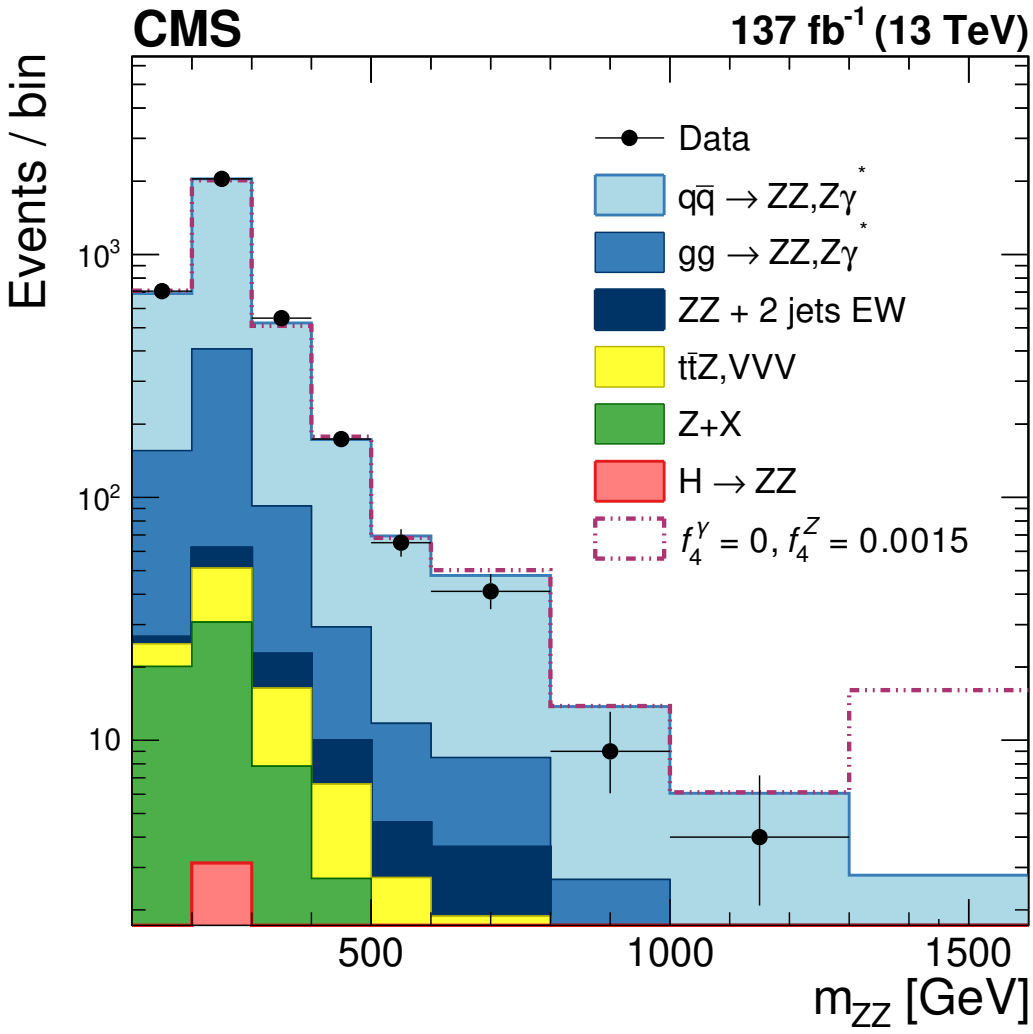

Figure 7.8: Distribution of the reconstructed ZZ mass for the combined 4e, 2e2μ, and 4μ channels. Points represent the data with error bars showing the statistical uncertainties, the shaded histograms represent the SM prediction including signal and irreducible background from simulation, and the reducible background estimate from data. Dashed histogram represents an example of the aTGC signal. The last bin includes contribution from all events with mass above 1300 GeV.

tween 0 and 0.03. For each distribution, only one or two couplings are varied while all others are set to zero, thus creating a grid of points in the $(f_4^{\mathrm{Z}}, f_4^{\gamma})$ and $(f_5^{\mathrm{Z}}, f_5^{\gamma})$ parameter planes and the corresponding invariant mass distributions. In each m_{ZZ} bin, expected signal values are interpolated between the two-dimensional grid points using a second-order polynomial (eqn. 7.13), since the cross section for the signal depends quadratically on the coupling parameters.

$$y\left(f^{\mathrm{Z}}, f^{\gamma}\right) = x_0 + x_1 f^{\mathrm{Z}} + x_2 f^{\gamma} + x_3 f^{\mathrm{Z}} f^{\gamma} + x_4 \left(f^{\mathrm{Z}}\right)^2 + x_5 \left(f^{\gamma}\right)^2 \tag{7.13}$$

where $y\left(f^{\mathrm{Z}}, f^{\gamma}\right)$ is the yield in the bin, f^{V} can be f_4^{Z} and f_4^{γ} or f_5^{Z} and f_5^{γ}, and x_i are the parameters to be fit.

A simultaneous fit to the values of aTGCs is performed for all lepton channels, see Ref. [165] for details. A profile likelihood method [166], Wald Gaussian approximation, and Wilks theorem [167] are used to derive one- (1D) and two-dimensional limits at 68 and 95% confidence levels (CL) on each of the aTGC parameters and combination of two of them, while all other parameters are set to their SM values. Systematic uncertainties are included by varying the number of expected signal and background events within their uncertainties. No form factor [30] is used when deriving the limits so that the results do not depend on any assumed energy scale characterizing new physics.

Chapter 8

Results

The analysis strategy described in Chapter 7 is applied to the cumulative dataset collected in 2016-2018 (described in Section 4.2.8). The results presented in this thesis have been made public in a journal article and a Physics Analysis Summary document released by the CMS collaboration. The first CMS measurement of the ZZ inclusive cross section at 13 TeV used roughly half the 2015 dataset ($1.34\,\text{fb}^{-1}$) and was made public in Ref. [168] in December 2015 as one of the first measurements done on 13 TeV collision data. That analysis was expanded to use the whole $2.6\,\text{fb}^{-1}$ collected in 2015, and to include the $\text{Z} \to 4\ell$ branching fraction measurement, as reported in Ref. [52], submitted in July 2016 and published the following December. With the full 2016 dataset, the ZZ cross section and $\text{Z} \to 4\ell$ branching ratio were measured again to greater precision in Ref. [169], which also included differential cross section measurements and aTGC limits, made public in March 2017. A new paper including these measurements [51] also includes a combination of the 2015 and 2016 inclusive cross section measurements. With the full Run 2 data set, the ZZ production cross section was measured [54] and published in March 2019 as the most precise diboson cross section measurement at the time. Those results were expanded

to include differential cross section measurements and the most stringent limits to date on anomalous ZZZ and ZZγ triple gauge couplings which improved the previous strictest results from CMS by ≈30-40%. The journal article for these is currently in review and expected to be published soon. In the following sections, these latest results are presented which significantly exceed the accuracy of the results that came before [51].

8.1 ZZ Production Inclusive Cross Section

The p_{T} and η distributions for individual leptons are shown in Fig. 8.1. Both distributions contain four leptons per event. The invariant mass of the ZZ system, the individual mass of reconstructed Z boson candidates in the ZZ events, and their corresponding p_{T} distributions are shown in Fig. 8.2. The last bins in m_{ZZ} and all p_{T} distributions contain events from the overflow. The m_{Z} and Z p_{T} distributions contain two Z candidates for each event. These distributions are shown for data and simulated events to demonstrate comparisons with SM expectations. The signal expectations include contributions from nonresonant ZZ production shown separately for $\mathrm{q\bar{q}} \to \mathrm{ZZ}$ and $\mathrm{gg} \to \mathrm{ZZ}$ processes in all figures and combined as "Signal" in Table 8.1.

The EW ZZ and the SM Higgs boson production contribute together less than 1% of the total number of ZZ events. They are combined with the irreducible background, which amounts to 1–1.5% of the total ZZ yield, and reducible background in Table 8.1. The total background in this analysis is ≈ 4%. The estimated yields agree well with the measured ones. The individual distributions are well described, except the m_{ZZ} distribution at high values of invariant masses and the $p_{\mathrm{T}}^{\mathrm{Z}}$ distribution at high values of p_{T}. This is a place where the EW corrections may become important and will be discussed later in Section 8.3.

Process	eeee	ee$\mu\mu$	$\mu\mu\mu\mu$	$2\ell 2\ell'$
	2016			
Background	8.3 ± 0.6 ± 1.8	15.6 ± 0.8 ± 1.9	8.1 ± 0.5 ± 0.9	32.1 ± 1.1 ± 4.1
Signal	167.0 ± 1.0 ± 10.0	432.0 ± 1.6 ± 17.3	272.0 ± 1.3 ± 8.2	870.9 ± 2.3 ± 31.1
Total expected	175.4 ± 1.2 ± 10.4	447.5 ± 1.8 ± 17.7	280.0 ± 1.4 ± 8.4	903.0 ± 2.6 ± 32.0
Data	176	478	296	950
	2017			
Background	8.2 ± 0.4 ± 1.5	16.8 ± 0.8 ± 1.8	10.9 ± 0.7 ± 1.6	35.8 ± 1.2 ± 4.5
Signal	199.7 ± 0.3 ± 12.0	509.7 ± 0.6 ± 20.4	320.7 ± 0.5 ± 9.6	1030.0 ± 0.8 ± 36.9
Total expected	207.9 ± 0.6 ± 12.4	526.5 ± 1.0 ± 20.9	331.5 ± 0.8 ± 9.9	1065.9 ± 1.4 ± 38.0
Data	193	540	328	1061
	2018			
Background	12.9 ± 0.6 ± 2.5	30.7 ± 1.1 ± 4.2	20.2 ± 1.1 ± 4.0	63.8 ± 1.7 ± 9.7
Signal	303.2 ± 0.4 ± 18.2	754.2 ± 0.8 ± 30.1	463.8 ± 0.6 ± 13.9	1521.3 ± 1.0 ± 54.7
Total expected	316.2 ± 0.8 ± 18.7	784.9 ± 1.4 ± 31.1	484.0 ± 1.3 ± 14.8	1585.0 ± 2.0 ± 56.6
Data	309	797	480	1586

Table 8.1: Observed and expected prefit yields of ZZ events, and estimated yields of background events, shown for each final state and combined. The statistical (first) and systematic (second) uncertainties are presented.

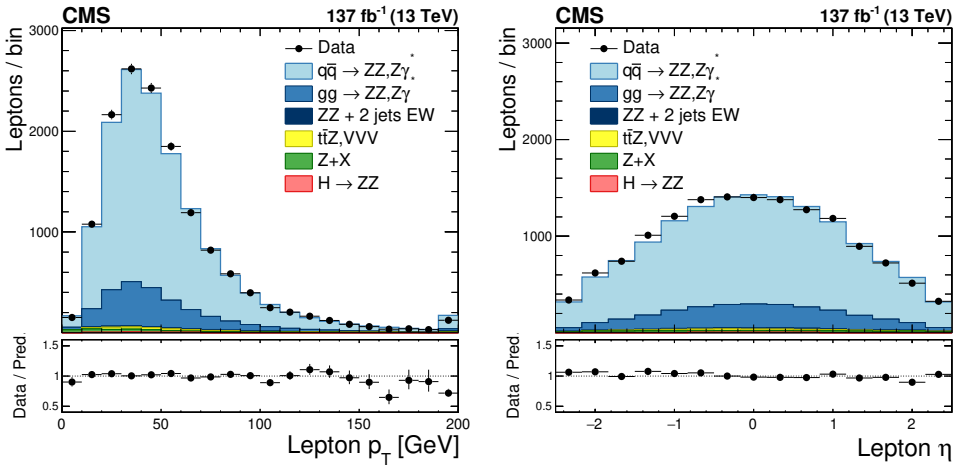

Figure 8.1: Distributions of (left) transverse momentum and (right) pseudorapidity for individual leptons. Points represent the data with error bars showing the statistical uncertainties, histograms the expected SM predictions and reducible background estimated from data.

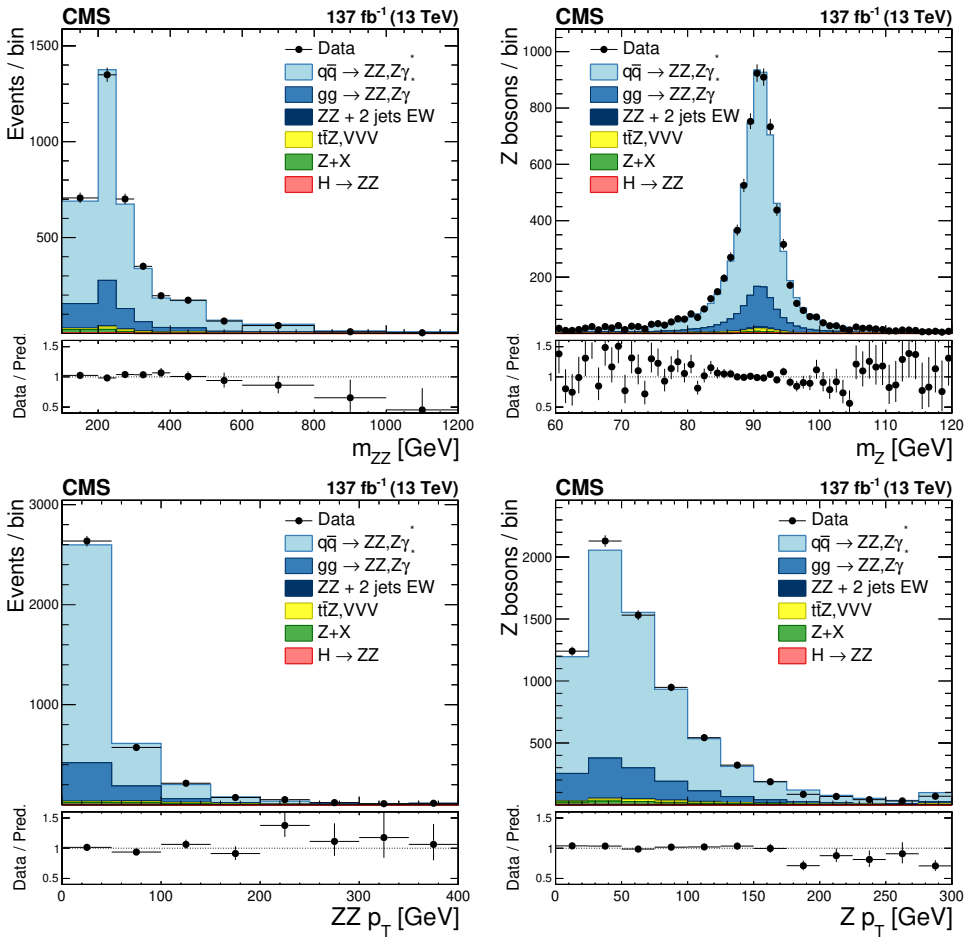

Figure 8.2: Distributions of (upper left) m_{ZZ} for ZZ events with $60 < m_{\mathrm{Z_1,Z_2}} < 120\,\mathrm{GeV}$; (upper right) mass of selected Z boson candidates; (lower left) transverse momentum of the ZZ system; (lower right) transverse momentum of individual Z boson candidates. Points represent the data with error bars showing the statistical uncertainties, histograms the expected SM predictions and reducible background estimated from data.

The measured yields are used to evaluate the ZZ production cross section in the fiducial phase space. The signal acceptance is evaluated from simulation and corrected for each individual lepton flavor in bins of p_{T} and η using factors obtained with the tag-and-probe technique. To include all final states in the cross section calculation, a simultaneous fit to the number of observed events in all decay channels is performed. The likelihood is composed as a combination of individual channel likelihoods for the signal and background hypotheses with the statistical and systematic uncertainties treated as scaling nuisance parameters. The combination of various data-taking periods is performed treating the theoretical uncertainties as fully correlated among various periods, whereas the experimental uncertainties are either correlated or uncorrelated, depending on their origin.

Year	Fiducial cross section, fb
2016	$41.6 \pm 1.4\,(\mathrm{stat}) \pm 1.3\,(\mathrm{syst})^{+1.1}_{-1.0}\,(\mathrm{lumi})$
2017	$39.2 \pm 1.2\,(\mathrm{stat})^{+1.3}_{-1.2}\,(\mathrm{syst})^{+1.0}_{-0.9}\,(\mathrm{lumi})$
2018	$39.3 \pm 1.0\,(\mathrm{stat})^{+1.3}_{-1.1}\,(\mathrm{syst}) \pm 1.0\,(\mathrm{lumi})$
Combined	$40.1 \pm 0.7\,(\mathrm{stat}) \pm 1.1\,(\mathrm{syst}) \pm 0.7\,(\mathrm{lumi})$

Table 8.2: Measured fiducial cross section for each data sample and combined. The first uncertainty is statistical, the second is experimental systematic, and the third is associated with the integrated luminosity.

Year	Total cross section, pb
2016	$17.9 \pm 0.6\,(\mathrm{stat})^{+0.6}_{-0.5}\,(\mathrm{syst}) \pm 0.4\,(\mathrm{theo})^{+0.5}_{-0.4}\,(\mathrm{lumi})$
2017	$16.8 \pm 0.5\,(\mathrm{stat})^{+0.6}_{-0.5}\,(\mathrm{syst}) \pm 0.4\,(\mathrm{theo}) \pm 0.4\,(\mathrm{lumi})$
2018	$16.9 \pm 0.4\,(\mathrm{stat}) \pm 0.5\,(\mathrm{syst}) \pm 0.4\,(\mathrm{theo}) \pm 0.4\,(\mathrm{lumi})$
Combined	$17.2 \pm 0.3\,(\mathrm{stat}) \pm 0.5\,(\mathrm{syst}) \pm 0.4\,(\mathrm{theo}) \pm 0.3\,(\mathrm{lumi})$

Table 8.3: Measured total $\sigma(\mathrm{pp} \to \mathrm{ZZ})$ cross section for each data sample, and combined. The first uncertainty is statistical, the second is experimental systematic, the third is theoretical systematic. The fourth uncertainty is associated with the integrated luminosity.

The measured ZZ fiducial cross section presented in Table 8.2 can be compared to $39.3^{+0.8}_{-0.7} \pm 0.6\,\mathrm{fb}$ calculated with POWHEG+MCFM using the same settings as the

simulated samples with K factors applied. The first uncertainty corresponds to the factorization and renormalization scales and the second to PDF, as described above. The POWHEG calculations used dynamic factorization and renormalization scales $\mu_{\mathrm{F}} = \mu_{\mathrm{R}} = m_{2\ell 2\ell'}$, whereas the contribution from MCFM is computed with dynamic scales $\mu_{\mathrm{F}} = \mu_{\mathrm{R}} = 0.5 m_{2\ell 2\ell'}$. It can also be compared to the prediction from MATRIX v2.0.0_beta1 of $38.0^{+1.1}_{-1.0}$. The uncertainty in the MATRIX prediction includes only the uncertainty due to the variation of μ_{F} and μ_{R}.

The total ZZ production cross section for both dileptons produced in the mass range 60–120 GeV and $m_{\ell^+\ell^-} > 4$ GeV is presented in Table 8.3. The measured total cross section can be compared to the theoretical value of $16.9^{+0.6}_{-0.5} \pm 0.2$ pb, calculated from POWHEG+MCFM with the same settings that is used for $\sigma_{\mathrm{fid}}(\mathrm{pp} \to \mathrm{ZZ} \to 2\ell 2\ell')$. It can also be compared to $16.5^{+0.6}_{-0.5}$ pb, calculated with MATRIX v2.0.0_beta1, or $15.0^{+0.7}_{-0.6} \pm 0.2$ pb, calculated with MCFM at NLO in QCD with additional contributions from LO gg $\to$ ZZ diagrams and with the NLO NNPDF3.0 PDF set and fixed factorization and renormalization scales set to $\mu_{\mathrm{F}} = \mu_{\mathrm{R}} = m_{\mathrm{Z}}$.

The total ZZ cross section is shown in Fig. 8.3 as a function of the pp center-of-mass energy. Results from CMS [46, 47] and ATLAS [49, 53, 170] are compared to predictions from MATRIX v2.0.0_beta1 and MCFM. The uncertainties are statistical (inner bars) and statistical and systematic combined, as obtained from the fit (outer bars). The band around the MATRIX predictions reflects scale uncertainties, while the band around the MCFM predictions reflects both scale and PDF uncertainties.

These are the first such distributions published at $\sqrt{s} = 13$ TeV with the largest dataset collected at the LHC, and statistical uncertainties are smaller than those published at any energy before, allowing theorists to make more detailed comparisons to their models.

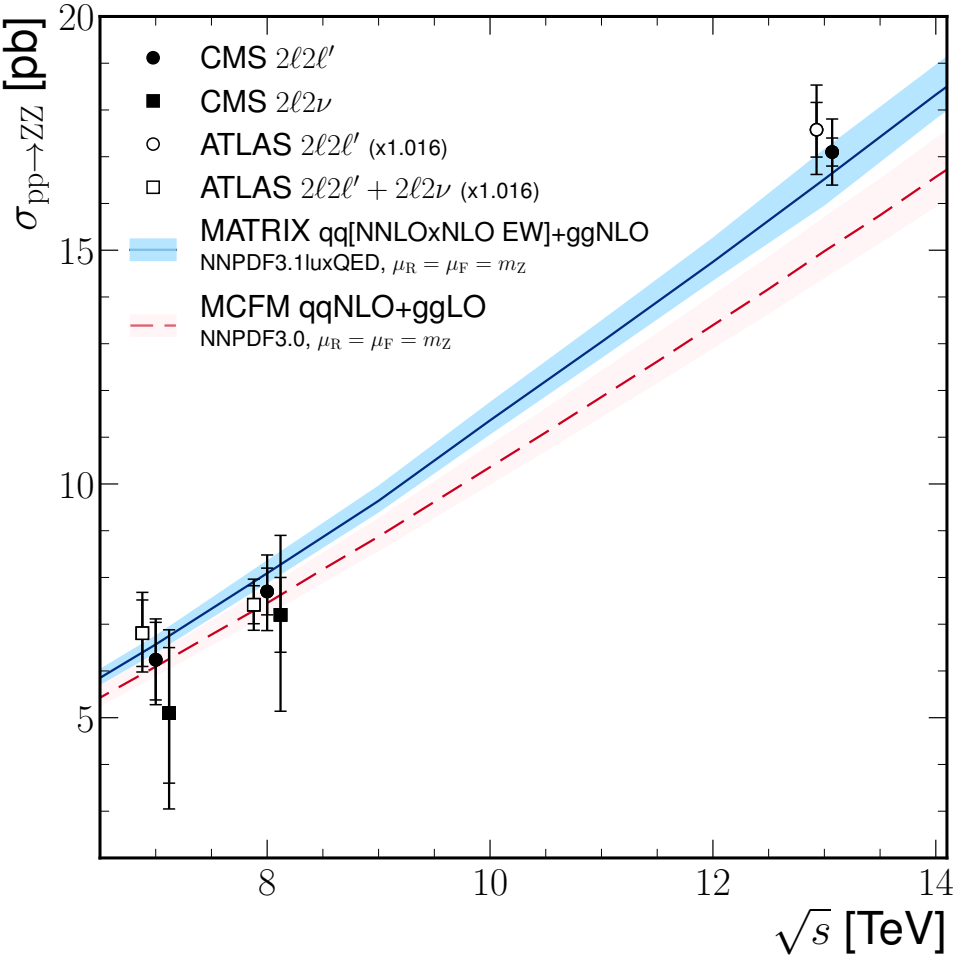

Figure 8.3: The total ZZ cross section as a function of the proton-proton center-of-mass energy. Results from the CMS [46, 47] and ATLAS [49, 53, 170] experiments are compared to predictions from MATRIX at NNLO in QCD and NLO in EW, and MCFM at NLO in QCD. The MCFM prediction also includes gluon-gluon initiated production at LO in QCD. The predictions use NNPDF31_nnlo_as_0118_luxqed and NNPDF3.0 PDF sets, respectively, and fixed factorization and renormalization scales $\mu_F = \mu_R = m_Z$. Details of the calculations and uncertainties are given in the text. The ATLAS measurements were performed with a Z boson mass window of 66–116 GeV, instead of 60–120 GeV used by CMS, and are corrected for the resulting 1.6% difference in acceptance. Measurements at the same center-of-mass energy are shifted slightly along the horizontal axis for clarity.

8.2 Differential Cross Sections

The differential distributions normalized to the inclusive fiducial cross section (such that integral of each is unity), are presented in Figs. 8.4–8.6 for the combination of the 4e, 2e2μ, and 4μ decay channels using the whole data sample. The fiducial cross section definition includes p_{T}^{ℓ} and $\left|\eta^{\ell}\right|$ selections on each lepton, and the 60–120 GeV mass requirement, as described in Section 4. Figure 8.4 shows the differential cross sections in bins of p_{T} for: (left) all leptons in the event, (right) both Z bosons in the event, and in Fig. 8.5 (left) for the p_{T} of the ZZ system. Figure 8.5 (right) shows the normalized $\mathrm{d}\sigma/\mathrm{d}m_{\mathrm{ZZ}}$ distribution. All $p_{\mathrm{T}}$and m_{ZZ} distributions include overflow in the last bin. Figure 8.6 shows the angular correlations between Z bosons. The data are corrected for background contributions and unfolded for detector effects using a matrix inversion method without regularization as described in Ref. [159], and compared with the theoretical predictions from POWHEG+MCFM, MadGraph-5_aMC@NLO+MCFM and MATRIX The distributions include both Z boson candidates or all four leptons, where applicable, and are normalized to the numbers of objects in the event and to the fiducial cross section. The bottom part of each plot shows the ratio of the measured to the predicted values. The bin sizes are chosen according to the resolution of the relevant variables, trying also to keep the statistical uncertainties at a similar level for all the bins.

The distributions predicted by POWHEG+MCFM and MadGraph5_aMC@-NLO+MCFM agree well with data, except for m_{ZZ}. This distribution shows a small overestimate in the cross section at high invariant masses. The MATRIX predictions describe this region better, which can be explained by presence of the EW corrections in the MATRIX calculations. On the other hand, the MATRIX predictions show some deviation from the measurements as a function of $p_{\mathrm{T}}^{\mathrm{ZZ}}$ and for the azimuthal

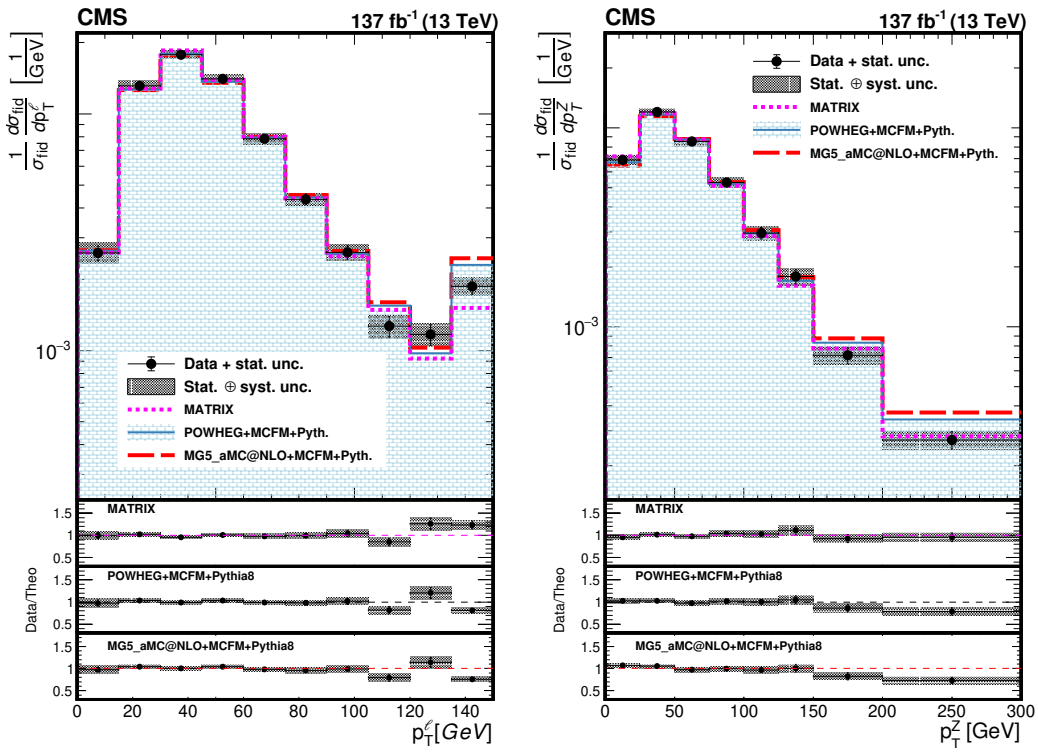

Figure 8.4: Differential cross sections normalized to the fiducial cross section for the combined 4e, 2e2μ, and 4μ decay channels as a function of p_{T} for (left) all leptons, (right) all Z bosons in the event. The points represent the unfolded data with error bars showing the statistical uncertainties, the shaded histogram the POWHEG+MCFM ZZ predictions, and the dashed curves correspond to the results of the MATRIX and MadGraph5_aMC@NLO+MCFM calculations. The three lower panels represent the ratio of the measured cross section to the expected distributions from MATRIX, POWHEG+MCFM and MadGraph5_aMC@NLO+MCFM. The shaded areas in all the panels represent the full uncertainties calculated as the quadratic sum of the statistical and systematic uncertainties, whereas the crosses represent only the statistical uncertainties.

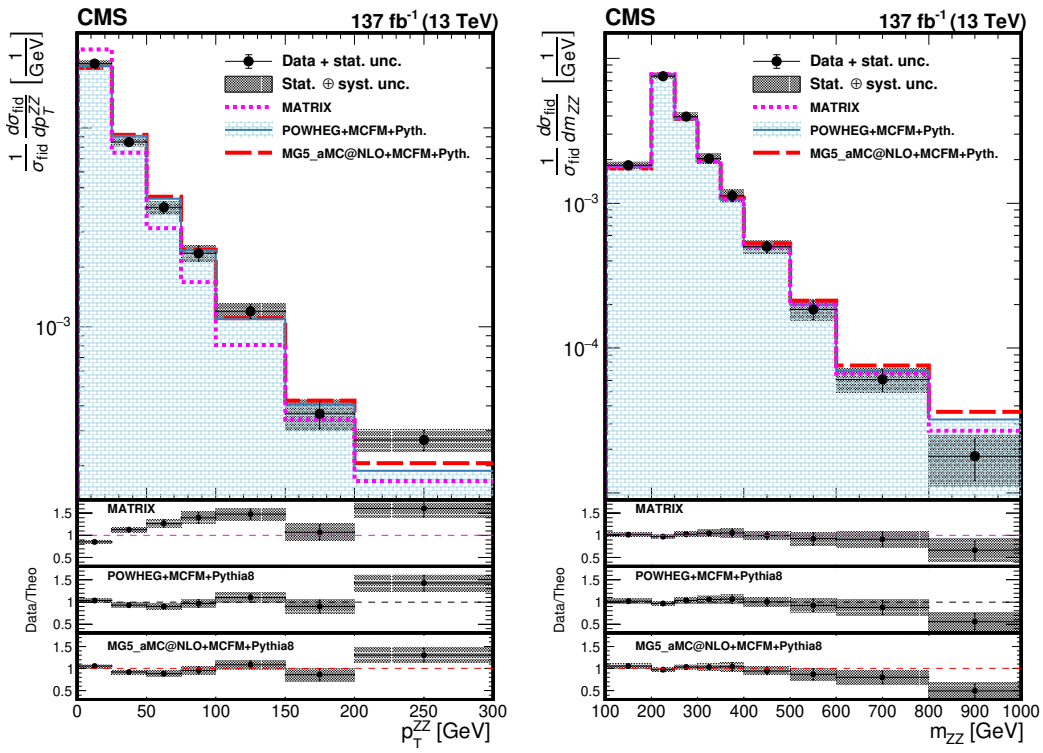

Figure 8.5: Differential cross sections normalized to the fiducial cross section for the combined 4e, 2e2μ, and 4μ decay channels as a function of (left) p_{T} of the ZZ system, (right) the invariant mass of the ZZ system. The points represent the unfolded data with error bars showing the statistical uncertainties, shaded histogram the POWHEG+MCFM ZZ predictions, and the dashed curves correspond to the results of the MATRIX and MadGraph5_aMC@NLO+MCFM calculations. The three lower panels represent the ratio of the measured cross section to the expected distributions from MATRIX, POWHEG+MCFM and MadGraph5_aMC@NLO+MCFM. The shaded areas in all the panels represent the full uncertainties calculated as the quadratic sum of the statistical and systematic uncertainties, whereas the crosses represent only the statistical uncertainties.

separation between the two Z bosons, which is not observed for POWHEG+MCFM and MadGraph5_aMC@NLO+MCFM predictions.

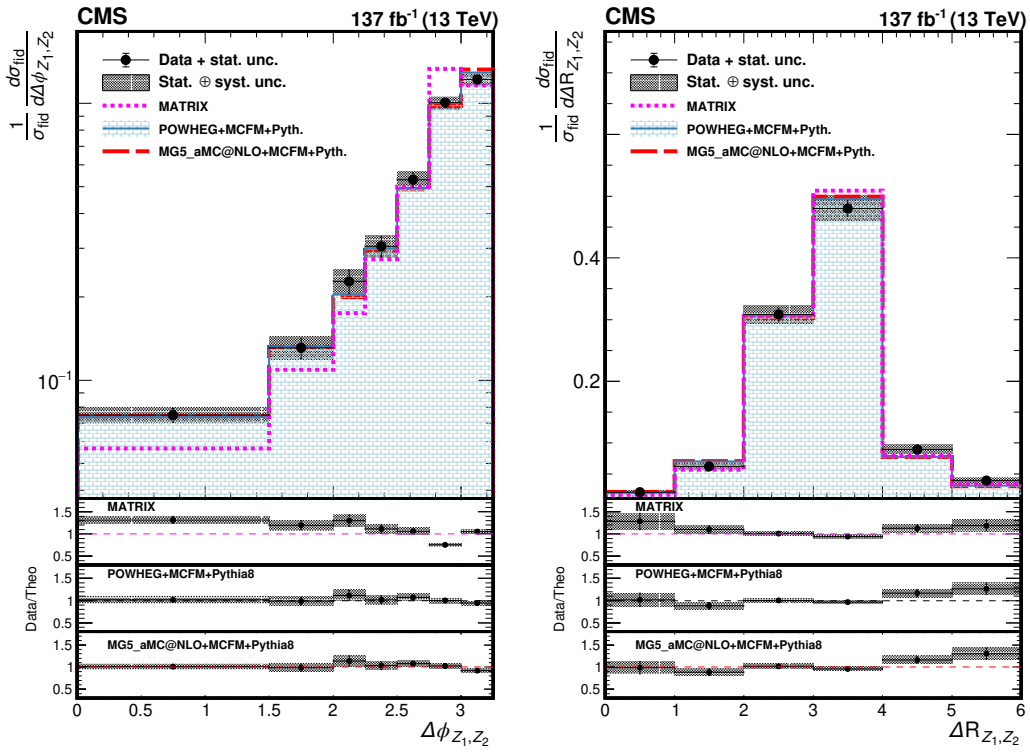

Figure 8.6: Differential cross sections normalized to the fiducial cross section for the combined 4e, 2e2μ, and 4μ decay channels as a function of the azimuthal and ΔR separation of the two Z bosons. The points represent the unfolded data with error bars showing the statistical uncertainties, the shaded histogram the POWHEG+MCFM ZZ predictions, and the dashed curves correspond to the results of the MATRIX and MadGraph5_aMC@NLO+MCFM calculations. The three lower panels represent the ratio of the measured cross section to the expected distributions from MATRIX, POWHEG+MCFM and MadGraph5_aMC@NLO+MCFM. The shaded areas in all the panels represent the full uncertainties calculated as the quadratic sum of the statistical and systematic uncertainties, whereas the crosses represent only the statistical uncertainties.

8.3 Limits on anomalous triple gauge couplings

Following the procedure described in section 7.7, constraints on anomalous triple gauge couplings are derived and displayed in in Fig. 8.7. The curves indicate 68 and 95% CL contours; the dots indicate where the likelihoods reach their maximum. Coupling values outside the contours are excluded at the corresponding CL. The crosses in the middle represent the observed 1D limits that are summarized in Table 8.4. The sensitivity is dominated by the statistical uncertainties.

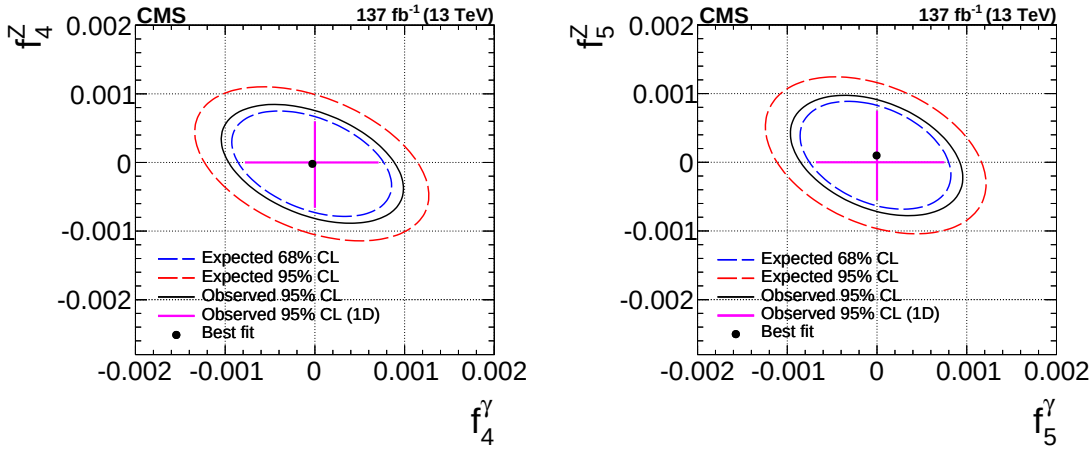

Figure 8.7: Two-dimensional observed (solid) and expected (dashed) contours exclusion limits at 95% CL, and at 68 and 95% CL, respectively, on the ZZZ and ZZγ aTGCs. The plots show the exclusion contours in the $(f^{Z}_{4(5)}, f^{\gamma}_{4(5)})$ parameter planes. Dots show where the likelihoods reach their maximum. The coupling values outside the contours are excluded at the corresponding confidence level. The crosses in the middle represent the observed 1D limits. No form factor is used.

Complete one-loop EW corrections to massive vector boson pair production [172, 173] were applied as a cross-check. The EW corrections to the ZZ production cause the ZZ mass spectrum to fall more rapidly at large masses. In addition, the overall cross section decreases by about 4%. The effect of NLO EW corrections is estimated by reweighting the SM SHERPA sample as a function of m_{ZZ} using weights derived from the calculations described in Ref. [172]. This reweighting improves the expected

Table 8.4: Expected and observed one-dimensional 95% CL limits on aTGC parameters. The corresponding constrains on EFT parameters are estimated using the transformation from Ref. [171].

	Expected 95% CL	Observed 95% CL
aTGC parameter	$\times 10^{-4}$	$\times 10^{-4}$
f_4^Z	-8.8 ; 8.3	-6.6 ; 6.0
f_5^Z	-8.0 ; 9.9	-5.5 ; 7.5
f_4^γ	-9.9 ; 9.5	-7.8 ; 7.1
f_5^γ	-9.2 ; 9.8	-6.8 ; 7.5
EFT parameter	TeV^{-4}	TeV^{-4}
$C_{\tilde{\mathrm{B}}\mathrm{W}}/\Lambda^4$	-3.1 ; 3.3	-2.3 ; 2.5
$C_{\mathrm{WW}}/\Lambda^4$	-1.7 ; 1.6	-1.4 ; 1.2
$C_{\mathrm{BW}}/\Lambda^4$	-1.8 ; 1.9	-1.4 ; 1.3
$C_{\mathrm{BB}}/\Lambda^4$	-1.6 ; 1.6	-1.2 ; 1.2

limits by about 4–6%.

These results can be also expressed in terms of EFT parameters. The numerical relations between aTCGs and EFT parameters are given in Ref. [171]. The expected and measured limits in terms of EFT are presented in Table 8.4.

Chapter 9

Conclusions

9.1 Summary

A precise measurement of both inclusive and differential ZZ cross sections is presented. Four-lepton final states from ZZ production in proton-proton collisions at $\sqrt{s} = 13\,\text{TeV}$ with the CMS detector at the CERN LHC have been studied. The data sample corresponds to an integrated luminosity of $137\,\text{fb}^{-1}$, collected during 2016–2018. The measured $\text{pp} \to \text{ZZ}$ total cross section is $\sigma_{\text{tot}}(\text{pp} \to \text{ZZ}) = 17.2 \pm 0.3\,(\text{stat}) \pm 0.5\,(\text{syst}) \pm 0.4\,(\text{theo}) \pm 0.3\,(\text{lumi})\,\text{pb}$, where the Z boson masses are in the range $60 < m_{\text{Z}} < 120\,\text{GeV}$. The results agree with the SM predictions, discussed in Section 8.1. Differential cross sections were also measured as functions of a number of important observables including fully leptonic kinematic variables. The differential cross sections also agree well with the SM predictions. Finally a search was performed for anomalous triple gauge couplings using the invariant mass of the inclusive ZZ events to set limits on ZZZ and ZZγ coupling parameters as well as their corresponding EFT parameters. Two-dimensional limits were also set. These are the most stringent limits to date on anomalous ZZZ and ZZγ triple gauge couplings and

they improve the previous strictest results from CMS by ≈30–40%.

9.2 Outlook

The ZZ inclusive cross section measurement presented in this thesis is now systematically limited and systematics should dominate even with higher luminosities in the future even if new techniques are developed to reduce lepton efficiency and trigger uncertainties somewhat. However, diboson measurements at higher center-of-mass energies are of great interest because new physics is most likely at high $\sqrt{s}$. With high energy colliders far into the future, most progress will come from processes and decay channels that are in principle accessible now. As noted in this thesis, differential cross section measurements and searches for anomalous couplings in ZZ are dominated by statistical uncertainties and will be statistically limited for some time. The statistical power for the aTGC searches comes largely from the highest-mass bins, where the number of events observed have jumped from three above 800 GeV with 2016 data to twelve with the data analyzed in this thesis. There were no events observed 1 TeV before and now there are three. Potentially one needs about 10-20 events above 1 TeV to place stringent restrictions on BSM neutral gauge boson couplings or discover them and that can only come with the luminosities promised by the HL-LHC.

Bibliography

[1] W. Buchmüller and C. Lüdeling, *Field theory and standard model*, 2006. arXiv: hep-ph/0609174 [hep-ph].

[2] D. J. Griffiths, *Introduction to elementary particles; 2nd rev. version*, ser. Physics textbook. New York, NY: Wiley, 2008.

[3] F. Halzen and A. Martin, *Quarks & Leptons: An introductory course in modern particle physics*. New York, USA: John Wiley & Sons, 1984.

[4] O. W. Greenberg, "Spin and unitary-spin independence in a paraquark model of baryons and mesons," *Phys. Rev. Lett.*, vol. 13, p. 598, 20 1964. DOI: 10.1103/PhysRevLett.13.598. https://link.aps.org/doi/10.1103/PhysRevLett.13.598.

[5] S. L. Glashow, "Partial Symmetries of Weak Interactions," *Nucl. Phys.*, vol. 22, p. 579, 1961. DOI: 10.1016/0029-5582(61)90469-2.

[6] S. Weinberg, "A Model of Leptons," *Phys. Rev. Lett.*, vol. 19, p. 1264, 1967. DOI: 10.1103/PhysRevLett.19.1264.

[7] A. Salam, "Weak and Electromagnetic Interactions," *Conf. Proc.*, vol. C680-519, p. 367, 1968.

[8] UA1 Collaboration, "Experimental Observation of Isolated Large Transverse Energy Electrons with Associated Missing Energy at s**(1/2) = 540-GeV," *Phys. Lett. B*, vol. 122, pp. 103–116, 1983. DOI: 10.1016/0370-2693(83)91177-2.

[9] UA1 Collaboration, "Experimental Observation of Lepton Pairs of Invariant Mass Around 95 GeV/c^2 at the CERN SPS Collider," *Phys. Lett. B*, vol. 126, p. 398, 1983. DOI: 10.1016/0370-2693(83)90188-0.

[10] G. 't Hooft, "Renormalizable Lagrangians for Massive Yang-Mills Fields," *Nucl. Phys. B*, vol. 35, J. Taylor, Ed., pp. 167–188, 1971. DOI: 10.1016/0550-3213(71)90139-8.

[11] F. Englert and R. Brout, "Broken symmetry and the mass of gauge vector mesons," *Phys. Rev. Lett.*, vol. 13, p. 321, 9 Aug. 1964. DOI: 10.1103/PhysRevLett.13.321. https://link.aps.org/doi/10.1103/PhysRevLett.13.321.

[12] P. W. Higgs, "Broken symmetries and the masses of gauge bosons," *Phys. Rev. Lett.*, vol. 13, p. 508, 16 Oct. 1964. DOI: 10.1103/PhysRevLett.13.508. https://link.aps.org/doi/10.1103/PhysRevLett.13.508.

[13] G. S. Guralnik, C. R. Hagen, and T. W. B. Kibble, "Global conservation laws and massless particles," *Phys. Rev. Lett.*, vol. 13, p. 585, 20 Nov. 1964. DOI: 10.1103/PhysRevLett.13.585. https://link.aps.org/doi/10.1103/PhysRevLett.13.585.

[14] G. Aad, B. Abbott, J. Abdallah, O. Abdinov, R. Aben, M. Abolins, O. S. AbouZeid, H. Abramowicz, H. Abreu, R. Abreu, and et al., "Combined measurement of the higgs boson mass inppcollisions ats=7and 8 tev with the atlas and cms experiments," *Physical Review Letters*, vol. 114, no. 19, May 2015,

ISSN: 1079-7114. DOI: 10.1103/physrevlett.114.191803. http://dx.doi.org/10.1103/PhysRevLett.114.191803.

[15] Particle Data Group, C. Patrignani, *et al.*, "Review of Particle Physics," *Chin. Phys. C*, vol. 40, p. 100 001, 2016. DOI: 10.1088/1674-1137/40/10/100001.

[16] ATLAS Collaboration, "Observation of a new particle in the search for the Standard Model Higgs boson with the ATLAS detector at the LHC," *Phys. Lett. B*, vol. 716, p. 1, 2012. DOI: 10.1016/j.physletb.2012.08.020. arXiv: 1207.7214 [hep-ex].

[17] CMS Collaboration, "Observation of a new boson at a mass of 125 GeV with the CMS experiment at the LHC," *Phys. Lett. B*, vol. 716, p. 30, 2012. DOI: 10.1016/j.physletb.2012.08.021. arXiv: 1207.7235 [hep-ex].

[18] Super-Kamiokande Collaboration, "Evidence for oscillation of atmospheric neutrinos," *Phys. Rev. Lett.*, vol. 81, pp. 1562–1567, 1998. DOI: 10.1103/PhysRevLett.81.1562. arXiv: hep-ex/9807003 [hep-ex].

[19] SNO Collaboration, "Measurement of the rate of $\nu_e + d \rightarrow p + p + e^-$ interactions produced by ^8B solar neutrinos at the Sudbury Neutrino Observatory," *Phys. Rev. Lett.*, vol. 87, p. 071 301, 2001. DOI: 10.1103/PhysRevLett.87.071301. arXiv: nucl-ex/0106015 [nucl-ex].

[20] V. C. Rubin, "Dark matter in spiral galaxies," *Scientific American*, vol. 248, p. 96, 1983. DOI: 10.1038/scientificamerican0683-96.

[21] K. Garrett and G. Duda, "Dark Matter: A Primer," *Adv. Astron.*, vol. 2011, p. 968 283, 2011. DOI: 10.1155/2011/968283. arXiv: 1006.2483 [hep-ph].

[22] J. Ellis, "Searching for Particle Physics Beyond the Standard Model at the LHC and Elsewhere," *AIP Conf. Proc.*, vol. 1446, p. 9, 2012. DOI: 10.1063/1.4727987. arXiv: 1102.5009 [hep-ph].

[23] H. Georgi, H. R. Quinn, and S. Weinberg, "Hierarchy of Interactions in Unified Gauge Theories," *Phys. Rev. Lett.*, vol. 33, p. 451, 1974. DOI: 10.1103/PhysRevLett.33.451.

[24] E. Gildener, "Gauge Symmetry Hierarchies," *Phys. Rev. D*, vol. 14, p. 1667, 1976. DOI: 10.1103/PhysRevD.14.1667.

[25] A. J. Buras, J. R. Ellis, M. K. Gaillard, and D. V. Nanopoulos, "Aspects of the Grand Unification of Strong, Weak and Electromagnetic Interactions," *Nucl. Phys. B*, vol. 135, p. 66, 1978. DOI: 10.1016/0550-3213(78)90214-6.

[26] S. P. Martin, "A supersymmetry primer," in *Perspectives on Supersymmetry II*. DOI: 10.1142/9789814307505_0001. arXiv: hep-ph/9709356 [hep-ph].

[27] C. Autermann, "Experimental status of supersymmetry after the LHC Run-I," *Prog. Part. Nucl. Phys.*, vol. 90, p. 125, 2016. DOI: 10.1016/j.ppnp.2016.06.001. arXiv: 1609.01686 [hep-ex].

[28] K. Hagiwara, R. D. Peccei, D. Zeppenfeld, and K. Hikasa, "Probing the Weak Boson Sector in $e^+e^- \to W^+W^-$," *Nucl. Phys. B*, vol. 282, p. 253, 1987. DOI: 10.1016/0550-3213(87)90685-7.

[29] G. J. Gounaris, J. Layssac, and F. M. Renard, "New and standard physics contributions to anomalous Z and γ self-couplings," *Phys. Rev. D*, vol. 62, p. 073 013, 2000. DOI: 10.1103/PhysRevD.62.073013. arXiv: hep-ph/0003143 [hep-ph].

[30] U. Baur and D. L. Rainwater, "Probing neutral gauge boson self-interactions in ZZ production at hadron colliders," *Phys. Rev. D*, vol. 62, p. 113 011, 2000. DOI: 10.1103/PhysRevD.62.113011. arXiv: hep-ph/0008063 [hep-ph].

[31] C. Degrande, N. Greiner, W. Kilian, O. Mattelaer, H. Mebane, T. Stelzer, S. Willenbrock, and C. Zhang, "Effective field theory: A modern approach to anomalous couplings," *Annals of Physics*, vol. 335, pp. 21–32, Aug. 2013, ISSN: 0003-4916. DOI: 10.1016/j.aop.2013.04.016. http://dx.doi.org/10.1016/j.aop.2013.04.016.

[32] SLD Electroweak Group, DELPHI Collaboration, ALEPH Collaboration, SLD Collaboration, SLD Heavy Flavour Group, OPAL Collaboration, LEP Electroweak Working Group, L3 Collaboration, "Precision electroweak measurements on the Z resonance," *Phys. Rept.*, vol. 427, p. 257, 2006. DOI: 10.1016/j.physrep.2005.12.006. arXiv: hep-ex/0509008 [hep-ex].

[33] Particle Data Group Collaboration, "Review of Particle Physics (RPP)," *Phys. Rev. D*, vol. 86, p. 010 001, 2012. DOI: 10.1103/PhysRevD.86.010001.

[34] T. Binoth, G. Ossola, C. G. Papadopoulos, and R. Pittau, "NLO QCD corrections to tri-boson production," *JHEP*, vol. 06, p. 082, 2008. DOI: 10.1088/1126-6708/2008/06/082. arXiv: 0804.0350 [hep-ph].

[35] V. Hankele and D. Zeppenfeld, "QCD corrections to hadronic WWZ production with leptonic decays," *Phys. Lett. B*, vol. 661, p. 103, 2008. DOI: 10.1016/j.physletb.2008.02.014. arXiv: 0712.3544 [hep-ph].

[36] F. Cascioli, T. Gehrmann, M. Grazzini, S. Kallweit, P. Maierhöfer, A. von Manteuffel, S. Pozzorini, D. Rathlev, L. Tancredi, and E. Weihs, "ZZ production at hadron colliders in NNLO QCD," *Phys. Lett. B*, vol. 735, p. 311, 2014. DOI: 10.1016/j.physletb.2014.06.056. arXiv: 1405.2219 [hep-ph].

[37] J. M. Campbell, R. K. Ellis, and C. Williams, "Vector boson pair production at the LHC," *JHEP*, vol. 07, p. 018, 2011. DOI: 10.1007/JHEP07(2011)018. arXiv: 1105.0020 [hep-ph].

[38] L3 Collaboration, "Study of neutral current four fermion and Z Z production in e+ e- collisions at S**(1/2) = 183-GeV," *Phys. Lett. B*, vol. 450, pp. 281–293, 1999. DOI: 10.1016/S0370-2693(99)00103-3.

[39] OPAL Collaboration, "Study of Z pair production and anomalous couplings in e^+e^- collisions at $\sqrt{s}$ between 190 GeV and 209 GeV," *Eur. Phys. J. c*, vol. 32, p. 303, 2003. DOI: 10.1140/epjc/s2003-01467-x. arXiv: hep-ex/0310013 [hep-ex].

[40] DELPHI Collaboration, "ZZ production in e^+e^- interactions at $\sqrt{s} = 183$–209 GeV," *Eur. Phys. J. C*, vol. 30, p. 447, 2003. DOI: 10.1140/epjc/s2003-01287-0. arXiv: hep-ex/0307050 [hep-ex].

[41] ALEPH Collaboration, "Measurement of Z-pair production in e^+e^- collisions and constraints on anomalous neutral gauge couplings," *JHEP*, vol. 04, p. 124, 2009. DOI: 10.1088/1126-6708/2009/04/124.

[42] "A Combination of preliminary electroweak measurements and constraints on the standard model," Feb. 2001. arXiv: hep-ex/0103048.

[43] D0 Collaboration, "Measurement of the ZZ production cross section in $p\bar{p}$ collisions at $\sqrt{s} = 1.96$ TeV," *Phys. Rev. D*, vol. 84, p. 011 103, 2011. DOI: 10.1103/PhysRevD.84.011103. arXiv: 1104.3078 [hep-ex].

[44] D0 Collaboration, "A measurement of the WZ and ZZ production cross sections using leptonic final states in 8.6 fb^{-1} of $p\bar{p}$ collisions," *Phys. Rev. D*, vol. 85, p. 112 005, 2012. DOI: 10.1103/PhysRevD.85.112005. arXiv: 1201.5652 [hep-ex].

[45] CDF Collaboration, "Measurement of ZZ production in leptonic final states at $\sqrt{s}$ of 1.96 TeV at CDF," *Phys. Rev. Lett.*, vol. 108, p. 101 801, 2012. DOI: 10.1103/PhysRevLett.108.101801. arXiv: 1112.2978 [hep-ex].

[46] CMS Collaboration, "Measurement of the ZZ production cross section and search for anomalous couplings in $2\ell 2\ell'$ final states in pp collisions at $\sqrt{s} = 7\,\text{TeV}$," *JHEP*, vol. 01, p. 063, 2013. DOI: 10.1007/JHEP01(2013)063. arXiv: 1211.4890 [hep-ex].

[47] CMS Collaboration, "Measurement of the pp $\to$ ZZ production cross section and constraints on anomalous triple gauge couplings in four-lepton final states at $\sqrt{s} = 8\,\text{TeV}$," *Phys. Lett. B*, vol. 740, p. 250, 2015, [Corrigendum: DOI: 10.1016/j.physletb.2016.04.010]. DOI: 10.1016/j.physletb.2014.11.059. arXiv: 1406.0113 [hep-ex].

[48] CMS Collaboration, "Measurements of the ZZ production cross sections in the $2\ell 2\nu$ channel in proton–proton collisions at $\sqrt{s} = 7$ and $8\,\text{TeV}$ and combined constraints on triple gauge couplings," *Eur. Phys. J. C*, vol. 75, p. 511, 2015. DOI: 10.1140/epjc/s10052-015-3706-0. arXiv: 1503.05467 [hep-ex].

[49] ATLAS Collaboration, "Measurement of ZZ production in pp collisions at $\sqrt{s} = 7\,\text{TeV}$ and limits on anomalous ZZZ and ZZγ couplings with the ATLAS detector," *JHEP*, vol. 03, p. 128, 2013. DOI: 10.1007/JHEP03(2013)128. arXiv: 1211.6096 [hep-ex].

[50] ATLAS Collaboration, "Measurement of the ZZ production cross section in proton-proton collisions at $\sqrt{s} = 8\,\text{TeV}$ using the ZZ $\to \ell^-\ell^+\ell'^-\ell'^+$ and ZZ $\to \ell^-\ell^+\nu\bar{\nu}$ channels with the ATLAS detector," *JHEP*, vol. 01, p. 099, 2017. DOI: 10.1007/JHEP01(2017)099. arXiv: 1610.07585 [hep-ex].

[51] CMS Collaboration, "Measurements of the pp $\to$ ZZ production cross section and the $\text{Z} \to 4\ell$ branching fraction, and constraints on anomalous triple gauge couplings at $\sqrt{s} = 13\,\text{TeV}$," 2017, submitted to *Eur. Phys. J. C*. arXiv: 1709.08601 [hep-ex].

[52] CMS Collaboration, "Measurement of the ZZ production cross section and $Z \to \ell^+\ell^-\ell'^+\ell'^-$ branching fraction in pp collisions at $\sqrt{s} = 13\,\text{TeV}$," *Phys. Lett. B*, vol. 763, p. 280, 2016. DOI: 10.1016/j.physletb.2016.10.054. arXiv: 1607.08834 [hep-ex].

[53] ATLAS Collaboration, "$ZZ \to \ell^+\ell^-\ell'^+\ell'^-$ cross-section measurements and search for anomalous triple gauge couplings in 13 TeV *pp* collisions with the ATLAS detector," *Phys. Rev. D*, vol. 97, no. 3, p. 032 005, 2018. DOI: 10.1103/PhysRevD.97.032005. arXiv: 1709.07703 [hep-ex].

[54] "Measurement of the pp $\to$ ZZ production cross section at $\sqrt{s} = 13$ TeV with the Run 2 data set," Mar. 2019.

[55] G. Gounaris, J. Layssac, and F. Renard, "Off-shell structure of the anomalous Z and γ selfcouplings," *Phys. Rev. D*, vol. 65, p. 017 302, 2002. DOI: 10.1103/PhysRevD.65.017302. arXiv: hep-ph/0005269.

[56] CDF Collaboration, D0 Collaboration, "Diboson Physics at the Tevatron," *EPJ Web Conf.*, vol. 28, p. 06 001, 2012. DOI: 10.1051/epjconf/20122806001. arXiv: 1201.4771 [hep-ex].

[57] D0 Collaboration, "Search for ZZ and Zγ^* production in p$\bar{\text{p}}$ collisions at $\sqrt{s} = 1.96\,\text{TeV}$ and limits on anomalous ZZZ and ZZγ^* couplings," *Phys. Rev. Lett.*, vol. 100, p. 131 801, 2008. DOI: 10.1103/PhysRevLett.100.131801. arXiv: 0712.0599 [hep-ex].

[58] L. Evans and P. Bryant, "LHC Machine," *JINST*, vol. 3, S08001, 2008. DOI: 10.1088/1748-0221/3/08/S08001.

[59] C. Lefèvre, "The CERN accelerator complex. Complexe des accélérateurs du CERN," Dec. 2008. https://cds.cern.ch/record/1260465.

[60] ATLAS Collaboration, "The ATLAS Experiment at the CERN Large Hadron Collider," *JINST*, vol. 3, S08003, 2008. DOI: 10.1088/1748-0221/3/08/S08003.

[61] LHCb Collaboration, "The LHCb Detector at the LHC," *JINST*, vol. 3, S08005, 2008. DOI: 10.1088/1748-0221/3/08/S08005.

[62] ALICE Collaboration, "The ALICE experiment at the CERN LHC," *JINST*, vol. 3, S08002, 2008. DOI: 10.1088/1748-0221/3/08/S08002.

[63] L. Coull, D. Hagedorn, V. Remondino, and F. Rodríguez-Mateos, "LHC magnet quench protection system," no. CERN-AT-93-42-MA. LHC-NOTE-251. CERN-LHC-Note-251, 5 p, Feb. 1994. DOI: 10.1109/20.305593. https://cds.cern.ch/record/259538.

[64] J. Wenninger, "Operation and Configuration of the LHC in Run 2," Mar. 2019. https://cds.cern.ch/record/2668326.

[65] R. Steerenberg and J. Wenninger, "Operational challenges and performance of the LHC during Run II," in *61st ICFA Advanced Beam Dynamics Workshop on High-Intensity and High-Brightness Hadron Beams*, 2018, THA2WD01. DOI: 10.18429/JACoW-HB2018-THA2WD01.

[66] CMS Collaboration, "Measurement of the inelastic proton-proton cross section at $\sqrt{s} = 13$ TeV," *JHEP*, vol. 07, p. 161, 2018. DOI: 10.1007/JHEP07(2018)161. arXiv: 1802.02613 [hep-ex].

[67] M. Aaboud, G. Aad, B. Abbott, J. Abdallah, O. Abdinov, B. Abeloos, R. Aben, O. S. AbouZeid, N. L. Abraham, H. Abramowicz, and et al., "Measurement of the inelastic proton-proton cross section at s=13 tev with the atlas detector at the lhc," *Physical Review Letters*, vol. 117, no. 18, Oct. 2016, ISSN:

1079-7114. DOI: 10.1103/physrevlett.117.182002. http://dx.doi.org/10.1103/PhysRevLett.117.182002.

[68] CMS Collaboration, "The CMS experiment at the CERN LHC," *JINST*, vol. 3, S08004, 2008. DOI: 10.1088/1748-0221/3/08/S08004.

[69] CMS Collaboration, "Precise Mapping of the Magnetic Field in the CMS Barrel Yoke using Cosmic Rays," *JINST*, vol. 5, T03021, 2010, arXiv:0910.5530. DOI: 10.1088/1748-0221/5/03/T03021. arXiv: 0910.5530 [physics.ins-det].

[70] A. Dominguez and et al., "Cms technical design report for the pixel detector upgrade," Sep. 2012. DOI: 10.2172/1151650.

[71] CMS Collaboration, "Description and performance of track and primary-vertex reconstruction with the CMS tracker," *JINST*, vol. 9, P10009, 2014. DOI: 10.1088/1748-0221/9/10/P10009. arXiv: 1405.6569 [physics.ins-det].

[72] CMS Collaboration, "Energy Calibration and Resolution of the CMS Electromagnetic Calorimeter in *pp* Collisions at $\sqrt{s} = 7$ TeV," *JINST*, vol. 8, p. 9009, 2013. DOI: 10.1088/1748-0221/8/09/P09009. arXiv: 1306.2016 [hep-ex].

[73] B. Isildak, "Measurement of the differential dijet production cross section in proton-proton collisions at $\sqrt{s} = 7$ TeV," Ph.D. dissertation, Bogazici U., 2011. arXiv: 1308.6064 [hep-ex]. https://inspirehep.net/record/1251416/files/arXiv:1308.6064.pdf.

[74] P. Adzic *et al.*, "Energy resolution of the barrel of the CMS electromagnetic calorimeter," *JINST*, vol. 2, P04004, 2007, doi:10.1088/1748-0221/2/04/P04004. DOI: 10.1088/1748-0221/2/04/P04004.

[75] P. Cushman, A. Heering, J. Nelson, C. Timmermans, S. R. Dugad, S. Katta, and S. Tonwar, "Multi-pixel hybrid photodiode tubes for the CMS hadron calorimeter," *Nucl. Instrum. Meth.*, vol. A387, pp. 107–112, 1997,

doi:10.1016/S0168-9002(96)00972-2. DOI: 10.1016/S0168-9002(96)00972-2.

[76] CMS Collaboration, "First results from the CMS SiPM-based hadronic endcap calorimeter," *J. Phys. Conf. Ser.*, vol. 1162, no. 1, p. 012 009, 2019. DOI: 10.1088/1742-6596/1162/1/012009.

[77] V. D. Elvira, "Measurement of the Pion Energy Response and Resolution in the CMS HCAL Test Beam 2002 Experiment," 2004, cds:CMS-NOTE-2004-020.

[78] C. Collaboration, "Identification and filtering of uncharacteristic noise in the CMS hadron calorimeter," *Journal of Instrumentation*, vol. 5, no. 03, T03014–T03014, Mar. 2010. DOI: 10.1088/1748-0221/5/03/t03014. https://doi.org/10.1088%2F1748-0221%2F5%2F03%2Ft03014.

[79] G. Bayatian *et al.*, "Design, performance and calibration of the CMS forward calorimeter wedges," *Eur. Phys. J. C*, vol. 53, pp. 139–166, 2008. DOI: 10.1140/epjc/s10052-007-0459-4.

[80] C. Collaboration, "Performance of the cms cathode strip chambers with cosmic rays," *Journal of Instrumentation*, vol. 5, no. 03, T03018–T03018, Mar. 2010, ISSN: 1748-0221. DOI: 10.1088/1748-0221/5/03/t03018. http://dx.doi.org/10.1088/1748-0221/5/03/T03018.

[81] CMS Collaboration, "Experience with Trigger Electronics for the CSC System of CMS," 2004.

[82] CMS Collaboration, "CMS Technical Design Report for the Level-1 Trigger Upgrade," Tech. Rep. CERN-LHCC-2013-011. CMS-TDR-12, Jun. 2013. https://cds.cern.ch/record/1556311.

[83] CMS Collaboration, "CMS. The TriDAS project. Technical design report, vol. 1: The trigger systems," 2000, cds:CERN-LHCC-2000-038.

[84] A. Zabi *et al.*, "Triggering on electrons, jets and tau leptons with the CMS upgraded calorimeter trigger for the LHC RUN II," *JINST*, vol. 11, no. 02, p. C02008, 2016, doi:10.1088/1748-0221/11/02/C02008. DOI: 10.1088/1748-0221/11/02/C02008.

[85] A. Svetek, M. Blake, M. Cepeda Hermida, S. Dasu, L. Dodd, R. Fobes, B. Gomber, T. Gorski, Z. Guo, P. Klabbers, A. Levine, I. Ojalvo, T. Ruggles, N. Smith, W. Smith, J. Tikalsky, M. Vicente, and N. Woods, "The Calorimeter Trigger Processor Card: the next generation of high speed algorithmic data processing at CMS," *JINST*, vol. 11, p. C02011, 2016. DOI: 10.1088/1748-0221/11/02/C02011.

[86] D. Trocino, "The CMS high level trigger," *Journal of Physics: Conference Series*, vol. 513, no. 1, p. 012 036, Jun. 2014. DOI: 10.1088/1742-6596/513/1/012036. https://doi.org/10.1088%2F1742-6596%2F513%2F1%2F012036.

[87] CMS Collaboration Collaboration, "CMS luminosity measurement for the 2017 data-taking period at $\sqrt{s} = 13$ TeV," CERN, Geneva, Tech. Rep. CMS-PAS-LUM-17-004, 2018. https://cds.cern.ch/record/2621960.

[88] CMS Collaboration Collaboration, "CMS luminosity measurement for the 2018 data-taking period at $\sqrt{s} = 13$ TeV," CERN, Geneva, Tech. Rep. CMS-PAS-LUM-18-002, 2019. https://cds.cern.ch/record/2676164.

[89] S. Van der Meer, "Calibration of the Effective Beam Height in the ISR," 1968.

[90] CMS Collaboration Collaboration, "CMS Luminosity Measurements for the 2016 Data Taking Period," CERN, Tech. Rep. CMS-PAS-LUM-17-001, 2017. http://cds.cern.ch/record/2257069.

[91] N. Metropolis and S. Ulam, "The monte carlo method," *Journal of the American Statistical Association*, vol. 44, no. 247, pp. 335–341, 1949, doi:10.1080/01621459.1949. DOI: 10.1080/01621459.1949.10483310.

[92] B. Webber, "Parton shower Monte Carlo event generators," *Scholarpedia*, vol. 6, no. 12, p. 10 662, 2011, revision #128236. DOI: 10.4249/scholarpedia.10662.

[93] CTEQ Collaboration, "Handbook of perturbative QCD: Version 1.0," *Rev. Mod. Phys.*, vol. 67, p. 157, 1995. DOI: 10.1103/RevModPhys.67.157.

[94] S. Höche, "Introduction to parton-shower event generators," in *Theoretical Advanced Study Institute in Elementary Particle Physics: Journeys Through the Precision Frontier: Amplitudes for Colliders*, 2015, pp. 235–295. DOI: 10.1142/9789814678766_0005. arXiv: 1411.4085 [hep-ph].

[95] V. Barger and R. Phillips, *Collider Physics*, ser. Frontiers in physics. Avalon Publishing, 1997, ISBN: 9780201149456.

[96] NNPDF Collaboration, "Parton distributions for the LHC Run II," *JHEP*, vol. 04, p. 040, 2015. DOI: 10.1007/JHEP04(2015)040. arXiv: 1410.8849 [hep-ph].

[97] NNPDF Collaboration, "Parton distributions from high-precision collider data," 2017. arXiv: 1706.00428 [hep-ph].

[98] J. Pumplin, D. R. Stump, J. Huston, H.-L. Lai, P. Nadolsky, and W.-K. Tung, "New generation of parton distributions with uncertainties from global qcd analysis," *Journal of High Energy Physics*, vol. 2002, no. 07, pp. 012–

012, Jul. 2002, ISSN: 1029-8479. DOI: 10.1088/1126-6708/2002/07/012. http://dx.doi.org/10.1088/1126-6708/2002/07/012.

[99] A. D. Martin, W. J. Stirling, R. S. Thorne, and G. Watt, "Parton distributions for the lhc," *The European Physical Journal C*, vol. 63, no. 2, pp. 189–285, Jul. 2009, ISSN: 1434-6052. DOI: 10.1140/epjc/s10052-009-1072-5. http://dx.doi.org/10.1140/epjc/s10052-009-1072-5.

[100] N. D. Christensen and C. Duhr, "Feynrules – feynman rules made easy," *Computer Physics Communications*, vol. 180, no. 9, pp. 1614–1641, Sep. 2009, ISSN: 0010-4655. DOI: 10.1016/j.cpc.2009.02.018. http://dx.doi.org/10.1016/j.cpc.2009.02.018.

[101] N. Christensen, P. de Aquino, C. Degrande, C. Duhr, B. Fuks, M. Herquet, F. Maltoni, and S. Schumann, "A comprehensive approach to new physics simulations," *The European Physical Journal C*, vol. 71, no. 2, Feb. 2011, ISSN: 1434-6052. DOI: 10.1140/epjc/s10052-011-1541-5. http://dx.doi.org/10.1140/epjc/s10052-011-1541-5.

[102] A. Alloul, N. D. Christensen, C. Degrande, C. Duhr, and B. Fuks, "Feynrules 2.0 — a complete toolbox for tree-level phenomenology," *Computer Physics Communications*, vol. 185, no. 8, pp. 2250–2300, Aug. 2014, ISSN: 0010-4655. DOI: 10.1016/j.cpc.2014.04.012. http://dx.doi.org/10.1016/j.cpc.2014.04.012.

[103] J. Alwall, R. Frederix, S. Frixione, V. Hirschi, F. Maltoni, O. Mattelaer, H.-S. Shao, T. Stelzer, P. Torrielli, and M. Zaro, "The automated computation of tree-level and next-to-leading order differential cross sections, and their matching to parton shower simulations," *JHEP*, vol. 07, p. 079, 2014. DOI: 10.1007/JHEP07(2014)079. arXiv: 1405.0301 [hep-ph].

[104] S. Frixione, P. Nason, and C. Oleari, "Matching NLO QCD computations with Parton Shower simulations: the POWHEG method," *JHEP*, vol. 11, p. 070, 2007. DOI: 10.1088/1126-6708/2007/11/070. arXiv: 0709.2092 [hep-ph].

[105] Sjöstrand, T. and Skands, Peter Z., "Multiple interactions and the structure of beam remnants," *JHEP*, vol. 03, p. 053, 2004. DOI: 10.1088/1126-6708/2004/03/053. arXiv: hep-ph/0402078 [hep-ph].

[106] R. Field, *Min-bias and the underlying event at the lhc*, 2011. arXiv: 1110.5530 [hep-ph].

[107] J. M. Campbell, J. W. Huston, and W. J. Stirling, "Hard interactions of quarks and gluons: A primer for lhc physics," *Reports on Progress in Physics*, vol. 70, no. 1, pp. 89–193, Dec. 2006, ISSN: 1361-6633. DOI: 10.1088/0034-4885/70/1/r02. http://dx.doi.org/10.1088/0034-4885/70/1/R02.

[108] Sjöstrand, Torbjörn and Ask, Stefan and Christiansen, Jesper R. and Corke, Richard and Desai, Nishita and Ilten, Philip and Mrenna, Stephen and Prestel, Stefan and Rasmussen, Christine O. and Skands, Peter Z., "An Introduction to PYTHIA 8.2," *Comput. Phys. Commun.*, vol. 191, p. 159, 2015. DOI: 10.1016/j.cpc.2015.01.024. arXiv: 1410.3012 [hep-ph].

[109] M. Bahr *et al.*, "Herwig++ Physics and Manual," *Eur. Phys. J. C*, vol. 58, p. 639, 2008. DOI: 10.1140/epjc/s10052-008-0798-9. arXiv: 0803.0883 [hep-ph].

[110] S. Höche and S. Prestel, "The midpoint between dipole and parton showers," *Eur. Phys. J.*, vol. C75, no. 9, p. 461, 2015, arXiv:1506.05057. DOI: 10.1140/epjc/s10052-015-3684-2. arXiv: 1506.05057 [hep-ph].

[111] B. Andersson, G. Gustafson, G. Ingelman, and T. Sjostrand, "Parton Fragmentation and String Dynamics," *Phys. Rept.*, vol. 97, pp. 31–145, 1983. DOI: 10.1016/0370-1573(83)90080-7.

[112] S Banerjee, "CMS Simulation Software," *Journal of Physics: Conference Series*, vol. 396, p. 022 003, 2012. %7Bhttp://stacks.iop.org/1742-6596/396/i=2/a=022003%7D.

[113] M Hildreth and V N Ivanchenko and D J Lange and M J Kortelainen, "CMS Full Simulation for Run-2," *Journal of Physics: Conference Series*, vol. 664, p. 072 022, 2015. %7Bhttp://stacks.iop.org/1742-6596/664/i=7/a=072022%7D.

[114] T. Melia, P. Nason, R. Röntsch, and G. Zanderighi, "W^+W^-, WZ and ZZ production in the POWHEG BOX," *JHEP*, vol. 11, p. 078, 2011. DOI: 10.1007/JHEP11(2011)078. arXiv: 1107.5051 [hep-ph].

[115] P. Nason, "A New method for combining NLO QCD with shower Monte Carlo algorithms," *JHEP*, vol. 11, p. 040, 2004. DOI: 10.1088/1126-6708/2004/11/040. arXiv: hep-ph/0409146 [hep-ph].

[116] S. Alioli, P. Nason, C. Oleari, and E. Re, "A general framework for implementing NLO calculations in shower Monte Carlo programs: the POWHEG BOX," *JHEP*, vol. 06, p. 043, 2010. DOI: 10.1007/JHEP06(2010)043. arXiv: 1002.2581 [hep-ph].

[117] S. Alioli, P. Nason, C. Oleari, and E. Re, "NLO vector-boson production matched with shower in POWHEG," *JHEP*, vol. 07, p. 060, 2008. DOI: 10.1088/1126-6708/2008/07/060. arXiv: 0805.4802 [hep-ph].

[118] J. M. Campbell and R. K. Ellis, "MCFM for the Tevatron and the LHC," *Nucl. Phys. Proc. Suppl.*, vol. 205, p. 10, 2010. DOI: 10.1016/j.nuclphysbps.2010.08.011. arXiv: 1007.3492 [hep-ph].

[119] F. Caola, K. Melnikov, R. Röntsch, and L. Tancredi, "QCD corrections to ZZ production in gluon fusion at the LHC," *Phys. Rev. D*, vol. 92, p. 094 028, 2015. DOI: 10.1103/PhysRevD.92.094028. arXiv: 1509.06734 [hep-ph].

[120] CMS Collaboration, "Event generator tunes obtained from underlying event and multiparton scattering measurements," *Eur. Phys. J. C*, vol. 76, p. 155, 2016. DOI: 10.1140/epjc/s10052-016-3988-x. arXiv: 1512.00815 [hep-ex].

[121] A. M. Sirunyan, A. Tumasyan, W. Adam, F. Ambrogi, E. Asilar, T. Bergauer, J. Brandstetter, M. Dragicevic, J. Erö, and et al., "Extraction and validation of a new set of cms pythia8 tunes from underlying-event measurements," *The European Physical Journal C*, vol. 80, no. 1, J 2020, ISSN: 1434-6052. DOI: 10.1140/epjc/s10052-019-7499-4. http://dx.doi.org/10.1140/epjc/s10052-019-7499-4.

[122] GEANT4 Collaboration, "GEANT4: A Simulation toolkit," *Nucl. Instrum. Meth. A*, vol. 506, p. 250, 2003. DOI: 10.1016/S0168-9002(03)01368-8.

[123] R. Brun, F. Bruyant, F. Carminati, S. Giani, M. Maire, A. McPherson, G. Patrick, and L. Urban, "GEANT Detector Description and Simulation Tool," Oct. 1994. DOI: 10.17181/CERN.MUHF.DMJ1.

[124] S. Piperov, "Geant4 validation with CMS calorimeters test-beam data," in *Hadron collider physics. Proceedings, 19th Symposium, HCP2008, Galena, USA, May 27-31, 2008*, FERMILAB-CONF-08-371-CMS, 2008. arXiv: 0808.0130 [physics.ins-det]. http://lss.fnal.gov/cgi-bin/find_paper.pl?conf-08-371.

[125] CMS Collaboration Collaboration, "Validation of Geant4 Physics Models with LHC Collision Data," CERN, Geneva, Tech. Rep. CMS-CR-2011-038, Feb. 2011, cds:CMS-CR-2011-038. http://cds.cern.ch/record/1345317.

[126] CMS Collaboration Collaboration, "Validation and Tuning of the CMS Simulation Software," CERN, Geneva, Tech. Rep. CMS-CR-2011-019, Jan. 2011, cds:CMS-CR-2011-019. http://cds.cern.ch/record/1326921.

[127] CMS Collaboration, "Particle-flow reconstruction and global event description with the CMS detector," vol. 12, P10003, 2017. DOI: 10.1088/1748-0221/12/10/P10003. arXiv: 1706.04965 [physics.ins-det].

[128] R. Frühwirth, "Application of Kalman filtering to track and vertex fitting," *Nucl. Instrum. Meth. A*, vol. 262, p. 444, 1987. DOI: 10.1016/0168-9002(87)90887-4.

[129] R. Mankel, "A Concurrent track evolution algorithm for pattern recognition in the HERA-B main tracking system," *Nucl. Instrum. Meth.*, vol. A395, pp. 169–184, 1997, doi:10.1016/S0168-9002(97)00705-5. DOI: 10.1016/S0168-9002(97)00705-5.

[130] D. Funke, T. Hauth, V. Innocente, G. Quast, P. Sanders, and D. Schieferdecker, "Parallel track reconstruction in CMS using the cellular automaton approach," *J. Phys. Conf. Ser.*, vol. 513, D. Groep and D. Bonacorsi, Eds., p. 052 010, 2014. DOI: 10.1088/1742-6596/513/5/052010.

[131] "2017 tracking performance plots," Apr. 2017. https://cds.cern.ch/record/2290524.

[132] W. Adam, R. Frühwirth, A. Strandlie, and T. Todor, "Reconstruction of Electrons with the Gaussian-Sum Filter in the CMS Tracker at the LHC," 2005.

[133] CMS Collaboration, "Performance of Electron Reconstruction and Selection with the CMS Detector in Proton-Proton Collisions at $\sqrt{s} = 8\,\text{TeV}$," *JINST*, vol. 10, P06005, 2015. DOI: 10.1088/1748-0221/10/06/P06005. arXiv: 1502.02701 [physics.ins-det].

[134] CMS Collaboration, "Performance of the CMS muon detector and muon reconstruction with proton-proton collisions at $\sqrt{s} = 13$ TeV," *Submitted to: JINST*, 2018, arXiv:1804.04528. arXiv: 1804.04528 [physics.ins-det].

[135] K. Rose, "Deterministic annealing for clustering, compression, classification, regression, and related optimization problems," *Proceedings of the IEEE*, vol. 86, p. 2210, Nov. 1998, ISSN: 0018-9219. DOI: 10.1109/5.726788.

[136] CMS Collaboration, "Measurement of the Inclusive W and Z Production Cross Sections in pp Collisions at $\sqrt{s} = 7\,\text{TeV}$," *JHEP*, vol. 10, p. 132, 2011. DOI: 10.1007/JHEP10(2011)132. arXiv: 1107.4789 [hep-ex].

[137] CMS Collaboration, "CMS Electron and Photon Performance at 13 TeV," *J. Phys. Conf. Ser.*, vol. 1162, no. 1, p. 012008, 2019. DOI: 10.1088/1742-6596/1162/1/012008.

[138] T. Chen and C. Guestrin, "Xgboost," *Proceedings of the 22nd ACM SIGKDD International Conference on Knowledge Discovery and Data Mining*, Aug. 2016. DOI: 10.1145/2939672.2939785. http://dx.doi.org/10.1145/2939672.2939785.

[139] "Measurements of properties of the Higgs boson in the four-lepton final state in proton-proton collisions at $\sqrt{s} = 13$ TeV," Mar. 2019.

[140] *CMS EGamma POG. CERN, Geneva.* https://twiki.cern.ch/twiki/bin/viewauth/CMS/CutBasedPhotonIdentificationRun2#SPRING15_selections_bunch_crossi.

[141] *CMS Higgs Working Group, "Higgs to ZZ to four leptons Legacy Run II Analysis". CERN, Geneva.* https://twiki.cern.ch/twiki/bin/viewauth/CMS/HiggsZZ4lRunIILegacy#Photons_for_FSR.

[142] CMS Collaboration, "Reconstruction and identification of τ lepton decays to hadrons and ν_τ at CMS," *JINST*, vol. 11, no. 01, P01019, 2016, arXiv:1510.07488. DOI: 10.1088/1748-0221/11/01/P01019. arXiv: 1510.07488 [physics.ins-det].

[143] CMS Collaboration Collaboration, "Performance of reconstruction and identification of tau leptons in their decays to hadrons and tau neutrino in LHC Run-2," CERN, Geneva, Tech. Rep. CMS-PAS-TAU-16-002, 2016, cds:CMS-PAS-TAU-16-002. https://cds.cern.ch/record/2196972.

[144] G. P. Salam, "Towards Jetography," *Eur. Phys. J.*, vol. C67, pp. 637–686, 2010, arXiv:0906.1833. DOI: 10.1140/epjc/s10052-010-1314-6. arXiv: 0906.1833 [hep-ph].

[145] M. Cacciari, G. P. Salam, and G. Soyez, "The Anti-k_{T} jet clustering algorithm," *JHEP*, vol. 04, p. 063, 2008. DOI: 10.1088/1126-6708/2008/04/063. arXiv: 0802.1189 [hep-ph].

[146] CMS Collaboration, "Study of Pileup Removal Algorithms for Jets," Tech. Rep. CMS-PAS-JME-14-001, 2014. https://cds.cern.ch/record/1751454.

[147] CMS Collaboration, "Jet energy scale and resolution in the CMS experiment in pp collisions at 8 TeV," *JINST*, vol. 12, P02014, 2017. DOI: 10.1088/1748-0221/12/02/P02014. arXiv: 1607.03663 [hep-ex].

[148] CMS Collaboration, "Jet algorithms performance in 13 TeV data," Tech. Rep., 2017. https://cds.cern.ch/record/2256875.

[149] *CMS JME POG, "Jet Identification for the 13 TeV data Run2017". CERN, Geneva.* https://twiki.cern.ch/twiki/bin/view/CMS/JetID13TeVRun2017.

[150] *CMS JME POG, "Jet Identification for the 13 TeV data Run2018". CERN, Geneva.* https://twiki.cern.ch/twiki/bin/view/CMS/JetID13TeVRun2018.

[151] CMS Collaboration, "Identification of heavy-flavour jets with the CMS detector in pp collisions at 13 TeV," *JINST*, vol. 13, no. 05, P05011, 2018, arXiv:1712.07158. DOI: 10.1088/1748-0221/13/05/P05011. arXiv: 1712.07158 [physics.ins-det].

[152] CMS Collaboration, "Performance of the CMS missing transverse momentum reconstruction in pp data at $\sqrt{s} = 8$ TeV," *JINST*, vol. 10, P02006, 2015. DOI: 10.1088/1748-0221/10/02/P02006. arXiv: 1411.0511 [physics.ins-det].

[153] CMS Collaboration Collaboration, "Performance of missing transverse momentum in pp collisions at sqrt(s)=13 TeV using the CMS detector," CERN, Geneva, Tech. Rep. CMS-PAS-JME-17-001, 2018, cds:CMS-PAS-JME-17-001. http://cds.cern.ch/record/2628600.

[154] *CMS JME POG. CERN, Geneva.* https://twiki.cern.ch/twiki/bin/view/CMS/MissingETOptionalFiltersRun2.

[155] *CMS JME POG, "2017 MET recipe v2" CERN, Geneva.* https://hypernews.cern.ch/HyperNews/CMS/get/JetMET/1865.html.

[156] CMS Collaboration, "Measurement of the properties of a Higgs boson in the four-lepton final state," *Phys. Rev. D*, vol. 89, p. 092 007, 2014. DOI: 10.1103/PhysRevD.89.092007. arXiv: 1312.5353 [hep-ex].

[157] J. Butterworth *et al.*, "PDF4LHC recommendations for LHC Run II," *J. Phys. G*, vol. 43, p. 023 001, 2016. DOI: 10.1088/0954-3899/43/2/023001. arXiv: 1510.03865 [hep-ph].

[158] G. Bohm and G. Zech, *Introduction to statistics and data analysis for physicists*. DESY, 2010, ISBN: 9783935702416. https://books.google.ch/books?id=aQBHcgAACAAJ.

[159] T. Adye, "Unfolding algorithms and tests using RooUnfold," in *Proceedings, PHYSTAT 2011 Workshop on Statistical Issues Related to Discovery Claims in Search Experiments and Unfolding, CERN, Geneva, Switzerland 17–20 January 2011*, CERN, Geneva: CERN, 2011, p. 313. DOI: 10.5170/CERN-2011-006.313. arXiv: 1105.1160 [physics.data-an]. https://inspirehep.net/record/898599/files/arXiv:1105.1160.pdf.

[160] G. D'Agostini, "A Multidimensional unfolding method based on Bayes' theorem," *Nucl. Instrum. Meth. A*, vol. 362, p. 487, 1995. DOI: 10.1016/0168-9002(95)00274-X.

[161] A. P. Dempster, N. M. Laird, and D. B. Rubin, "Maximum likelihood from incomplete data via the EM algorithm," *J. R. Stat. Soc. B*, vol. 39, p. 1, 1977, ISSN: 00359246. http://www.jstor.org/stable/2984875.

[162] L. B. Lucy, "An iterative technique for the rectification of observed distributions," *Astron. J.*, vol. 79, p. 745, Jun. 1974. DOI: 10.1086/111605.

[163] W. H. Richardson, "Bayesian-based iterative method of image restoration," *J. Opt. Soc. Am.*, vol. 62, p. 55, Jan. 1972. DOI: 10.1364/JOSA.62.000055. http://www.osapublishing.org/abstract.cfm?URI=josa-62-1-55.

[164] L. A. Shepp and Y. Vardi, "Maximum likelihood reconstruction for emission tomography," *IEEE Transactions on Medical Imaging*, vol. 1, p. 113, Oct. 1982, ISSN: 0278-0062. DOI: 10.1109/TMI.1982.4307558.

[165] ATLAS, CMS, and the LHC Higgs Combinaiton Group Collaboration, "Procedure for the LHC Higgs boson search combination in summer 2011," CERN, Technical Report CMS-NOTE-2011-005, ATL-PHYS-Pub-2011-11, 2011. https://cds.cern.ch/record/1379837.

[166] Particle Data Group, M. Tanabashi, *et al.*, "Review of particle physics," *Phys. Rev. D*, vol. 98, p. 030 001, 2018. DOI: 10.1103/PhysRevD.98.030001.

[167] G. Cowan, K. Cranmer, E. Gross, and O. Vitells, "Asymptotic formulae for likelihood-based tests of new physics," *Eur. Phys. J. C*, vol. 71, p. 1554, 2011, [Erratum: DOI: 10.1140/epjc/s10052-013-2501-z]. DOI: 10.1140/epjc/s10052-011-1554-0. arXiv: 1007.1727 [physics.data-an].

[168] CMS Collaboration, "Measurement of the ZZ production cross section in $\ell\ell\ell'\ell'$ decays in pp collisions at $\sqrt{s} = 13\,\text{TeV}$," Tech. Rep. CMS-PAS-SMP-15-005, 2015. https://cds.cern.ch/record/2114822.

[169] CMS Collaboration, "Measurement of the pp $\rightarrow$ ZZ production cross section, Z $\rightarrow 4\ell$ branching fraction and constraints on anomalous triple gauge couplings at $\sqrt{s} = 13\,\text{TeV}$," Tech. Rep. CMS-PAS-SMP-16-017, 2017. https://cds.cern.ch/record/2256100.

[170] ATLAS Collaboration, "Measurements of four-lepton production in pp collisions at $\sqrt{s} = 8\,\text{TeV}$ with the ATLAS detector," *Phys. Lett. B*, vol. 753, p. 552, 2016. DOI: 10.1016/j.physletb.2015.12.048. arXiv: 1509.07844 [hep-ex].

[171] C. Degrande, "A basis of dimension-eight operators for anomalous neutral triple gauge boson interactions," *JHEP*, vol. 02, p. 101, 2014. DOI: 10.1007/JHEP02(2014)101. arXiv: 1308.6323 [hep-ph].

[172] A. Bierweiler, T. Kasprzik, and J. H. Kuhn, "Vector-boson pair production at the LHC to $\mathcal{O}(\alpha^3)$ accuracy," *JHEP*, vol. 12, p. 071, 2013. DOI: 10.1007/JHEP12(2013)071. arXiv: 1305.5402 [hep-ph].

[173] J. Baglio, L. D. Ninh, and M. M. Weber, "Massive gauge boson pair production at the LHC: a next-to-leading order story," *Phys. Rev. D*, vol. 88, p. 113 005, 2013. DOI: 10.1103/PhysRevD.88.113005. arXiv: 1307.4331.

[174] J. H. Jeans, "The Motions of Stars in a Kapteyn Universe," *Monthly Notices of the Royal Astronomical Society*, vol. 82, pp. 122–132, Jan. 1922. DOI: 10.1093/mnras/82.3.122.

[175] F. Zwicky, "Republication of: The redshift of extragalactic nebulae," *General Relativity and Gravitation*, vol. 41, no. 1, pp. 207–224, Jan. 2009. DOI: 10.1007/s10714-008-0707-4.

[176] V. C. Rubin, W. K. Ford, and N. Thonnard, "Rotational properties of 21 sc galaxies with a large range of luminosities and radii, from ngc 4605 /r = 4kpc/ to ugc 2885 /r = 122 kpc/," 1980.

[177] K. Begeman, A. Broeils, and R. Sanders, "Extended rotation curves of spiral galaxies: Dark haloes and modified dynamics," *Mon. Not. Roy. Astron. Soc.*, vol. 249, p. 523, 1991.

[178] K. Freese, "Review of Observational Evidence for Dark Matter in the Universe and in upcoming searches for Dark Stars," *EAS Publ. Ser.*, vol. 36, pp. 113–126, 2009. DOI: 10.1051/eas/0936016. arXiv: 0812.4005 [astro-ph].

[179] M. Bartelmann and M. Maturi, *Weak gravitational lensing*, 2016. arXiv: 1612.06535 [astro-ph.CO].

[180] P. Natarajan, U. Chadayammuri, M. Jauzac, J. Richard, J.-P. Kneib, H. Ebeling, F. Jiang, F. van den Bosch, M. Limousin, E. Jullo, and et al., "Mapping substructure in the hst frontier fields cluster lenses and in cosmological simulations," *Monthly Notices of the Royal Astronomical Society*, vol. 468, no. 2, pp. 1962–1980, Feb. 2017, ISSN: 1365-2966. DOI: 10.1093/mnras/stw3385. http://dx.doi.org/10.1093/mnras/stw3385.

[181] G. Bertone, D. Hooper, and J. Silk, "Particle dark matter: Evidence, candidates and constraints," *Physics Reports*, vol. 405, no. 5-6, pp. 279–390, Jan. 2005, ISSN: 0370-1573. DOI: 10.1016/j.physrep.2004.08.031. http://dx.doi.org/10.1016/j.physrep.2004.08.031.

[182] N. Jarosik, C. L. Bennett, J. Dunkley, B. Gold, M. R. Greason, M. Halpern, R. S. Hill, G. Hinshaw, A. Kogut, E. Komatsu, and et al., "Seven-year wilkinson microwave anisotropy probe (wmap) observations: Sky maps, systematic errors, and basic results," *The Astrophysical Journal Supplement Series*, vol. 192, no. 2, p. 14, Jan. 2011, ISSN: 1538-4365. DOI: 10.1088/0067-0049/192/2/14. http://dx.doi.org/10.1088/0067-0049/192/2/14.

[183] D. Clowe, M. Bradač, A. H. Gonzalez, M. Markevitch, S. W. Randall, C. Jones, and D. Zaritsky, "A direct empirical proof of the existence of dark matter," *The Astrophysical Journal*, vol. 648, no. 2, pp. L109–L113, Aug. 2006, ISSN: 1538-4357. DOI: 10.1086/508162. http://dx.doi.org/10.1086/508162.

[184] F. D. Steffen, "Dark-matter candidates," *The European Physical Journal C*, vol. 59, no. 2, pp. 557–588, Jan. 2009, ISSN: 1434-6052. DOI: 10.1140/epjc/s10052-008-0830-0. http://dx.doi.org/10.1140/epjc/s10052-008-0830-0.

[185] L. Bergström, "Dark matter candidates," *New Journal of Physics*, vol. 11, no. 10, p. 105 006, Oct. 2009, ISSN: 1367-2630. DOI: 10.1088/1367-2630/11/10/105006. http://dx.doi.org/10.1088/1367-2630/11/10/105006.

[186] J. Goodman, M. Ibe, A. Rajaraman, W. Shepherd, T. M. P. Tait, and H.-B. Yu, "Constraints on dark matter from colliders," *Physical Review D*, vol. 82, no. 11, Dec. 2010, ISSN: 1550-2368. DOI: 10.1103/physrevd.82.116010. http://dx.doi.org/10.1103/PhysRevD.82.116010.

[187] J. Goodman, M. Ibe, A. Rajaraman, W. Shepherd, T. M. Tait, and H.-B. Yu, "Constraints on light majorana dark matter from colliders," *Physics Letters B*, vol. 695, no. 1-4, pp. 185–188, Jan. 2011, ISSN: 0370-2693. DOI: 10.1016/j.physletb.2010.11.009. http://dx.doi.org/10.1016/j.physletb.2010.11.009.

[188] D. Abercrombie, N. Akchurin, E. Akilli, J. A. Maestre, B. Allen, B. A. Gonzalez, J. Andrea, A. Arbey, G. Azuelos, P. Azzi, and et al., "Dark matter benchmark models for early lhc run-2 searches: Report of the atlas/cms dark matter forum," *Physics of the Dark Universe*, vol. 27, p. 100 371, Jan. 2020, ISSN: 2212-6864. DOI: 10.1016/j.dark.2019.100371. http://dx.doi.org/10.1016/j.dark.2019.100371.

[189] Y. Bai, P. J. Fox, and R. Harnik, "The tevatron at the frontier of dark matter direct detection," *Journal of High Energy Physics*, vol. 2010, no. 12, Dec. 2010, ISSN: 1029-8479. DOI: 10.1007/jhep12(2010)048. http://dx.doi.org/10.1007/JHEP12(2010)048.

[190] A. Birkedal, K. Matchev, and M. Perelstein, "Dark matter at colliders: A model-independent approach," *Physical Review D*, vol. 70, no. 7, Oct. 2004,

ISSN: 1550-2368. DOI: 10.1103/physrevd.70.077701. http://dx.doi.org/10.1103/PhysRevD.70.077701.

[191] Y. Gershtein, F. Petriello, S. Quackenbush, and K. M. Zurek, "Discovering hidden sectors with monophotonz searches," *Physical Review D*, vol. 78, no. 9, Nov. 2008, ISSN: 1550-2368. DOI: 10.1103/physrevd.78.095002. http://dx.doi.org/10.1103/PhysRevD.78.095002.

[192] P. J. Fox, R. Harnik, J. Kopp, and Y. Tsai, "Lep shines light on dark matter," *Physical Review D*, vol. 84, no. 1, Jul. 2011, ISSN: 1550-2368. DOI: 10.1103/physrevd.84.014028. http://dx.doi.org/10.1103/PhysRevD.84.014028.

[193] A. Crivellin, U. Haisch, and A. Hibbs, "Lhc constraints on gauge boson couplings to dark matter," *Physical Review D*, vol. 91, no. 7, Apr. 2015, ISSN: 1550-2368. DOI: 10.1103/physrevd.91.074028. http://dx.doi.org/10.1103/PhysRevD.91.074028.

[194] F. J. Petriello, S. Quackenbush, and K. M. Zurek, "Invisiblez at the cern lhc," *Physical Review D*, vol. 77, no. 11, Jun. 2008, ISSN: 1550-2368. DOI: 10.1103/physrevd.77.115020. http://dx.doi.org/10.1103/PhysRevD.77.115020.

[195] L. M. Carpenter, A. Nelson, C. Shimmin, T. M. P. Tait, and D. Whiteson, "Collider searches for dark matter in events with azboson and missing energy," *Physical Review D*, vol. 87, no. 7, Apr. 2013, ISSN: 1550-2368. DOI: 10.1103/physrevd.87.074005. http://dx.doi.org/10.1103/PhysRevD.87.074005.

[196] Z.-H. Yu, X.-J. Bi, Q.-S. Yan, and P.-F. Yin, "Dark matter searches in the mono-zchannel at high energye+e−colliders," *Physical Review D*, vol. 90, no. 5, Sep. 2014, ISSN: 1550-2368. DOI: 10.1103/physrevd.90.055010. http://dx.doi.org/10.1103/PhysRevD.90.055010.

[197] A. Boveia, O. Buchmueller, G. Busoni, F. D'Eramo, A. D. Roeck, A. D. Simone, C. Doglioni, M. J. Dolan, M.-H. Genest, K. Hahn, U. Haisch, P. C. Harris, J. Heisig, V. Ippolito, F. Kahlhoefer, V. V. Khoze, S. Kulkarni, G. Landsberg, S. Lowette, S. Malik, M. Mangano, C. McCabe, S. Mrenna, P. Pani, T. du Pree, A. Riotto, D. Salek, K. Schmidt-Hoberg, W. Shepherd, T. M. P. Tait, L.-T. Wang, S. Worm, and K. Zurek, *Recommendations on presenting lhc searches for missing transverse energy signals using simplified s-channel models of dark matter*, 2016. arXiv: 1603.04156 [hep-ex].

[198] H. An, X. Ji, and L.-T. Wang, "Light dark matter and z dark force at colliders," *Journal of High Energy Physics*, vol. 2012, no. 7, Jul. 2012, ISSN: 1029-8479. DOI: 10.1007/jhep07(2012)182. http://dx.doi.org/10.1007/JHEP07(2012)182.

[199] H. An, R. Huo, and L.-T. Wang, "Searching for low mass dark portal at the lhc," *Physics of the Dark Universe*, vol. 2, no. 1, pp. 50–57, Mar. 2013, ISSN: 2212-6864. DOI: 10.1016/j.dark.2013.03.002. http://dx.doi.org/10.1016/j.dark.2013.03.002.

[200] M. T. Frandsen, F. Kahlhoefer, A. Preston, S. Sarkar, and K. Schmidt-Hoberg, "Lhc and tevatron bounds on the dark matter direct detection cross-section for vector mediators," *Journal of High Energy Physics*, vol. 2012, no. 7, Jul. 2012, ISSN: 1029-8479. DOI: 10.1007/jhep07(2012)123. http://dx.doi.org/10.1007/JHEP07(2012)123.

[201] G. Arcadi, Y. Mambrini, M. H. G. Tytgat, and B. Zaldıvar, "Invisible z and dark matter: Lhc vs lux constraints," *Journal of High Energy Physics*, vol. 2014, no. 3, Mar. 2014, ISSN: 1029-8479. DOI: 10.1007/jhep03(2014)134. http://dx.doi.org/10.1007/JHEP03(2014)134.

[202] A. Alves, S. Profumo, and F. S. Queiroz, "The dark z portal: Direct, indirect and collider searches," *Journal of High Energy Physics*, vol. 2014, no. 4, Apr. 2014, ISSN: 1029-8479. DOI: 10.1007/jhep04(2014)063. http://dx.doi.org/10.1007/JHEP04(2014)063.

[203] G. Busoni, A. De Simone, J. Gramling, E. Morgante, and A. Riotto, "On the validity of the effective field theory for dark matter searches at the lhc, part ii: Complete analysis for the s-channel," *Journal of Cosmology and Astroparticle Physics*, vol. 2014, no. 06, pp. 060–060, Jun. 2014, ISSN: 1475-7516. DOI: 10.1088/1475-7516/2014/06/060. http://dx.doi.org/10.1088/1475-7516/2014/06/060.

[204] A. Alves, A. Berlin, S. Profumo, and F. S. Queiroz, "Dark matter complementarity and thez portal," *Physical Review D*, vol. 92, no. 8, Oct. 2015, ISSN: 1550-2368. DOI: 10.1103/physrevd.92.083004. http://dx.doi.org/10.1103/PhysRevD.92.083004.

[205] A. M. Sirunyan, A. Tumasyan, W. Adam, F. Ambrogi, E. Asilar, T. Bergauer, J. Brandstetter, E. Brondolin, M. Dragicevic, J. Erö, and et al., "Search for new physics in final states with an energetic jet or a hadronically decaying w or z boson and transverse momentum imbalance at s=13 tev," *Physical Review D*, vol. 97, no. 9, May 2018, ISSN: 2470-0029. DOI: 10.1103/physrevd.97.092005. http://dx.doi.org/10.1103/PhysRevD.97.092005.

[206] CMS Collaboration, "Searches for dark matter with CMS," *PoS*, vol. ICHEP2018, p. 071, 2019. DOI: 10.22323/1.340.0071.

[207] A. M. Sirunyan, A. Tumasyan, W. Adam, F. Ambrogi, E. Asilar, T. Bergauer, J. Brandstetter, E. Brondolin, M. Dragicevic, and et al., "Search for new physics in events with a leptonically decaying z boson and a large trans-

verse momentum imbalance in proton–proton collisions at s = 13tev," *The European Physical Journal C*, vol. 78, no. 4, Apr. 2018, ISSN: 1434-6052. DOI: 10.1140/epjc/s10052-018-5740-1. http://dx.doi.org/10.1140/epjc/s10052-018-5740-1.

[208] A. M. Sirunyan, A. Tumasyan, W. Adam, F. Ambrogi, E. Asilar, T. Bergauer, J. Brandstetter, M. Dragicevic, J. Erö, and et al., "Search for new physics in final states with a single photon and missing transverse momentum in proton-proton collisions at s=13 tev," *Journal of High Energy Physics*, vol. 2019, no. 2, Feb. 2019, ISSN: 1029-8479. DOI: 10.1007/jhep02(2019)074. http://dx.doi.org/10.1007/JHEP02(2019)074.

[209] Planck Collaboration, "Planck 2018 results. VI. Cosmological parameters," Jul. 2018. arXiv: 1807.06209 [astro-ph.CO].

[210] V. Khachatryan, A. M. Sirunyan, A. Tumasyan, W. Adam, T. Bergauer, M. Dragicevic, J. Erö, C. Fabjan, M. Friedl, R. Frühwirth, and et al., "Search for dark matter, extra dimensions, and unparticles in monojet events in proton–proton collisions at s = 8 tev," *The European Physical Journal C*, vol. 75, no. 5, May 2015, ISSN: 1434-6052. DOI: 10.1140/epjc/s10052-015-3451-4. http://dx.doi.org/10.1140/epjc/s10052-015-3451-4.

[211] G. Aad, B. Abbott, J. Abdallah, S. Abdel Khalek, O. Abdinov, R. Aben, B. Abi, M. Abolins, O. S. AbouZeid, and et al., "Search for new phenomena in final states with an energetic jet and large missing transverse momentum in pp collisions at s = 8 tev with the atlas detector," *The European Physical Journal C*, vol. 75, no. 7, Jul. 2015, ISSN: 1434-6052. DOI: 10.1140/epjc/s10052-015-3517-3. http://dx.doi.org/10.1140/epjc/s10052-015-3517-3.

[212] V. Khachatryan, A. Sirunyan, A. Tumasyan, W. Adam, T. Bergauer, M. Dragicevic, J. Erö, M. Friedl, R. Frühwirth, V. Ghete, and et al., "Search for new phenomena in monophoton final states in proton–proton collisions at s=8 tev," *Physics Letters B*, vol. 755, pp. 102–124, Apr. 2016, ISSN: 0370-2693. DOI: 10.1016/j.physletb.2016.01.057. http://dx.doi.org/10.1016/j.physletb.2016.01.057.

[213] G. Aad, B. Abbott, J. Abdallah, S. Abdel Khalek, O. Abdinov, R. Aben, B. Abi, M. Abolins, O. S. AbouZeid, H. Abramowicz, and et al., "Search for new phenomena in events with a photon and missing transverse momentum inppcollisions ats=8 tevwith the atlas detector," *Physical Review D*, vol. 91, no. 1, Jan. 2015, ISSN: 1550-2368. DOI: 10.1103/physrevd.91.012008. http://dx.doi.org/10.1103/PhysRevD.91.012008.

[214] V. Khachatryan, A. M. Sirunyan, A. Tumasyan, W. Adam, E. Asilar, T. Bergauer, J. Brandstetter, E. Brondolin, M. Dragicevic, J. Erö, and et al., "Search for dark matter and unparticles produced in association with a z boson in proton-proton collisions at s = 8 tev," *Physical Review D*, vol. 93, no. 5, Mar. 2016, ISSN: 2470-0029. DOI: 10.1103/physrevd.93.052011. http://dx.doi.org/10.1103/PhysRevD.93.052011.

[215] G. Aad, T. Abajyan, B. Abbott, J. Abdallah, S. Abdel Khalek, O. Abdinov, R. Aben, B. Abi, M. Abolins, O. S. AbouZeid, and et al., "Search for dark matter in events with azboson and missing transverse momentum inppcollisions ats=8 tevwith the atlas detector," *Physical Review D*, vol. 90, no. 1, Jul. 2014, ISSN: 1550-2368. DOI: 10.1103/physrevd.90.012004. http://dx.doi.org/10.1103/PhysRevD.90.012004.

[216] C. Amole, M. Ardid, I. J. Arnquist, D. M. Asner, D. Baxter, E. Behnke, P. Bhattacharjee, H. Borsodi, M. Bou-Cabo, P. Campion, and et al., "Dark matter search results from the pico−60 c3f8 bubble chamber," *Physical Review Letters*, vol. 118, no. 25, Jun. 2017, ISSN: 1079-7114. DOI: 10.1103/physrevlett.118.251301. http://dx.doi.org/10.1103/PhysRevLett.118.251301.

[217] *Dark matter summary plots cern, geneva.* 2018. https://twiki.cern.ch/twiki/bin/view/CMSPublic/SummaryPlotsEXO13TeV#Dark_Matter_Summary_plots.

[218] M. L. Mangano, M. Moretti, F. Piccinini, and M. Treccani, "Matching matrix elements and shower evolution for top-quark production in hadronic collisions," *JHEP*, vol. 01, p. 013, 2007. DOI: 10.1088/1126-6708/2007/01/013. arXiv: hep-ph/0611129 [hep-ph].

[219] R. Frederix and S. Frixione, "Merging meets matching in MC@NLO," *JHEP*, vol. 12, p. 061, 2012. DOI: 10.1007/JHEP12(2012)061. arXiv: 1209.6215 [hep-ph].

[220] Y. Bai, J. Bourbeau, and T. Lin, "Dark matter searches with a mono-z jet," *Journal of High Energy Physics*, vol. 2015, no. 6, Jun. 2015, ISSN: 1029-8479. DOI: 10.1007/jhep06(2015)205. http://dx.doi.org/10.1007/JHEP06(2015)205.

[221] *CMS EGamma POG. CERN, Geneva.* https://twiki.cern.ch/twiki/bin/view/CMS/EgHLTRunIISummary.

[222] CMS Collaboration, "Performance of missing transverse momentum reconstruction in proton-proton collisions at $\sqrt{s} = 13$ TeV using the CMS detector," *JINST*, vol. 14, no. 07, P07004, 2019. DOI: 10.1088/1748-0221/14/07/P07004. arXiv: 1903.06078 [hep-ex].

[223] CMS Collaboration, "Search for dark matter produced with an energetic jet or a hadronically decaying W or Z boson at $\sqrt{s} = 13$ TeV," *JHEP*, vol. 07, p. 014, 2017. DOI: 10.1007/JHEP07(2017)014. arXiv: 1703.01651 [hep-ex].

[224] J. H. Kuhn, A. Kulesza, S. Pozzorini, and M. Schulze, "Electroweak corrections to hadronic photon production at large transverse momenta," *JHEP*, vol. 03, p. 059, 2006. DOI: 10.1088/1126-6708/2006/03/059. arXiv: hep-ph/0508253.

[225] S. Kallweit, J. M. Lindert, S. Pozzorini, M. Schönherr, and P. Maierhöfer, "NLO QCD+EW automation and precise predictions for V+multijet production," in *50th Rencontres de Moriond on QCD and High Energy Interactions*, May 2015, pp. 121–124. arXiv: 1505.05704 [hep-ph].

[226] S. Kallweit, J. M. Lindert, P. Maierhöfer, S. Pozzorini, and M. Schönherr, "NLO electroweak automation and precise predictions for W+multijet production at the LHC," *JHEP*, vol. 04, p. 012, 2015. DOI: 10.1007/JHEP04(2015)012. arXiv: 1412.5157 [hep-ph].

[227] S. Kallweit, J. M. Lindert, P. Maierhofer, S. Pozzorini, and M. Schönherr, "NLO QCD+EW predictions for V + jets including off-shell vector-boson decays and multijet merging," *JHEP*, vol. 04, p. 021, 2016. DOI: 10.1007/JHEP04(2016)021. arXiv: 1511.08692 [hep-ph].

[228] S. Mrenna and P. Skands, "Automated Parton-Shower Variations in Pythia 8," *Phys. Rev. D*, vol. 94, no. 7, p. 074 005, 2016. DOI: 10.1103/PhysRevD.94.074005. arXiv: 1605.08352 [hep-ph].

Appendix A

Unfolding Technial Plots

A sample of Response and covariance matrices are shown for some unfolded quantities are shown in Figures A.1–A.9.

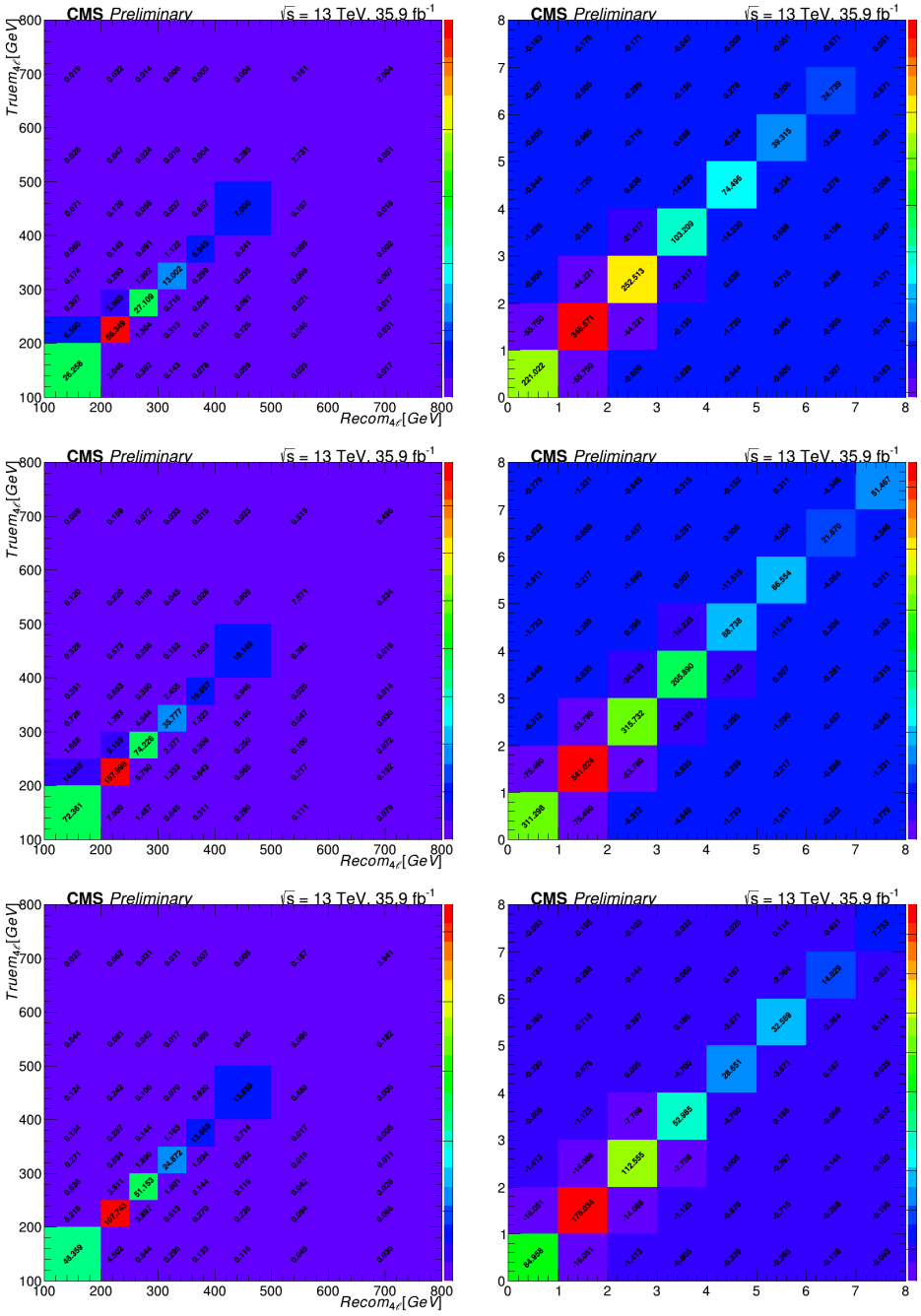

Figure A.1: Response matrices (left) and covariance matrices (right) for four-lepton mass with 35.9 fb^{-1}in the 4e channel (top), 2e2μ channel (middle), and 4μ channel (bottom). The x-axis is for the reconstruction-level quantity, the y-axis is for the true-level quantity.

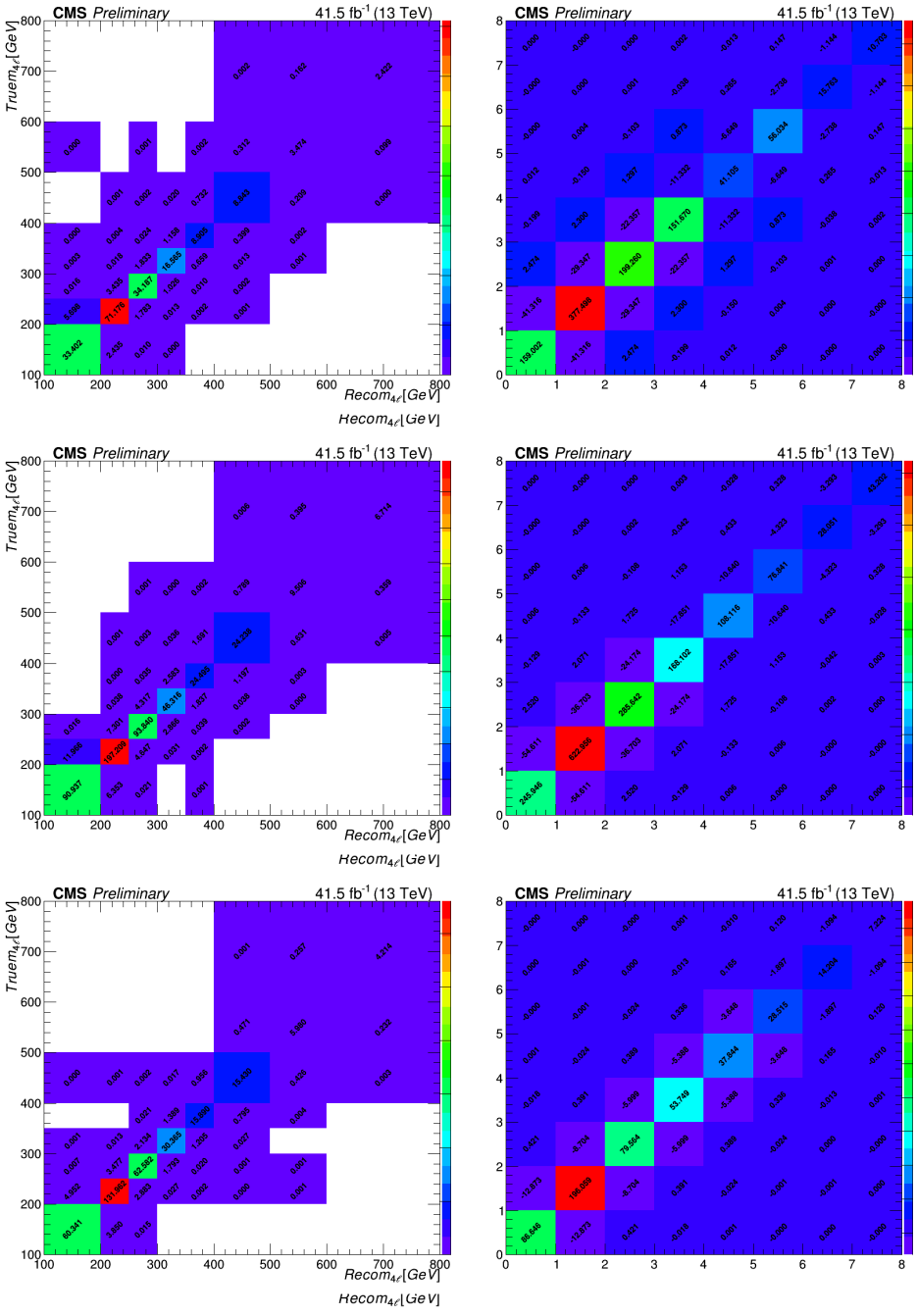

Figure A.2: Response matrices (left) and covariance matrices (right) for four-lepton mass with 41.5 fb^{-1}in the 4e channel (top), 2e2μ channel (middle), and 4μ channel (bottom). The x-axis is for the reconstruction-level quantity, the y-axis is for the true-level quantity.

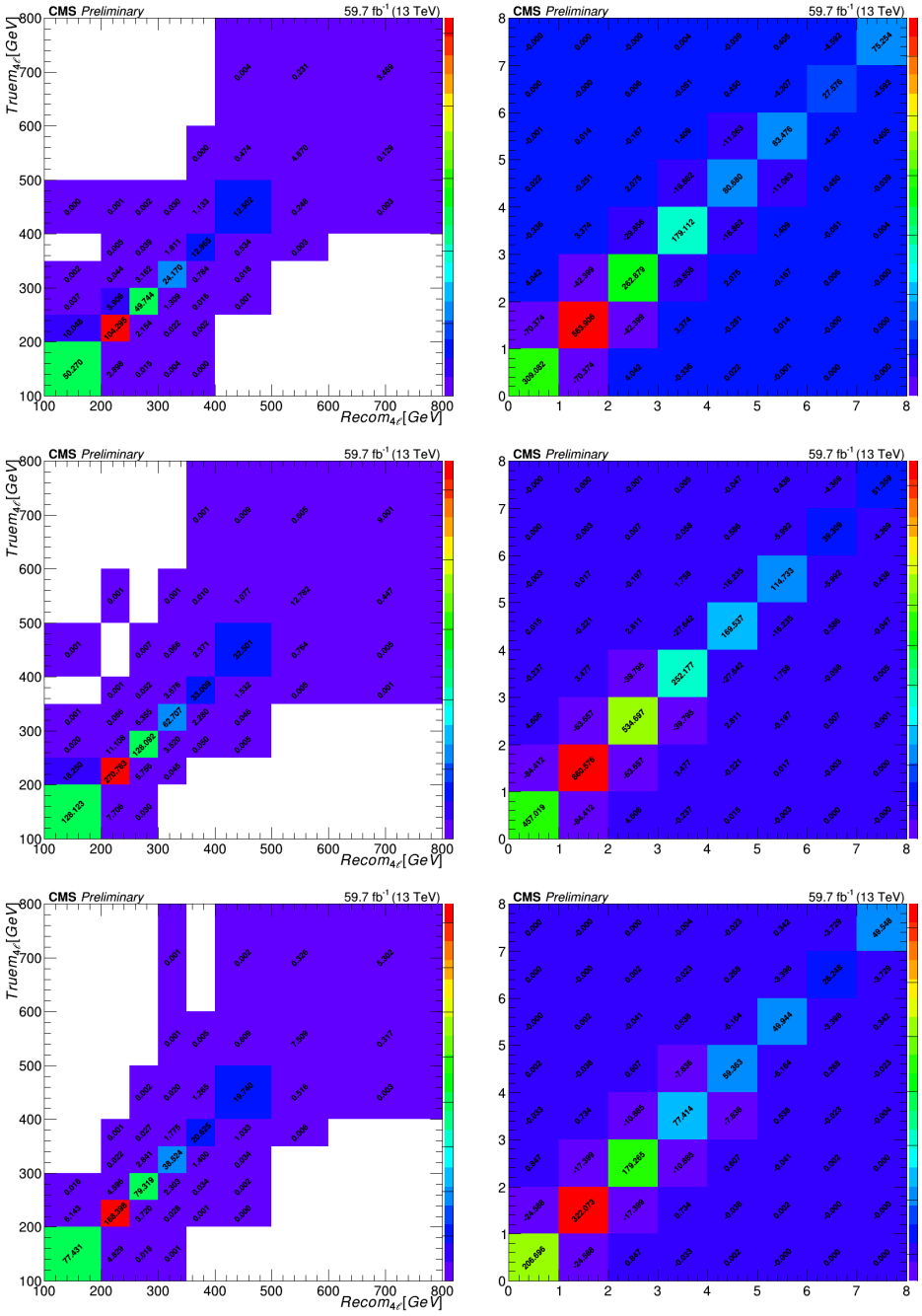

Figure A.3: Response matrices (left) and covariance matrices (right) for four-lepton mass with 59.7 fb^{-1}in the 4e channel (top), 2e2μ channel (middle), and 4μ channel (bottom). The x-axis is for the reconstruction-level quantity, the y-axis is for the true-level quantity.

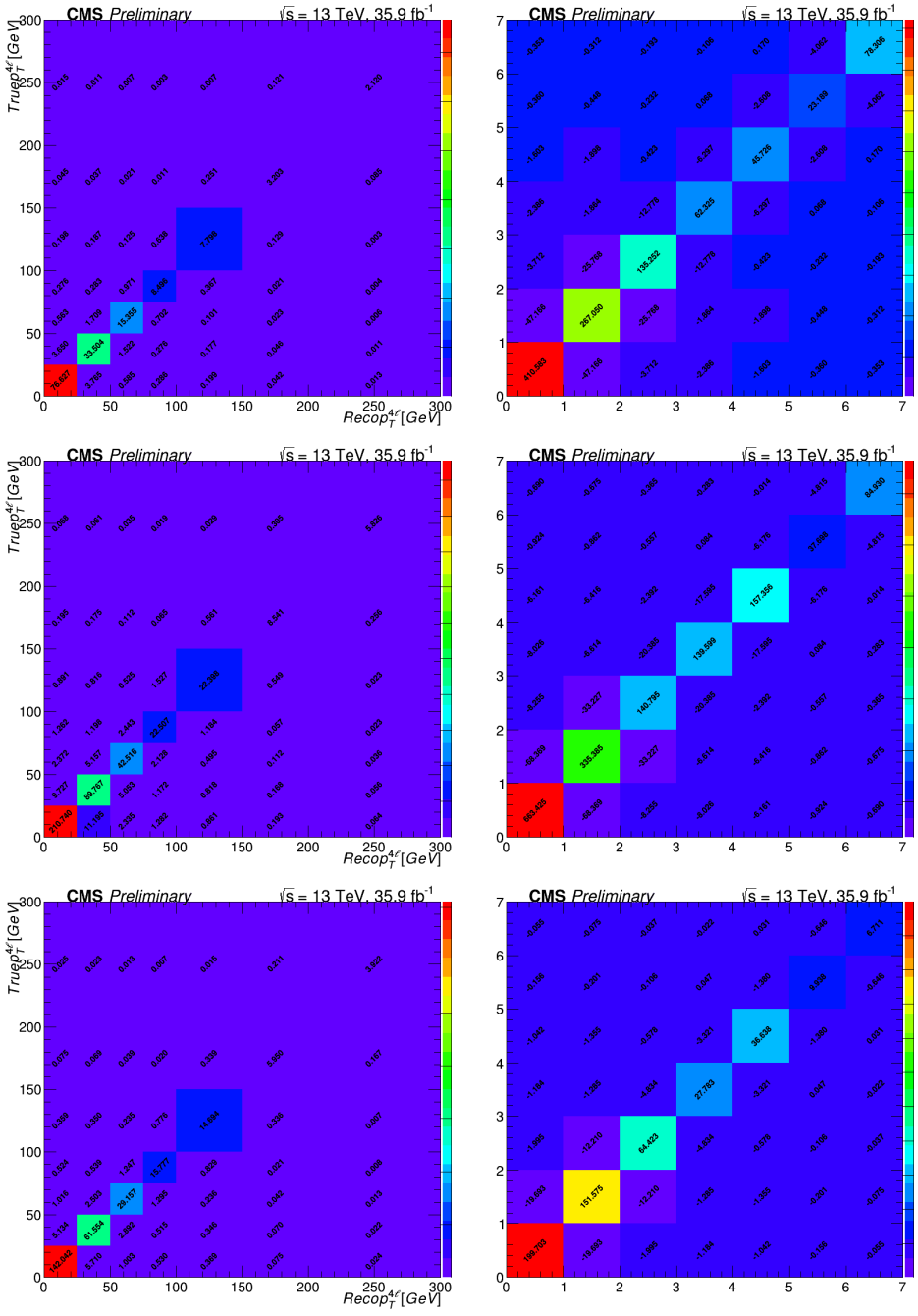

Figure A.4: Response matrices (left) and covariance matrices (right) for four-lepton p_{T} with 35.9 fb^{-1}in the 4e channel (top), 2e2μ channel (middle), and 4μ channel (bottom). The x-axis is for the reconstruction-level quantity, the y-axis is for the true-level quantity.

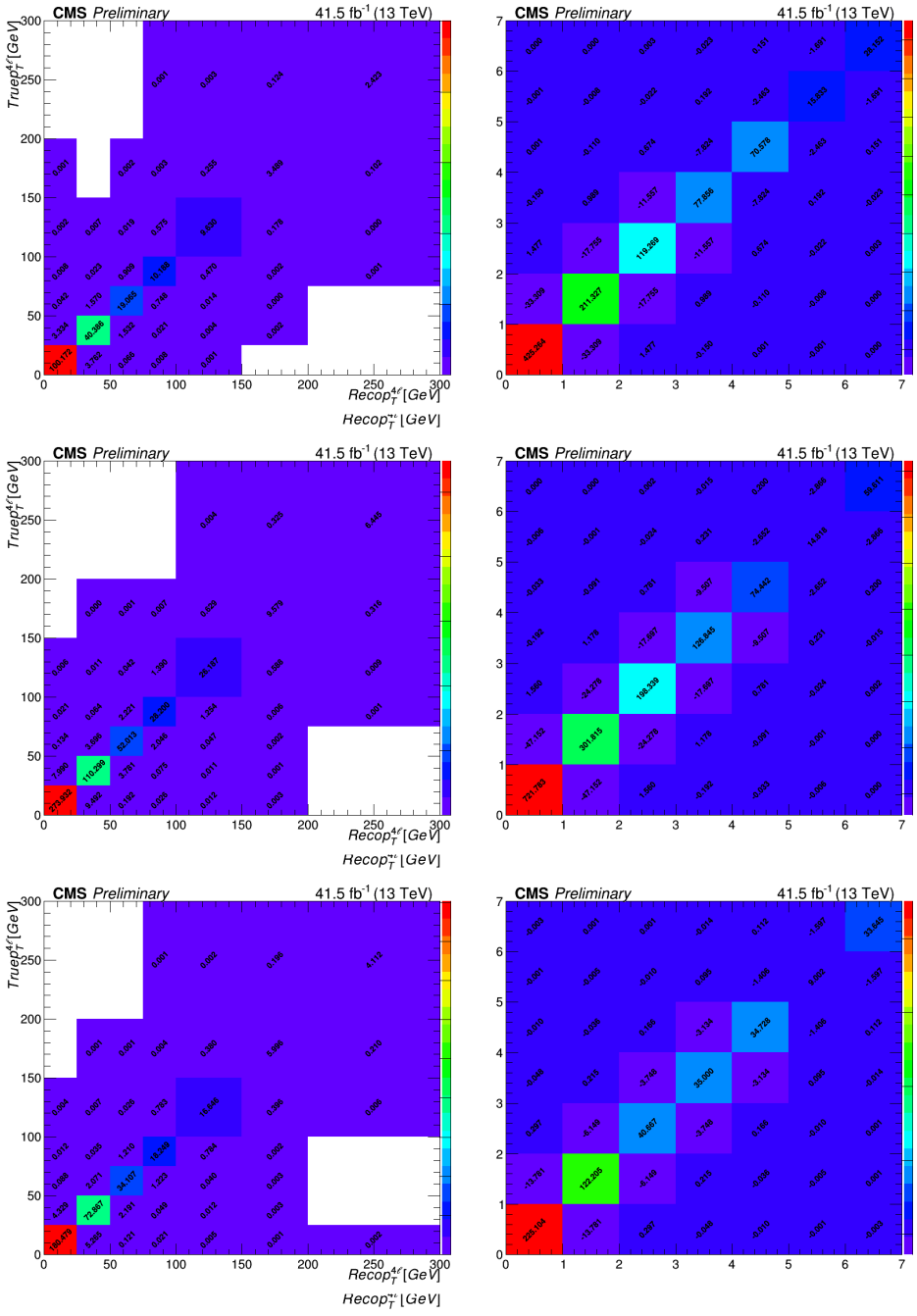

Figure A.5: Response matrices (left) and covariance matrices (right) for four-lepton p_{T} with 41.5 fb^{-1}in the 4e channel (top), 2e2μ channel (middle), and 4μ channel (bottom). The x-axis is for the reconstruction-level quantity, the y-axis is for the true-level quantity.

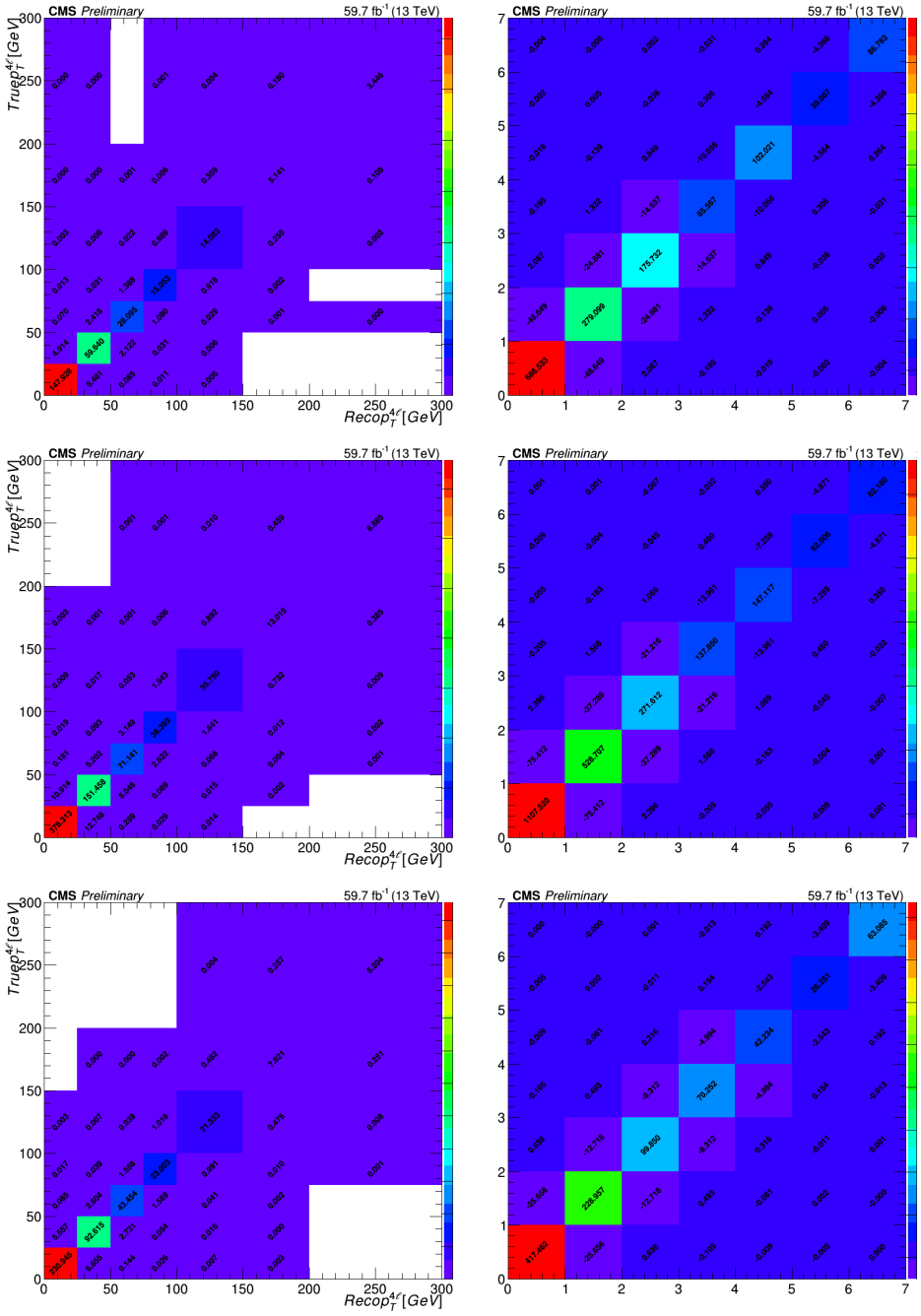

Figure A.6: Response matrices (left) and covariance matrices (right) for four-lepton p_{T} with 59.7 fb^{-1}in the 4e channel (top), 2e2μ channel (middle), and 4μ channel (bottom). The x-axis is for the reconstruction-level quantity, the y-axis is for the true-level quantity.

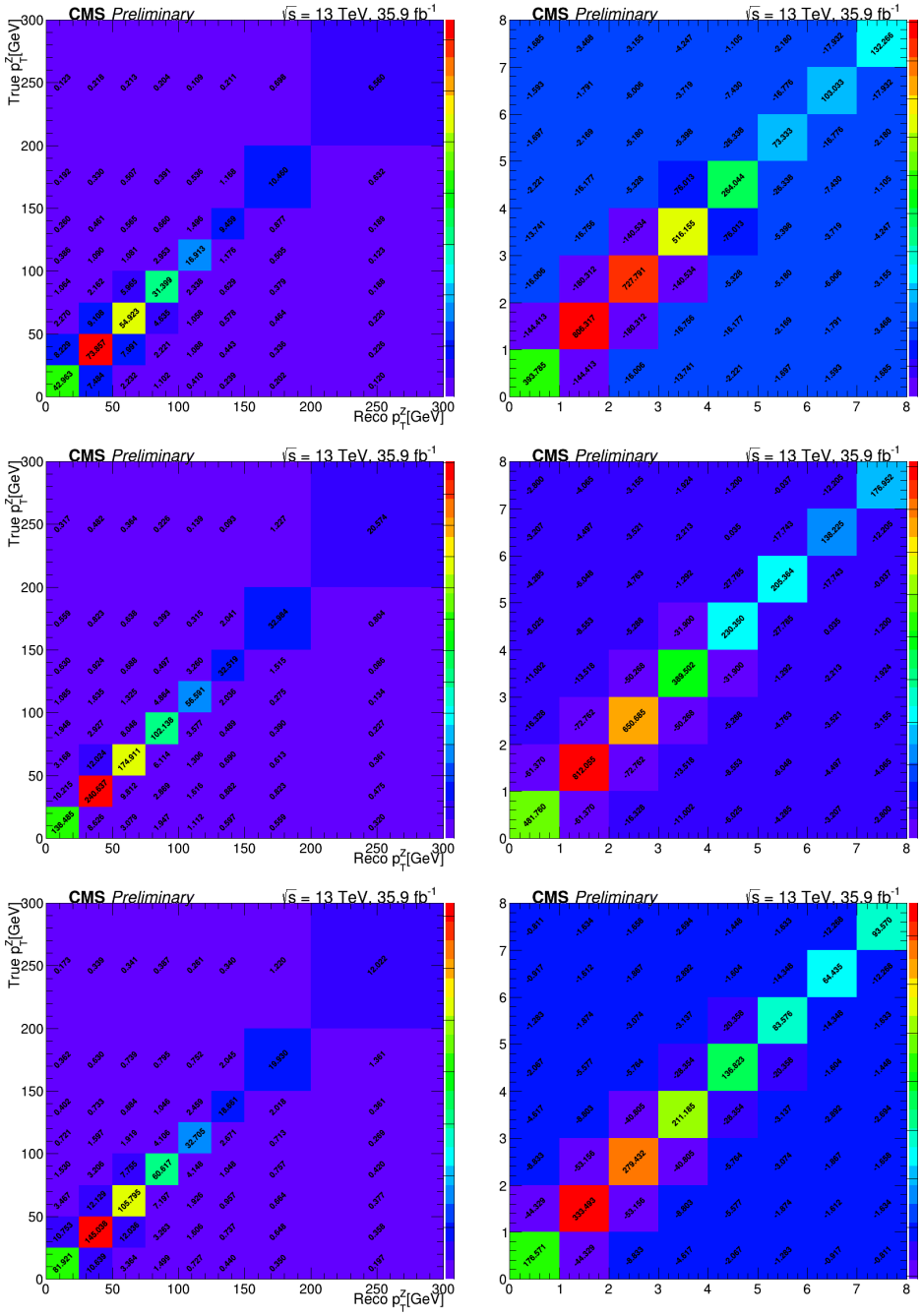

Figure A.7: Response matrices (left) and covariance matrices (right) for the p_{T} of all Z bosons with 35.9 fb^{-1}in the 4e channel (top), 2e2μ channel (middle), and 4μ channel (bottom). The x-axis is for the reconstruction-level quantity, the y-axis is for the true-level quantity.

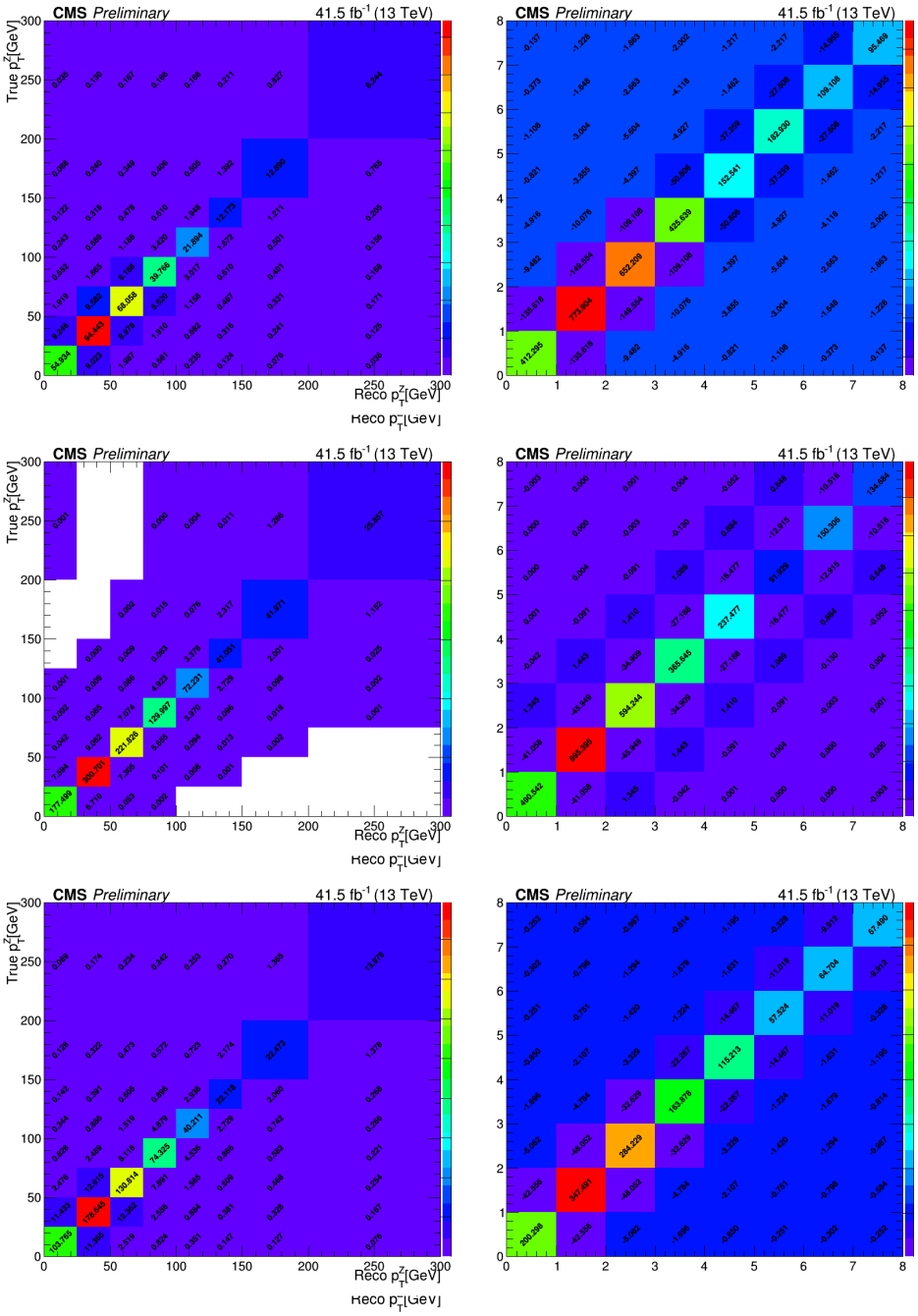

Figure A.8: Response matrices (left) and covariance matrices (right) for the p_{T} of all Z bosons with 41.5 fb^{-1}in the 4e channel (top), 2e2μ channel (middle), and 4μ channel (bottom). The x-axis is for the reconstruction-level quantity, the y-axis is for the true-level quantity.

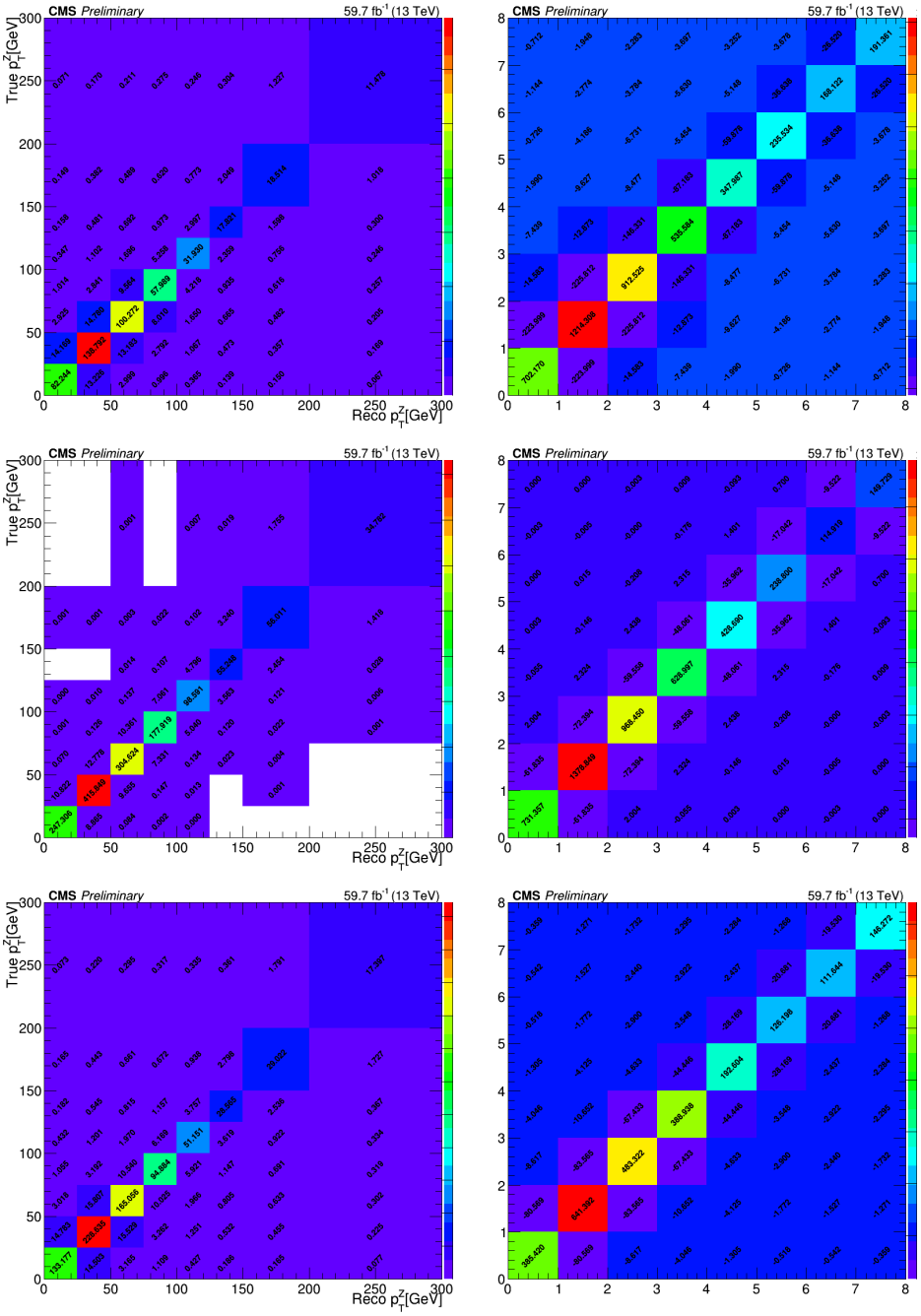

Figure A.9: Response matrices (left) and covariance matrices (right) for the p_{T} of all Z bosons with 59.7 fb^{-1}in the 4e channel (top), 2e2μ channel (middle), and 4μ channel (bottom). The x-axis is for the reconstruction-level quantity, the y-axis is for the true-level quantity.

Appendix B

Status of Mono-Z' Analysis

The status of a search for new physics in events with a mono-Z' jet and large missing transverse energy at 13 TeV proton-proton collisions collected by the CMS experiment at the LHC in the 2016-2018 running period corresponding to an integrated luminosity of 137 fb^{-1} is also presented. Results are interpreted in terms of a signal in which a pair of dark matter particles are produced with the final state radiation of a light Z' which can appear as a narrow jet after it decays hadronically. A dedicated search for dark matter is performed using the unique substructure of this Mono-Z' Pencil Jet. No significant deviations from the background expectations are found so far, and limits will be set on relevant model parameters, significantly extending the results previously achieved in MonoJet initial state radiation searches.

A Simplifed particle dark matter models

A.1 Motivation for simplified particle dark matter

The nature of dark matter (DM) is by far one of the most exciting open questions in modern physics. The discovery of dark matter can be traced back to the 1920s

when measurements of vertical motions of stars near the Galactic plane implied the gravitational influence of some invisible dark component [174]. In 1933, Fritz Zwicky deduced the existence of a non-luminous constituent of the Coma cluster by measuring the velocities of the galaxies within and famously called it **dark matter** [175]. Evidence for dark matter from cosmological and astrophysical observation has piled up over the last century making it hard to ignore.

Evidence of dark matter has been confirmed through study of galactic rotation curves [176, 177] where rotation velocity of stars in galaxies does not behave in accordance with the visible mass distribution. By Newton's law of gravity, the rotational velocity should steadily decrease for stars further away from the center. On the contrary, it can be observed from the flattening of the galactic rotation curves at radii beyond the visible edges of galaxies that significant non-visible matter must exist. As shown in Fig. B.1 reproduced from Ref.[178] , rotational velocity v(r) becomes constant in r towards the edges of the galaxy resulting in this dark matter "halo" enshrouding the galaxy.

The astrophysical evidence also includes observations of gravitational lensing (strong and weak) by clusters [179, 180] and X-ray emissions from hot gas in dense clusters that can provide direct measurements of dark matter density [181]. Furthermore, cosmological observations of the cosmic-microwave-background (CMB) anisotropies in combination with the Λ_{CDM}, the so-called "Standard Model of Cosmology" [15], constrain the dark-matter density of the Universe to be $\Omega_{dm} = 0.222 \pm 0.026$ while the density of baryonic matter is $\Omega_b = 0.0449 \pm 0.0028$ in units of critical density [182].

Despite the abundance of evidence for the *existence* of dark matter, the *nature* remains elusive and all this mounting evidence has been derived solely from the observation of gravitational effects. This raises the legitimate question of whether

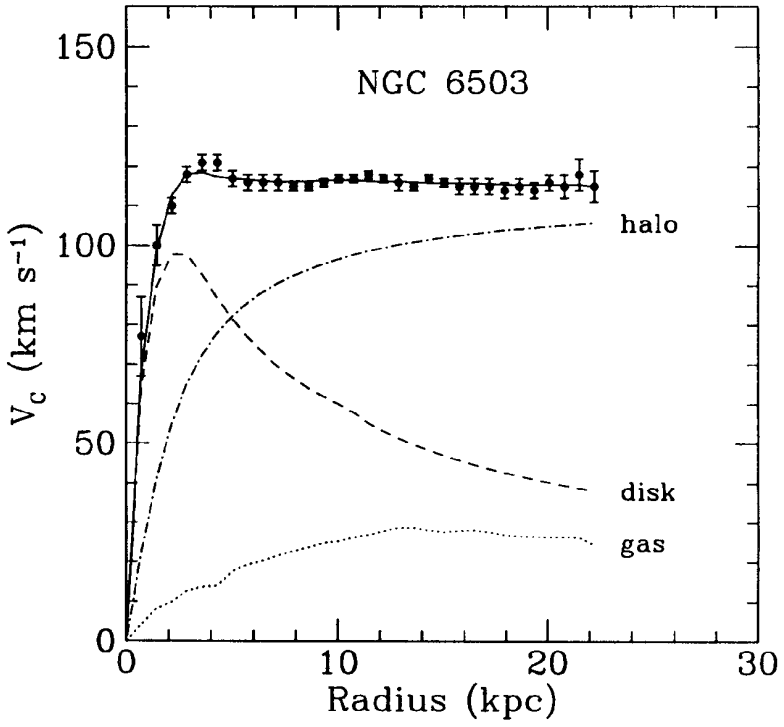

Figure B.1: NGC 6503 galactic rotation curves showing the various contributions of dark matter needed to agree with observation.

these observations could be explained by a modified theory of gravity without any need for extra DM particles. However, Einstein's general relativity has been tested time and again and proven to be remarkably accurate from distance scales of 1mm to large distance scales such as the size of the solar system. In addition to its success, the bullet cluster referenced above has a total mass distribution significantly displaced from its visible which makes it even harder to accept a modified theory of gravity without any DM [183]. Therefore, there are numerous viable theories that predict the existence of dark matter candidates. These particles are expected to have properties that can not only explain all of the preceding cosmological observations but might also allow to them to be detected experimentally. There are several well-motivated candidates; sterile neutrinos, supersymmetric neutralinos and gravitinos, axions, and

Kaluza-Klein excitations in theories with extra dimensions are among the ones widely studied (reviews are given in e.g, Refs. [181, 183–185]).

According to the Λ_{CDM} model, DM was in thermal equilibrium with baryonic matter in the early moments of the Universe which means interactions with the SM should become relevant at a certain energy scale. Furthermore, the **temperature** of the dark matter must be fairly cold. Just before the Universe became matter dominated, dark matter must have been able to collapse gravitationally to form small-scale early galactic structures. Therefore, DM must have a small or nonrelativistic velocity at that time not to free stream out of density perturbations. This temperature argument rules out relativistic neutrinos [15]. Weakly interacting massive particles (WIMPS) are the most popular dark matter candidate as they satisfy all the criteria laid out above. The so-called **WIMPs** with weak-scale masses ($\sim$100 GeV) naturally have a relic abundance close to that observed for dark matter.

In the search for WIMPs, there are three major avenues for dark matter detection as shown in Fig. B.2. **Indirect Detection** involves looking for Standard Model decay products of Dark Matter annihilation from astrophysical sources. **Direct Detection** means looking for recoil due to DM scattering off target nuclei. A thorough review of both direct and indirect experimental results is available in [185].

Then, there are **collider** searches which aim to produce Dark Matter via collisions of SM particles. A review of previous collider results will be included in Section 4.2.

A.2 Simplified Dark Matter Models

While the idea of the **WIMP miracle** is alive and well, it remains elusive. No indirect detection of DM has been made via telescopes or any other technologies and no DM has been found via direct detection even if substantial phase space remains for direct detection experiments to explore. Producing and studying the properties of

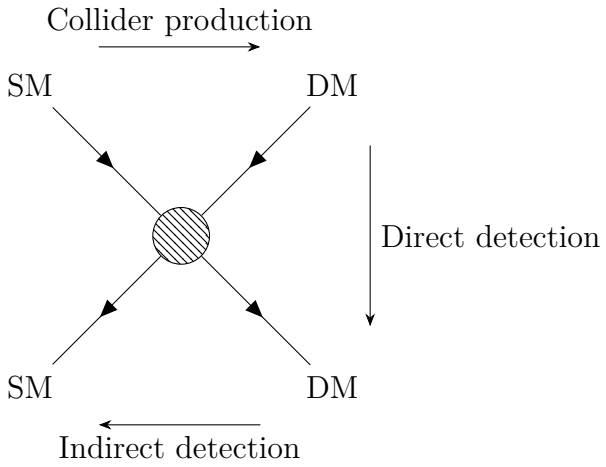

Figure B.2: Three paths to particle dark matter; indirect detection, direct detection and collider production.

DM at the LHC is an exciting possibility and current bounds from ATLAS and CMS complement those from direct and indirect searches. In order compare the results across different experimental approaches, some theoretical foundations are needed. As shown in Fig. B.3, there is a large number of qualitatively different DM models that populate the theory space of all possibilities of physics beyond the SM. In recent years, the DM-EFT approach [186, 187] has proved very successful in analyzing LHC Run 1 data and a lot of progress has also been made in exploring and understanding a variety of complete models.

The concept of the Effective Field Theory (EFT) approach is based on describing the unknown DM interactions with the SM in a direct/economical way. Its simplicity and flexibility allows it to be used in different search contexts making it model-independent. It depends on two parameters: DM mass and the interaction scale where energy scale of the interaction $\sqrt{s} \ll \Lambda$. A more detailed understanding of the EFT treatment of collider DM production and the EFT of WIMP couplings can be gained from Ref.[186].

The main takeaway is that at the energy scales (and coupling strengths) accessi-

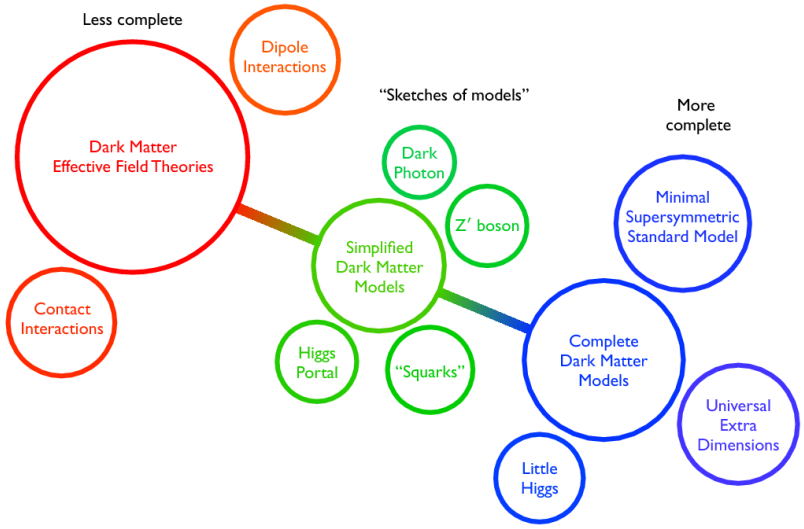

Figure B.3: Dark Matter theory space.

Figure B.4: Feynman diagrams showing basic difference between EFT operator and Simplified Dark Matter Models.

ble to the LHC, the validity of the EFT approximation can not be guaranteed and therefore, there has been a shift towards using simplified models to probe dark matter at the LHC. These simplified models contain a resolved mediator between DM and the SM [188] where a fermionic dark matter candidate with mass m_χ couples to a mediator of mass m_{med} with coupling g_χ and the mediator in turn couples to SM quarks with coupling g_q as shown in the Fig. B.4. The mediator, denoted Z', can take four different spin-party configurations and the respective operators in the DM Lagrangian are given:

$$
\begin{aligned}
\mathscr{L}_{\text{vector}} &= g_\chi {Z'}_\mu \bar{\chi}\gamma^\mu\chi + g_q \sum_q {Z'}_\mu \bar{q}\gamma^\mu q, \\
\mathscr{L}_{\text{axial vector}} &= g_\chi {Z'}_\mu \bar{\chi}\gamma^5\gamma^\mu\chi + g_q \sum_q {Z'}_\mu \bar{q}\gamma^5\gamma^\mu q, \\
\mathscr{L}_{\text{scalar}} &= g_\chi \phi\bar{\chi}\chi + g_q \frac{\phi}{\sqrt{2}} \sum_q y_q \bar{q}q, \\
\mathscr{L}_{\text{pseudoscalar}} &= i g_\chi \phi\bar{\chi}\gamma^5\chi + g_q \frac{i\phi}{\sqrt{2}} \sum_q y_q \bar{q}\gamma^5 q.
\end{aligned}
\tag{B.1}
$$

Since the dark matter particles would go undetected in a collider experiment, some additional SM interaction is needed. The most common and well studied form of additional interaction is initial state radiation (ISR) where a SM boson (gluon, photon or Z boson) is radiated from one of the incoming quarks and there is a large set of signatures that have been proposed and searched at the LHC; mono-jet [186, 189], mono-photon [190–192], mono-Z [193–196] and many more.

According to the LHC-DM group, kinematic distributions are robust to different coupling values and hence the choice of $g_q = 0.25$, $g_\chi = 1.0$ is recommended to reduce the parameter space to be scanned for any simplified model. The minimal set of parameters under consideration are g_χ, g_q, m_χ and m_{med} and after fixing g_q, g_χ, collider constraints on (m_χ,m_{med}) can be translated into constraints on DM-nucleon cross section from direct detection experiments using the formula given [197].

$$
\begin{aligned}
F(g_q, g_{\text{DM}}, m_{\text{med}}, m_{\text{DM}}) &= \left(\frac{g_q g_{\text{DM}}}{0.25}\right)^2 \left(\frac{1\,\text{TeV}}{m_{\text{med}}}\right)^4 \left(\frac{m_n m_{\text{DM}}}{(m_n + m_{\text{DM}})\cdot 1\,\text{GeV}}\right)^2, \\
\sigma_{\text{SI}} &= 6.9 \times 10^{-41}\,\text{cm}^2 \cdot F(\ldots), \quad \text{(vector)} \\
\sigma_{\text{SD}} &= 2.4 \times 10^{-42}\,\text{cm}^2 \cdot F(\ldots), \quad \text{(axial vector)}
\end{aligned}
\tag{B.2}
$$

where $m_n = 0.939\,\text{GeV}$ is the average mass of a nucleon.

B Particle Dark Matter Models and Previous Results

B.1 Introduction

As described in section A.2, collider searches for dark matter have moved towards signatures that are less model-dependent and produce results that are complimentary to direct and indirect detection experiments. The simplified model of dark matter in association with a Z' has also been studied [198–204] but the mono-Z' model relevant to this thesis has never been studied before and hence there are no previous experimental results for this specific final state. While the most recent mono-jet result from CMS [205] can be used as a benchmark for this analysis, there is an important difference between this analysis and all previous mono-X studies.

In this chapter, a summary of previous experimental results from several dark matter analyses is presented with special focus on the most stringent experimental limits set by the ATLAS and CMS experiments. As none of these analyses report significant direct evidence of dark matter, results are reported in terms of exclusion limits on model parameters. Upper limits are placed at 95% confidence level (CL) on signal strength $\mu = \frac{\sigma}{\sigma_{th}}$ (the ratio of observed to theoretical signal cross section) as a function of model parameters. The threshold value of a given model parameter where the 95% CL upper limit on μ crosses unity determines the exclusion space.

B.2 Particle dark matter models

Since there are no previous experimental results for FSR Z' models, we will use the mono-X ISR searches as benchmarks for this work. Fig. B.5 compares the limits set by three such mono-X searches within CMS. The most stringent limits are set

by the mono-jet analysis followed by monophoton and the mono-Z searches. While all three analysis have similar final states of large missing energy ($\overrightarrow{p}_T^{miss}$) with an ISR gluon, ISR photon or a Z boson, the production rates differ due to the type of the ISR particle(s) that emerge against the $\overrightarrow{p}_T^{miss}$. The most stringent limits on the simplified model parameters are placed by the 35.9 fb^{-1} result of CMS in the mono-Jet channel [205] which establishes observed (expected) lower limits on the mediator mass of $m_{med} > 950(1150)$ GeV for 1 GeV dark matter mass for both the vector and axial vector mediated DM production models in the on-shell ($2m_{DM} \leq m_{med}$) regime.

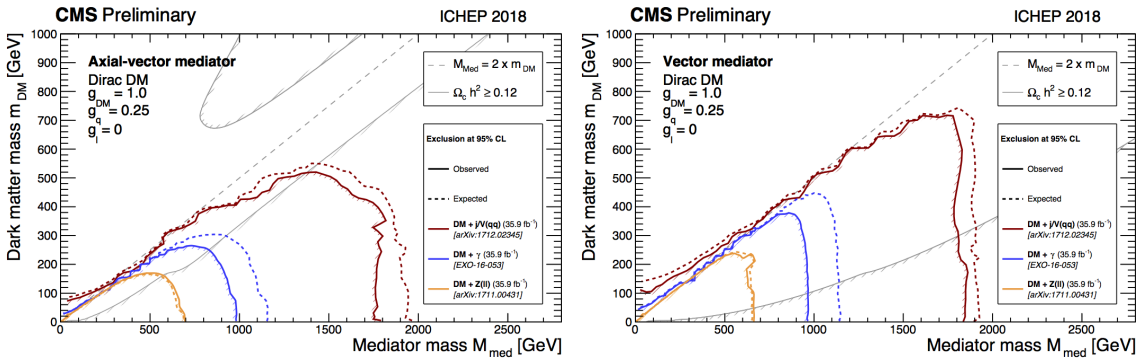

Figure B.5: Summary plots of limits on DM simplified model parameters, shown in [206]. Simplified models are excluded at 95% CL or above for parameter values under the contours. Results based on three different final states are shown: mono-$Z(ll)$ [207] in yellow, mono-$j/V(qq)$ [205] in red, and monophoton [208] in blue,the latter corresponding to the new results presented in this thesis. The Ω_c^2 curves correspond to constraints on the cosmological DM abundance set by Planck satellite measurements [209].

As mentioned in section A.2, the LHC run 1 CMS and ATLAS mono-X (X $\rightarrow$ Jet, Photon, Z) searches [210–215] followed the DM-EFT approach which makes it difficult to interpret those results in the context of simplified models. However, during LHC Run 2, there has been a transition to simplified models following the ATLAS–CMS Dark Matter Forum recommendations [188] which allow collider results to be compared directly with limits set by direct detection (DD) and Indirect detection

(ID) experiments. As introduced in section A.1, DD experiments rely on DM-nucleon scattering and these scattering processes can be classified as following: spin-dependent (SD) scattering or spin-independent (SI) scattering. SD scattering cross-sections are directly proportional to J(J+1), the nuclear angular momentum of the detection material whereas SI cross sections increase considerably with the mass of the target nuclei. Therefore, DD experiments with heavy target nuclei are much more sensitive to SI couplings whereas ID and collider searches are less affected by the spin structure.

In Fig. B.6 and Fig. B.7 recent limits from dark matter searches at the CMS experiment are compared to the direct detection results, for spin-dependent and spin-independent interactions, respectively. An axial-vector/vector mediator corresponds to spin-dependent (SD)/ spin-independent (SI) DM-nucleon scattering, respectively. From these comparisons, we note that the LHC is especially competitive in limits on the Spin Dependent (Axial Vector mediators) cross sections and also better at low mass. As shown in Fig. B.6, the PICO-60 experiment has established the most stringent non-collider limits on the spin-dependent parameter space to date, excluding DM-nucleon cross sections down to 3.4 x $10^{-41} cm^2$ for a 30 GeV WIMP[216].

C Samples Used in Mono-Z' Analysis

The two main backgrounds to the analysis are Z($\nu\nu$) + jets and W + jets. In both cases, samples are produced at leading order (LO) in QCD using the MadGraph generator in several bins of hadronic transverse energy sum (H_T). Drell-Yan processes, Z($\ell\ell'$) + jets, passes the analysis selection and hence mimics signal-like events in the case where the leptons from the Z boson decay pass undetected. In addition, Z(ee) + jets and Z($\mu\mu$) + jets events are also used as control samples for estimating the Z($\nu\nu$) + jets background. Monte Carlo samples for this process are generated at LO

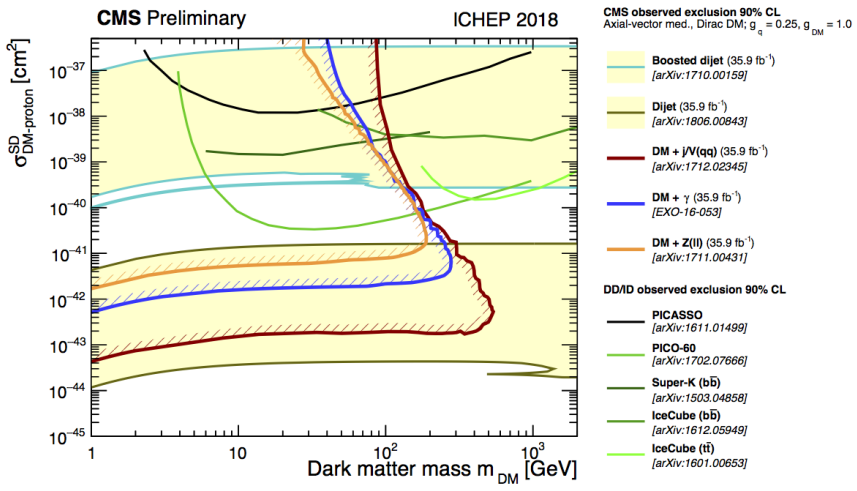

Figure B.6: A comparison of CMS results to the $m_{DM} - \sigma_{SD}$ plane. Unlike in the mass-mass plane, the limits are shown at 90% CL. The CMS contour in the SD plane is for an Axial-vector mediator, Dirac DM and couplings $g_q = 0.25$ and $g_{DM} = 1.0$. The SD exclusion contour is compared with limits from PICASSO and PICO experiments, the IceCube limit for the $t\bar{t}$, $b\bar{b}$ annihilation channels, and the Super-Kamiokande limit for the $b\bar{b}$ annihilation channel. It should be noted that the CMS limits do not include a constraint on the relic density and also the absolute exclusion of the different CMS searches as well as their relative importance will strongly depend on the chosen coupling and model scenario. Therefore, the shown CMS exclusion regions in this plot are not applicable to other choices of coupling values or models. Reproduced from Ref.[217]

in QCD using the MadGraph generator in several bins of H_T.

γ + jets and QCD samples are also produced at LO in QCD using the MadGraph generator in several bins of H_T. There are also Next-to-leading order (NLO) $t\bar{t}$ samples which are produced with the MadGraph5_aMC@NLO generator. Diboson samples for WW, WZ and ZZ production are generated at LO with Pythia8.

The 2016 samples use the NNPDF3.0 PDF sets [96] whereas the 2017 and 2018 MC samples use the NNPDF3.1 [97] PDF sets. The simulation steps including parton showering, hadronization and UE simulation are done with Pythia8 using the CUETP8M1 tune [120] for the 2016 samples and CP5 tune [121] for the 2017,2018 samples. In the case of the MadGraph5_aMC@NLO samples, jets from the matrix

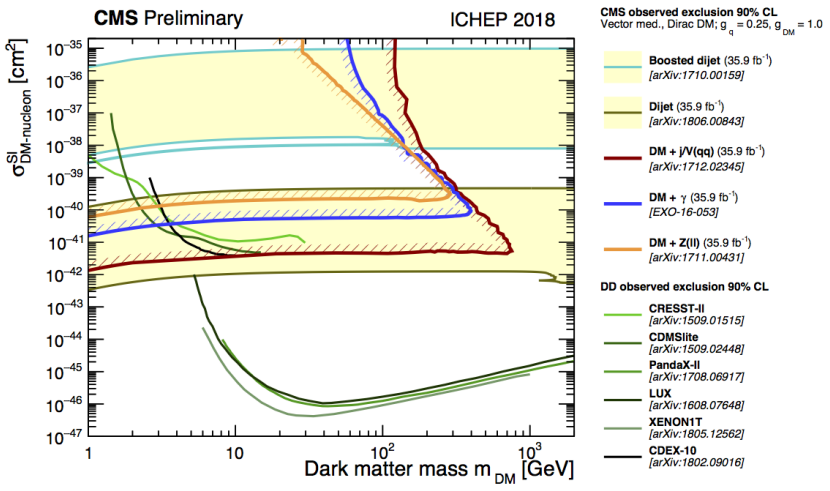

Figure B.7: A comparison of CMS results to the $m_{DM} - \sigma_{SI}$ plane. Unlike in the mass-mass plane, the limits are shown at 90% CL. The CMS contour in the SI plane is for a Vector mediator, Dirac DM and couplings $g_q = 0.25$ and $g_{DM} = 1.0$. The CMS SI exclusion contour is compared with the XENON1T 2017, LUX 2016, PandaX-II 2016, CDMSLite 2015 and CRESST-II 2015 limits, which constitutes the strongest documented constraints in the shown mass range. It should be noted that the CMS limits do not include a constraint on the relic density and also the absolute exclusion of the different CMS searches as well as their relative importance will strongly depend on the chosen coupling and model scenario. Therefore, the shown CMS exclusion regions in this plot are not applicable to other choices of coupling values or models. Reproduced from Ref.[217]

element calculations are matched to the parton shower (PS) description following the MLM [218] (FxFx [219]) prescription to match jets from matrix element calculations and parton shower description for LO (NLO) samples.

C.1 Generation of Mono-Z' signals

In the mono-Z' analysis, the simplified models described in section A.2 are considered. After performing checks comparing cross sections with the EFT model of mono-Z' and in consultation with the authors of the Mono-Z' model [220], a simplified model was used for signal event generation following the LHC-DMF Run 2 recommenda-

tions [188]. The used signal samples were generated with MadGraph5_aMC@NLO interfaced with Pythia tune CP5 [121]. Since a light Z' and large recoil are essential requirements in the Mono-Z' model, the following model parameters were fixed; $M_{Z'} = 1\,\text{GeV}$, $E_T^{miss} > 200\,\text{GeV}$ and the recommended [188] couplings $g_{SM} = 0.25$ and $g_{DM} = 1.0$. The scanned mediator masses (m_{MED}) for particular dark matter masses (m_χ) are given in Table B.1

$m_\chi[GeV]$	$m_{MED}[GeV]$
1	10,20,50,100,200,300,500,1000,10000
10	10,15,50,100,10000
50	10,50,95,200,300,10000
150	10,200,295,500,1000,10000
500	10,500,995,10000
1000	10,1000,10000

Table B.1: Mono-Z' signal samples phase space.

D Mono-Z' Analysis Strategy and Results

As discussed in section A.1, there are many searches for dark matter from direction detection, indirect detection and accelerator-based experiments. At the LHC, there are possibilities of extending the dark mater search to models beyond the capabilities of both direct and indirect detection. The so-called monojet search, where the detection of dark matter is done by looking for missing momentum in association with one or more jets, has been a popular and promising channel at the LHC. Like monojet, many existing mono-X studies have concentrated on identifying signals using the initial state radiation (ISR) of partons inside an accelerated proton, in this thesis, the search for dark matter in events with large missing transverse energy ($E_{\text{T}}^{\text{miss}}$), plus final state radiation (FSR) of a GeV-scale Z' is presented. The Z from FSR can

decay back to SM particles and behave as a visible object in the collider while there is large missing energy ($E_{\mathrm{T}}^{\mathrm{miss}}$) from the dark matter particles as shown in Fig. below.

Alter Fig. 2.9 to make the Mono-Z' Feynman diagram

The focus in this particular search is on the dominant decay of the Z' into quarks. With a light (GeV-scale) Z', there are two important effects that result in a new and unique collider signature.

- The Z' appears as a narrow (Pencil) jet with a small multiplicity of charged pions and neutral pions that decay to photons.
- The rate for dark matter FSR of Z' jets can be larger than the rate for ISR jets.

Therefore, the narrow but highly boosted jet + $p_{\mathrm{T}}^{\mathrm{miss}}$ final state defines the signal region (SR) of this search. Backgrounds in the signal region are estimated both via simulation and and control regions (CRs) in data (section D.2) and systematic uncertainties are assigned accordingly. Finally, a simple statistical model is implemented to derive one- and two-dimensional expected limits in the Mono-Z' signal phase space described in Table B.1.

D.1 Trigger selection

Events collected for the signal region of this analysis are selected using a set of triggers that have large $p_{\mathrm{T}}^{\mathrm{miss}}$ and large $H_{\mathrm{T}}^{\mathrm{miss}}$ where $E_{\mathrm{T}}^{\mathrm{miss}}$ is the magnitude of the negative vectorial sum of the $p_{\mathrm{T}}$of all particles at trigger level and $H_{\mathrm{T}}^{\mathrm{miss}}$ is the magnitude of the negative vectorial sum of the momenta of all jets with $p_{\mathrm{T}} > 20\,\mathrm{GeV}$. Based on the online particle flow (PF) algorithm, identified PF muons are removed from the $E_{\mathrm{T}}^{\mathrm{miss}}$ and $H_{\mathrm{T}}^{\mathrm{miss}}$ calculation so the same trigger paths can also be used to select single

and double muon CR events for the W and Z CRs respectively. Furthermore, tight requirements are placed on the jets used in the $H_{\mathrm{T}}^{\mathrm{miss}}$ calculation in order to avoid collecting events that contain noise signals coming from the detector.

As expected, HLT parameters change over the course of three years of data taking so a full list of trigger paths used for this analysis is provided in Tables B.2–B.3. The remaining control regions used in the analysis include single and dielectric events which are selected using the unprescaled single electron trigger with the lowest p_{T} threshold in each year. As given in the trigger tables B.2–B.3, this single electron trigger is used in combination with a higher p_{T} threshold single electron trigger as well as a single photon trigger [221] which provides a safeguard against failures of track reconstruction at the HLT live. Finally, the events in the photon control region are selected with the same single photon trigger.

Trigger Paths (pp collisions 2016)
MET
`HLT_PFMETNoMu90_PFMHTNoMu90_IDTight_v*`
`HLT_PFMETNoMu110_PFMHTNoMu110_IDTight_v*`
`HLT_PFMETNoMu120_PFMHTNoMu120IDTight_v*`
`HLT_PFMET170_HBHECleaned_v*`
Single Electron
`HLT_Ele27_WPTight_Gsf_v*`
`HLT_Ele115_CaloIdVT_GsfTrkIdT_v*`
Single Photon
`HLT_Photon175_v*`

Table B.2: Triggers used in the 2016 analysis

The trigger efficiencies were measured in the 2016 monojet search [205] to be 97% for events passing the analysis selection for $p_{\mathrm{T}}^{\mathrm{miss}} > 250\,\mathrm{GeV}$ and becomes fully efficient for events with $p_{\mathrm{T}}^{\mathrm{miss}} > 350\,\mathrm{GeV}$. Similar studies will be performed by the UW Mono-Z' group but are likely to yield similar results.

Trigger Paths (pp collisions 2017-2018)
MET
`HLT_PFMETNoMu120_PFMHTNoMu120_IDTight_v*` `HLT_PFMETNoMu120_PFMHTNoMu120_IDTight_PFHT60_v*`
Single Electron
`HLT_Ele35_WPTight_Gsf_v*` (2017), `HLT_Ele32_WPTight_Gsf_v*` (2018) `HLT_Ele115_CaloIdVT_GsfTrkIdT_v*`
Single Photon
`HLT_Photon200_v*`

Table B.3: Triggers used in the 2017 and 2018 analysis

D.2 Event Selection

In this section, the selections used to identify events in the signal region as well as the five control regions are described while all relevant object definitions and different identification requirements have been discussed in detail in Chapter 6.

D.2.1 Signal region

Candidate events in the signal region are selected with the following requirements.

- Events pass the $E_{\mathrm{T}}^{\mathrm{miss}}$ triggers described in section D.1 corresponding to the MET primary dataset
- Events pass the $E_{\mathrm{T}}^{\mathrm{miss}}$ filters described in [222] which suppress detector noise and beam backgrounds
- Leading AK4 jet in the event has $p_{\mathrm{T}} > 200\,\mathrm{GeV}$
- $E_{\mathrm{T}}^{\mathrm{miss}} > 250\,\mathrm{GeV}$
- $\Delta\phi(\mathrm{jet}, E_{\mathrm{T}}^{\mathrm{miss}}) > 0.5$ for the first four leading AK4 jets in the event
- Lepton veto *i.e.* no loose electrons, muons or taus
- Photon veto *i.e.* no loose photons

- B-jet veto

D.2.2 Single muon control region

Events in the single muon control region are obtained using the same selection as signal region with the following differences.

- Events must have exactly one loose muon, passing tight identification requirements with $p_T > 20\,\mathrm{GeV}$.
- Transverse mass of the muon-$p_{\mathrm{T}}^{\mathrm{miss}}$ system must be less than 160 GeV
- $\left|E_{\mathrm{T}}^{\mathrm{miss}} + \tau_{\mu}\right| > 250\,\mathrm{GeV}$

D.2.3 Single electron control region

Events in the single electron control region are obtained using the same selection as signal region with the following differences.

- Events are selected using the single electron triggers described in section D.1 corresponding to the Single Electron datasets
- Events must have exactly one loose electron which also passes tight identification and isolation requirements with $p_T > 40\,\mathrm{GeV}$.
- Transverse mass of the muon-$p_{\mathrm{T}}^{\mathrm{miss}}$ system must be less than 160 GeV
- $\left|E_{\mathrm{T}}^{\mathrm{miss}} + \tau_{\mathrm{e}}\right| > 250\,\mathrm{GeV}$
- $E_{\mathrm{T}}^{\mathrm{miss}} > 50GeV$ to suppress QCD multijet background events

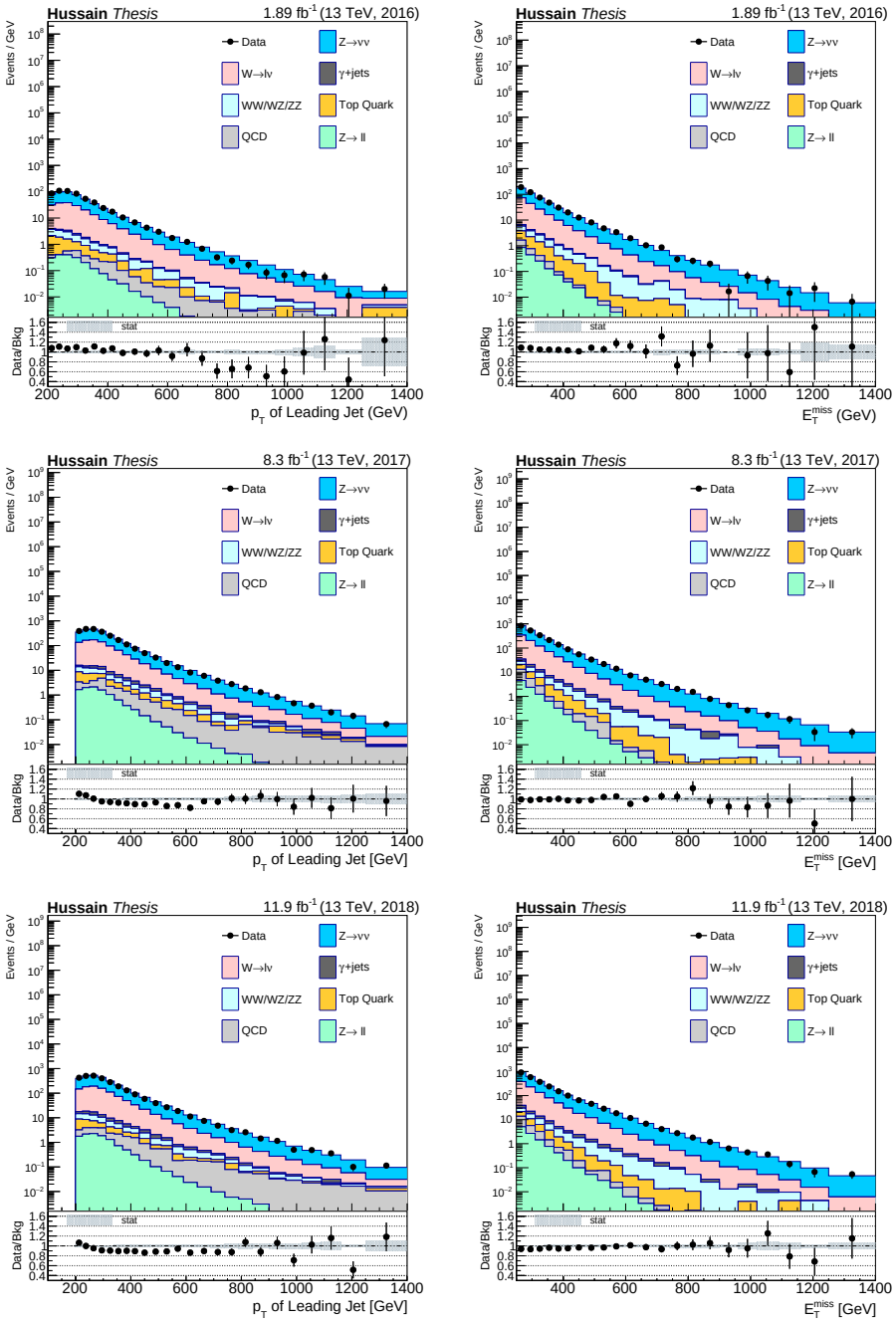

Figure B.8: Blinded Signal region distributions of the transverse momentum of the leading jet in the event (left) and $E_{\mathrm{T}}^{\mathrm{miss}}$ (right) for three years of data-taking 2016-2018.

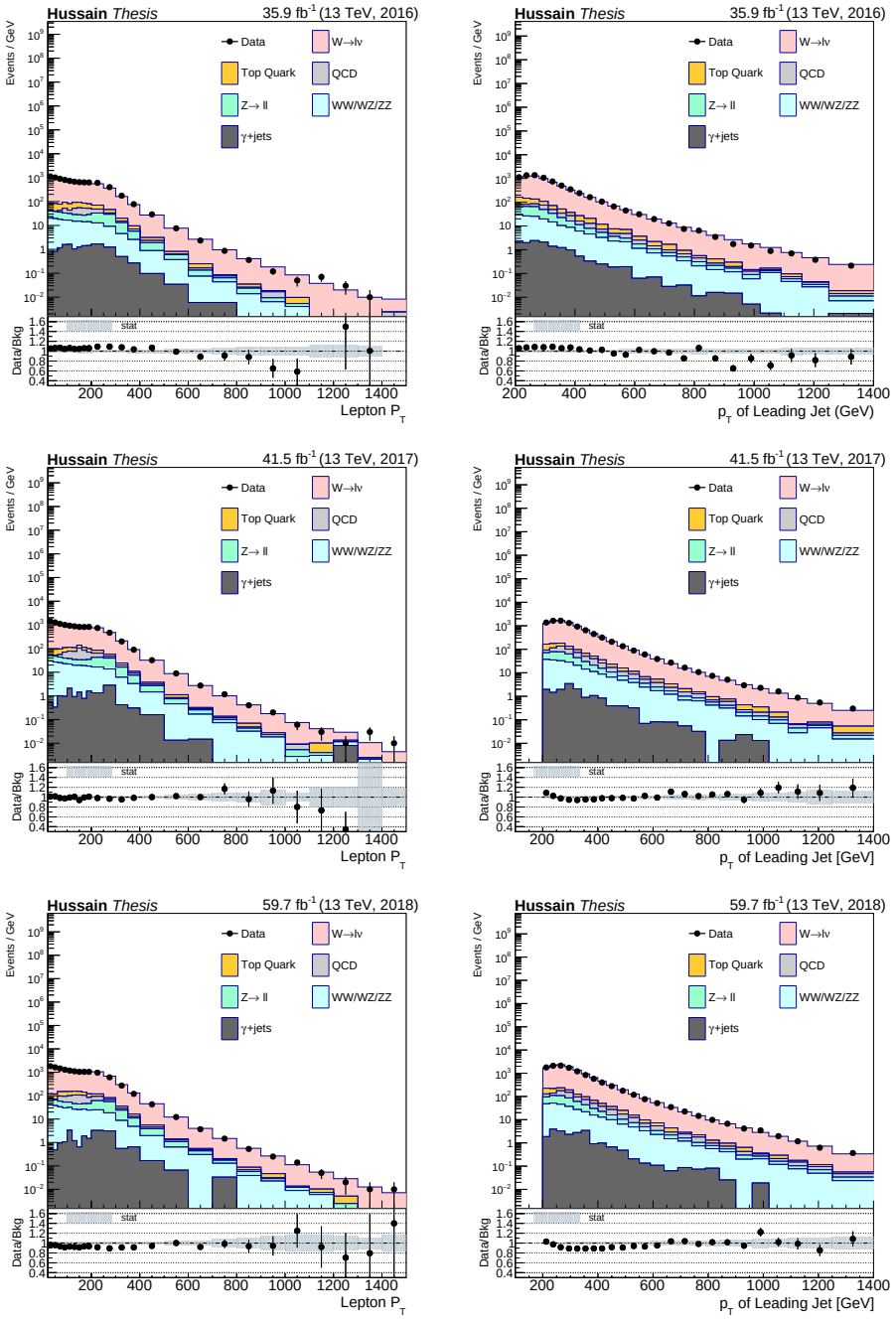

Figure B.9: Transverse momentum of the Muon (left) and the leading jet (right) in the single muon CR. As usual, distributions for three years of data-taking 2016-2018 are provided.

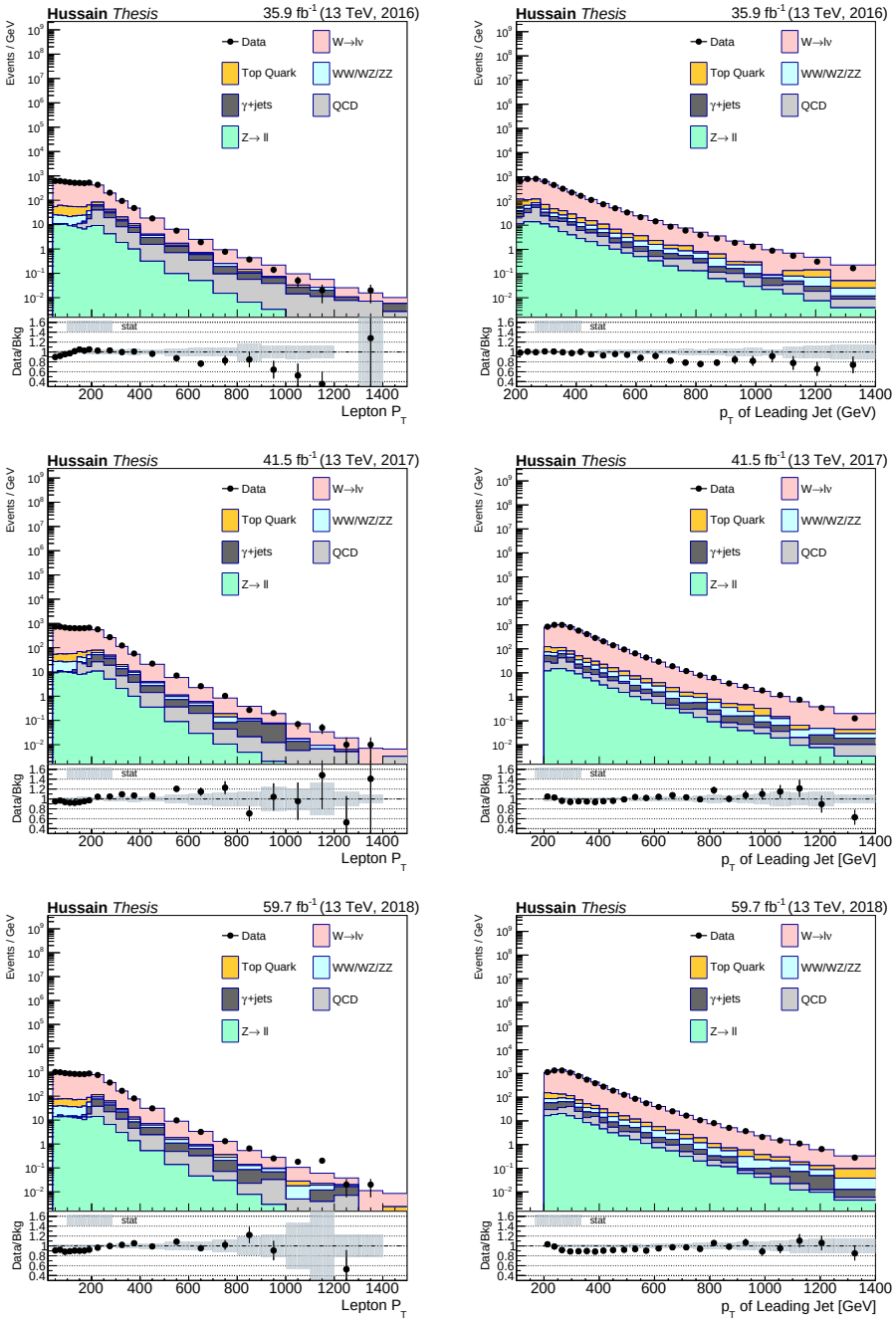

Figure B.10: Transverse momentum of the Electron (left) and the leading jet (right) in the single electron CR. As usual, distributions for three years of data-taking 2016-2018 are provided.

D.2.4 Double muon control region

Events in the double muon control region are obtained using the same selection as signal region with the following differences.

- Events must have exactly two loose muons with opposite charge
- At least one of the muons passes the tight identification requirements with the leading (subleading) muon $p_T > 20\,\text{GeV}(10\,\text{GeV})$
- The invariant mass of the two muons is between the range 60 and 120 GeV
- $\left|E_{\text{T}}^{\text{miss}} + \tau_{\mu\mu}\right| > 250\,\text{GeV}$

D.2.5 Double electron control region

Events in the double electron control region are obtained using the same selection as signal region with the following differences.

- Events are selected using the single electron and photon triggers described in section D.1
- Events must have exactly two loose electrons with opposite charge
- At least one of the electrons passes the tight identification requirements with the leading (subleading) electron $p_T > 40\,\text{GeV}(10\,\text{GeV})$
- The invariant mass of the two electrons is between the range 60 and 120 GeV
- $\left|E_{\text{T}}^{\text{miss}} + \tau_{\text{ee}}\right| > 250\,\text{GeV}$

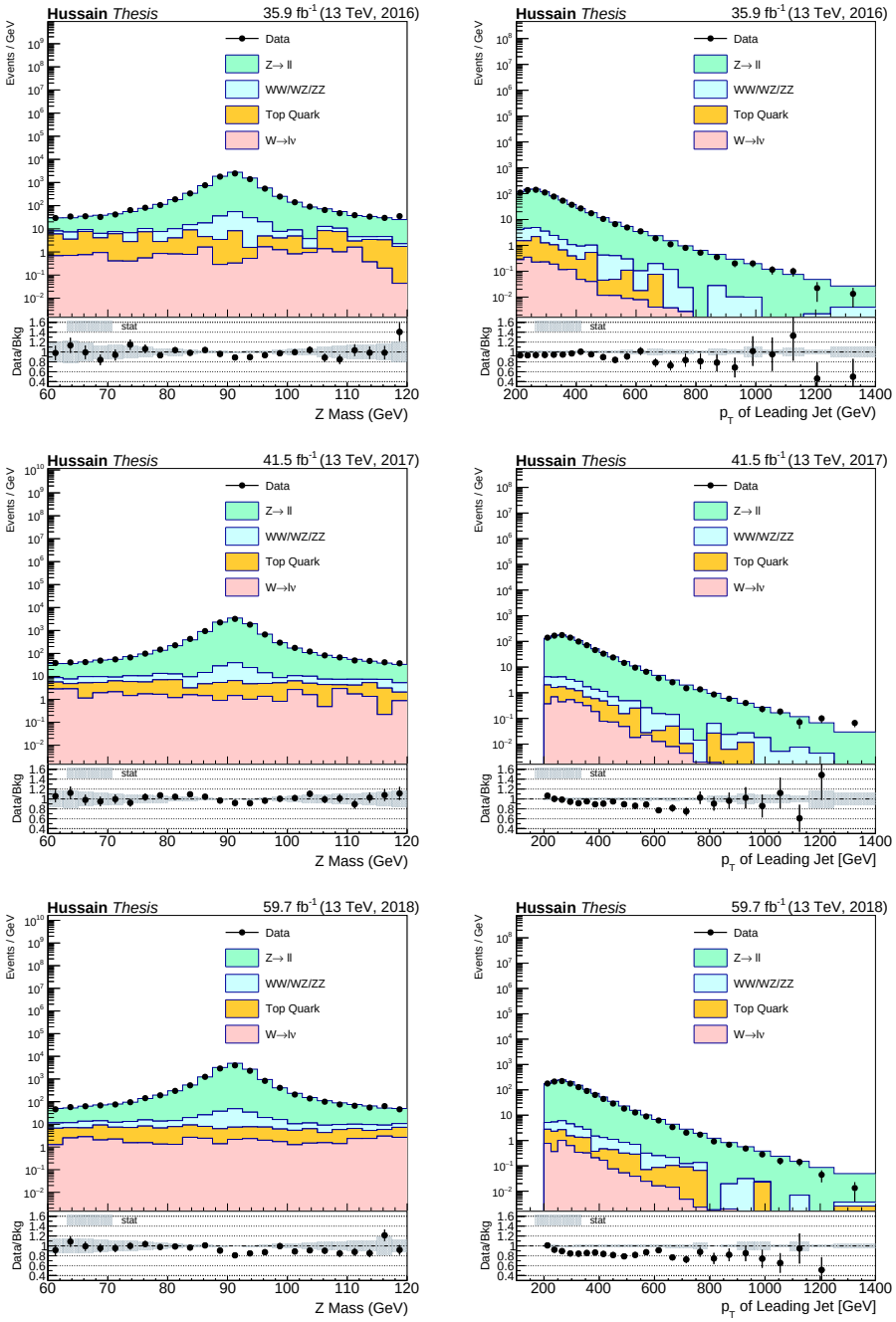

Figure B.11: Invariant mass of the di-muon system (left) and the leading jet (right) in the double muon CR. As usual, distributions for three years of data-taking 2016-2018 are provided.

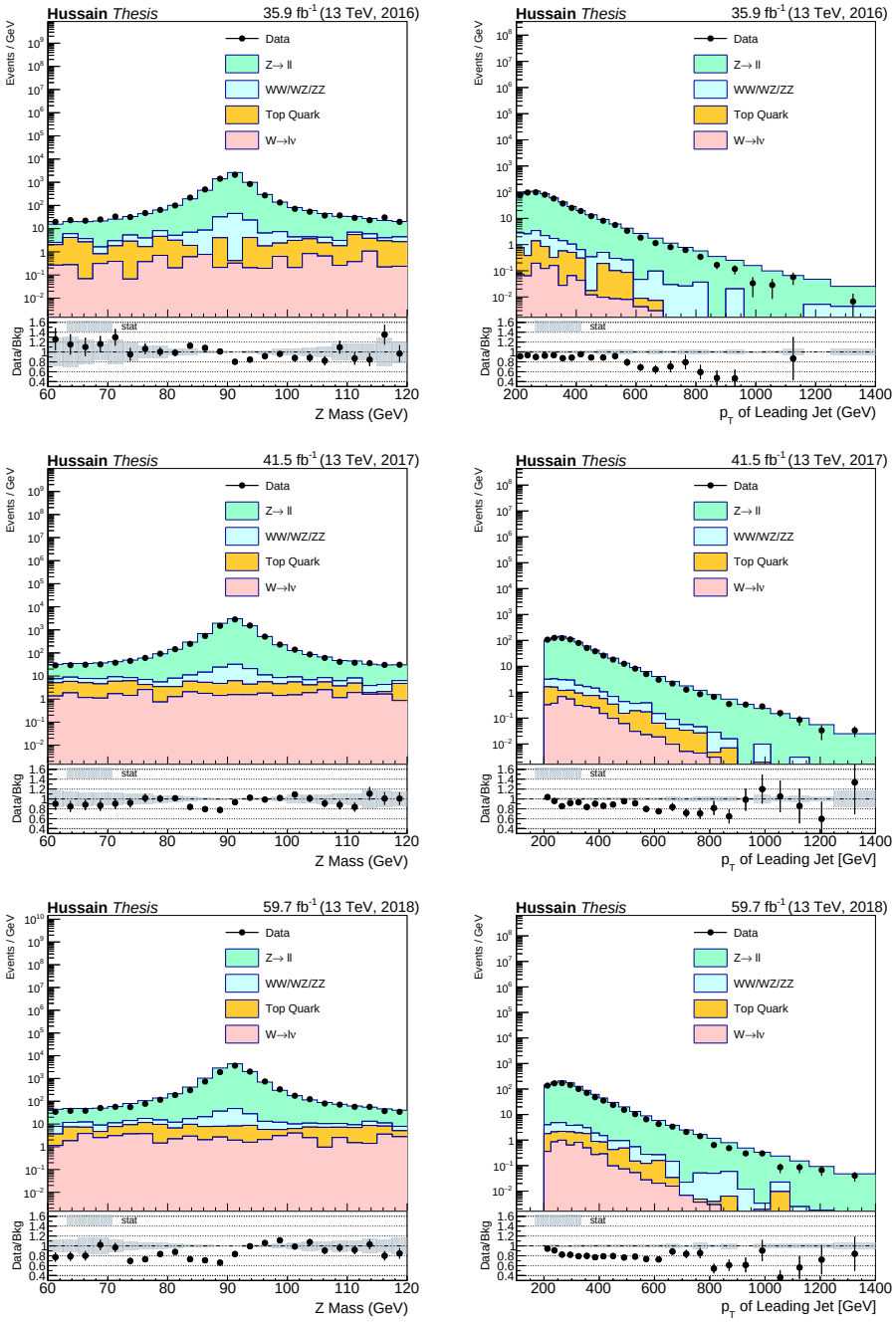

Figure B.12: Invariant mass of the di-electron system (left) and the leading jet in the double electron CR. As usual, distributions for three years of data-taking 2016-2018 are provided.

D.2.6 Photon control region

Events in the γ+jets control region are subject to the same selection requirements as the signal region with the following notable differences.

- Events are selected using the single photon trigger listed in Tables B.2–B.3
- Event must have exactly one loose photon that also passes the tight identification requirements
- Photon must have $p_{\mathrm{T}} > 230\,\mathrm{GeV}$
- $\left|E_{\mathrm{T}}^{\mathrm{miss}} + \tau_{\gamma}\right| > 250\,\mathrm{GeV}$

D.3 Signal Variable

As discussed in Section D, the Mono-Z' Pencil Jet signal led to using the jet substructure to discriminate between signal and backgrounds. After several studies of jet substructure variables consisting of kinematics of jet constituents, the analysis has settled on the following $p_{\mathrm{T}}^{123} Fraction$ variable which is referred as just "PtFraction" in rest of the text. It is defined as,

$$P_T^{123} Fraction = \frac{\sum_{i=1}^{3} \left(P_T\left(\pi_{PF}^{\pm}\right) + P_T\left(\gamma_{PF}\right)\right)}{\sum_{i=1}^{N} \left(P_T\left(\pi_{PF}^{\pm}\right) + P_T\left(\gamma_{PF}\right)\right)} \tag{B.3}$$

So, as shown in eqn. B.3, the PtFraction varaible is constructed using charged hadrons and photon candidates given by the particle-flow algorithm. As expected for the Mono-Z' jet, most of its energy is concentrated in the first few leading constituents. Usually, the first two or three leading jet constituents constitute more than 99% of the energy of the leading jet. Neutral hadrons are conveniently not used in the calculation as they do not contribute to the signal and the energy of neutral hadrons is

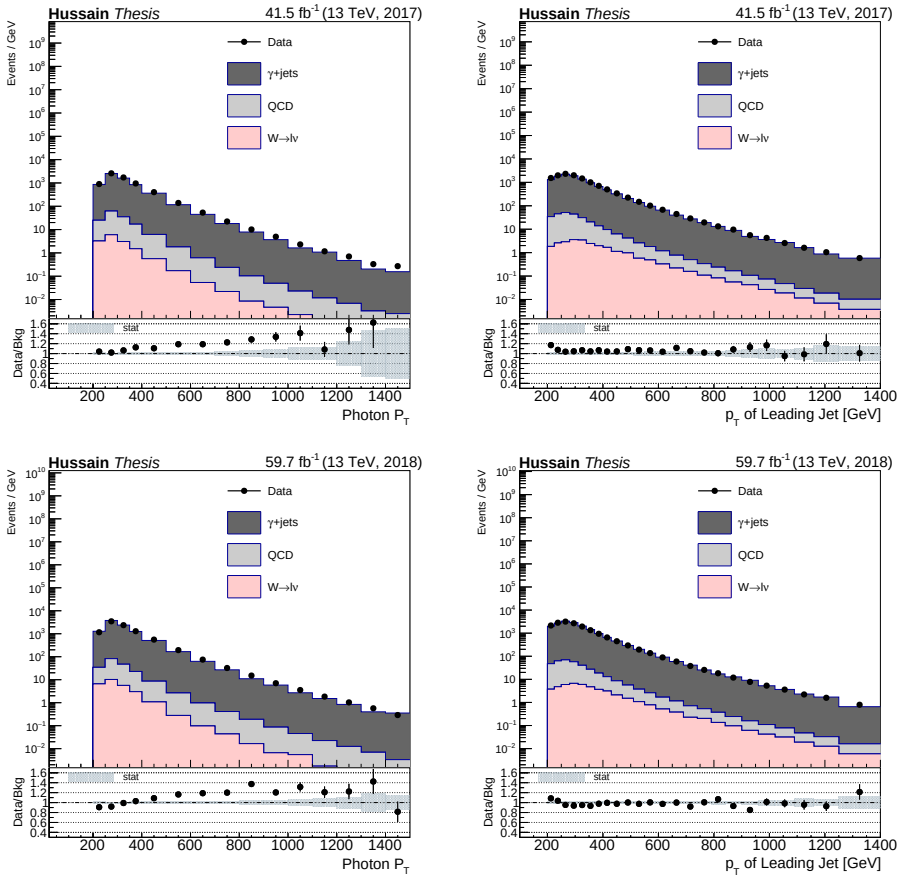

Figure B.13: Transverse momentum of the photon (left) and the leading jet in the Photon CR. Only distributions of 2017,2018 are provided, 2016 will be added.

poorly measured in the CMS detector. Although Kaons are the heaviest neutral particles that Z' could theoretically decay to (though highly unlikely) but several studies of signal MC samples have shown that the K_L contribution is $\approx$0% of the generator jet. In Figs. B.14– B.16, partially unblinded distributions for this signal variable are shown for all three years in the signal region. Modeling such a unique highly-boosted narrow Pencil-Jet has been a challenge especially in the higher PtFraction bins where most of the signal resides but overall, the parton shower uncertainties as explained in section. D.5.1 cover these discrepancies as expected.

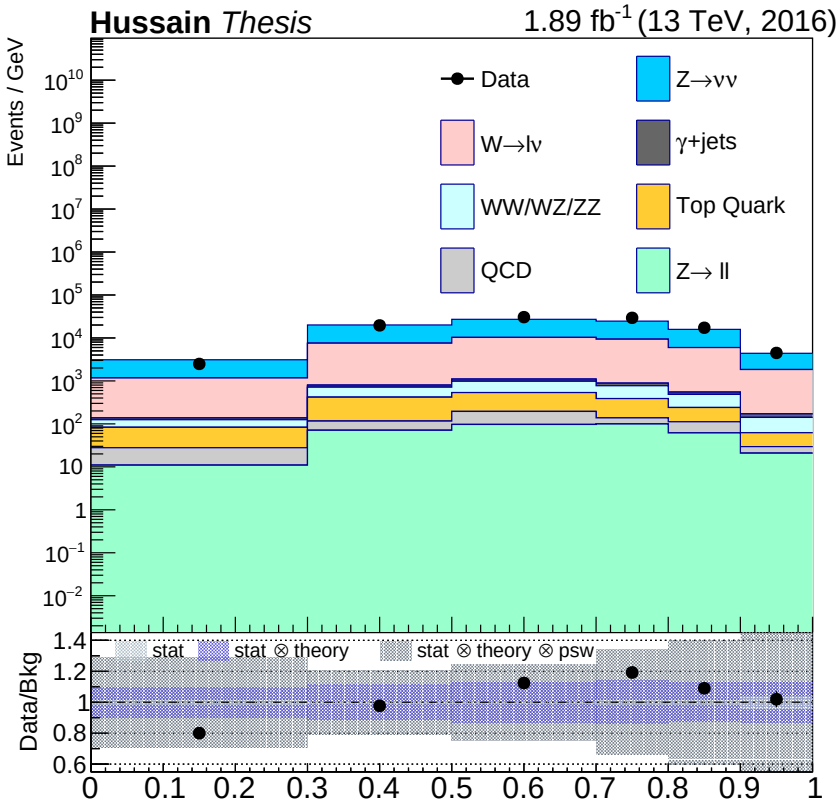

Figure B.14: Ch+NEM P_T^{123}Fraction of the leading jet. Distributions (partially unblinded) for 2016.

D.4 Background Estimation

The leading background in this search come from events with a Z boson produced together with a number of jets where the Z boson decays to two neutrinos. This creates the same signature in the detector as our signal and hence becomes a so-called irreducible background. The second largest background consists of W+jets events with a leptonically decaying W boson. As described in section D.2 above, this background is suppressed by the lepton veto but a fraction of these events still remain when the lepton is not identified or not reconstructed because its outside of the detector acceptance. The remaining background events come from top quark

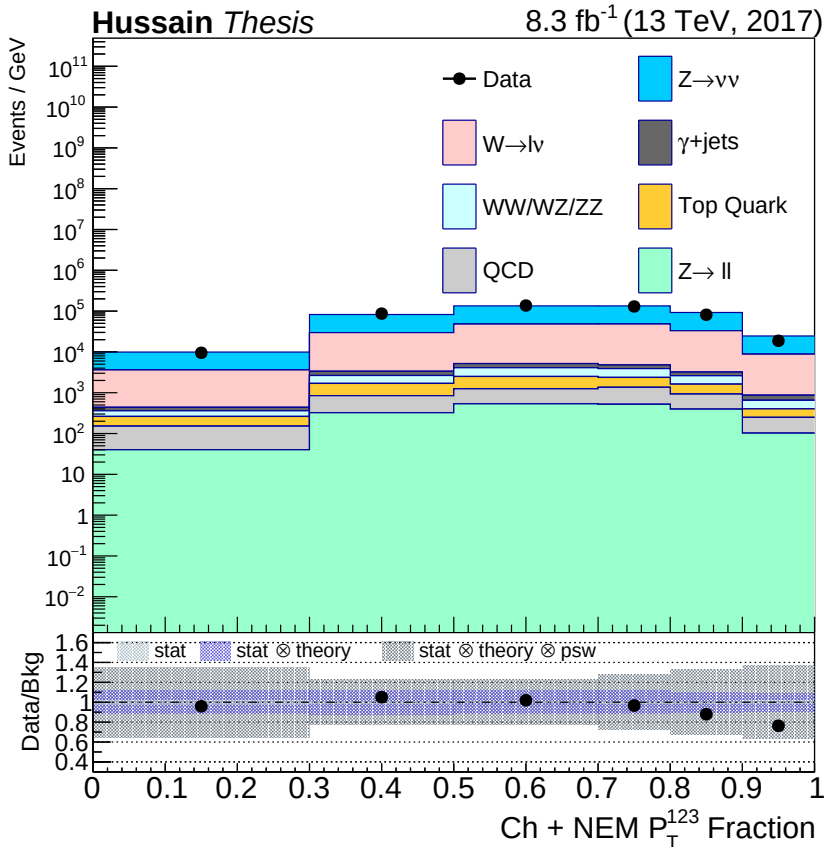

Figure B.15: Ch+NEM P_T^{123}Fraction of the leading jet. Distributions (partially unblinded) for 2017.

decays, which are suppressed by the b-jet veto, semileptonic decays of diboson pairs (WW, WZ, ZZ) and QCD multi jet events. The two leading backgrounds in this search, Z $\rightarrow \nu\nu$ + jets and W + jets are estimated using the five control regions in data which are dimuon, dielectric, single muon, single electron and photon + jets events. The rest of the backgrounds are estimated using simulated samples.

D.4.1 The Z and W background estimation

The yield of the two leading backgrounds in this search, namely Z $\rightarrow \nu\nu$ + jets and W + jets, is estimated from five control regions by using the ratio between data and

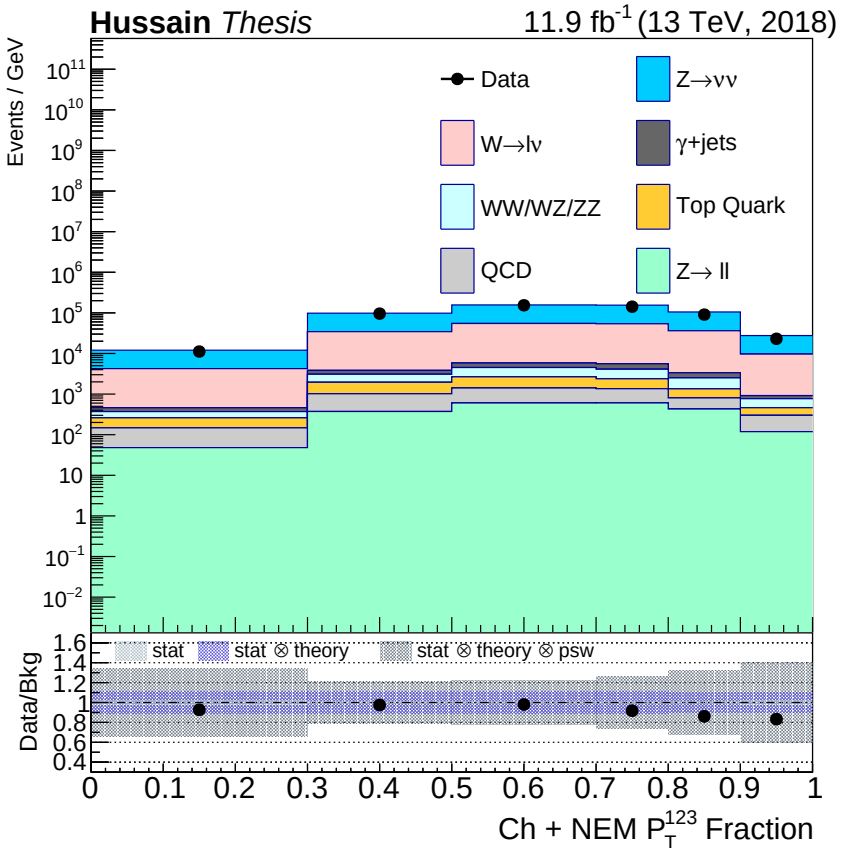

Figure B.16: Ch+NEM P_T^{123}Fraction of the leading jet. Distributions (partially unblinded) for 2018.

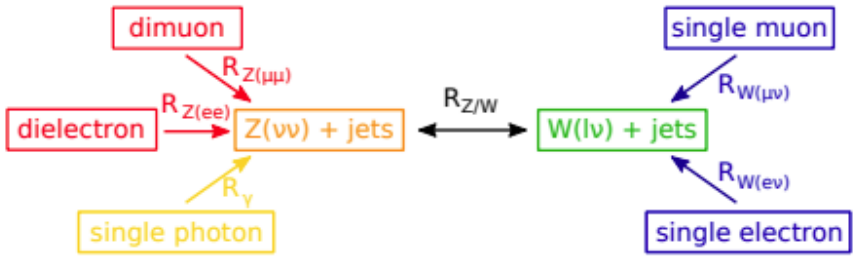

Figure B.17: Schematic overview of the five control regions used to estimate the Z($\nu\nu$) and W($\ell\nu$) + jets backgrounds with the transfer factors.

MC in the control region, per bin of the PtFraction distribution. As shown in the schematic diagram in Fig. B.17, the W($\ell\nu$) + jets background is estimated from the two single lepton CRs (single muon, single electron) and the Z($\nu\nu$) + jets background requires the two dilepton and the photon + jets CRs. The following equation is used to derive the five transfer factors that are needed to link the control regions to the signal region.

$$R_i^{\mathrm{Z}} = \frac{N_{i,MC}^{\mathrm{Z}\to\nu\nu}}{N_{i,MC}^{\mathrm{Z}\to\mu^+\mu^-}} \tag{B.4}$$

where N_i is the number of events in bin i of the PtFraction distribution and R_i is the transfer factor. The transfer factors are computed as a function of the signal PtFraction variable and are shown for the three years in Fig.B.18–Fig.B.20. The Z/W ratio shown in the bottom right plot of Fig.B.20 provides an additional constraint between Z($\nu\nu$) + jets and W($\ell\nu$) + jets backgrounds. A combined maximum likelihood fit to the data is performed simultaneously in the five different CRs and in the SR for events selected for the Mono-Z' signature in each PtFraction bin. The methodology for this fit is taken from Ref.[223] and while the method is summarized below more details about the process can be found there.

$$\begin{aligned}
\mathcal{L}(\boldsymbol{\mu}^{\mathrm{Z}\to\nu\nu}, \boldsymbol{\mu}, \boldsymbol{\theta}) = &\prod_i \mathcal{P}\left(\mathrm{d}_i^{\gamma}\middle|B_i^{\gamma}(\boldsymbol{\theta}) + \frac{\mu_i^{\mathrm{Z}\to\nu\nu}}{R_i^{\gamma}(\boldsymbol{\theta})}\right) \\
&\times \prod_i \mathcal{P}\left(\mathrm{d}_i^{\mathrm{Z}}\middle|B_i^{\mathrm{Z}}(\boldsymbol{\theta}) + \frac{\mu_i^{\mathrm{Z}\to\nu\nu}}{R_i^{\mathrm{Z}}(\boldsymbol{\theta})}\right) \\
&\times \prod_i \mathcal{P}\left(\mathrm{d}_i^{\mathrm{W}}\middle|B_i^{\mathrm{W}}(\boldsymbol{\theta}) + \frac{f_i(\boldsymbol{\theta})\mu_i^{\mathrm{Z}\to\nu\nu}}{R_i^{\mathrm{W}})(\boldsymbol{\theta})}\right) \\
&\times \prod_i \mathcal{P}\left(\mathrm{d}_i\middle|B_i(\boldsymbol{\theta}) + (1 + f_i(\boldsymbol{\theta}))\mu_i^{\mathrm{Z}\to\nu\nu} + \mu S_i(\boldsymbol{\theta})\right)
\end{aligned} \tag{B.5}$$

where $\mathcal{P}(X)$ is the Poisson probability, $\mathrm{d}_i^{\gamma/\mathrm{Z}/\mathrm{W}}$ are the observed number of events and $B_i^{\gamma/\mathrm{Z}/\mathrm{W}}$ is the background in each PtFraction bin of the respective control regions.

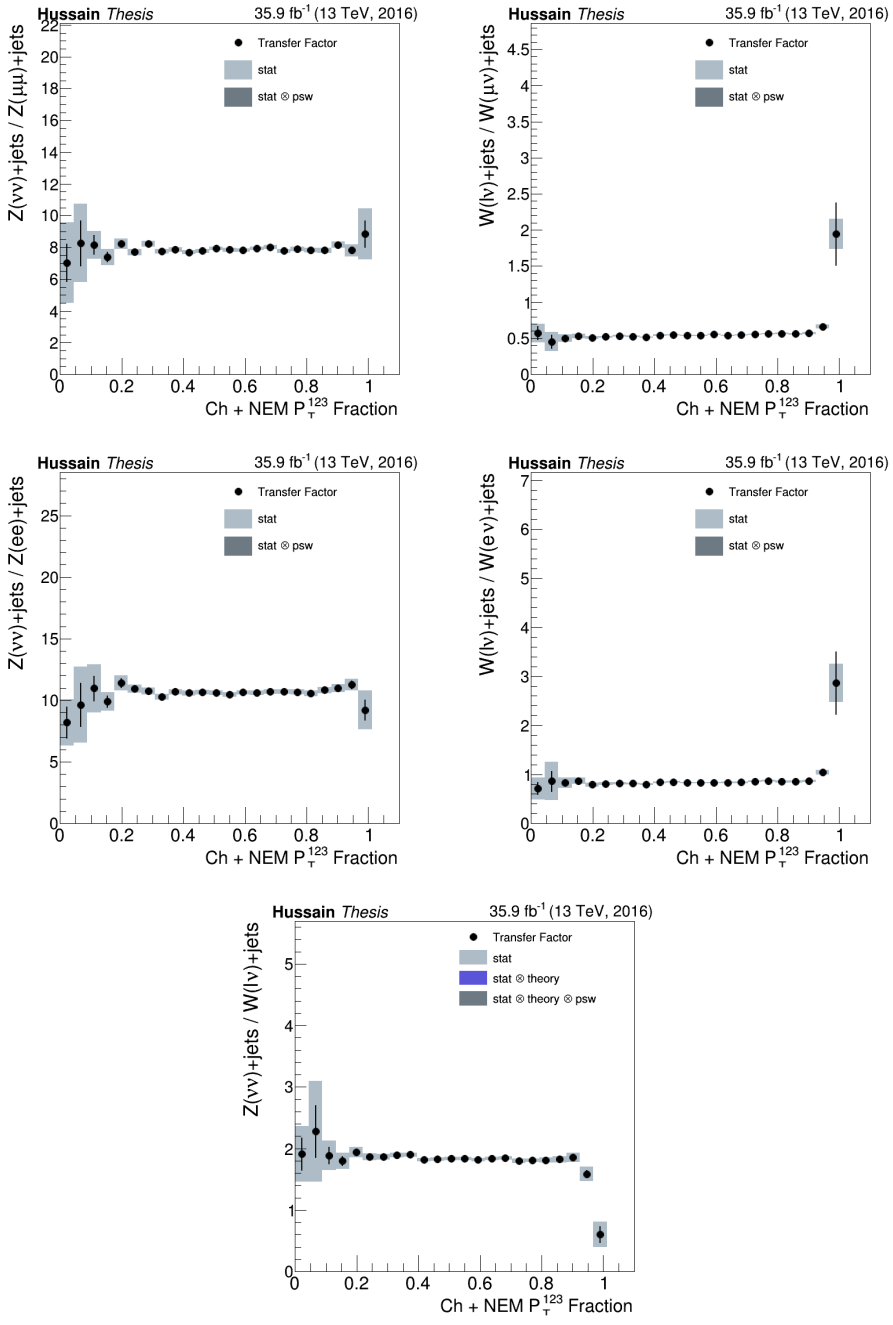

Figure B.18: Transfer factors for the 2016 dimuon (top left), single muon (top right), dielectron (middle left), single electron (middle right) control regions. Photon + jets needs to be added for 2016. The ratio of the Z and W transfer factors is shown in the bottom left plot.

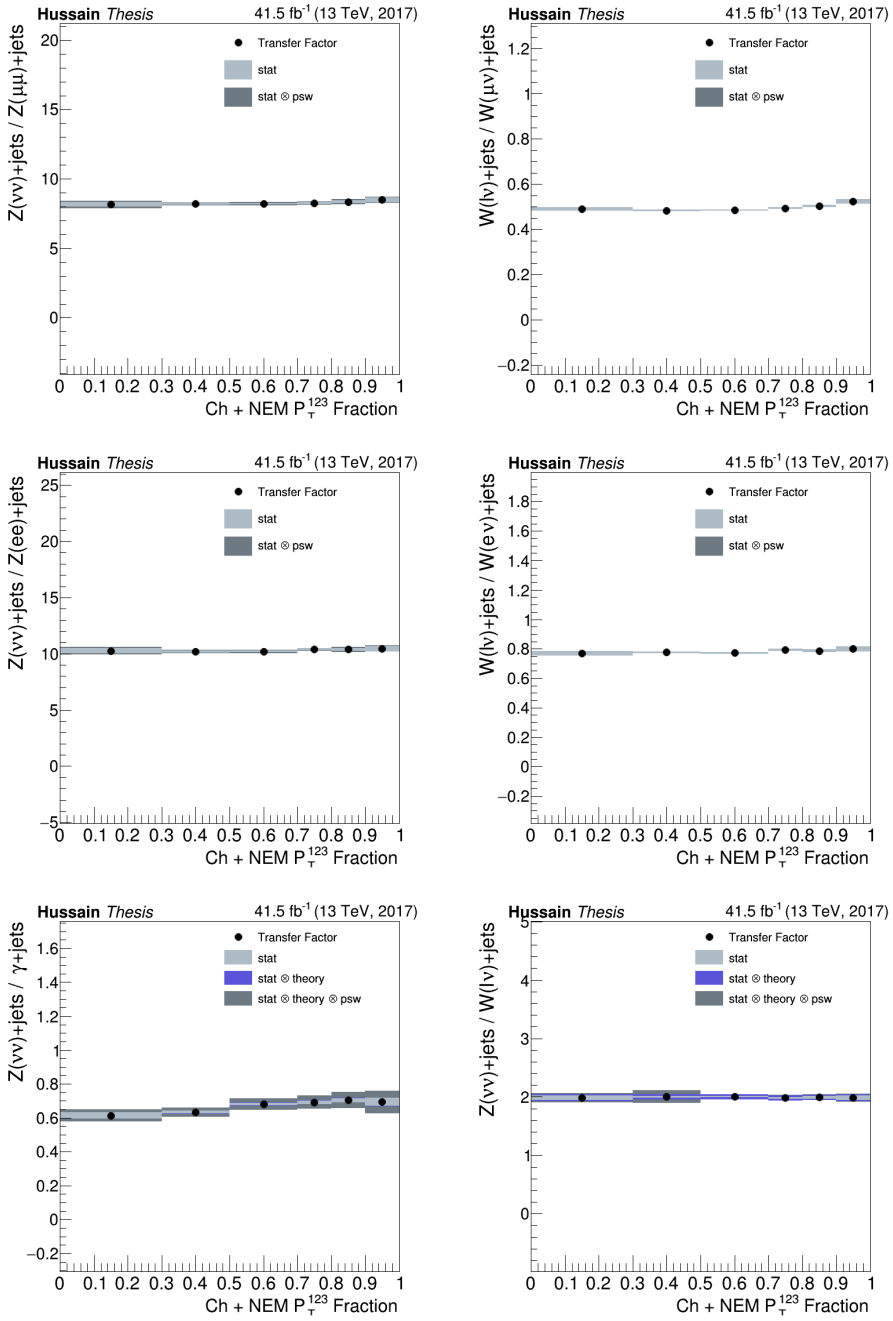

Figure B.19: Transfer factors for the 2017 dimuon (top left), single muon (top right), dielectron (middle left), single electron (middle right), and photon + jets (bottom left) control regions. The ratio of the Z and W transfer factors is shown in the bottom right plot.

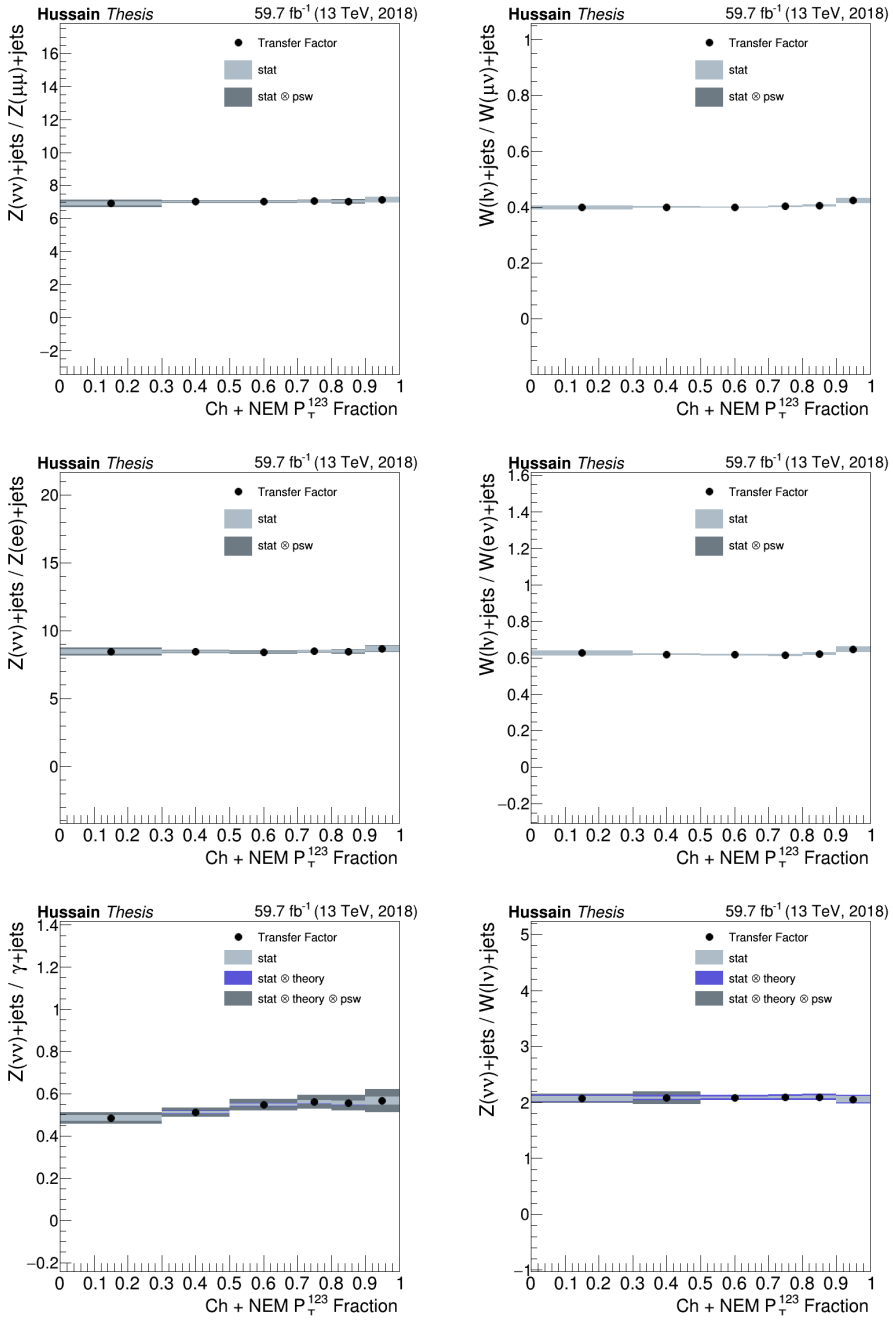

Figure B.20: Transfer factors for the 2018 dimuon (top left), single muon (top right), dielectron (middle left), single electron (middle right), and photon + jets (bottom left) control regions. The ratio of the Z and W transfer factors is shown in the bottom right plot.

The systematic uncertainties (θ) affect the likelihood as additive perturbations to the transfer factors and are modeled as Gaussians. The parameter $\mu_i^{\mathrm{Z}\to\nu\nu}$ represents the yield of the $\mathrm{Z}\to\nu\nu$ background in the i-th PtFraction bin into the signal region and is a free floating parameter in the fit. The function $f_i(\theta)$ is the transfer factor between the $\mathrm{Z}\to\nu\nu$ and $\mathrm{W}+jets$ backgrounds in the signal regions which represents a constraint between these backgrounds. Finally, the likelihood includes the signal region where B_i represents all the backgrounds, S represents the nominal signal prediction and μ being the signal strength left floating in the fit.

D.4.2 Simulation-based background estimation

While the two leading backgrounds make up more than 90% of the total backgrounds in this search, there are contributions expected from diboson production, top quark decays and from $\mathrm{Z}(\ell\ell)$ + jets (so-called Drell-Yan) events where the leptons are not detected. All these backgrounds are estimated from MC simulations and the description of how these samples are generated has been discussed in section C.

For instance, top quarks typically decay into a W boson and a b quark. The W boson can decay leptonically in association with a neutrino and hence producing genuine $E_{\mathrm{T}}^{\mathrm{miss}}$ in the event. If such an event is not removed by the b-jet veto and the lepton is not identified, it contributes as a background to the signal region. However, this process has a small production cross section and the event selections described in section D.2 ensure that less than 1% of the backgrounds are of this nature. In order to estimate the contribution of this background, relevant $\mathrm{t\bar{t}}$ MC samples are produced as described in section C.

For the diboson backgrounds, when one of the weak bosons decays leptonically while the other one decays hadronically (*e.g.* $\mathrm{W}\to\ell\nu, \mathrm{Z}\to\nu\nu$), jets and $E_{\mathrm{T}}^{\mathrm{miss}}$ are produced in the event. The relevant samples used to estimate this background are

produced as described in sectionC as well.

Finally, there are QCD multijet events where mismeasured or undetected jet events can serve as background events, γ + jets can produce fake $E_{\mathrm{T}}^{\mathrm{miss}}$ due to events in which the photon goes undetected and when the leptons in the $\mathrm{Z}(\ell\ell)$ + jet event are lost or go out of the detector acceptance, they can produce some fake $E_{\mathrm{T}}^{\mathrm{miss}}$ and mimic the mono-Z' signal. However, all these backgrounds are negligible after all the event selections are applied and are estimated using appropriate MC samples described in sectionC.

D.5 Systematic uncertainties

In the context of the main backgrounds (section D.4.1), several systematic uncertainties on the transfer factors are considered. Across three years, all experimental uncertainties are uncorrelated between the years unless otherwise noted and theoretical uncertainties are correlated. Systematic uncertainties related to the leptons and photons reconstruction, identification and isolation efficiencies are all taken from the relevant POGs similar to what is done for the ZZ analysis described in this thesis. Additional shape uncertainties are added to take into account the MET, electron and photon triggers. All these uncertainties are considered to be full correlated across the bins in PtFraction. Apart from the **Parton Shower Uncertainties** which are discussed in detail in section D.5.1, the jet energy scale uncertainty dominates the modeling of the jet substructure variables as well as recoil. The uncertainty on the integrated luminosity of the data sample is 2.5% (2016) [90], 2.3% (2017) [87], and 2.5% (2018) [88]. All these uncertainties and their overall effect is shown in Table B.4.

In addition to the aforementioned uncertainties, variations of the factorization and renormalisation scales, PDF uncertainties, and the NLO electroweak corrections[224–227] are also considered. The procedures to evaluate and apply these uncertainties are

Table B.4: The experimental and theoretical uncertainties that will be considered for the setting limits in the Mono-Z' search and are used for the combined likelihood fit performed with transfer factors to estimate the main backgrounds as described in section D.4.1. The parton shower uncertainties are discussed in the section below.

Source	Uncertainty
Electron Trigger	1%(shape)
MET Trigger	2%(shape)
B-jet veto	1%
JES	4%
Pileup	2%(shape)
Lepton veto uncertainties	1–2%(shape based)
Parton shower ISR	8%
Parton shower FSR	10%
Integrated luminosity	2.5% (2016), 2.3% (2017), 2.5%(2018)

taken directly from the monojet analysis[205] and more details can be found there. In summary, for the PDF uncertainty, the samples are reweighted with event-by-event scale factors representing the shift in the kinematic distributions from variations in the PDF. The renormalisation and factorisation scales are varied up and down by a factor 2, and the uncertainties are derived from the resulting transfer factors. For the electroweak corrections, the full correction is taken as an uncertainty[205].

D.5.1 Parton Shower uncertainties

There are four main elements of general purpose monte-carlo event generators at the LHC namely hard process, parton shower, hadronization and the underlying event. Beyond SM hard process, parton shower is the only component directly connected to the SM (QCD) Lagrangian and it holds the key to precision in the MC prediction. It should be noted that there are two basic input parameters influencing MC predictions; choice of the order of the PDF sets and the value of the strong coupling α_s. For instance, the 2016 MC samples are generated with NNPDF3.0 [96] ($\alpha_s = 0.130$) and

2017,2018 MC predictions are generated with NNPDF3.1 [97] ($\alpha_s = 0.118$).

Therefore, parton shower weights encapsulate the effects of such parameter variations in the parton shower part of the MC prediction. By varying the scale at which the α_s value is evaluated for each quark/gluon splitting or radiation in the shower, and therefore the rate and kinematics of these splittings leads to differences in the shape of the jets and the momentum distribution of the constituents of the jet. Hence, this would affect the selection based on the leading three constituents associated with our high energy but narrow "Pencil" Jets. Through studies of these variations encoded as parton shower weights, it was discovered that **renormalisation FSR/ISR scale variations** and **splitting-kernel variations** cover the most important settings in Pythia relevant to jet formation via PS which can also be varied within reasonable bounds.

While more details on how the effect of such parameter variations in the PS is estimated and how these variations are encoded as appropriate event weights can be found in Ref.[228], there are 32 decorrelated PS variations that are included in all latest MC samples which can be represented in a short-form: (ISR, FSR) $\otimes$ (μ_R,cNS) $\otimes$ ($\mathrm{g} \to \mathrm{gg}, \mathrm{g} \to \mathrm{q\bar{q}}, \mathrm{q} \to \mathrm{gq}, x \to x\mathrm{g}$) $\otimes$ (up,down) where x is b, t or heavier with UncertaintyBands:nFlavQ = 4 [228].

D.6 Results

The results are extracted by performing a binned fit to the PtFraction distribution, fitting simultaneously over the five control regions (signal region is not considered yet), and using all three years of data. Eventually, the fit will include the signal region and the 2016 photon+jets control region which is currently not included. Z($\nu\nu$) has one yield parameter per bin and are treated as uncorrelated and all other processes are defined thorugh transfer factors relative to Z($\nu\nu$). Experimental uncertainties are

treated as uncorrelated between the years but theoretical uncertainties are correlated. The systematic uncertainties described in Section. D.5 are modelled as nuisance parameters and their uncertainties are propagated as shape and normalization variations of the Z($\nu\nu$) + jets and W + jets background. Figs. B.21– B.23 show that post-fit predictions correspond well with the data in this CR-only fit.

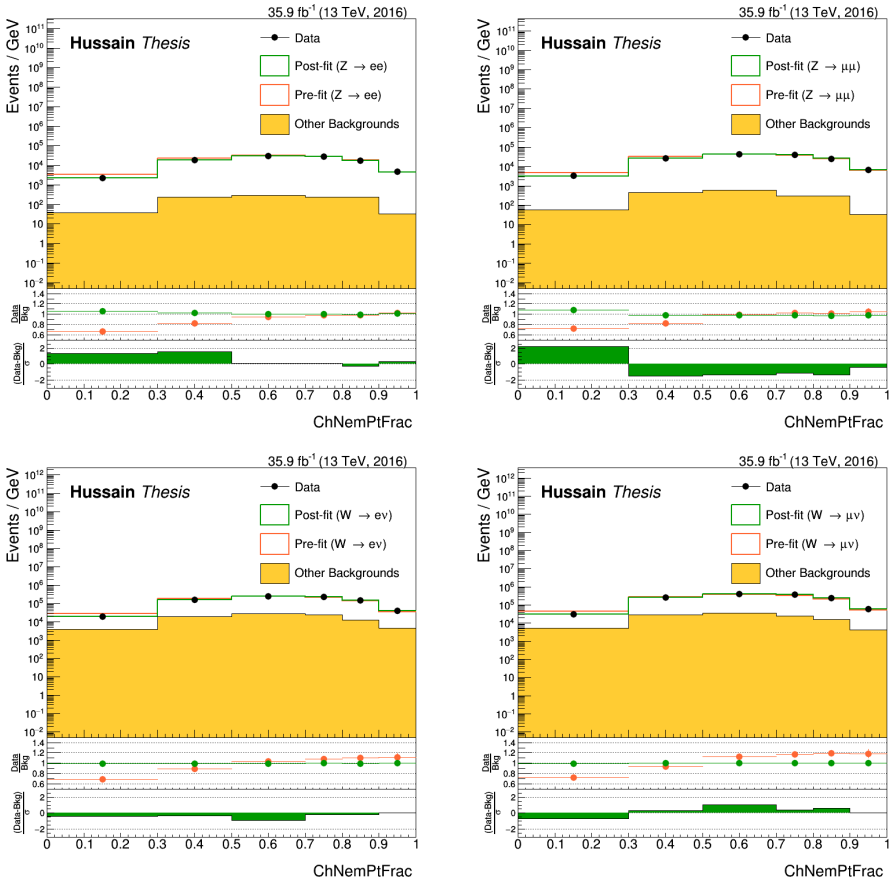

Figure B.21: Comparison between data and MC simulation in the dielectron (top left), dimuon (top right), single electron (middle left) and single muon (middle right) control samples before and after performing the simultaneous fit across all the control samples. A combined fit is performed using the 2016-2018 datasets at the same time but the resulting distributions are shown separately for 2016 here.

Finally, using the signal samples described in Table. B.1, the 95% CL expected limits on σ/σ_{theory} are shown in Fig. B.24 for the simplified dark matter model with

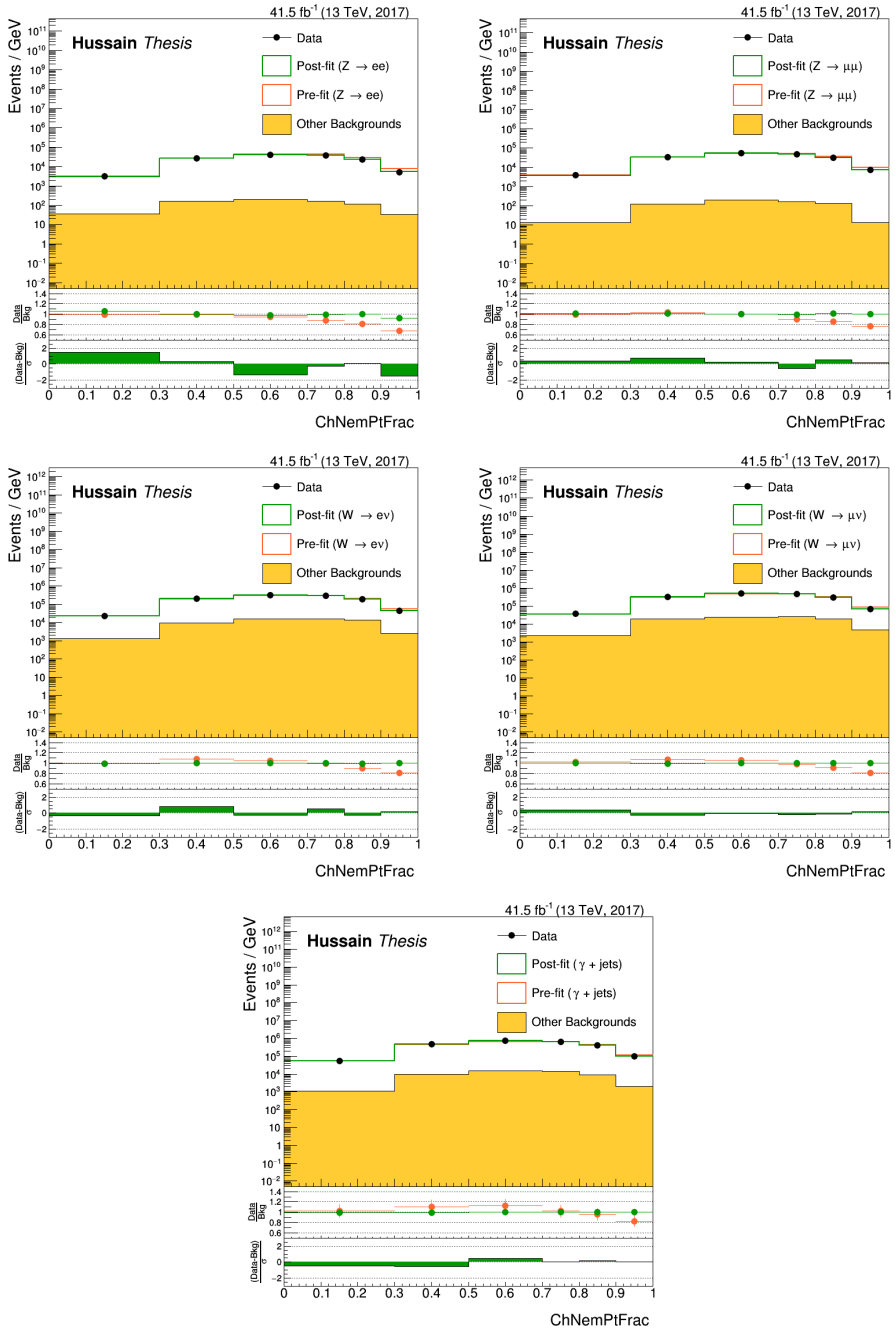

Figure B.22: Comparison between data and MC simulation in the dielectron (top left), dimuon (top right), single electron (middle left), single muon (middle right), and photon + jets (bottom left) control samples before and after performing the simultaneous fit across all the control samples. A combined fit is performed using the 2016-2018 datasets at the same time but the resulting distributions are shown separately for 2017 here.

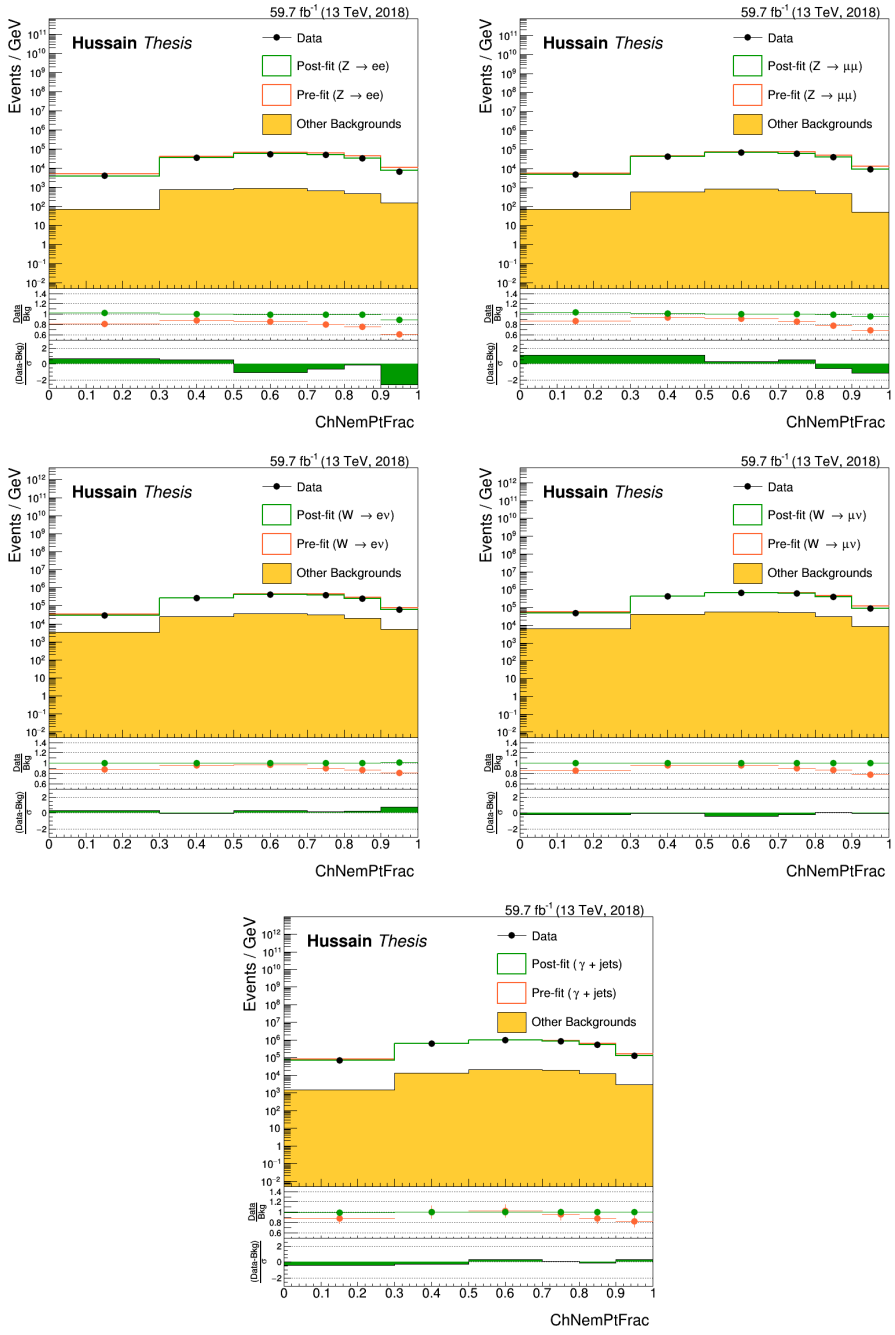

Figure B.23: Comparison between data and MC simulation in the dielectron (top left), dimuon (top right), single electron (middle left), single muon (middle right), and photon + jets (bottom left) control samples before and after performing the simultaneous fit across all the control samples. A combined fit is performed using the 2016-2018 datasets at the same time but the resulting distributions are shown separately for 2018 here.

couplings $g_q = 0.25$ and $g_{DM} = 1.0$. These expected limits are preliminary results and final results and observed limits in this context are expected soon as the UW CMS group continues the work and progress on this analysis.

D.7 Summary and Outlook

The current status and progress of the search for new physics in events with a narrow mono-Z' Pencil-Jet" with small number of constituents and a large transverse momentum imbalance has been presented. This search is based on a data set of proton-proton collisions collected with the CMS experiment during three years of data taking from 2016 to 2018, corresponding to an integrated luminosity of 137 fb^{-1} at $\sqrt{s} = 13\,\text{TeV}$. This is a unique signature with FSR whereas most existing searches for new physics in similar channels have focused on ISR jets and the expected exclusion limits calculated suggest that the mono-Z' search can provide stronger exclusionary limit than previous mono-jet searches especially for the low dark-matter mass regions such as $m_\chi < 200\,\text{GeV}$. However, with the eventual unblinding of the results in the near future, these conclusions might evolve. By presenting the report of the current status of the analysis, the hope is that the final requirements to publish this analysis will be satisfied soon as it will be a unique and interesting result in the myriad of dark matter searches performed at the LHC.

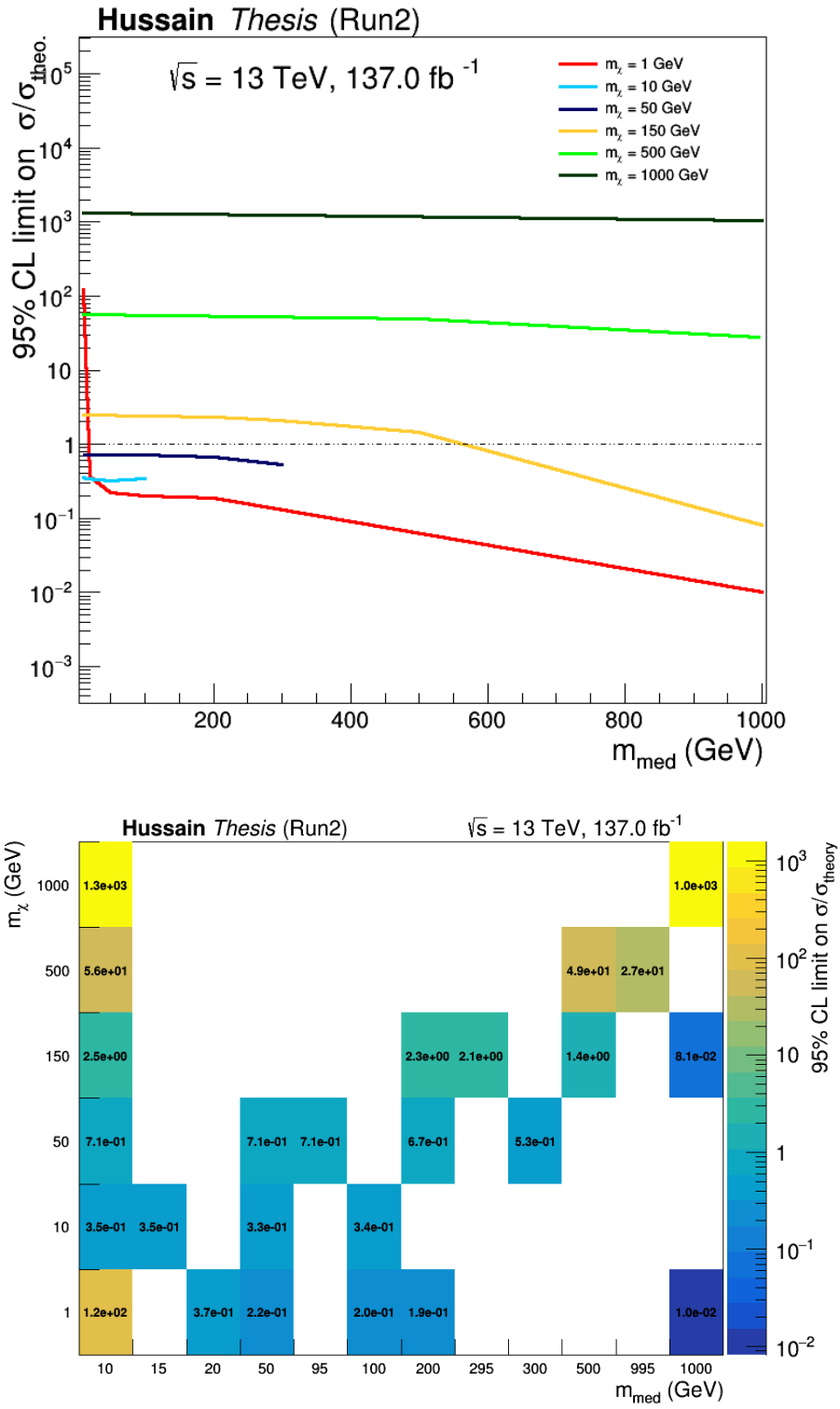

Figure B.24: The 95% CL expected limits on σ/σ_{theory} for a particular $m_{\chi} - m_{med}$ phase-space. The expected limits suggest strong exclusion for low dark matter masses.